

# MEASUREMENT OF EDGE ELECTROSTATIC TURBULENCE IN THE TCV TOKAMAK PLASMA BOUNDARY

THÈSE N° 3524 (2006)

PRÉSENTÉE LE 5 MAI 2006  
À LA FACULTÉ SCIENCES DE BASE  
CRPP Association Euratom  
SECTION DE PHYSIQUE

ÉCOLE POLYTECHNIQUE FÉDÉRALE DE LAUSANNE

POUR L'OBTENTION DU GRADE DE DOCTEUR ÈS SCIENCES

PAR

Jan HORACEK

Magister, Université Carolina, Prague, République Tchèque  
et de nationalité tchèque

acceptée sur proposition du jury:

Prof. H. Brune, président du jury  
Dr R. Pitts, directeur de thèse  
Prof. A. Bay, rapporteur  
Dr M. Endler, rapporteur  
Dr C. Hidalgo, rapporteur



ÉCOLE POLYTECHNIQUE  
FÉDÉRALE DE LAUSANNE

Lausanne, EPFL  
2006

Contact to the author

E-mail: [horacek@ipp.cas.cz](mailto:horacek@ipp.cas.cz) or [horacek@go.to](mailto:horacek@go.to)  
<http://server.ipp.cas.cz/~horacek> or <http://go.to/horacek>

Contact to the supervisor

E-mail: [richard.pitts@epfl.ch](mailto:richard.pitts@epfl.ch), tel. +41-21-693 6003, <http://crppwww.epfl.ch/~pitts>

- Thesis on-line: <http://library.epfl.ch/theses> or <http://go.to/horacek/phd>
- Concepts written in *italics* are present either in the Index or in the Appendix B.
- Scientifically the most important is Chapter 5.
- Most figures are in colour online. Even though all of them are understandable in black and white, it is recommended to print in colours the following pages: 76, 80, 83, 85, 87, 89, 91-92, 103, 108, 112, 113, 119, 121, 127, 129, 133, 136, 139-140



Aeolus, the Greek God of turbulent winds  
dedicates this thesis to Richard Pitts

## Abstract

Almost since the first density profile measurements were made in the scrape-off layer (SOL) of the early tokamaks, it has been recognized that the rate of particle transport perpendicular to magnetic surfaces exceeds that expected on the basis of classical collisional diffusion by as much as three orders of magnitude. Plasma turbulence has rightfully been claimed as the origin of such large discrepancies, much as it has for enhanced (over classical or neoclassical) transport rates observed in the confined plasma.

But in the SOL, the "bursty" or "blobby" nature of the measured density fluctuations is of a much higher amplitude than that found in the core, making large-scale, convective fluid turbulence a strong candidate mechanism. This thesis will demonstrate quantitatively and unequivocally, for the first time, that such interchange motions are indeed the driver for the edge density and particle flux fluctuations observed on the Tokamak a Configuration Variable (TCV). Since the principle driver of this turbulence is a curved magnetic field, with gradient direction matching that of the local edge plasma pressure profile, together with a region of open magnetic field lines, the interchange mechanism identified here is very likely to be the very same process at the root of transport in all tokamak SOLs. In showing that the measured turbulence driven cross-field particle flux in TCV is quantitatively consistent with interchange physics, a path is opened by which the anomalous transport rates might be estimated in a predictive way for larger tokamaks, like the ITER device, which are yet to be built but for which concerns are now being raised that such transport might lead to excessive plasma-wall interactions.

Using a fast reciprocating Langmuir probe, fluctuation measurements have been made in the TCV low-field-side SOL across a wide range of ohmic discharges comprising variations in plasma shape and configuration (limiter and divertor), plasma current, confinement mode (L and H), plasma density, toroidal magnetic field direction and plasma fuel species (deuterium and helium). Statistical analysis of the time series is used to demonstrate a remarkable degree of similarity across the database and to show that the radial dependence of the probability distribution functions (PDFs) of flux and density fluctuations can be well approximated by the known Gamma and Lognormal analytic PDFs, characterized in terms only of the relative fluctuation levels. In the vicinity of the SOL-main chamber interface, where particles interact with the walls, the density fluctuations exhibit clear evidence of self-similarity over two orders of magnitude in frequency and a PDF which is universal in shape. The observed constancy of the correlation between density and poloidal field fluctuations in turn implies a universal PDF for the radial particle flux which moreover is found to scale almost linearly with the local mean density.

Careful comparison of one particular case inside the experimental database with the results of 2D fluid turbulence simulations of the TCV SOL using the ESEL code developed at the Risø National Laboratory, Denmark has shown a remarkable level of agreement between theory and experiment when the simulation output time series is analyzed in exactly the same way as that applied to the tokamak data. Quantitative agreement between model and experiment has been found for radial profiles of mean values, fluctuation levels, PDF shapes, timescales and power spectra of both density and turbulent driven flux throughout the main SOL and even partially inside the separatrix. Automatically,

this level of agreement also implies that the code output conforms quite closely to the Gamma and Lognormal distributions.

Parallel SOL flow data have also been gathered simultaneously with the turbulence measurements. An extensive database of radial Mach flow profiles has been assembled, most notably including a direct comparison of the density dependence of the flow dynamics in carefully matched discharges with forward and reversed toroidal field. These constitute the first measurements of their kind in TCV and reveal the presence of very strong flows, up to Mach numbers of  $\sim 0.6$ . The magnitude and direction of the measured flows is found to be surprisingly well described by neoclassical return parallel flows (Pfirsch-Schlüter) compensating the poloidal ExB and diamagnetic drifts. Combining the forward and reversed field data uncovers a slight, field independent offset thought to originate from the excess transport, driven by the interchange motions, in the outboard midplane vicinity. The flow and fluctuation data have been combined to test the possible link between flow generation and turbulence first demonstrated from similar data on JET. No such correlations have been found on TCV throughout most of the SOL, supporting the finding that the neoclassical component can account for the majority of the measured parallel flow.

*Keywords:* physics, plasma, tokamak, TCV, ESEL model, turbulence, scrape-off layer, Langmuir probe, anomalous transport, cross-field transport, drift, self-similar, interchange instability, blob, parallel flow, Pfirsch-Schlüter flow, ballooning, wall sink, Reynolds stress, Gamma distribution

## Version abrégée

Quasiment dès les premières mesures du profil de densité effectuées dans la couche périphérique (SOL, Scrape-Off Layer) des plasmas de tokamak, il a été constaté que, dans la direction perpendiculaire aux surfaces magnétiques, le taux de transport des particules excède largement celui prédit par la diffusion collisionnelle. Que ce soit dans le SOL ou dans la région de confinement du plasma, l'origine de la différence entre le transport mesuré et le transport prédit par les théories classiques ou néoclassiques est attribuée à la turbulence du plasma.

Dans le SOL, le caractère intermittent et la structure en gouttelette des fluctuations de densité sont nettement plus prononcés qu'au centre du plasma et la turbulence convective à grande échelle y est par conséquent potentiellement beaucoup plus impliquée dans le transport des particules. Pour la première fois, le travail de recherche effectué pendant cette thèse démontrera quantitativement et sans équivoque que de tels mouvements d'échanges (interchange instability) sont en effet à l'origine des fluctuations de densité et du flux de particules, observées au bord des plasmas du Tokamak à Configuration Variable (TCV). Puisque cette turbulence est principalement due à la courbure du champ magnétique, quand son gradient s'aligne avec celui du profil de pression local, en conjonction avec une région où les lignes de champs sont ouvertes, il est très vraisemblable que les mouvements d'échange identifiés soient plus généralement à l'origine du transport dans le SOL de tous les tokamaks. L'accord quantitatif, obtenu sur TCV, entre les mesures de la turbulence responsable du flux de particules perpendiculairement aux surfaces magnétiques et la physique des mouvements d'échange, ouvre la voie à la prédiction du taux de transport dans les futurs tokamaks de grande taille, tels qu'ITER. Pour ITER, dont la construction est sur le point de commencer, une des préoccupations majeure est liée au transport des particules au bord du plasma, qui pourrait conduire à une interaction excessive du plasma avec les parois du tokamak.

Des mesures de fluctuations ont été réalisées dans le SOL des plasmas de TCV, à l'aide d'une sonde Langmuir rapide insérée depuis le côté bas champ. Une large gamme de plasmas ohmiques a été explorée en variant la forme du plasma ainsi que sa configuration (limitée ou divergée), le mode de confinement (L ou H), la densité et le courant du plasma, la direction du champ magnétique toroïdal, et pour finir, les éléments principaux constituant le plasma (deutérium ou hélium). L'analyse statistique des séries temporelles obtenues montre un remarquable degré de similitude à travers toute la base de données. En outre, la dépendance radiale des fonctions de distribution de probabilité (PDF) des fluctuations de densité et du flux de particules est très bien représentée par des distributions analytiques Gamma et Lognormal ne dépendant que de deux paramètres, à savoir leur valeur moyenne et leur fluctuation relative. Au voisinage du lieu d'interaction entre les particules et les parois (interface SOL-enceinte principale), les fluctuations de densité présentent un caractère extrêmement auto-similaire, sur plus de deux ordres de magnitude en fréquence, et la forme de leur PDF est identique. La corrélation observée étant constante entre les fluctuations de densité et le champ électrique poloïdal, le flux radial de particules possède lui aussi une PDF de forme constante. Par ailleurs, il a été observé que le flux radial de particules est quasiment proportionnel à la densité moyenne locale.

Un cas particulier de la base de données expérimentale a été minutieusement comparé aux résultats des simulations fluides 2D effectuées pour le SOL de TCV avec le code ESEL, développé à Risø Laboratoire National au Danemark. L'accord entre les résultats expérimentaux et théoriques, tous deux analysés de façon rigoureusement identique, est remarquable. Que ce soit pour les profils radiaux et leurs valeurs moyennes, les niveaux de fluctuations, la forme des PDF ou encore les échelles de temps et la densité spectrale du flux de particules et de la densité du plasma, un bon accord quantitatif est observé entre l'expérience et le modèle, dans tout le SOL principal et même, partiellement, à l'intérieur de la séparatrice. Un tel niveau d'accord implique automatiquement que les résultats du code possèdent aussi des PDF très proches des distributions Gamma et Lognormal.

Le profil radial du flux du plasma parallèle au champ magnétique a également été obtenu lors des mesures de turbulence. Une vaste base de donnée a été constituée, incluant notamment une comparaison de l'influence de la densité sur le flux du plasma pour un champ toroïdal standard et inversé. Ces mesures sont les premières de ce type sur TCV et révèlent la présence de flux très intenses d'une vitesse de Mach d'environ 0.6. L'intensité et la direction du flux mesuré sont étonnamment bien décrits par la théorie néoclassique des flux parallèles de retour (Pfirsch-Schlüter) compensant les dérives ExB poloïdales et diamagnétiques. La comparaison des données en champ standard et inversé montre toutefois l'existence d'un léger flux ne dépendant pas de la direction du champ. Ce flux est attribué à l'excès de transport provoqué par les mouvements d'échange, à proximité du plan médian du plasma, côté bas champ. Les données concernant le flux du plasma et ses fluctuations ont été analysées afin de tester si, comme à JET où les premières mesures de ce type ont été réalisées, un lien existe entre la génération de flux et la turbulence. À travers la majeure partie du SOL, aucune corrélation entre le flux et la turbulence n'a été observée pour les données de TCV, confirmant le fait que la majeure partie du flux mesuré y est due à la composante néoclassique.

*Mots clés:* physique, plasma, tokamak, TCV, model d'ESEL, turbulence, la couche périphérique, sonde Langmuir, transport anormal, transport radial, dérive, auto-similaire, mouvements d'échange, gouttelette, flux parallèle, flux de Pfirsch-Schlüter, ballonnement, tension de Reynolds, distribution de Gamma

# Contents

Contents	7
<b>I Introduction</b>	<b>11</b>
<b>1 Fusion, tokamaks and plasma boundary physics</b>	<b>13</b>
1.1 Thermonuclear fusion . . . . .	13
1.2 Tokamak principle . . . . .	15
1.3 Edge plasma physics . . . . .	16
1.3.1 Sheath and presheath . . . . .	17
1.3.2 Particle transport . . . . .	20
<b>2 Turbulence in the tokamak plasma boundary</b>	<b>25</b>
2.1 Introduction to fluid turbulence . . . . .	25
2.1.1 Definition of turbulence . . . . .	25
2.1.2 Kolmogorov theory . . . . .	27
2.2 Self-organized criticality . . . . .	28
2.2.1 Self-similarity . . . . .	31
2.2.2 Marginal stability . . . . .	32
2.3 Reynolds stress . . . . .	33
2.4 Zonal flow shear . . . . .	34
2.5 Instabilities . . . . .	35
2.5.1 $\nabla B \times B$ interchange instability . . . . .	36
2.5.2 Drift waves . . . . .	36
2.6 Experimental observations . . . . .	38
2.6.1 Turbulent transport . . . . .	41
2.7 Theory and numerical models . . . . .	42
2.7.1 Transport of an isolated blob . . . . .	42
2.7.2 2D models . . . . .	44
2.7.3 3D models . . . . .	46
<b>3 The fast reciprocating Langmuir probe</b>	<b>49</b>
3.1 Introduction . . . . .	49
3.2 Probe construction . . . . .	49

3.2.1	Geometry of TCV . . . . .	49
3.2.2	Plant implementation . . . . .	51
3.2.3	Drive system . . . . .	52
3.2.4	Probe heads . . . . .	55
3.3	Electronics and data acquisition . . . . .	55
3.4	Signal processing . . . . .	60
3.5	Langmuir probe theory . . . . .	61
3.6	Fast electron temperature measurement . . . . .	63
3.7	Probe effective collection area . . . . .	65
3.8	Estimation of radial gradients . . . . .	66
3.9	Fluctuation induced flux . . . . .	66
3.10	Parallel Mach number . . . . .	69
<b>II Results of turbulence studies on TCV</b>		<b>71</b>
<b>4</b>	<b>Universality of electrostatic fluctuations</b>	<b>73</b>
4.1	Elementary statistics . . . . .	73
4.1.1	Statistical moments . . . . .	74
4.1.2	Various distributions . . . . .	74
4.1.3	Temporal characteristics . . . . .	77
4.2	Detailed analysis of a single probe reciprocation . . . . .	79
4.3	Universality across various discharges . . . . .	81
4.3.1	The TCV edge database description . . . . .	82
4.3.2	Universality of density fluctuations . . . . .	86
4.3.3	Universality of cross-field flux . . . . .	88
4.3.4	Diffusion versus convection . . . . .	92
4.3.5	Scaling with $\bar{n}_e$ . . . . .	93
4.3.6	Conditionally averaged waveform . . . . .	93
<b>5</b>	<b>TCV SOL turbulence: interchange motions</b>	<b>97</b>
5.1	Description of the ESEL model . . . . .	98
5.1.1	Model equations . . . . .	98
5.1.2	Reduced model equations . . . . .	99
5.1.3	Transport coefficients . . . . .	100
5.1.4	Effect of connection length . . . . .	102
5.1.5	Boundary conditions . . . . .	102
5.2	Model-experiment comparison . . . . .	106
5.2.1	Parameter settings . . . . .	106
5.2.2	Characterization of the 2D time evolution . . . . .	107
5.2.3	Particle density . . . . .	111
5.2.4	Electron temperature . . . . .	114
5.2.5	Spatial dimensions of potential . . . . .	115

5.2.6	Radial particle flux . . . . .	118
5.2.7	Absolute magnitude of the flux . . . . .	118
5.2.8	Conditional averaged waveform . . . . .	120
<b>6</b>	<b>Parallel SOL flows</b>	<b>123</b>
6.1	Introduction . . . . .	123
6.2	Experiment in forward and reversed magnetic field . . . . .	124
6.2.1	Influence of ballooning and wall sink . . . . .	128
6.3	Comparison with Pfirsch-Schlüter flow . . . . .	131
6.3.1	Theory-experiment comparison: restricted database . . . . .	132
6.3.2	Theory-experiment comparison: extended database . . . . .	134
6.4	Dynamical interplay between $\Gamma_r$ and $M_{  }$ . . . . .	137
6.4.1	Motivation . . . . .	137
6.4.2	Joint probability . . . . .	137
6.4.3	Validity of the Expectation value . . . . .	138
6.4.4	Alternative explanation due to probe location . . . . .	141
6.5	Dynamical interplay between $\nabla_r I_s$ and $\Gamma_r$ . . . . .	142
<b>7</b>	<b>Summary and conclusions</b>	<b>145</b>
<b>III</b>	<b>Appendices</b>	<b>149</b>
<b>A</b>	<b>Vorticity link to potential</b>	<b>151</b>
<b>B</b>	<b>Used Abbreviations and Symbols</b>	<b>153</b>
<b>C</b>	<b>Acknowledgments</b>	<b>155</b>
	<b>Bibliography</b>	<b>157</b>
	<b>Index</b>	<b>169</b>
<b>D</b>	<b>Curriculum Vitae</b>	<b>171</b>



# Part I

## Introduction



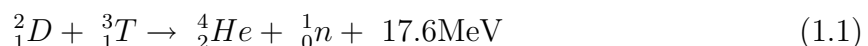
# Chapter 1

## Fusion, tokamaks and plasma boundary physics

Most current methods of large-scale energy production, fossil fuel combustion and nuclear fission, are unsustainable either from the environmental point of view or due to lack of primary sources. Controlled thermonuclear fusion is considered to be one of the most promising candidate options for a long-term, safe, environmentally friendly and economically competitive energy source [1, 2, 3].

### 1.1 Thermonuclear fusion

Of all the possible fusion reactions between light elements, the deuterium-tritium reaction has the highest cross-section at the lowest energies and will be the basis for terrestrial fusion power plants [2, chap. 1.2]:



The fusion reaction cross-section reaches a maximum for ion energies of  $\sim 100\text{keV}$ , with each  $D - T$  fusion releasing  $17.6\text{MeV}$  in the form of kinetic energy of the neutron and the alpha-particle ( ${}^4_2He$ ). The nuclear physics of this process is well understood and led to the first thermonuclear hydrogen bomb test explosion in 1952. To provide a large-scale, controlled power source ( $\sim 1\text{GW}$ ), a reaction rate of  $1\text{GW}/17.6\text{MeV} \sim 10^{21}\text{s}^{-1}$  is necessary and can only be achieved if particles are allowed to collide indefinitely with energies (or temperature) close to the cross-section maximum. At these temperatures, the ions form part of a hot, quasi-neutral plasma in which ions in the tail of the Maxwellian energy distributions achieve the fusion reactions. Lawson was the first to show, in 1955 [4], that a fusion plasma would "ignite" if the product of pulse duration and plasma density exceeded a given threshold for a fixed temperature. This is now more usually expressed in terms of the fusion "triple product" [2, p. 11]:

$$n \cdot T \cdot \tau_e \geq C_{crit,D+T} \approx (3 - 5) \times 10^{21} \text{sm}^{-3} \text{keV}, \quad (1.2)$$

where  $\tau_e$  is the *energy confinement time* and  $n, T$  are the volume-averaged density and temperature, respectively. In a star, a natural thermonuclear reactor, the plasma confinement is provided by the force of gravity due to the huge amount of matter. On Earth, alternative confinement methods must be used: either magnetic fields or the force of inertia. The Lawson criteria [2, 4] is achieved, for example, for  $n = 10^{20} \text{m}^{-3}$ ,  $T = 10 \text{keV}$  and  $\tau_E = 3 \text{s}$ , with the optimum temperature lower than that corresponding to the cross-section maximum in order to reduce radiation losses that increase strongly with temperature. To achieve and maintain these conditions, a device based on magnetic confinement called a "tokamak" was proposed by Sakharov and Tamm in 1950's and subsequently developed by a Russian team led by Artsimovich [1]. Alternative magnetic confinement schemes also exist (e.g. stellarators), but the tokamak concept is currently by far the most advanced in terms of its development.

In the process of "inertial" confinement fusion, frozen pellets of  $D - T$  are heated and compressed by powerful lasers to produce a high density plasma which is held together long enough by its own inertia for fusion to occur. This is the process behind the H-bomb and is being studied in many laboratories worldwide. But whilst values of the triple product close to those achieved in magnetic confinement have been obtained, the process is far behind tokamaks in terms of its feasibility for an eventual power plant.

Compared with other conventional energy production sources, a fusion power plant would have a number of advantages:

- Inherent safety
  - no danger of uncontrolled nuclear chain reactions
  - negligible latent energy: only a few grams of the fuel are present in the reactor chamber at any one time compared to about 100 tons in a fission reactor
- no danger of nuclear material proliferation for military purposes
- like fission, fusion produces no greenhouse gases ( $CO_2$ ) nor acid rain gases ( $SO_2, NO_2$ )
- fuel source is cheap and inexhaustible: deuterium can be extracted from water by electrolysis and lithium, for supply of tritium, can be extracted from sea water in the form of  $Li_2CO_3$ ; the fuel price is only about  $10^{-4}$  of the current cost of electricity [2, chap. 1.8]
- the  $D - T$  fusion reactions produce only helium gas as waste byproduct. Structural components of a tokamak power plant will be activated by neutron impact, but the activity will decay in a few 10's of years to the harmless levels of any conventional coal-fired plant.

After more than 50 years of fusion research, the international community finally agreed in summer 2005 to construct the next step fusion device ITER<sup>1</sup>, which will be built in Cadarache (France). ITER's objective is to demonstrate the scientific and technological feasibility of fusion energy for peaceful purposes [5]. Over the next 12 years whilst ITER is being constructed, the job of fusion researchers is to continue the exploitation of current

---

<sup>1</sup><http://www.iter.org/>

tokamaks in order to allow ITER to be used more efficiently. Today's experiments also of course have a role to play in furthering fundamental understanding of the tokamak plasma. This thesis makes a contribution to this process in the area of plasma edge physics.

## 1.2 Tokamak principle

The tokamak consists of a toroidal vacuum vessel inside which a strong toroidal magnetic field ( $B_T$ ) is generated by external poloidally wound magnetic coils. A toroidal plasma current is driven by transformer action using a solenoid passing through the torus centre as primary winding with the plasma ring as secondary. Because particles can move easily along the magnetic field lines, the plasma is nearly axisymmetric. But as a result of the toroidal geometry,  $B_T$  is not uniform ( $B_T \propto R^{-1}$ , where  $R$  is the major radius) and the resulting  $\nabla B \times \mathbf{B}$  drift [6] separates ions and electrons, producing a vertical electric field which in turn leads, through the  $\mathbf{E} \times \mathbf{B}$  drift, to an outward collective motion for both ions and electrons, making the plasma unstable. To prevent this, the toroidal current (also used for ohmically heating the plasma) generates a small poloidal magnetic field, typically  $B_{\text{pol}} \sim B_T/10$  which combines with  $B_T$  to produce a resultant helical field, Fig. 1.1 . The field lines wind gently around the torus and lie on nested surfaces centred on the magnetic axis.

For any given field line, the number of toroidal turns required to perform one full poloidal turn is called the *safety factor*, which, in the case of a cylindrical, large aspect ratio approximation, may be written as:

$$q = \frac{rB_T}{RB_{\text{pol}}}. \quad (1.3)$$

where  $r$  is the plasma minor radius. In this configuration the plasma is stable with respect to the  $\nabla B$  drift because the drift alternately increases/decreases the minor radius of a particle along its trajectory on a field line, depending on whether it is below/above the magnetic axis. Particles following these field lines may therefore only transport radially (i.e. across magnetic flux surfaces) through collisions with other particles or more complex collective phenomena such as large scale MHD activity or the convective plasma "blobs" that form the core of this thesis. These blobs are in fact a "residue" of this instability in regions of open magnetic field lines in the tokamak scrape-off layer (SOL), where the  $\nabla B \times \mathbf{B}$  drift is not fully stabilized since the field lines are not closed poloidally. Note that the terms "radial", "cross-field" and "perpendicular" (labelled as  $r$  or  $\perp$ ) all refer to the direction along the minor radius, away from the plasma centre, perpendicular to the magnetic flux surfaces. In contrast, "parallel" (labelled as  $\parallel$ ) refers to the direction along any particular magnetic field line.

Since particle drifts play an essential role in this thesis, it is worth recalling the basics of the  $\nabla B \times \mathbf{B}$  and  $\mathbf{E} \times \mathbf{B}$  drifts. In the individual particle picture, both ions and electrons circulate on Larmor orbits of radius,  $\rho_L = \frac{mv_{\perp}}{eB}$ , where  $m, v_{\perp}$  are the particle mass and

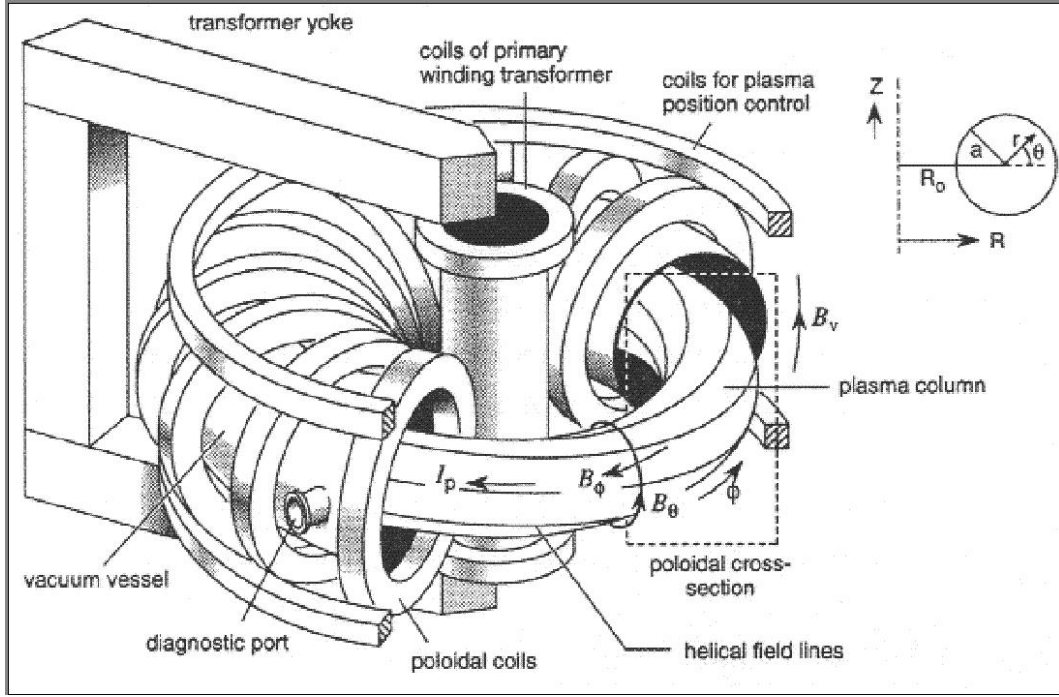


Fig. 1.1 : Schematic view of the tokamak device

perpendicular velocity, respectively. In non-uniform potential or magnetic fields, the Larmor radius is slightly different at each side of the orbit, resulting in a particle guiding centre drift with velocity perpendicular to all  $\mathbf{B}$ , and  $\nabla\phi = -\mathbf{E}$  or  $\nabla B$ ,

$$\mathbf{v}_{\mathbf{E} \times \mathbf{B}} = \frac{\mathbf{E} \times \mathbf{B}}{B^2}, \quad \mathbf{v}_{\nabla B} = \pm \frac{1}{2} v_{\perp} r_L \frac{\nabla B \times \mathbf{B}}{B^2}, \quad (1.4)$$

It can be shown [6] that the  $\nabla B \times \mathbf{B}$  drift (Eq. (1.4)) is always accompanied with the magnetic curvature drift  $\mathbf{R} \times \mathbf{B}$  in the same direction, determined by  $v_{\parallel}$  instead of  $v_{\perp}$ . In SOL plasma with isotropic velocity distribution they are just identical and thus in the following the term " $\nabla B \times \mathbf{B}$  drift" is assumed to mean sum of both. Note that the  $\nabla B \times \mathbf{B}$  drift is charge ( $\pm$ ) dependent; ions and electrons drift in opposite directions, generating an electric field perpendicular to both  $\mathbf{B}$  and  $\nabla B$ . In contrast, the  $\mathbf{E} \times \mathbf{B}$  drift is charge independent. In all situations of relevance to this thesis, the electron and ion Larmor frequencies,  $\omega_c = eB/m$  (in TCV 60 MHz for ions and 200 GHz for electrons) are much greater than the timescale of the events under study (for example the turbulent "bursts" in the SOL). Particle trajectories can thus be averaged out (simplified) over the Larmor orbits, leaving just a residual drift velocity of the guiding centre.

### 1.3 Edge plasma physics

The edge plasma is generally thought of as the region at the plasma periphery encompassing the "gradient" region in the vicinity of the *last closed flux surface* (LCFS) or magnetic

*separatrix*. This surface is defined by a limiter (a solid object in direct contact with the plasma), or it can be produced by "pulling out" plasma using external coils to create a null (or *X-point*) in the poloidal field (see Fig. 1.2). To one side of this separatrix lies the confined plasma on closed flux surfaces. On the other side lies the *Scrape-Off Layer* (SOL) plasma where field lines are open and terminate on material structures. A compressed tutorial on edge plasma physics can be found in [7] and in much more detail in [8]. Here only basic concepts will be outlined, sufficient for understanding of the terminology and background in the later research chapters (4,5,6).

Some tokamaks still use limiters and circular poloidal plasma cross-sections. However, a limiter is always by definition close to the confined plasma (since it defines the LCFS), so that any impurities released from the plasma-surface interaction can easily penetrate and contaminate the core. In addition, because most of the neutral reionisation in the limiter configuration also occurs inside the core plasma, the SOL region remains hot, increasing limiter heat fluxes and exacerbating the impurity release problem.

As a result, most tokamaks now favour the X-point configuration, which allows open field lines to be diverted away from the "main chamber" region into a special divertor volume and onto target plates where the plasma-surface interaction can be localized. Because of the low poloidal field in the X-point vicinity, magnetic field lines can be extremely long as they make their way from the main chamber SOL to the target plates. For sufficiently high density, this allows particles to collide amongst themselves many times in their transit along the field, leading to the formation of strong parallel temperature gradients. Temperatures can fall to extremely low values at the target plates - sufficiently low ( $< 5\text{eV}$ ) that neutrals released from the targets cannot be reionized. A "cushion" of neutral pressure accumulates, allowing for efficient pumping (so that He exhaust can be managed in a reactor). Ion-neutral collisions can transfer momentum away from the incoming ion fluid and neutral excitation exhausts power through radiation. Temperatures can fall low enough ( $< 1\text{eV}$ ) for electron-ion recombination to become important, at which point charged particles are removed and the plasma flow can be locally extinguished or "detached" from the targets. ITER, and future reactors will depend on this detachment for the management of the enormous expected power fluxes. Without it, material erosion would exceed acceptable limits.

The presence of an X-point also brings another important benefit - tokamaks using such a field configuration access more easily a regime of higher confinement known as the *H-mode*, first discovered in 1980's on the ASDEX tokamak [9]. In this mode, the energy confinement is  $\sim 2\times$  higher than in the normal *L-mode* or "low confinement" mode. The H-mode occurs beyond a certain threshold in heating power and is due to the creation of a transport barrier in the separatrix region. The mechanisms responsible for the formation of this barrier are not fully understood but theories abound [2].

### 1.3.1 Sheath and presheath

In front of any material surface in contact with plasma, either the tokamak vacuum vessel wall or a diagnostic probe, an electrostatic sheath appears, characterized by a drop in

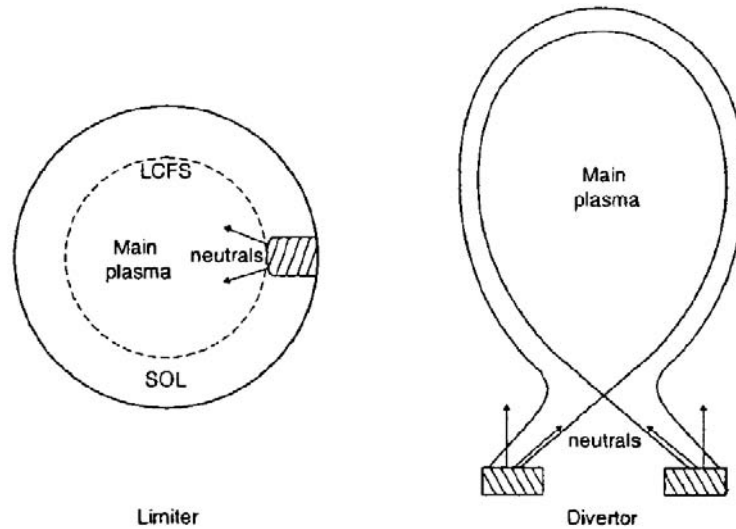


**Fig. 1.2 :** Poloidal plasma cross-sections illustrating the limiter (left) and divertor (right) configurations. From [7].

potential and pressure (shown schematically in Fig. 1.3 ). In the first  $\mu\text{s}$  after plasma is initiated, the electrons rush ahead of the ions, due to their higher mobility (lower mass), leaving the plasma at a positive potential with respect to the surface [8]. This generates a parallel electric field of such magnitude such that the loss rates of both  $e^-$  and  $i^+$  equalize, resulting in the so-called *ambipolar transport*. This parallel electric field, known as the presheath, extends far back from the solid surface into the SOL plasma. Its effect is to provoke a parallel density gradient, leading (in the standard "isothermal fluid" case) to a pressure decrease from the unperturbed plasma (where the effects of the solid surface are not felt) down to the surface. Since, in the absence of the complex detached plasma scenarios, the total pressure must remain constant along any given field line, the loss of static pressure  $n(T_i + T_e)$  must be compensated by the dynamic pressure due to the fluid momentum ( $mnv^2$ ). Thus, the fluid velocity increases towards the surface, and must reach a value of at least the sound speed,  $c_s = \sqrt{k_B(T_i + T_e)/m_i}$  at the sheath-presheath interface in order for a stable sheath to form. This is known as the *Bohm criterion* [8, p.73]. The curves in Fig. 1.3 are derived from a simple 1D, isothermal fluid model describing conservation of particles and momentum in the parallel direction. The essential physics is derived from the first and second moments of the 1D Fokker-Planck kinetic equation. More details can be found in Chapters 9 and 10 of the Stangeby book [8]. In this simple 1D picture, cross-field transport plays no role other than to provide one element of the particle source (others can come, for example, from neutral ionisation in the SOL).

Beyond this presheath, the potential drops further in the *sheath* region by

$$\frac{1}{2}T_e \ln \left[ \frac{m_i}{2\pi m_e} \frac{T_e}{T_i + T_e} \right] \quad (1.5)$$

which is  $(2 - 3)k_b T_e$  for isothermal ( $T_i = T_e$ ) fluid model in deuterium plasma. The exact value of the sheath potential drop depends on the secondary electron emission coefficient,

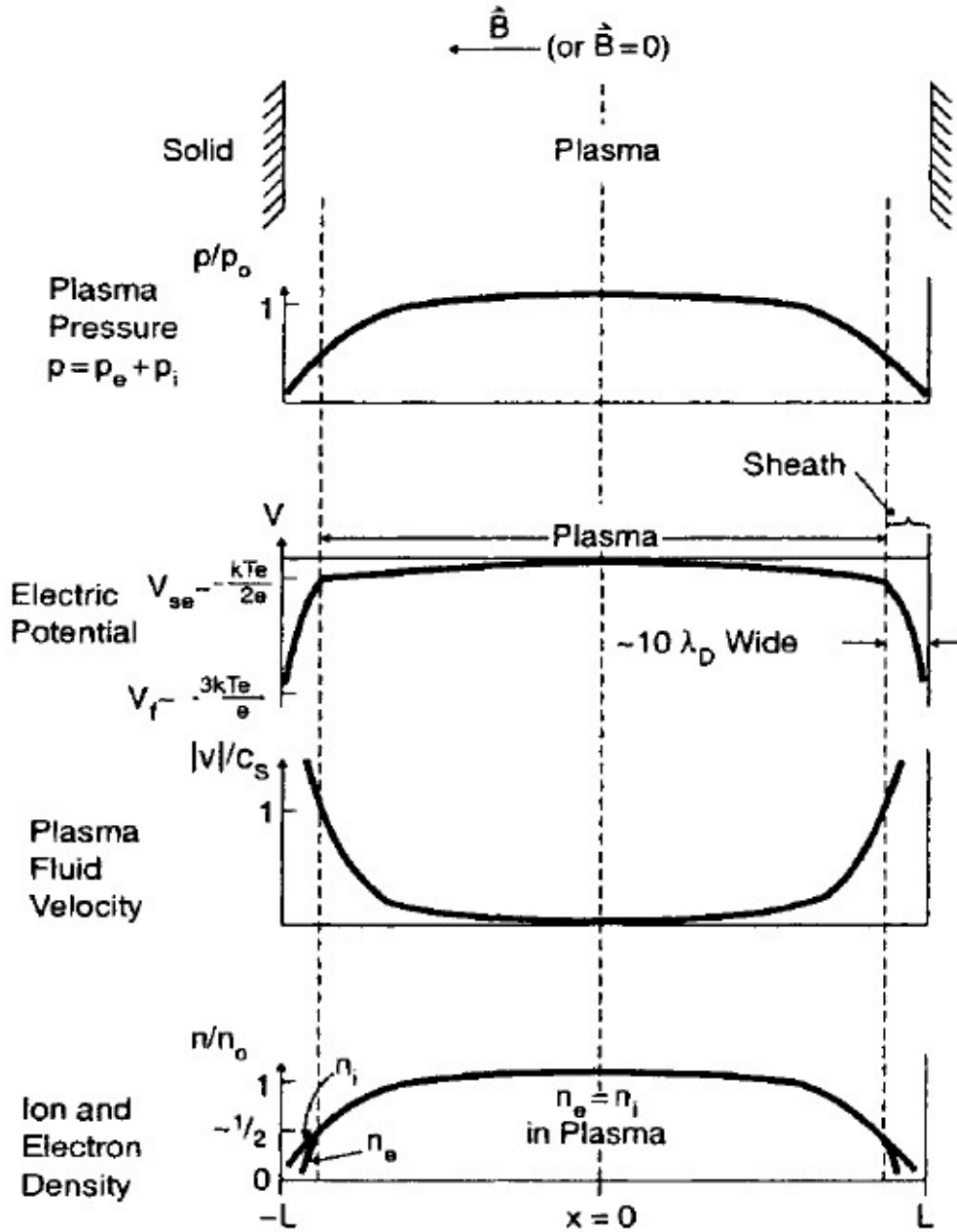


**Fig. 1.3 :** Variation of plasma pressure, electric potential, ion and electron densities and fluid velocity for magnetized plasma flow along the field, bounded by solid surfaces at  $\pm L$ . Sheath thickness is exaggerated for clarity. From [7].

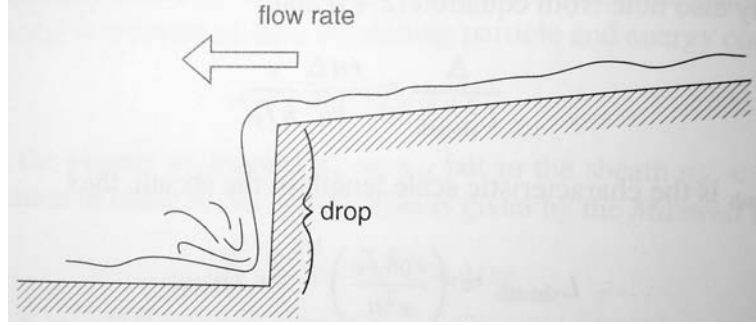


**Fig. 1.4 :** Analogy between plasma flow through the sheath and presheath potential falls and a waterfall. The flow rate over a fall is determined by the conditions upstream (the pre-sheath electric field) rather than by the waterfall height. From [8].

$\delta_e$  at the surface. For a deuterium plasma with  $\delta_e = 0$ , the sheath potential fall is  $2.8 k_B T_e$ . In the sheath, plasma is not macroscopically neutral but instead a cloud of ions forms,  $n_i > n_e$ . Its thickness is  $\sim 10\lambda_D$ , where the Debye length is

$$\lambda_D = \sqrt{\frac{\epsilon_0 k_B T_e}{n_e e^2}} \sim 10\mu\text{m}$$

under typical conditions in a tokamak SOL. Note that although the pre-sheath electric field is much weaker than that of the sheath (by a factor of  $\frac{0.7\lambda_D}{(2-3)L_{\parallel}} \sim 10^{-6}$ ), it plays an extremely important role in establishing conditions for the sheath to form. This is nicely illustrated by analogy with a waterfall (Fig. 1.4): the flow magnitude is not determined by the magnitude of the drop (the sheath) but by the river slope upstream (the pre-sheath electric field in the SOL).

### 1.3.2 Particle transport

In order to determine both particle loss from the confined region and the plasma interaction with the first wall and divertor targets, it is important to understand the mechanisms of particle transport (sinks and sources) that determine the SOL density profile. The particle source is the result both of the SOL volumetric ionization of neutrals recycled from the material walls or gas-puffed into the plasma, and that of ions from the core plasma arriving in the SOL by some cross-field mechanism (diffusion and convection, Fig. 1.5). Particle sinks are provided both by parallel and cross-field transport in the SOL. The standard way of describing the cross-field particle flux is a combination of diffusive (Fick's law) and convective fluxes:

$$\Gamma_r = \overbrace{-D_{\perp} dn/dr}^{\text{diffusion}} + \overbrace{vn_e}^{\text{convection}}, \quad (1.6)$$

Transport parallel to the magnetic field is well understood, being determined in the simplest case mostly by classical non-turbulent diffusive and convective processes. Radial

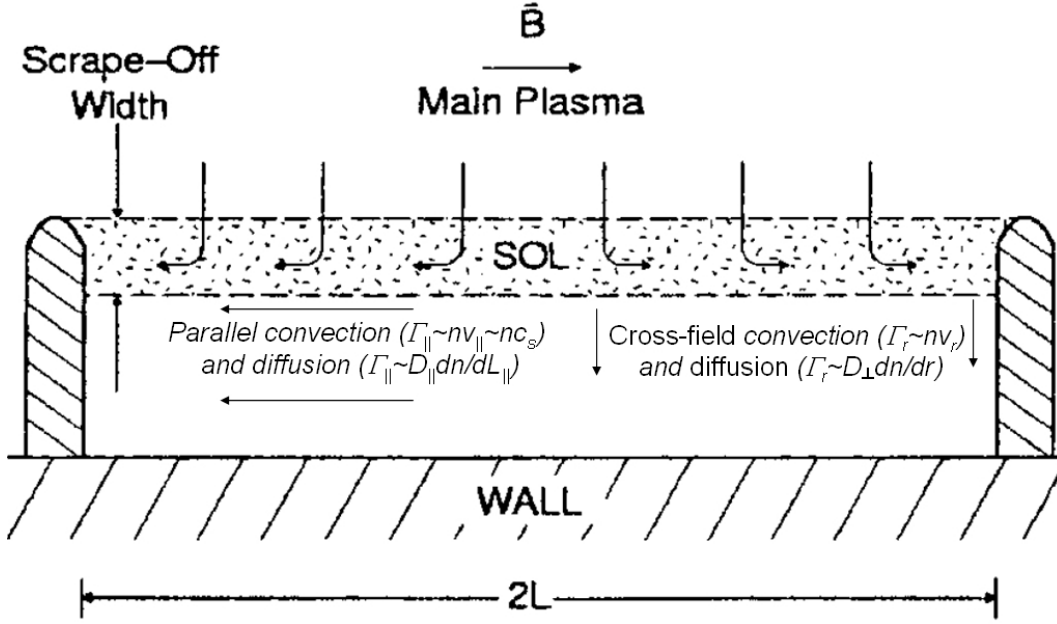


**Fig. 1.5 :** Interplay between parallel and cross-field particle fluxes in the SOL, straightened out along the magnetic field. Energy and particles flow from the main plasma into the SOL by slow cross-field transport, followed by rapid transport along  $\mathbf{B}$  to the divertor targets. From [7].

transport in the SOL, by contrast, is very definitely not classical, occurring at rates far in excess of those expected on the basis of diffusive collisional arguments. Such (random walk) arguments yield a collisional diffusion coefficient in non-turbulent plasmas [10]:

$$D_{\perp}^{Collision} = \rho_{Le}^2 \nu_{ei}, \quad (1.7)$$

where  $\nu_{ei}$  is the ion-electron collision frequency and  $\rho_{Le}$  the electron Larmor radius. In terms of macroscopic plasma parameters [11]:

$$D_{\perp}^{Collision} = 8 \times 10^{-4} T_e^{-3/2} n e (T_e + T_i) / B^2 \sim 10^{-3} \text{m}^2/\text{s}, \quad (1.8)$$

assuming  $T_i \sim T_e$ .

Almost all measurements in the tokamak SOL have found exponential behaviour in the density profile [12, 13, 14, 15] (Fig. 4.5), which is indeed expected in the simple SOL on the basis of a diffusive description of cross-field transport. The radial plasma density profile can be described in terms of a simple radial particle balance equation [8],

$$\frac{d\Gamma_r}{dr} = -\frac{n}{\tau_{||}} + S_{iz}, \quad (1.9)$$

where  $S_{iz}$  is the SOL ionization source and  $\tau_{||}$  the parallel loss time, which can be estimated as  $\tau_{||} = 2L_c/c_s$ , where  $L_c$  is the parallel connection length and  $c_s$  the sound speed. Assuming no ionization ( $S_{iz} = 0$ , corresponding to the low density or sheath limited

regime), the experimentally observed exponential decay,

$$n(r) = n(0) \exp(-r/\lambda_{\text{SOL}}) \quad \Leftrightarrow \quad \lambda_{\text{SOL}} = -\frac{n}{\nabla_r n}, \quad (1.10)$$

combined with Eq. (1.9) and Eq. (1.6), yields

$$\lambda_{\text{SOL}}^2 - v_{\perp} \tau_{\parallel} \lambda_{\text{SOL}} - D_{\perp} \tau_{\parallel} = 0, \quad (1.11)$$

with solution

$$\lambda_{\text{SOL}} = v_{\perp} \tau_{\parallel} / 2 \pm \sqrt{(v_{\perp} \tau_{\parallel} / 2)^2 + D_{\perp} \tau_{\parallel}}. \quad (1.12)$$

Assuming simple collisional diffusion alone (i.e. without convection,  $v_{\perp} = 0$ ) this yields a very thin SOL:

$$\lambda_{\text{SOL}}^{\text{Collision}} = \sqrt{\frac{2D_{\perp}^{\text{Collision}} L_c}{c_s}} = \sqrt{\frac{2 \cdot 10^{-3} \text{m}^2/\text{s} \cdot 20\text{m}}{60\text{km/s}}} = 1\text{mm}. \quad (1.13)$$

This should be compared to the typical SOL width found on many tokamaks [14, 16], as well as in TCV (Fig. 4.9 (a)),

$$\lambda_{\text{SOL}} = 10 - 30 \text{ mm} = \lambda_{\text{SOL}}^{\text{Collision}} \sqrt{\frac{D_{\perp}^{\text{experiment}}}{D_{\perp}^{\text{Collision}}}}, \quad (1.14)$$

which yields experimental value of the diffusion coefficient  $D_{\perp}^{\text{experiment}} \sim 1\text{m}^2\text{s}^{-1}$ . This is consistent with the well known empirical *Bohm scaling* [17], derived in 1949 from experiments in non-toroidal plasmas

$$D_{\perp}^{\text{Bohm}} = 0.06 T_e / B. \quad (1.15)$$

For TCV, assuming  $T_e = 30\text{eV}$ ,  $B = 1.2\text{T}$ , one obtains  $D_{\perp}^{\text{Bohm}} = 1.5\text{m}^2/\text{s}$ .

In the plasma core, this discrepancy  $D_{\perp}^{\text{Bohm}} \gg D_{\perp}^{\text{Collision}}$ , or rather  $\Gamma_r^{\text{Bohm}} \gg \Gamma_r^{\text{Collision}}$  for a given density gradient, can be partially explained by *neoclassical transport* theory [2], which accounts for particle drifts arising from the non-uniform magnetic field in toroidal geometry. Core *microturbulence* induces additional strong particle transport through electrostatic and magnetic fluctuations. This includes e.g. modes driven by the ion and electron temperature gradients (ITG, ETG) and trapped electron modes, creating radially elongated convective cells and also zonal flows through which the modes saturate.

In the SOL, fluctuation levels are generally orders of magnitude higher than in the core and the associated particle transport is generally ascribed to turbulence. These edge turbulent models are discussed in some detail in the next chapter and this thesis will show how experiments on TCV, in combination with modelling, have made significant progress in improving the understanding of the particular turbulent drive at work in the SOL. It should be also noted that in most SOLs the assumption of negligible volumetric

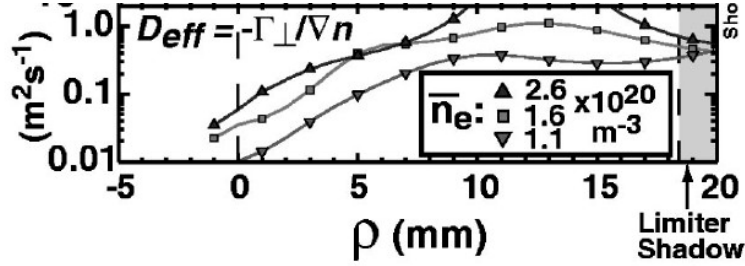


**Fig. 1.6** : Radial profile of the diffusion coefficient in the Alcator C-Mod tokamak SOL, computed assuming a purely diffusive ansatz:  $D_{\perp} = -\Gamma_r / \nabla_r n$ . From [19].

ionization in the SOL with respect to that inside the separatrix [18] is not really valid, further complicating the analysis.

Non-turbulent models of the SOL, attempting to reproduce experimental profiles of density and temperature, require some assumption for  $\Gamma_r$ . In principle, assuming pure convective or pure diffusive cross-field transport in Eq. (1.6) is equivalent if the convective velocity and the diffusion coefficient are related in the following simple way:

$$v_{\perp} = \sqrt{D_{\perp} / \tau_{\parallel}}. \quad (1.16)$$

When modelling the SOL, the two terms in the transport ansatz Eq. (1.6) are simply intended as a prescription of the radial transport in terms of a flux, not necessarily revealing its underlying nature [14]. In some cases, experimental measurements can be used to ascertain the relative importance of convective versus diffusive components, but quantitative estimates remain difficult. The radial and poloidal variations of  $D_{\perp}$  and  $v_r$  remain largely unknown. Simulations employing one of the major codes used for tokamak edge modelling, the SOLPS5 (B2.5-Eirene) [20], usually consider only the diffusive term, assuming the flux to be proportional to the density gradient,  $\langle \Gamma_r \rangle = -D_{\perp}^{\text{eff}} dn/dr$  and, moreover, often taking  $D_{\perp}^{\text{eff}}$  to be constant with radius. An attempt to include the convective term has recently been performed on the TCV tokamak, allowing the observed anomalous divertor plasma detachment to be explained in terms of enhanced plasma-main chamber wall interactions. Extensive measurements on the C-Mod tokamak (Fig. 1.6) have also shown conclusively that SOL profiles can only be explained in terms of a radially strongly varying effective diffusivity. It is the principal conclusion of Chapter 5 in this thesis that the diffusive description of radial particle flux in the tokamak SOL should be abandoned in favour of a convective ansatz, the absolute magnitude and radial variation of which is determined by large scale fluid interchange motions.

One major consequence of the strong cross-field transport is the enhanced interaction between the SOL plasma and the main chamber walls, called *main chamber recycling*, which has been observed at high density, notably in the C-Mod [18] and DIII-D [21] tokamaks. Until this strong transport was properly recognized, it had always been assumed that fast parallel transport along magnetic field lines would quickly remove power and particles entering the SOL from the confined plasma to the divertor [7]. The long density

profile "tails" seen in the SOL at high plasma density, coupled with large first wall surface area in the main chamber (compared to the divertor strike zones), mean that the total main wall ion and divertor ion fluxes can be of similar magnitude. When this occurs, true divertor action is lost and fuel recycling is determined principally by the main chamber (see Fig. 1.7). There is as yet no evidence that such a regime exists in the very large tokamaks (JET and JT-60U), but were it to be important in ITER, there are potentially worrying consequences for issues such as tritium retention and erosion of main chamber surfaces. The latter are not designed to withstand long term, localized ion fluxes. The results obtained during this thesis and reported in Chapter 5 hopefully provide one of the first steps towards the longer term goal of a predictive model for the SOL cross-field turbulent fluxes.

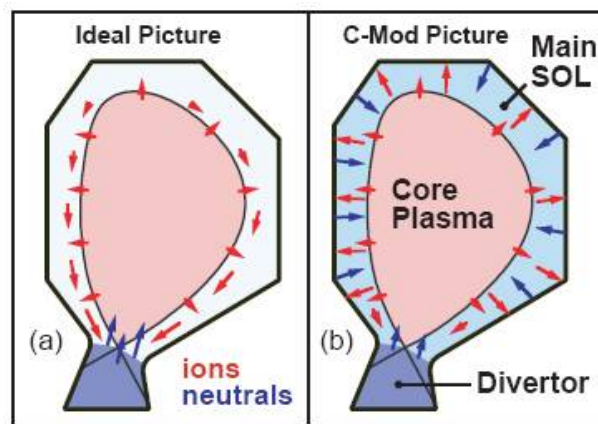


**Fig. 1.7** : In (a) the ideal picture of divertor action in contrast to the realistic picture (b) observed in C-mod in which the main chamber walls constitute an important particle recycling source. From [18].

# Chapter 2

## Turbulence in the tokamak plasma boundary

Chapter 1 has briefly introduced the concept of the tokamak SOL as a fundamentally turbulent medium, with high levels of density fluctuations and cross-field transport rates far in excess of classical collisional (diffusive) expectations. Indeed, natural turbulence and transport rates in the SOL are considerably higher than those found anywhere else in the tokamak plasma. This chapter sets the scene for the research reports to appear in chapters 4 and 5 by briefly reviewing the basics of turbulence theory and describing the principal experimental findings from similar studies performed elsewhere. To date, anomalous transport levels and similar fluctuation characteristics have been found in the SOL of all tokamaks in which they have been measured, pointing to a common (turbulent) origin.

### 2.1 Introduction to fluid turbulence

#### 2.1.1 Definition of turbulence

”Turbulence” is the ”quality or state of being disturbed, in tumult, disorder, agitation”. Turbulent water flow, where local velocities fluctuate and the direction of flow changes abruptly and frequently at any particular location, resulting in disruption of laminar flow, provides a typical example. A nonlinear physical system in which energy is distributed over many degrees of freedom, far from equilibrium, is turbulent. Turbulence is irregular both in time and in space, and must be maintained by an external energy influx if it is not to decay as a result of internal friction on small scales. The term ”turbulence” first appeared in fluid mechanics and was later generalized to include plasma states far from equilibrium.

The characteristic features of turbulence are:

- irregularity or randomness requiring a statistical treatment, owing to the unpredictability of individual tempo-spatial structures

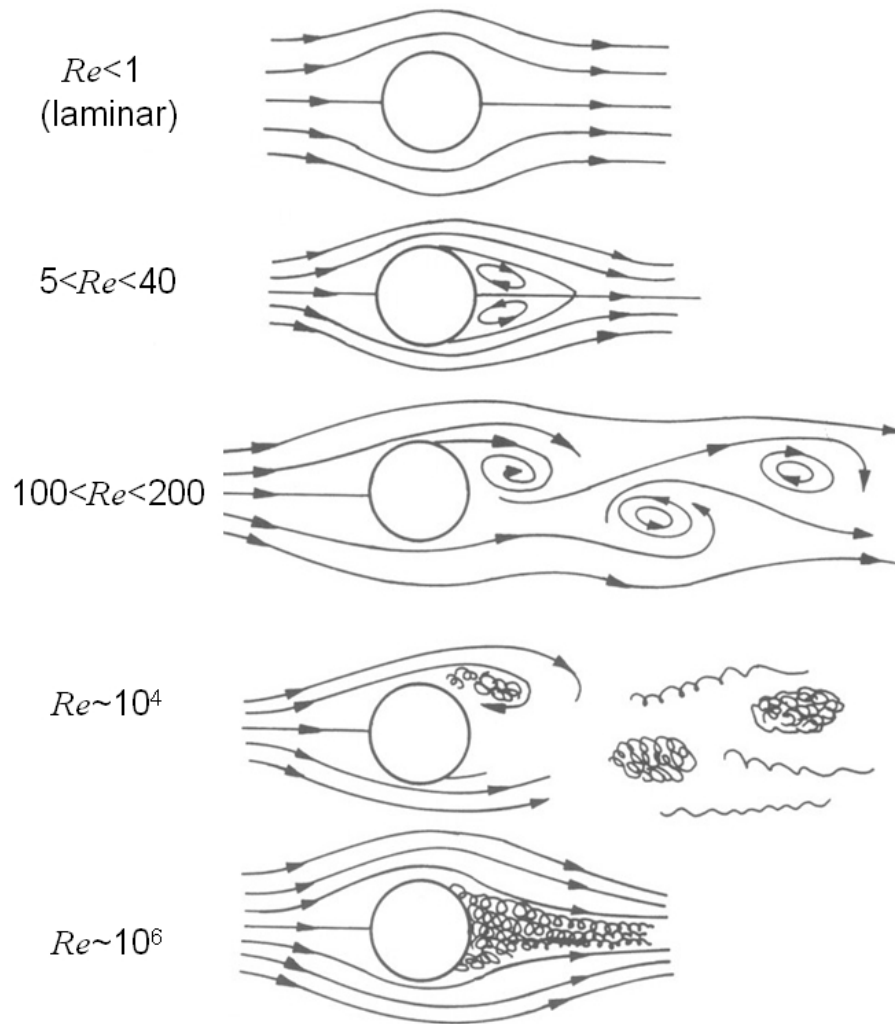


**Fig. 2.1** : Illustrating how fluid flow across an ideal cylinder varies with the Reynolds number. From [22].

- fluctuations on all scales
- rapid mixing strongly increases the transport of mass, energy etc.
- nonlinear interactions dominate most scale lengths
- cascading of energy: energy is interchanged between scales

Turbulence is often confused with *chaos*. The latter has, however, low dimensional behaviour and can be described by a small number of ordinary differential equations (for example a system of coupled pendulums). In contrast, a description of turbulence requires a large number of ordinary or partial differential equations.

Is there a universal theory of turbulence? A theory, such as those in quantum physics or gases, able to average out the apparently random motion of individual particles and produce a non-random, macroscopic, statistically predictable model? In the case of turbulent fluids, such a model might predict the rate of energy transfer between the mean fluid flow and the turbulent energy, the distribution of energy across the different eddy sizes, or the average rate of plasma impurity transport. Unfortunately, despite over a century of effort, only theories relevant to particular situations have emerged, without any unifying theoretical framework [22].

### 2.1.2 Kolmogorov theory

The transition from a linear to a turbulent state can be characterized by the dimensionless *Reynolds number*,  $Re$ , defined as  $Re = vd/\nu$  with  $v$  the fluid velocity,  $d$  the spatial dimension perpendicular to the flow direction and  $\nu$  the fluid viscosity. Fig. 2.1 demonstrates schematically how variations in  $Re$  describe modifications of turbulent character for flow across a cylinder of diameter  $d$ . For  $Re < 1$ , the flow is symmetric and laminar. As  $Re$  approaches unity, the upstream/downstream symmetry is broken and, in the range of  $Re \sim 5 - 40$ , steady vortices are attached to the rear of the cylinder. For  $Re \sim 40$ , an instability is observed in the form of an oscillation in the wake field and at  $Re \sim 100$  the vortices begin to peel off from the rear of the cylinder in a regular, periodic manner.

It is useful to describe turbulent media as a superposition of many *eddies* of different scales. The flow is random because the energy transfer between the eddies constantly modifies the eddy configuration on a timescale comparable to the eddy turnover time. In 1941 Kolmogorov [23] proposed that in a turbulent medium, the energy,  $\epsilon$  is filled in at large scales and then transferred into smaller and smaller scale structures. The eddy velocity remains constant because the energy transfer process is conservative; i.e. in the absence of viscosity at large scales, advection causes no loss of energy, only transfer of energy from motion at one scale to motion in another [10]. Below  $vl/\nu < 1$ , collisional (viscous) effects dominate over inertial energy transfer and the eddies no longer exist. The smallest value of  $l$  for which the eddies still persist is known as the dissipative scale. Energy is injected into large scales and cascades down (or is transported) to the dissipative scale. This process is known as the normal *energy cascade*, and is shown schematically in Fig. 2.2. Kolmogorov postulated that it must be possible to express this energy per unit mass and time in terms of  $l$  and  $v$ . From the dimensional point of view, it turns out that

there is only one way of writing  $\epsilon$ ,

$$\epsilon \sim v^3/l, \quad (2.1)$$

meaning that the velocity associated with eddies of a particular size is proportional to the cube root of the eddy size (Kolmogorov's scaling law) [23] [22, p.228]. Since the kinetic energy density,  $v^2/2$ , associated with some wavenumber around  $k \sim 1/l$  is  $E(k)k$ , then

$$E(k)k \propto v^2 \sim \epsilon^{2/3}k^{-2/3} \quad \leftrightarrow \quad E(k) \sim \epsilon^{2/3}k^{-5/3}, \quad (2.2)$$

which is the well-known *Kolmogorov 5/3 law* of turbulent scale power spectra [23]. In the tokamak edge, the  $k$ -spectrum of a two-dimensional turbulent plasma cannot be investigated using a single small probe. However, since the plasma flows by the probe, this spatial power spectrum is transformed into a frequency spectrum with  $f = kv$ , such that

$$E(f) \sim f^{-5/3}, \quad (2.3)$$

which is indeed close to what has been observed on C-Mod, PISCES, Tore Supra, MAST (self-similar power spectra,  $P(f) \propto f^{-1.6}$  [12]) and also on TCV (Section 4.2).

The arguments leading to the Kolmogorov energy spectrum are the same for 2D and 3D flows and are independent of whether the energy cascades forwards from large to small scales or in the inverse direction. In 2D turbulence, *inverse energy cascades* from intermediate to large scales can indeed appear and are a consequence of the conservation of vorticity [22, p.577]. An example of this phenomena is zonal flow generation (Section 2.4). In fact, the SOL plasma provides a good example of a quasi-2D system. Being strongly magnetized with fast transport rates parallel to the magnetic field, turbulent plasma eddies are highly elongated in the parallel direction, with resulting eddy motions being confined essentially to the radial and poloidal (strictly the diamagnetic) directions.

Fig. 2.3 provides a further example of the energy cascade via a non-linear simulation of drift wave turbulence [24]. The initial state at left evolves to the non-linearly saturated and highly turbulent state at right. As the system evolves, the turbulence breaks up the structures into finer and finer scales until the dissipative energy loss reaches the level of the input power to the system and the turbulence becomes non-linearly saturated.

## 2.2 Self-organized criticality

The term *self-organized criticality* (SOC) was introduced for the first time in [26] in 1987, where it was argued that SOC systems must have a  $f^{-\beta}$  i.e. self-similar or power-law power spectrum, like e.g. Eq. (2.3), and that dynamical systems with extended spatial degrees of freedom naturally evolve into SOC structures or states which are barely stable. Such a power-law spectrum has been observed in many physical systems. The definition of SOC is, however, quite vague; it concerns systems which are unstable if some *critical* threshold is overcome, independently of the detailed physical mechanism of this instability. A typical example of a SOC system is a *sandpile*, where the slope angle is a result of the dynamical interplay between gravity and sand grain friction. If locally, e.g. at the top of

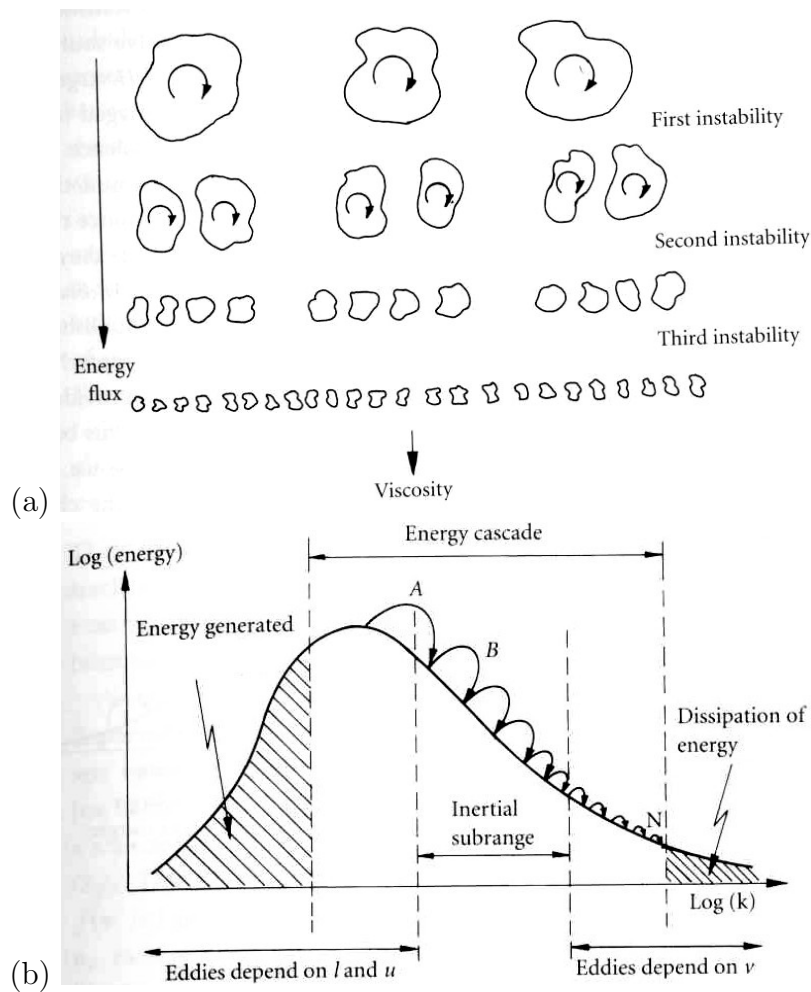


**Fig. 2.2** : Schematic of an energy cascade. (a) Energy injected into the system flows into large structures which break up into smaller and smaller structures that finally die through dissipation at scales corresponding to  $Re \sim 1$ . This process is illustrated in (b) in terms of the  $k$ -spectrum. Courtesy of [22].

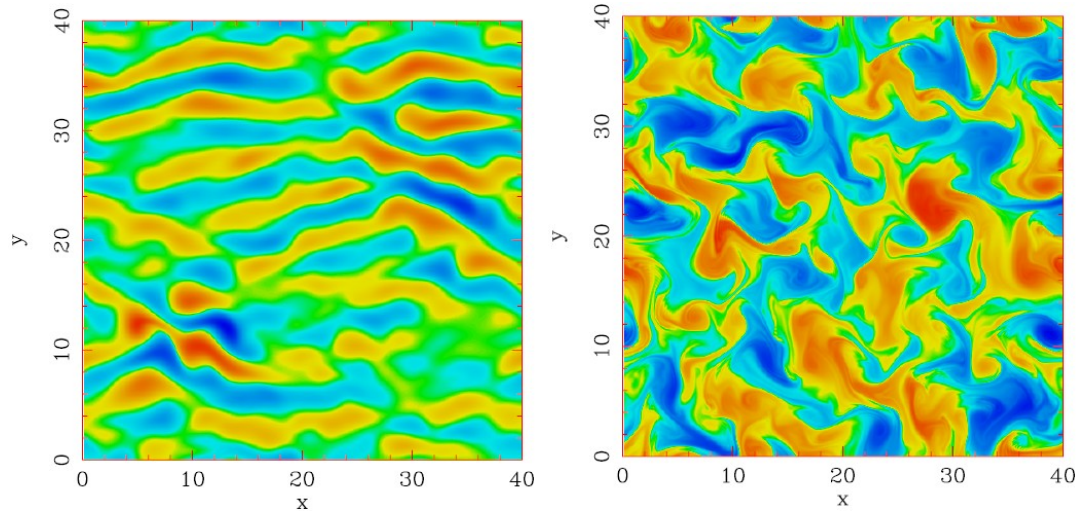


**Fig. 2.3 :** Development of *drift wave* turbulence illustrating cascade into the dissipative scale. Courtesy of [24].

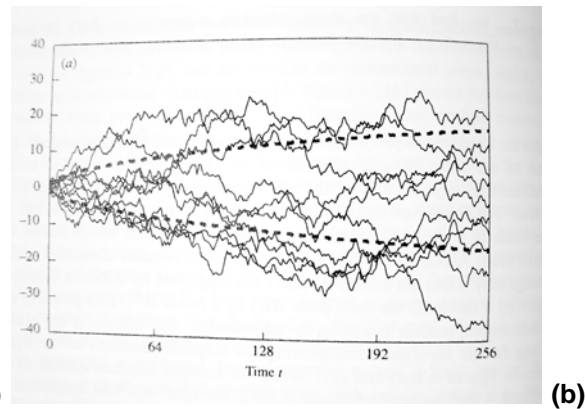


**Fig. 2.4 :** (a) A natural example of a self-similar object, fractal of the romanesco vegetable. (b) Self-similar time trace with Hurst exponent around  $1/2$ . From [25].

the pile where grains are added to the system, the slope increases over a certain threshold, a transport event starts and thus locally decreases the slope below the critical threshold. This local perturbation then propagates into surrounding regions, where the same critical threshold might be crossed and thus the situation repeats in an *avalanche* manner. Key ingredients of SOC systems are (illustrated by the sandpile example) [10]:

- An instability threshold (the critical gradient determined by static friction)
- Two disparate timescales: one associated with the drive (e.g. grain filling at the top) and the other with the instability relaxation (period of avalanches)

The size ( $\lambda$ ) of individual avalanches is distributed according to a self-similar probability distribution function (PDF):  $P(k) \propto k^{-\beta}$  [27] with  $k = 2\pi/\lambda$  and  $\beta$  a power-law exponent. An analogy between the sandpile and tokamak edge plasmas can be established in the following way by matching quantities in the two systems:

- slope of the sandpile  $\rightarrow$  radial gradient of plasma pressure
- sand grains  $\rightarrow$  individual ions on Larmor orbits
- force of gravity  $\rightarrow$  magnetic field curvature,  $\mathbf{R} \times \mathbf{B}$  and  $\nabla B \times \mathbf{B}$  drift
- static friction  $\rightarrow$  threshold to start an instability
- dynamic friction (damping the avalanche)  $\rightarrow$  turbulence dissipation at small scales and velocity shear

Though not based on any first-principle physics, the simple 1D sandpile model [28] demonstrates this avalanche transport based on the critical-gradient, SOC paradigm. Cellular automata are used to demonstrate this avalanche dynamics [29], the PDF of sandpile transport events has been obtained in [30], and is the very same Gamma distribution that is observed to approximate the PDF of density fluctuations in the TCV SOL (Chapter 4), and also those resulting from 2D turbulence modelling, described in Chapter 5. The turbulent structures in Fig. 2.12 are an example of avalanches in the SOL plasma.

### 2.2.1 Self-similarity

A Kolmogorov turbulent system has frequency spectrum following a power-law (Eq. (2.3)),  $f^{-5/3}$ . Such a power-law, or self-similar spectrum has been indeed observed in SOL electrostatic fluctuations in many experiments [31, 32, 33, 34, 35]. A self-similar object is characterized by the fact that by magnifying the object, the structure, or at least its statistical properties, stays the same. This is the characteristic of *fractals* [36] as demonstrated in Fig. 2.4 (a). The romanesco vegetable is an example of an *exact* fractal, since by zooming in by a characteristic magnification factor, the structure and its statistical properties remain identical. Some objects show only *statistical* self-similarity. The structure is not identical when magnified, but its statistical properties (for example the spatial spectrum) remain unchanged. To satisfy continuity in the power spectrum in this case, the spectral function must be described by  $P \propto f^{-\beta}$  with a scalar  $\beta$ . This feature is

defined [31] exactly such that the time series,  $x(t)$  is *self-similar* if there exists a number  $H$ , known as the *Hurst exponent* ( $0 < H < 1$ ), such that for all  $k > 0$

$$\langle x(t + \tau) - x(t) \rangle = k^{-H} \langle x(t + k\tau) - x(t) \rangle \quad (2.4)$$

or equivalently,

$$\langle [x(t + \tau) - x(t)]^p \rangle^{1/p} \propto \tau^H. \quad (2.5)$$

where  $p$  is a real positive number. This feature is demonstrated in Fig. 2.4 (b). Indeed, the envelope of several independent realizations of an uncorrelated *random walk* has the form of  $\tau^H$ . Chapter 4 will show (Eq. (4.16)) that a self-similar power spectrum is related to the Hurst exponent as  $\beta = 1 + 2H$ . If Eq. (2.5) holds only for  $p = 2$ , then the random walk is said to be *second order self-similar* and the left side of Eq. (2.5) is then called the *structure function* (SF). In general, the scaling exponent  $H$  depends on  $p$ , and this is known as *multifractal behaviour*. To understand the meaning of SF, note that  $\sqrt{\text{SF}}$  describes the departure of a randomly walking 'drunken sailor' from the origin, i.e.  $x(t + \tau) - x(t)$ . The SF simply averages over many 'sailors' at various times,  $t$  (Fig. 2.4 b). Independent (uncorrelated) steps in the classic example of Brownian motion yield  $\sqrt{\text{SF}} \propto \sqrt{\tau} = \tau^{1/2}$ , which corresponds to  $H = 1/2$ . For  $H > 1/2$  the time series are referred to as *persistent* (the sailor keeps drifting in a specific direction) and for  $H < 1/2$  *anti-persistent*. A persistent (anti-persistent) time series reverses itself less (more) often than an uncorrelated random series would; if the system had been up in the previous period, it is less (more) likely that it will be down in the next period and vice versa. Totally anti-persistent behaviour ( $H = 0$ ) is also known as pink noise or  $1/f$  noise.

Values of  $0.5 < H < 0.9$  and typically of  $H = 0.6 - 0.7$  are reported from many magnetically confined plasma devices using R/S statistics [37, 38]. Although using a different analysis technique (Eq. (4.12)), values of  $H = (\beta - 1)/2 = 0.35 - 0.7$  have been found on TCV (Fig. 4.9 (e)).

## 2.2.2 Marginal stability

With the velocity shear, due to the ExB drift defined and computed as

$$\omega_{E \times B} \stackrel{\text{def}}{=} \frac{dv_{\text{pol}}}{dr} = -\frac{1}{B} \cdot \frac{d^2\phi}{dr^2}, \quad (2.6)$$

it has been reported [39] that for electrostatic fluctuations in the SOL, the level of  $\omega_{E \times B}$  is comparable to  $\tau_c$ ,

$$\omega_{E \times B} \approx \tau_c^{-1} \quad (2.7)$$

where the autocorrelation time,  $\tau_c$  of electrostatic fluctuations was measured using a fixed Langmuir probe. This experimental observation can be interpreted using following argument: the turbulent structures pass the probe in the poloidal direction ( $v_r$  is usually slower [40]) with some typical speed,  $v_{\text{pol}}$  and a typical structure size,  $L_{\text{blob}}$ , yielding fluctuations on a single point measurement with typical timescales

$$\tau_c = L_{\text{blob}}/v_{\text{pol}}.$$

In experiment,  $L_{\text{blob}}$  is found to be of the order of  $\sim 2\text{cm}$  (see Section 2.6). In analogy to the density SOL width,  $n_e/\nabla_r n_e$ , a width determined by the velocity profile can be defined as

$$\lambda_{\text{SOL}} = \frac{v_{\text{pol}}}{\nabla_r v_{\text{pol}}} = \frac{v_{\text{pol}}}{\omega_{\text{E} \times \text{B}}}$$

and is typically 1-3 cm in experiment (see Fig. 4.7 (b) and Fig. 5.4 ). The experimental observation, Eq. (2.7) can then be rewritten in terms of  $\lambda_{\text{SOL}}$  as

$$L_{\text{blob}} = v_{\text{pol}} \tau_c \approx \lambda_{\text{SOL}},$$

with the obvious interpretation that the structure sizes are comparable to the SOL width, which can be expected from the simple picture Fig. 2.5 .

This observation has also been interpreted [39] as an indication that SOL turbulence is near *marginal stability*. A marginally stable system is defined as one which, if given an input impulse of finite magnitude, will *not* "blow up" into an unbounded output. However, oscillations in the output will persist indefinitely, and so in general there will be no final steady-state. A perturbation may not be fully dissipated but it persists, within some bounds, for all time [41]. It is a system which can be described by balanced turbulence growth and decay rates. This paradigm is closely related to SOC and appeared for the first time in the context of plasma turbulence in 1977 [42].

## 2.3 Reynolds stress

The Navier-Stokes equation of motion for a steady flow is [22]

$$n \left( \frac{\partial u_i}{\partial t} + (\mathbf{u} \cdot \nabla) u_i \right) = - \frac{\partial p}{\partial x_i} + \frac{\partial \tau_{ij}}{\partial x_j} \quad (2.8)$$

where  $n$  is the fluid density,  $\mathbf{u} = [u_x, u_y, u_z] = \langle \mathbf{u} \rangle + \tilde{\mathbf{u}}$  its velocity,  $p$  pressure and  $\tau_{ij}$  the stresses associated with the viscosity. This equation leads, for a fluid with a large Reynolds number, to a turbulent flow with chaotic behaviour. Time-averaging Eq. (2.8) yields a similar equation for the mean quantities [22]:

$$n \langle (\mathbf{u} \cdot \nabla) u_i \rangle = - \frac{\partial \bar{p}}{\partial x_i} + \frac{\partial}{\partial x_j} [\langle \tau_{ij} \rangle - n \langle \tilde{u}_i \tilde{u}_j \rangle], \quad (2.9)$$

but with appearance of a new stress term,  $n \langle \tilde{u}_i \tilde{u}_j \rangle$ , a time-averaged coupling between perpendicular turbulent velocities, called *Reynolds stress*. Note that while the conventional viscosity stress transfers (or dissipates) the flow kinetic energy into heat, i.e. chaotic motion of individual particles, the Reynolds stress couples the flow kinetic energy into turbulent energy of the fluid and vice versa. To predict the mean behaviour of the flow, an equation for the dynamics of  $\langle \tilde{u}_i \tilde{u}_j \rangle$  must be determined. Using the Navier-Stokes equation again leads, however, to an equation involving higher order correlations  $\langle \tilde{u}_i \tilde{u}_j \tilde{u}_k \rangle$ , whose dynamics involve a term of the fourth order, etc. Thus, there are always more

unknowns than equations, a dilemma known as the *closure problem of turbulence*. It is therefore impossible to develop a predictive, statistical model of turbulence simply by manipulating the equations of motion. To close the system, some additional *ad-hoc* assumption must be introduced, depending on the particular model. Experimentally, the Reynolds stress is measured assuming the usual  $\mathbf{E} \times \mathbf{B}$  drift:  $\langle \tilde{u}_i \tilde{u}_j \rangle = \langle \tilde{E}_r \tilde{E}_\theta \rangle / B^2$ .

Strong radial gradient of the electrostatic Reynolds stress is found experimentally in the vicinity of the velocity shear layer, demonstrating its possible link to significant flow generation [43]. The possible role of the Reynolds stress coupling of the SOL cross-field plasma turbulent transport into steady parallel flows has been suggested in [44]. This statistical treatment, first applied to data from JET, has been attempted on TCV data with the results described in Section 6.4 of this thesis. Reynolds stress coupling of turbulence into mean flow corresponds to the inverse energy cascade, where small turbulent eddies can generate stable *zonal flows*.

## 2.4 Zonal flow shear

Zonal flows are radially localized, electrostatic potential structures that are toroidally and poloidally symmetric. Due to the  $\mathbf{E} \times \mathbf{B}$  drift, poloidal flow is generated within this potential structure. Velocity *shear*,  $dv_{\text{pol}}/dr \neq 0$  is the principal mechanism by which coherent plasma structures may be destroyed, with consequent reductions of the radial particle flux [45]. Fig. 2.5 shows schematically how the coherent structures stretch (elongate) in the poloidal or toroidal direction, effectively destroying their radial structure (or, more precisely, shortening the radial correlation length); using an externally induced radial electric field this has been demonstrated experimentally [46]. In principle, the same role can also be played by shear in the toroidal or parallel flow,  $dv_{\parallel}/dr \neq 0$ , but since the structures are  $\sim 1000\times$  longer in this direction [47], whilst speeds are faster by only a factor of 10, its effect is much weaker than that of the poloidal flows. The velocity shear, Eq. (2.6) is therefore responsible for *transport barriers*, i.e. local reductions in radial transport rates. The H-mode is an example of a spontaneously generated edge transport barrier, forming the pressure pedestal, and thus increasing the global particle and energy confinement by approximately a factor of two. Shear in radial electric field is observed to increase just before the suppression of fluctuations [48], answering the question of causality.

As observed in 2D turbulence simulations (described in detail in Section 5.1.1), the intensity of the fluctuating motions shows irregular oscillations, with pronounced bursts [49]. Whenever this fluctuation level is large enough, an array of tilting convection cells appear, generating differential rotation through the *Reynolds stress*, a mechanism sometimes called the *tilting instability* [50] (in practise these two terms are just identical). This poloidal mean flow is non-uniform in the radial direction, thus possessing a net radial *shear*, because of net momentum conservation in the flow generation process. Such zonal flow generation has been demonstrated in both experiment and 2D fluid model [51]. The shear decorrelation mechanism (Fig. 2.5) then suppresses the level of fluctuation kinetic

energy while only slowly damping the flow energy. A repetition of this process results in quasi-periodic relaxation oscillations. Such dynamic regulation is a result of kinetic energy transfer from the fluctuating motions to the sheared flows followed, on a slower time-scale, by fluctuation damping through viscosity by the shear itself. This may also be consistent with the idea of the boundary plasma being near the *marginal stability*, discussed in Section 2.2.2. Zonal flows of radial width of  $\sim 1\text{cm}$  inside the separatrix have been observed [52] on the DIII-D tokamak using the BES technique and interpreted as the *Geodesic Acoustic Mode*, a class of zonal flows seen in nonlinear simulations of plasma turbulence, oscillating at  $c_s/(2\pi R) \sim 15\text{kHz}$  due to, possibly, the zonal flow generation and suppression mechanism explained above.

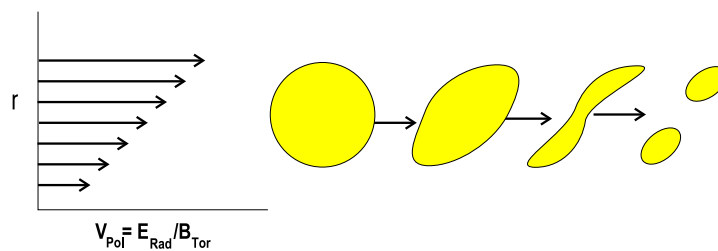


**Fig. 2.5 :** A demonstration of the destruction of coherent plasma structures by radial poloidal (or toroidal) velocity shear.

## 2.5 Instabilities

One of the most fundamental instabilities providing turbulence drive at the large (inertial) scales in plasmas and many other hydrodynamic systems is the interchange instability, variously called the flute, gravitational or Rayleigh-Taylor instability [6].

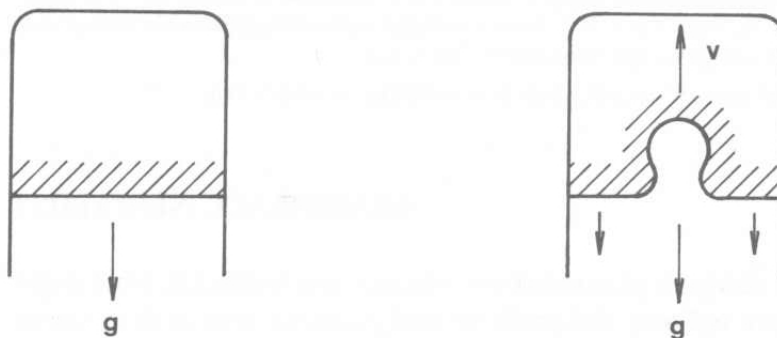


**Fig. 2.6 :** A gravitational instability develops when a heavy fluid sits above a lighter one in a gravitational field. From [6].

A basic well-known high school example (Fig. 2.6) is the interface between a heavy and light fluid (e.g. water and oil). Even though the water is suspended by the oil,

the equilibrium is unstable since any small fluctuation can grow exponentially, driven by the potential energy gained in the gravitational field. In the tokamak, the role of the gravitational field (which itself is negligible with respect to electromagnetic forces present in the plasma) can be played by the neutral wind [53], centrifugal force due to plasma poloidal rotation, or the  $\nabla B \times \mathbf{B}$  and curvature drifts. Note that in a linear plasma vessel curvature and  $\nabla B$  vanish; the former forces are, however, still present.

### 2.5.1 $\nabla B \times B$ interchange instability

In the tokamak SOL, the balance between the thermal (pressure) and Lorentz ( $\mathbf{j} \times \mathbf{B}$ ) forces is impeded by the resistivity of the SOL plasma itself (higher than in the core due to the low temperature) and the electrostatic sheaths at solid surfaces. Combined with the bad curvature region of magnetic field on the tokamak low-field-side, this leads to the destabilization of interchange modes driven by magnetic curvature and radial pressure gradients. The physical mechanism is clearly described in [54] in terms both of the reduced particle and fluid pictures. Plasma at higher pressure may be interchanged with neighbouring lower pressure regions in an overturning motion. The idea is illustrated in Fig. 2.7 depicting a local slab approximation with the pressure ( $p_0$ ) and field depending only on radius. If a small, sinusoidal perturbation is imposed on the equilibrium, according to the equations of particle continuity and thermal energy, the compressible flows lead to a local accumulation of particles and heat. The diamagnetic contribution corresponding to  $\nabla B$  and curvature drifts is charge dependent and hence leads to a poloidal charge polarization. From any closed fluid model it is readily shown that this leads to an electrostatic potential perturbation which lags the pressure fluctuation by a phase of  $\pi/2$ . In the fluid picture, the corresponding charge perturbation is caused by the diamagnetic current compressibility. The resulting fluctuation-induced electric drift advects the plasma pressure in the radial direction. In the upper half of the wave period illustrated, where the pressure fluctuation initially is positive, the equilibrium pressure gradient means that polarization drift convects more higher pressure outwards than inwards. In the lower half,  $\tilde{v}_r$  is directed radially inwards, thus locally taking in lower-pressure plasma. The net result is readily seen to be a temporal growth of the initial pressure perturbation, hence causing an instability.

This situation corresponds to the tokamak low-field-side (LFS) where  $\nabla B$  and  $\nabla p$  point in the same direction. On the high-field-side (HFS), however,  $\nabla p$  and  $\nabla B$  are in opposite directions and therefore the interchange mechanism pushes any pressure perturbations back into a region of higher pressure. The result is a stabilisation of the perturbation.

### 2.5.2 Drift waves

A drift wave [6] is a phenomena driven by the universal instability, where plasma pressure  $p_e = n_e(T_e + T_i)$  tries to expand the plasma, slowed by the magnetic pressure  $p = B^2/2\mu_0$ . The wave has finite wave length in both the poloidal and parallel directions [6]. The

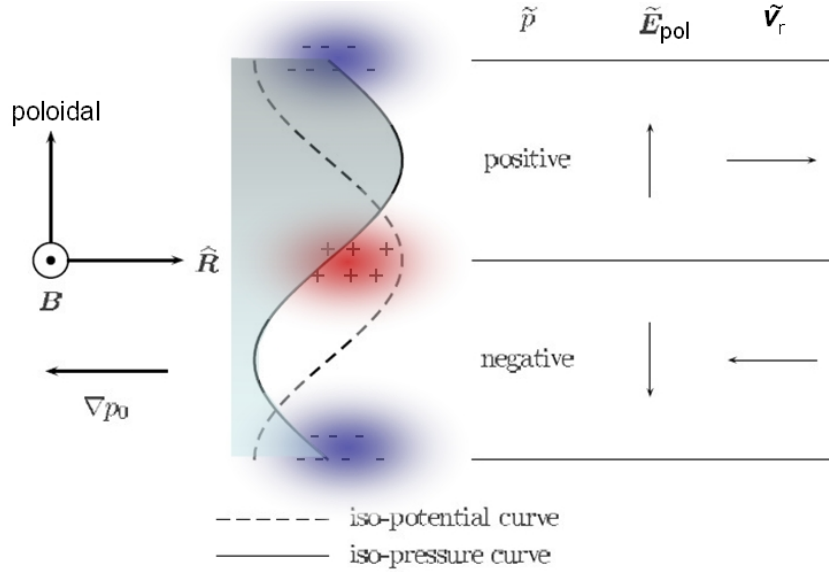


**Fig. 2.7 :** Illustration of the physical mechanism of the *interchange instability*. In this configuration the magnetic field points out of the paper plane and the electron gradient-B and curvature drifts are along the poloidal direction. The magnetic field strength and equilibrium plasma pressure are assumed to decrease with major radius R. From [54].

wave propagates in the direction perpendicular to both  $\nabla n$  and  $\mathbf{B}$  i.e. in the poloidal diamagnetic direction. The dispersion relation [11, p.374] is

$$\omega - k_z v_{\text{de}} - \frac{k_{\parallel}^2 c_s^2}{\omega} = 0 \quad \text{with} \quad v_{\text{de}} = -\frac{T_e}{n_e e B} \frac{dn_e}{dr} \quad (2.10)$$

In a uniform plasma, for which  $d/dr = 0$  and consequently the electron diamagnetic velocity,  $v_{\text{de}} = 0$ , the drift becomes the ion sound wave with  $\omega = k_{\parallel} c_s$ . For small normalized plasma pressure,  $\beta$ , which is the case in tokamaks, simple relation is derived for the Mach number of the drift wave:

$$M^{\text{dw}} \equiv \frac{v_{\text{de}}}{c_s} \approx \frac{\rho_s}{\lambda_{\text{SOL}}}, \quad (2.11)$$

where  $\lambda_{\text{SOL}}$  is the radial density scale length (Eq. (1.10)),  $\rho_s = c_s/\omega_{\text{ci}}$  is the hybrid thermal Larmor radius. This yields  $M^{\text{dw}} \approx 0.1$  in the TCV SOL for typical  $\lambda_{\text{SOL}} \sim 10$  mm in low density plasma, corresponding to  $6 \text{ kms}^{-1}$ , and  $M^{\text{dw}} \approx 0.02$ , i.e.  $1.2 \text{ kms}^{-1}$  for typical  $\lambda_{\text{SOL}} \sim 30$  mm in high density discharges. This velocity is comparable to the velocities observed in the TCV edge (an example is shown in Fig. 5.4) either using the cross-correlation technique or obtained from measurements of the radial electric field,  $v_{\text{pol}} = E_r/B$ . On TCV no systematic drift wave study has been performed. Since, however,  $\rho_s/\lambda_{\text{SOL}}$  is roughly constant across the SOL, whilst the measured  $v_{\text{pol}}$  in Fig. 5.4 varies significantly and even changes direction, it is probably not of drift wave origin.

## 2.6 Experimental observations

The most often used, oldest and simplest technique for plasma (turbulence) investigation is the electrostatic *Langmuir probe*, an electrical sensor immersed in the plasma, first used in the 1920's by Irving Langmuir [55]. Since the probe is in direct contact with the plasma, there are limitations to the depth at which probes can be inserted into the tokamak SOL, particularly in devices with high power densities. In practice, useful measurements can be obtained only up to the separatrix region. Beyond this point probe damage often occurs or the plasma is so seriously perturbed by the probe for measurements to be meaningful. The measured volt-ampere characteristic yields the electron distribution function. The probe tip can be as small as a millimeter in dimension and thus provides fine spatial resolution which, together with excellent time resolution (often limited only by capacitive effects of the measuring electronic circuits), makes it an ideal diagnostic for turbulence studies. The simplest probe measures fast fluctuations of saturation current,  $I_s$  and plasma floating potential,  $V_{fl}$ . The electron temperature may be extracted by sweeping the probe voltage, usually with the unavoidable drawback of significantly slower time resolution. Fast temperature fluctuations are therefore usually assumed to be negligible so that  $\tilde{I}_s \propto \tilde{n}_e$  and  $\tilde{V}_{fl} \approx \tilde{\phi}$  (the plasma potential) can be assumed (more discussion in Section 3.5).

Simultaneous measurements of  $\tilde{n}_e, \tilde{T}_e, \tilde{\phi}$  with Langmuir probes generally find that  $\tilde{n}_e/n_e \approx \tilde{T}_e/T_e$  [56] and that  $\tilde{n}_e$  is anticorrelated with  $\tilde{T}_e$  (i.e. phase difference of  $\pi$ ) [56]. Even though in L-mode and ELM-free H-mode some degree of correlation between bursts in  $\tilde{T}_e$  and  $\tilde{n}_e$  has been reported in [57], it is much weaker than that found between  $\tilde{n}_e$  and  $\tilde{v}_r$ . The phase angle between  $\tilde{I}_s$  and  $\tilde{V}_{fl}$  has been found to be in the range  $\frac{1}{4}\pi - \frac{1}{2}\pi$  [58].

Many variants of the single Langmuir probe have been developed to access turbulent quantities, even though some do not retain the advantage of fine spatial resolution. The emissive probe [59] and the ball-pen probe [60] provide direct measurements of plasma potential, the Mach probe (see Section 3.10) and Gundestrup probe [61] measure plasma flow, the tunnel probe [62] is for fast electron (and perhaps even ion) temperature measurement, the retarding field analyser [13] and Katsumata probe [63, 64] for slow ion temperature measurements. Langmuir probe arrays [65, 66] have also been used to observe the structure of turbulence in two dimensions. An exhaustive overview of these probe variants, their use and interpretation may be found in [63, 64, 67].

Single Langmuir probe measurements universally observe SOL plasma density fluctuations to be intermittent. On a background of Gaussian noise, there are rare events often referred to as *bursts* (Fig. 4.3 (a)). Most of the spectral power in SOL fluctuation measurements is found below 100 kHz (on TCV in Fig. 5.8 (d)). Using a poloidal array of probes, these structures have been observed to propagate with a velocity consistent with the  $E_r \times B_T$  drift (e.g. [58, 61]). The single-point bursty signal is believed to be a manifestation of coherent plasma structures, passing by the probe. These structures have also been observed using poloidal  $\times$  radial arrays of Langmuir probes [70, 66]. Similar observations are performed using non-perturbing fast imaging cameras collecting  $D_\alpha$  light resulting from edge plasma interactions with neutral gas [71]. The light emission intensity

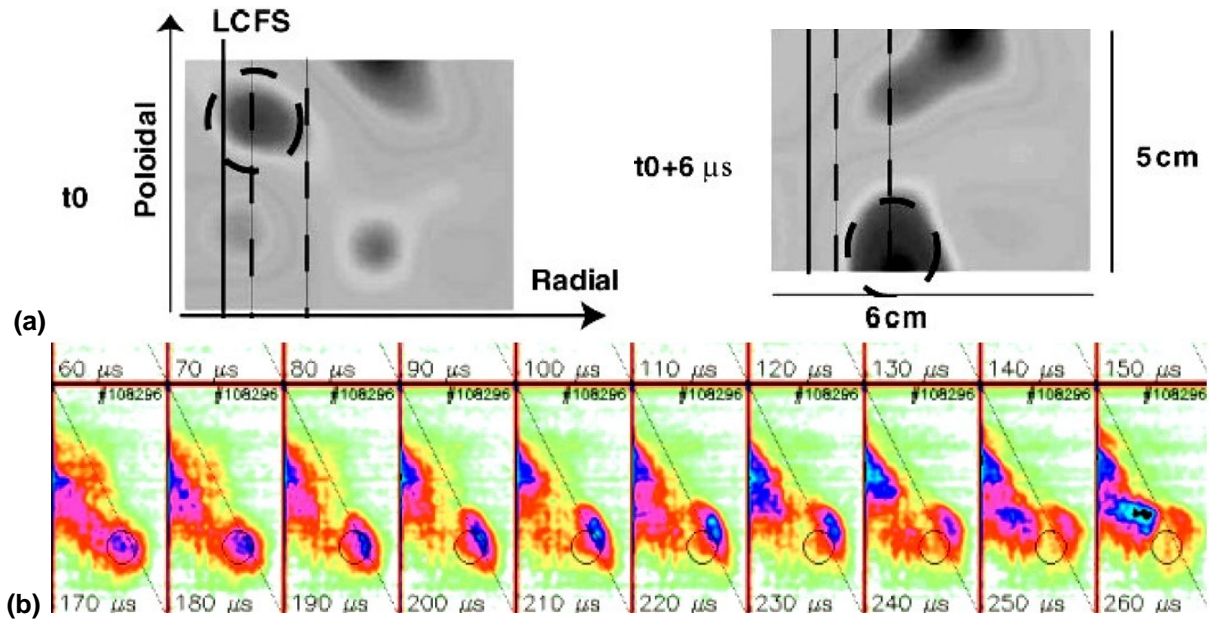


**Fig. 2.8** : Experimental observations of edge plasma turbulent structures: **(a)** Two frames from BES measurements in the DIII-D tokamak, showing 2D density plots [68]. There is a time difference of  $6\mu\text{s}$  between the successive frames. The structure marked with the dashed circle shown in both frames, clearly demonstrates both poloidal and radial motion. **(b)**  $10\mu\text{s}$  evolution of blob creation and propagation observed by fast gas-puff imaging on the NSTX tokamak [69].

is a complicated function, proportional to  $n_0 \times n_e^{0.5-0.8} \times T_e^{0.3-1.4}$ , where  $n_0$  is the density of neutrals. It is therefore difficult to estimate the particle or energy flux from such images. Nevertheless, the technique of *Gas puff imaging* (GPI), whereby neutral atoms are introduced by local gas puffing to "light up" the turbulent structures, has been used with great success on the C-Mod [71] and NSTX [69]<sup>1</sup> tokamaks (see Fig. 2.8 (b)). In the *beam emission spectroscopy* (BES) the  $D_\alpha$  light is emitted from collisional excitation of atoms in an externally introduced neutral beam with the plasma background ([68, 72], Fig. 2.8 (a)).

The intermittent structures seen by these diagnostics are characterized by poloidal dimensions of 1-4 cm, radially shorter by factor of two, and extending long distances along magnetic field lines ( $\sim 10$  m) [73]. In the parallel direction, correlations up to 90% over distances of  $\sim 6$  m have been reported (e.g. in [47]). The plasma turbulence thus has the 2D structure expected for particles moving freely along  $\mathbf{B}$ . The structures appear generally to be created in the separatrix vicinity, and then propagate radially at speeds in the range of 1 km/s [68, 69] and poloidally up to a factor of two more rapidly (e.g. [40]). The life-time of these structures is in the range 10 –  $50\mu\text{s}$ . These characteristics apply mostly to spatial and temporal structures in fluctuations of both  $I_s$  and  $V_{fl}$ ; the database for  $\tilde{T}_e$  is much smaller and non-existent for  $\tilde{T}_i$ .

Macroscopic turbulent structures have been observed using a hexagonal matrix of 86

<sup>1</sup>Experimental animations on [http://www.ppp1.gov/~szweben/NSTX04/NSTX\\_04.html](http://www.ppp1.gov/~szweben/NSTX04/NSTX_04.html)

probes covering the entire poloidal plasma cross-section of the Toroidal Plasma Experiment, TORPEX. The statistics of these blobs have been studied [65] as a function of confinement time by varying the magnetic pitch angle (by varying the vertical magnetic field) that determines the connection length. However, the turbulence character is quite different from that found in the tokamak SOL. This is due both to the lower magnetic field and density on TORPEX, compared to typical tokamak SOL parameters and the lack of rotational transform; both of them a consequence of missing toroidal electric current (the heating is purely non-inductive) and thus no poloidal magnetic field and poor confinement. Using Eq. (5.16), the Reynolds number of TORPEX plasma is 100-1000 $\times$  higher than in a tokamak (TCV) SOL, with consequently very different turbulence character (Fig. 2.1).

Two-dimensional arrays of Langmuir probes allow perturbative but well localized measurements (less than a centimeter) with excellent time resolution. Experiments on the circular cross-section CASTOR tokamak with limiter configuration demonstrate the existence of coherent structures with lifetimes significantly longer than the poloidal turn-over time ( $140\mu\text{s}$ ) [66]. This allows the distribution of turbulent structures to be reconstructed in the entire poloidal cross-section (Fig. 2.9), profiting from plasma roughly constant rotation velocity and turbulence being frozen into the plasma fluid.

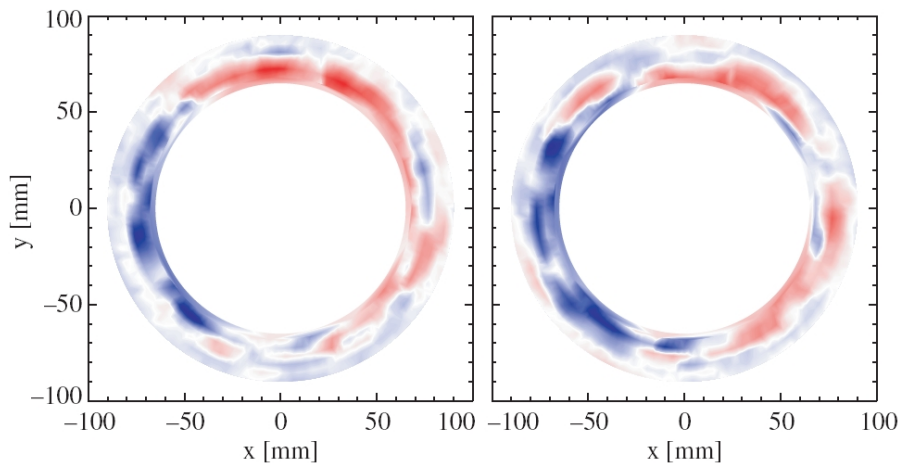


**Fig. 2.9** : Floating potential measured by a radial probe array in the CASTOR tokamak, mapped onto the poloidal plane. The two images refer to two subsequent poloidal rotation periods ( $140\mu\text{s}$ ). The estimated position of the LCFS is  $r = 65\text{--}70$  mm. From [66].

In all these papers different names are given to the observed structures, but it is believed that blobs, plasmoids, avaloids, intermittent plasma objects, streamers, filaments, avalanches and density fingers, intermittent events and bursts are simply different names [74] given to the coherent structures created by just a single edge plasma physics phenomena, perhaps a combination of the interchange instability and drift wave turbulence, observed by different diagnostics, models and physicists. For the sake of simplicity, the term "blob" is preferentially used in this thesis.

### 2.6.1 Turbulent transport

Section 1.3.2 has already made the important point that diffusion rates expected on the basis of classical collisional physics in the SOL are much smaller than those observed experimentally. A number of measurements over the past few years in the tokamak SOL indicate that the intermittent bursts seen on time traces of the turbulent flux are responsible for non-diffusive convective transport that can carry more than 50% of the cross-field particle flux [75] during events with amplitude several times higher than the main value occurring at only a small percentage (5%) of the total time, see e.g. [76].

There are both magnetic and electrostatic contributions to the fluctuation-driven drift cross-field transport (see Table 2.1), but in a tokamak, the strong external toroidal field means that magnetic fluctuations are generally found to be very weak in the edge,  $\frac{\tilde{B}_r}{B_T} \sim 10^{-5} - 10^{-4}$  [77]. This yields turbulent fluxes much smaller than those arising from the electrostatic contribution [78] since the level of density fluctuations,  $\sigma_n/\langle n \rangle$  is  $\sim 1 - 10\%$  in the confined plasma, and reaches typically 50 – 100% in the SOL. The fluctuating poloidal electric field,  $E_{\text{pol}}$ , yields, through the  $v_r = \mathbf{E} \times \mathbf{B}/B^2$  drift velocity, a fluctuating radial particle flux,  $\Gamma_r$ . In the SOL, measurements of this flux are generally only possible with Langmuir probes, though there have been attempts using heavy ion beam diagnostics [79].

Turbulent fluxes	Electrostatic contribution	Magnetic contribution
Particle flux	$\langle \tilde{n} \tilde{E}_{\text{pol}} \rangle / B_T$	$\langle \tilde{J}_{\parallel} \tilde{B}_r \rangle / e B_T$
Energy flux	$n \langle \tilde{T} \tilde{E}_{\text{pol}} \rangle / B_T + T \langle \tilde{n} \tilde{E}_{\text{pol}} \rangle / B_T$	$\langle \tilde{Q}_{\parallel} \tilde{B}_r \rangle / B_T$

Table 2.1: Radial fluctuation induced fluxes,  $\Gamma_r$ . From [10].

Probability distribution function (PDF) of the  $\mathbf{E} \times \mathbf{B}$  turbulent driven radial particle flux, computed as  $\Gamma_r = \tilde{n}_e \tilde{E}_{\text{pol}} / B$ , has been shown to have universal shape (rescaled by a scalar value of  $\sigma_r$ ) for both a small TJ-II stellarator and large JET tokamak [80]. The PDF is also found to be far from normally distributed, generally strongly positively skewed. Within the picture Fig. 2.7 of the  $(\nabla B \times \mathbf{B}) \times \mathbf{B}$  interchange instability, the edge pressure,  $p_e$  is correlated with  $E_{\text{pol}}$ . Since  $p_e = n_e T_e$  and given that  $n_e$  is partially correlated with  $T_e$ , then  $n_e$  and  $E_{\text{pol}}$  must be to some extent correlated. With forward toroidal field direction ( $B_T < 0$ ), whenever  $\tilde{E}_{\text{pol}}$  points upwards, plasma convects outwards from inner regions where  $n_e$  is higher, and vice versa for downward  $\tilde{E}_{\text{pol}}$ . As such, even though  $\Gamma_r$  fluctuates strongly, the mean value is directed outwards,  $\langle \Gamma_r \rangle > 0$ . Because the most probable value of  $\tilde{E}_{\text{pol}}$  is zero and close to zero for  $\tilde{n}_e$ , the most probable value of  $\Gamma_r$  is also zero. The PDF( $\Gamma_r$ ) must therefore be positively skewed, such that  $\langle \Gamma_r \rangle$  can be non-zero. These characteristics are illustrated in Fig. 2.10 using an analytic form for PDF( $\Gamma_r$ ), and by examples both from TCV experimental data and numerical simulations in Fig. 5.8 (b).

If turbulence is responsible for most of the cross-field particle transport, it should be possible to show experimentally that the turbulent driven radial flux can account for the total particle outflux. For a simple circular plasma, assuming the value of locally

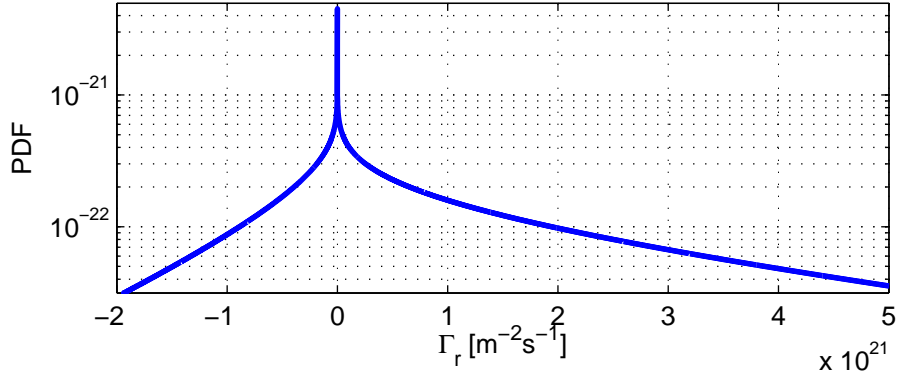


**Fig. 2.10** : Shape of the  $\mathbf{E} \times \mathbf{B}$  driven PDF( $\Gamma_r$ ) demonstrates that the most probable value is at the origin, and that the PDF is skewed towards the outward (positive) direction. The analytic form, taken from [81], assumes a realistic 60% correlation between  $\tilde{n}_e$  and  $\tilde{v}_r$ , both assumed to be normally distributed.

measured particle flux applies across the entire separatrix surface,  $4\pi^2 Ra$  (i.e. poloidally symmetric), the global particle outflux must balance the total number of particles leaving the confined plasma. The latter may be estimated (in steady state) using the line-averaged density,  $\bar{n}_e$ , plasma volume,  $2\pi^2 Ra^2$  and particle confinement time,  $\tau_p$ :

$$\Gamma_r 4\pi^2 Ra = 2\pi^2 Ra^2 \bar{n}_e \tau_p^{-1} \quad (2.12)$$

Agreement within a factor of two has been found (e.g. [78]), even though the transport is known to be poloidally asymmetric (favouring the low-field-side regions) and estimates of  $\tau_p$  are fraught with uncertainty. In many cases, notably for diverted configurations, this simple balance is not generally satisfied.

## 2.7 Theory and numerical models

### 2.7.1 Transport of an isolated blob

Most theoretical work related to blob transport in SOL plasmas has been based on analytical models describing the transient radial propagation of isolated plasma *blobs* due to the  $(\nabla B \times \mathbf{B}) \times \mathbf{B}$  interchange instability mechanism (described in Section 2.5.1). Such a blob is an excess of pressure propagating radially outwards (Fig. 2.11 (a,c)), or a pressure well propagating inwards (Fig. 2.11 (b)), due to the interchange motion, driven by the  $E_{\text{pol}} \times B_T$  drift, where the poloidal electric field, results from the  $\nabla B \times \mathbf{B}$  drift. Because such blobs have also been observed in linear plasma devices where  $\nabla B = 0$ , other forces have been suggested by which  $E_{\text{pol}}$  might be generated, e.g. the 'neutral wind' due to neutrals recycling from the wall [53].

The nonlinear evolution and radial propagation of isolated blob structures has recently been demonstrated by numerical simulations in [84, 85, 83, 86], which also confirms the asymmetric waveforms experimentally derived from single probe recordings. For a

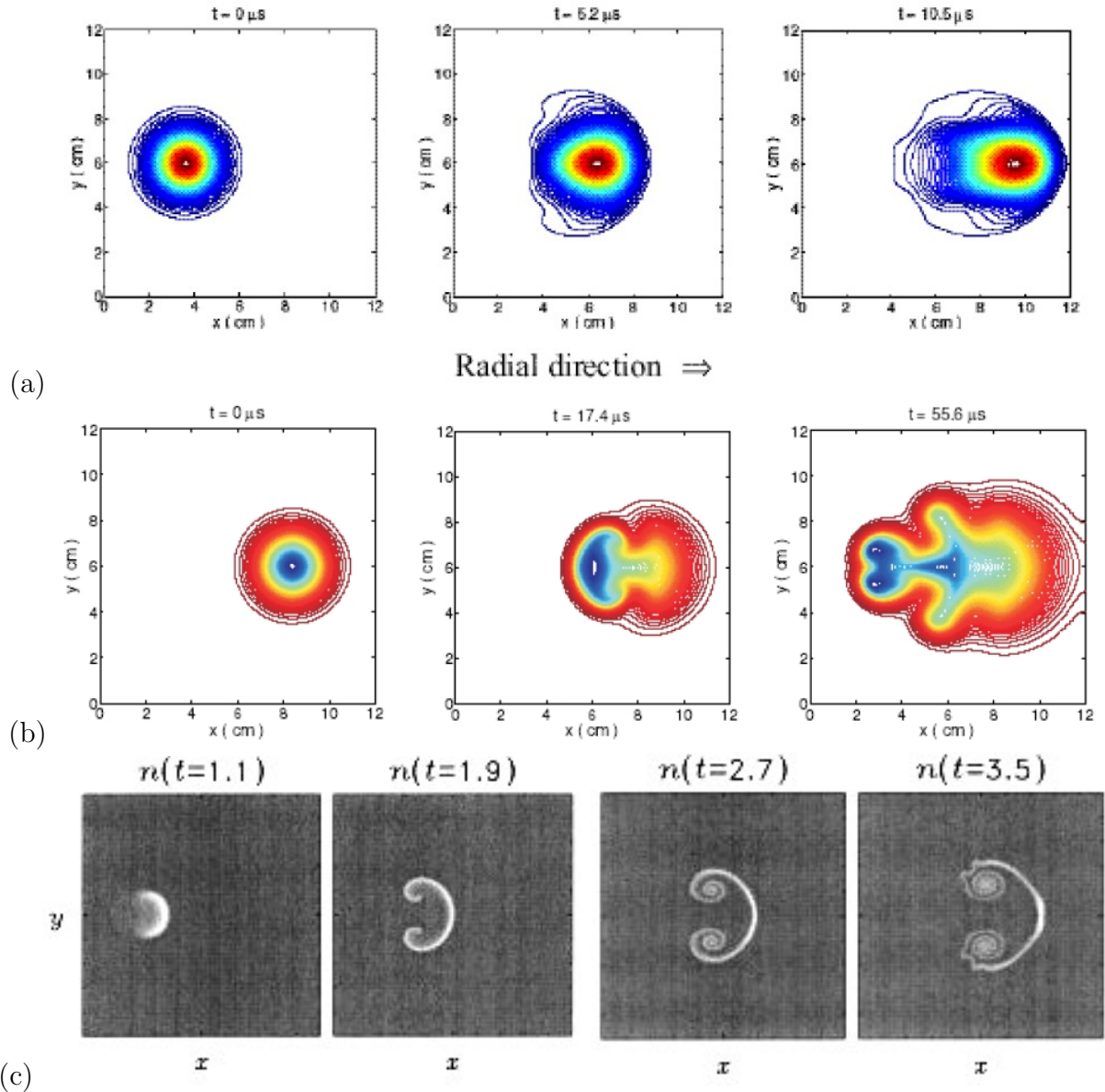


**Fig. 2.11** : Numerical simulations of single blob dynamics from two different modelling approaches. In all frames the positive radial direction is to the right, and the poloidal direction corresponds to the vertical axis. **(a)** Snapshots of blobs in time-frames separates by  $5 \mu\text{s}$  in the model of Krasheninnikov using the 3D turbulence code BOUT [82]. **(b)** The reversed process of holes propagating inwards [83]. **(c)** Contour plot shows how the blob evolves into a mushroom-shaped object in the model of Bian *et al* [84]. During the radial motion of the blob, the density concentrates at half of its periphery, creating a steep front.

blob with spatial dimension  $L_{\text{blob}}$ , it is found analytically in [87] that the blob radial velocity scales like  $v_r^{\text{blob}} \propto L_{\text{blob}}^{-2}$  as a result of the interaction between the blob and the electrostatic sheath at wall. An alternative approach in which the constraints imposed by sheath dissipation are relaxed (see [88] for a clear discussion of the relative merits of each approach) finds a contradictory scaling [86]:

$$\frac{v_r^{\text{blob}}}{c_s} \sim \sqrt{\frac{2L_{\text{blob}}}{R} \frac{\Delta n_e}{n_e}}, \quad (2.13)$$

where the factor  $\sqrt{\frac{1}{R}}$  originates from the magnetic field gradient and  $\frac{\Delta n_e}{n_e}$  is the blob relative density excess with respect to the background. This has been confirmed in experimentally [83]. Two different assumptions for the closure of the parallel current through the conducting first-wall surface (field line bending or not) are compared in [89].

Estimates in [87] show that the blobs with perpendicular scale  $L_{\text{blob}} = 1$  cm can propagate radially to distances of up to  $\sim 15$  cm, carrying  $\sim 10^{16}$  plasma particles. To establish the total cross-field plasma particle flux,  $\langle \Gamma_r \rangle = 10^{22} \text{ s}^{-1}$  (which is the typical experimentally measured value for the plasma flux through the separatrix on TCV) with such blobs requires a blob formation rate of  $\sim 10^6 \text{ s}^{-1}$ . For a poloidal length of  $\sim 50$  cm (on TCV) of the outboard separatrix where blobs are formed, this rate requires that the frequency of turbulent plasma oscillations producing blobs be about:

$$0.3 \text{ MHz} \frac{L_{\text{blob}}}{50 \text{ cm}} = 6 \text{ kHz} = \frac{1}{170 \mu\text{s}}, \quad (2.14)$$

which is in the range of *drift wave* frequency. Drift waves are therefore a candidate mechanism for the blob formation [87]. Section 5.2.8 will, however, demonstrate that the *interchange instability* itself can be responsible not only for the propagation but also the blob formation inside the separatrix. This is demonstrated in Fig. 5.17 (c) by the fact that the blob-generation frequency of  $\approx 190 \mu\text{s}$  is observed in SOL of both TCV experiment and the ESEL model, well comparable to Eq. (2.14).

## 2.7.2 2D models

Since the experimentally observed parallel correlation lengths [58] are much longer than those in the poloidal direction, a model in the radial  $\times$  poloidal plane should be a close approximation. On the other hand, in the tokamak geometry the situation on a single magnetic field line is complex since it passes through regions of favourable and unfavourable curvature, effects not accounted for in 2D models. Parallel drift wave dynamics and magnetic shear are also ignored in 2D models. Most 2D simulations (e.g. [49, 90, 91, 92, 24]) have relied on the *thin layer approximation* (defined in Section 5.1.1) and assumed a local turbulence drive within the SOL region [91, 92].

Developed by the Danish group in Risø, ESEL is a 2D fluid model describing the self-consistent time evolution of edge plasma fluctuations in density, temperature and vorticity [49]. It is used extensively in Chapter 5 of this thesis for comparison with TCV

data, described in detail in Section 5.1. In ESEL, the turbulence is driven by interchange motions due to magnetic field curvature in a local slab approximation.

The same interchange mechanism is the basis of the model due to Sarazin and Ghendrih [91, 92, 93]. Spatially localized sources are used in both models, allowing the profiles to evolve self-consistently. Both codes are very similar, but the Sarazin model differs from the ESEL approach in several key features:

- parallel damping is present everywhere in the computational region - no region of closed field lines is included
- $T_e$  is assumed constant, which, as discussed by Bisai [90], has important negative consequences. Including  $T_e$ -fluctuations, the 2D interchange model described in [90] results in the instability being driven by constant particle and heat flux, giving better agreement with experiment, even though the statistical comparison is only qualitative. In accordance with most models in the literature,  $T_i \ll T_e$  is assumed in order to avoid the necessity to include finite Larmor radius effects.
- the equations are solved numerically using a double spectral code, which implies periodic boundary conditions in both the poloidal, but also in the *radial* direction; Section 5.1.5 demonstrates that using radial periodic boundary conditions for the plasma potential leads to unrealistically fast poloidal flows
- the particle source is fixed at  $x = 0$  (Fig. 2.12), nicely demonstrating that towards the inner (left) boundary, the turbulence is damped since  $\nabla B$  is antiparallel to  $\nabla n$  at this point, the Sarazin model thus models both LFS and HFS of a tokamak at the same time
- the vorticity damping term is proportional to the electrostatic potential, effectively damping large scales of the fluctuations. To avoid any flaws due to damping at large scales (which are ubiquitous in interchange models), ESEL uses an ad-hoc damping on the vorticity itself. As discussed in [88], in the conduction-limited, collisional ( $\nu^* > 10$ ) regime (valid in TCV even at low density), this approach is more appropriate. The turbulent field produced by the Sarazin code, shown in Fig. 2.12, shows a behaviour somewhat different from the blob-like structures observed in experiment (Fig. 2.8) and in the ESEL simulations (Fig. 5.6); the explanation lies in the faster decay of larger structures in ESEL.

The poloidally localized convective cells elongated in the radial direction seen in Fig. 2.12 have been referred to as *streamers*, *avalanches* or density fingers. The Mach number of radial propagation is found to be  $M_\perp \sim 0.04$ , [92], consistent with experimental observations.

The pressure-driven interchange instability has also been modelled and compared directly with the Langmuir probe experimental data from the CASTOR tokamak [94]. The characteristic dimensions and timescales of the density, fluctuation induced particle flux and potential structures were found to be close to the experimental values obtained from a 2D matrix of Langmuir probes. The model has been used especially to simulate transitions into better confinement mode using an electrode biasing, the turbulent driven fluxes reduce remarkably in agreement with the experimental data. Example of the output, 2D

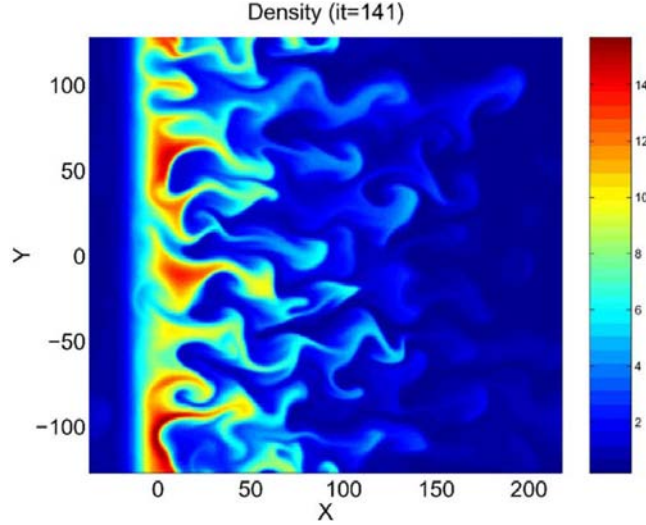


**Fig. 2.12** : The Sarazin model [91] produces 2D "density fingers" extending in the radial direction. Here the simulation domain is centred on the outside midplane. The poloidal direction is along the vertical axis and the direction radially outward is to the right.

density fluctuation contour on poloidal cross-section of the CASTOR tokamak is presented in Fig. 2.13 .

### 2.7.3 3D models

Three dimensional turbulence simulations represent a significant computational challenge and are currently less well developed than their 2D counterparts. In 1997 B. Scott presented a 3D plasma turbulence model [95] with the principal conclusion that "the type of turbulence which results from the collisional electron fluid equations in tokamak geometry is collisional drift wave turbulence, the magnetic curvature terms (responsible for the interchange instability) are hardly dominant." This is valid, however, only in the region of closed field lines and thus does not apply to the SOL plasma.

Edge plasma profiles and fluxes have been modelled by the 2D fluid code UEDGE coupled with the 3D turbulence code BOUT [96]. The latter solves fluid equations for plasma vorticity, density, ion and electron temperature and parallel momentum, and also includes regions of open and closed field lines. Comparison with experiment has been performed in terms of power spectra of the turbulent driven particle flux in [97]. Dipole structure (equivalent to mushroom-like in Fig. 5.6 ) of the blobs is reported in [98]. BOUT has also been used to demonstrate the increase in turbulence fluctuation levels and radial transport as density (thus collisionality) increases [99]. At high plasma density, a large part of the turbulent flux is found to arrive on the first wall instead of the divertor region. A large increase in the effective diffusivity,  $D_{\text{eff}} = -\Gamma_r / \nabla_r n$  occurs as the Greenwald *density limit* is approached, while the edge temperature and gradient drop precipitously, the strong  $E_r$  shear layer is also destroyed and the region of high diffusivity extends inward. The simulations further indicate that as density increases and

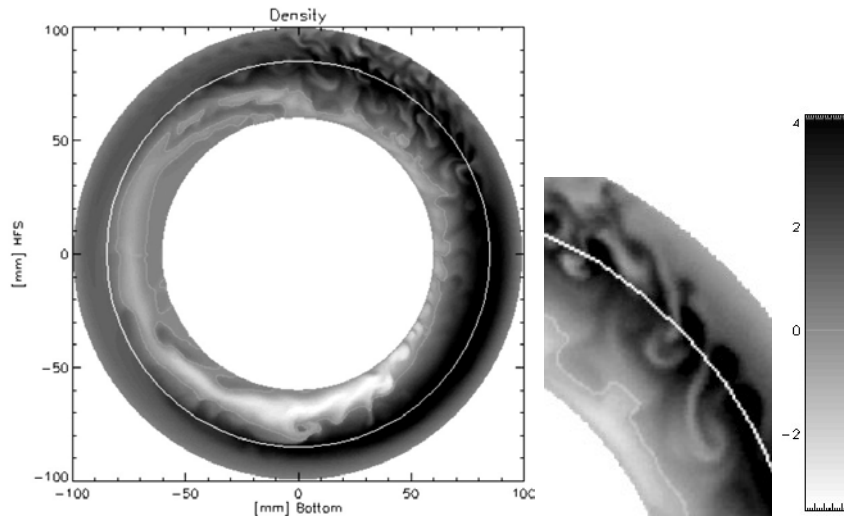


**Fig. 2.13** : 2D density fluctuation  $n(r, z, t) - \bar{n}(r)$  contour on a poloidal cross-section of the CASTOR tokamak; the plasma centre is not modelled, the limiter at  $r = 85$  mm is marked with the solid line. The top right corner is zoomed (in a different time frame), showing clearly both inward and outward propagating mushroom-like blobs with trailing wakes. The shading-bar scale is shown on the right in units of  $10^{18} m^{-3}$ . From [94].

temperature decreases, the fluctuation levels and the Reynolds stress drive increase while the sheath potential decreases, so that the region of negative  $E_r$  extends outward. Finally, the Greenwald density limit empirical scaling [100],  $n_G = I_p / \pi a^2$  has been also obtained within the BOUT model [99].



# Chapter 3

## The fast reciprocating Langmuir probe

### 3.1 Introduction

Probing the edge of modern tokamak plasmas requires fast reciprocating systems capable of sustaining high heat and particle fluxes but offering low level of contamination to the plasma. If, in addition, a modular design provides a compact, relatively inexpensive system allowing rapid probe head exchange and high bandwidth operation for turbulence measurements, then the system is well suited to use on TCV. Just such a fast reciprocating probe (RCP) system has been designed and constructed by a group at the University of California at San Diego (UCSD), USA and has been used successfully for many years on the TEXTOR and DIII-D tokamaks. One of these probe systems is on long term loan to CRPP from the UCSD group. The detailed probe design is described in [101]. It is with this RCP system that all the data presented in this thesis have been obtained.

Although the essential components of the system as presented in [101] remain unchanged, the diagnostic (in particular the probe head itself) as loaned to CRPP (used previously at the TEXTOR tokamak) has been completely refitted in Lausanne prior to the commencement of this thesis and somewhat adapted for use on TCV. During the course of this thesis, a number of new probe head designs have been manufactured and used in measurements. Details of those new heads and other relevant adaptations of the system will be given in this chapter, along with a discussion of signal treatment and how the important turbulence parameters are computed.

### 3.2 Probe construction

#### 3.2.1 Geometry of TCV

The TCV tokamak geometry is characterized by the major radius  $R = 0.875m$  and minor radius  $a = 0.24m$ . The probe enters the plasma edge through a port on the tokamak

low-field-side midplane. Fig. 3.1 illustrates the probe penetration into a typical diverted discharge. The equilibrium flux surfaces are reconstructed using poloidal magnetic flux measurements obtained with two arrays of in-vessel Mirnov coils. Reconstruction of the magnetic flux in the poloidal plane,  $\Psi(R, z, t)$  is performed with the LIUQE equilibrium solver [102], assuming toroidal symmetry. After that  $\Psi(R, z, t)$  may be readily manipulated using the TCV-PSI-Toolbox [103] to obtain all the relevant magnetic quantities, based on precise computation of space derivatives of  $\Psi$ .

A magnetic toolbox has been developed during the course of this thesis which computes many edge plasma physics relevant quantities for both TCV and JET tokamaks. Among others it calculates connection length with 3D field line tracing and intersecting the complex 3D vacuum vessel. Further, 3D magnetic field, flux mapping and expansion, 1st wall 3D strike angles are computed. All this is available in a graphical easy-to-use user interface, using independent Matlab<sup>®</sup> routines. This toolbox allowed also precise RCP probe head design (Section 3.2.4) and lead to co-authorship of [104, 105].

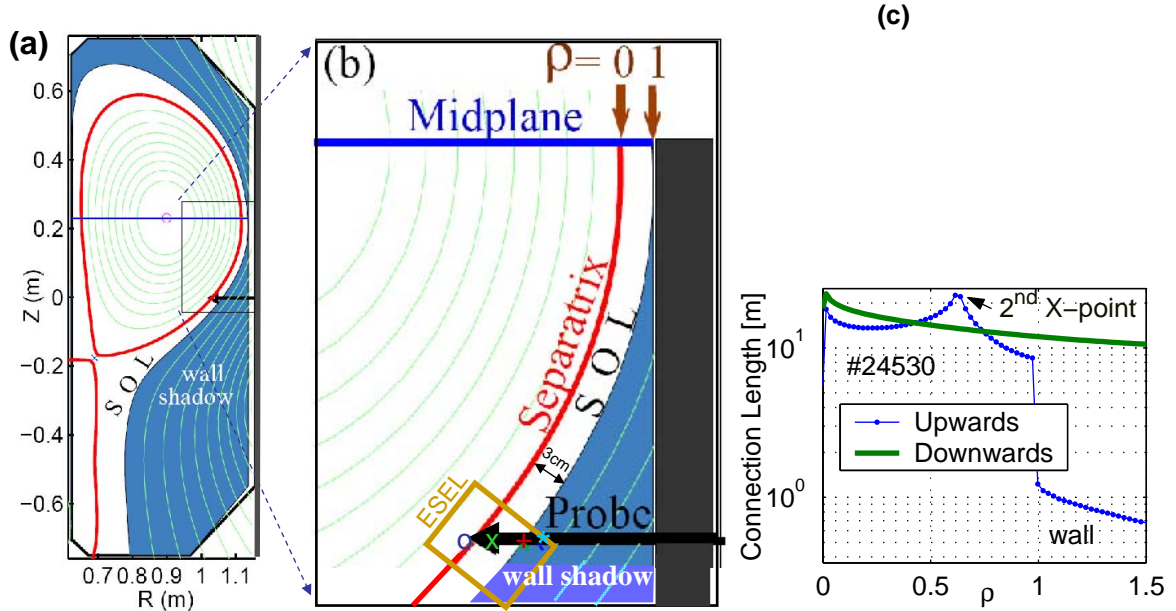


**Fig. 3.1 :** (a) Poloidal cross-section of the SNL, standard TCV diverted magnetic equilibrium (e.g. #24530). The Langmuir probe reciprocates on the outer machine midplane through the region enlarged in (b), in which mapping to the normalized coordinate,  $\rho$  on the midplane is also shown. Four probe positions corresponding to Fig. 4.3 and the ESEL model (used later in Chapter 5) computational region are marked. (c) Edge profile of the parallel connection length computed from the TCV magnetic reconstruction.

During a single insertion, the probe travels first through the "wall shadow", the region of SOL plasma in which field lines connect directly to the main chamber wall and lower divertor with  $L_{\parallel} \leq 2m$  upwards towards the inner target and  $L_{\parallel} \approx 10m$  downwards towards the outer target, see Fig. 3.1 (c). Deeper still, the probe finds itself in the main SOL where the field lines connect to the divertor plates and for which  $L \approx 10 - 20m$ .

Throughout this thesis, data are plotted in terms of a normalized distance,  $\rho$ , mapped from the probe location to the outside midplane. In this coordinate,  $\rho = 0$  at the separatrix and  $\rho = 1$  at the midplane wall (Fig. 3.1 (b)). For the majority of discharges studied  $\rho = 1$  corresponds to separatrix to wall distance in the range 18 – 33 mm. Any data for which  $\rho > 1$  corresponds to region outside the midplane wall radius and is thus in the "wall shadow".

On TCV, standard operation is performed with positive toroidal magnetic field direction,  $B_T > 0$ . For lower single null plasmas this means that the ion  $\nabla B \times \mathbf{B}$  drift is directed away from the X-point (i.e. upwards). On most other tokamaks (e.g. JET) the standard operation is with the  $\nabla B \times \mathbf{B}$  drift downward towards the X-point. The reason is largely historical originating from the early years of TCV operation, during which many experiments, particularly involving ECRH, required L-mode plasmas. For favourable  $\nabla B \times \mathbf{B}$  drift direction, ohmic H-mode is readily achieved on TCV, even at lower input power. Operation with  $B_T > 0$  is referred to here as *reversed field*, with  $B_T < 0$  being operation in *forward field*.

It should be noted that even though the extensive magnetic diagnostic system on TCV makes for rather precise magnetic reconstructions, still there are several discrepancies. Uncertainty in the separatrix position at the outside midplane is of particular interest because it is used as the point of origin of the midplane mapping,  $\rho = 0$ . Unfortunately, no direct calibration using a non-magnetic technique of separatrix position is available. Theoretically, the plasma potential,  $\phi$  must reach maximum at the separatrix, the transition between a sheath-limited open field lines ( $E_r > 0$ ) and the confined region ( $E_r < 0$ ) on closed field lines. Sharp density profile break at  $\rho = 1$  is also expected,  $dn_e/dr|_{\rho < 1} < dn_e/dr|_{\rho > 1}$  because of sharp drop of the connection length (Fig. 3.1 (c)) and consequent parallel plasma damping. Attempts have been made to locate the separatrix in this way using the probe data, but the noisy  $T_e$  and  $V_{fl}$  data from which  $E_r$  is estimated permit no improvement on that obtained from the magnetic equilibrium reconstruction. At best, such comparisons allow the separatrix position error to be estimated at  $\approx 2$  mm at the midplane. In [106] systematic error estimation of the midplane separatrix position (with respect to the vacuum chamber) from the magnetic reconstruction has been estimated to be below 1 mm. It can be therefore concluded that the probe position error is not significant. Far from the region of interest, however, the lower X-point position is observed to drift away by up to several centimeters with respect to estimations based on divertor Langmuir probes and infrared camera.

### 3.2.2 Plant implementation

Fig. 3.2 (a) illustrates the probe implementation on the TCV vacuum vessel. The probe enters horizontally through the midplane port using a re-entrant, bellow-ceramic-bellow flexible hose, permitting relative movement of the vacuum vessel with respect the probe (of order a few mm) during bake-out ( $210 - 230^\circ C$ ) when the vessel expands. A gate valve and standard vacuum pump system allow the probe to be removed from the torus without breaking torus vacuum, making for reasonably rapid probe head exchange. After each such

intervention, the main bellow systems are baked out and the system pumped for about two days, allowing base pressures of  $\sim 10^{-5} Pa$  to be reached before the gate valve is opened to TCV. As with all diagnostics and plant control systems, the probe is remotely controlled through the network of Vsystem databases running on the TCV VAX cluster. Interaction with the database proceeds via a dedicated Vsystem graphic interface. The database communicates via the BITBUS protocol with a dedicated electronic slave unit containing timer units to activate the slow and fast reciprocation systems (see Section 3.2.3) via programmable AnalogLogic (PAL) switches.

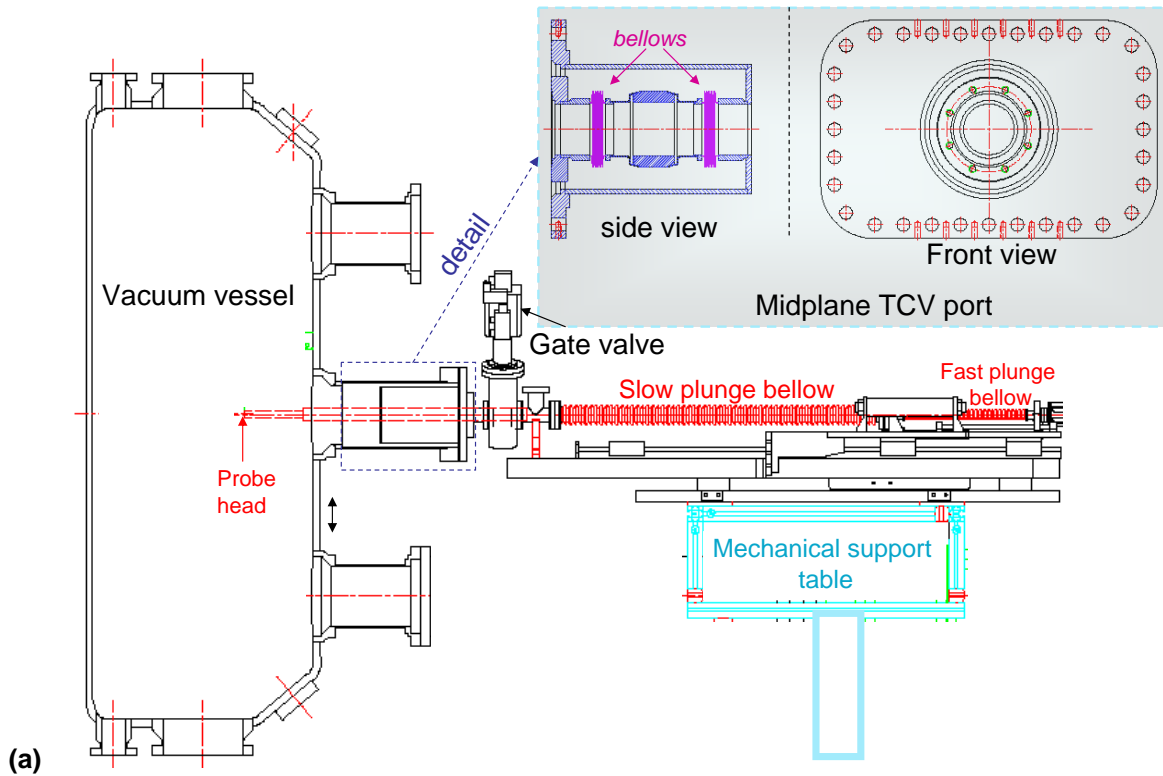
### 3.2.3 Drive system

The probe assembly, shown in Fig. 3.2 (b), is comprised of two main parts: the probe itself and the drive mechanism. The probe drive design is a compromise between the desire to obtain sufficient measurement statistics and to reduce damage to the probe due to the high heat fluxes experienced in the plasma edge. As shown by the compilation of typical signals in Fig. 3.3 (a), the reciprocation time of the system is  $\sim 300ms$  in total. With the exception of high power, low density electron cyclotron heated discharges, which destroyed both the pins and the boron-nitride matrix of the probe head, none of the ohmic discharges used to obtain the data reported here have ever caused serious damage to the diagnostic.

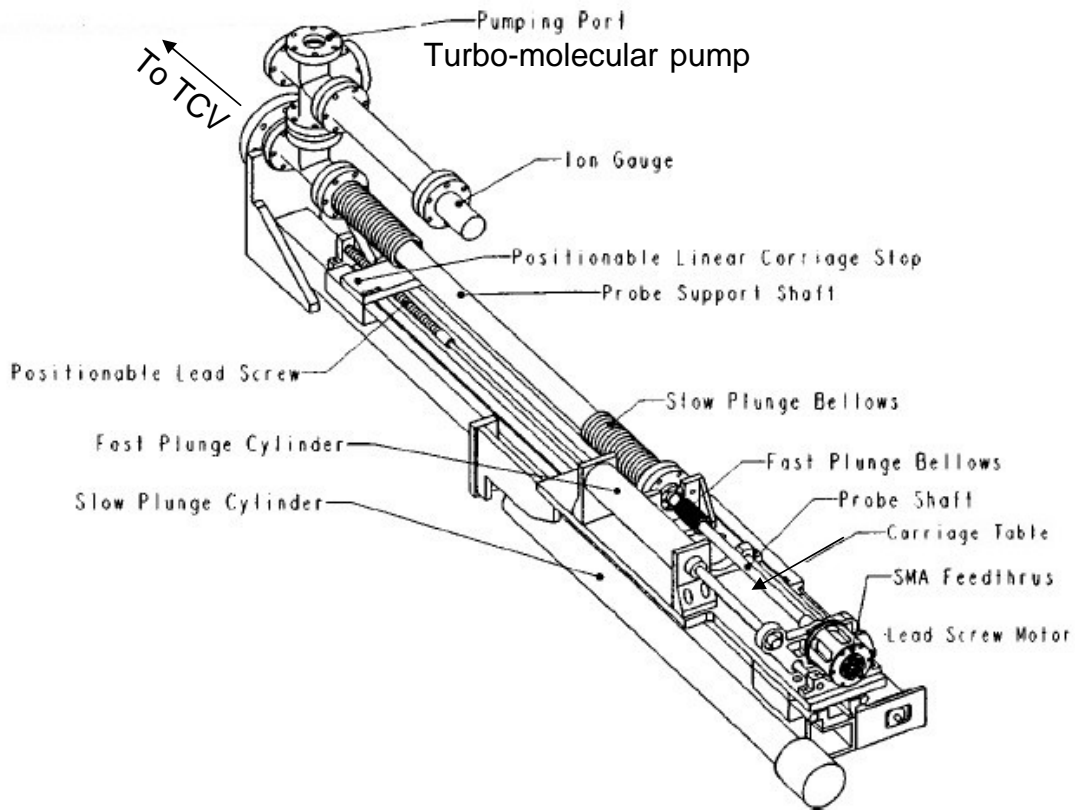
The drive mechanism is a two-stage pneumatic system which uses an air-driven piston to compress the "slow" bellow and position thus the probe inside the TCV port. Once triggered by the TCV control system, a second pneumatic cylinder under  $\sim 4bar$  helium pressure is activated and drives the probe head through a fixed, 15 cm return stroke using a smaller "fast" bellow. There is no adjustable dwell time or variable reciprocation time; these are determined uniquely by the piston length and adjustments to the mechanical exhaust valves. The resulting fast reciprocation trajectory is roughly parabolic with average speed  $|v| \approx 1$  m/s and maximum acceleration  $|a| < 40ms^{-2} \approx 4g$  (see Fig. 3.3 (b)). As discussed in Section 3.4, maximum penetration depth that can be tolerated is limited essentially by unipolar arcing from the graphite probe tips.

The head design comprises five independent Langmuir probe tips manufactured in polycrystalline graphite and mounted on a boron nitride tip holder (the head) for electrical insulation (Fig. 3.4 (a)). The whole structure is held together and protected against high heat fluxes by a graphite shroud. Each tip is exactly  $d = 1.5$  mm in diameter, but the length varies from pin to pin and head to head,  $l = 1.5 - 2.2$  mm. The length is, however, precisely measured before and after each set of experiments and used for calibration of the measured current in Eq. (3.2).

The modular probe head components, shown in exploded isometric view in Fig. 3.4 (a), have been entirely redrawn in metric form (from the original US imperial dimensions) and remachined at CRPP. All cables from the vacuum feedthrough to the probe head have been made fully coaxial, using  $50\Omega$  Kapton Coax cable, to reduce cross-talk and external pick-up. The original UCSD design also contained high precision  $100k\Omega$  resistors built in to the probe head and attached to pins 3 and 4 (see Fig. 3.5 (a-d)), allowing them to



(a)



(b)

**Fig. 3.2 :** (a) Implementation of the probe on TCV. (b) Illustrating the principal fast and slow probe drive components (from [101]).

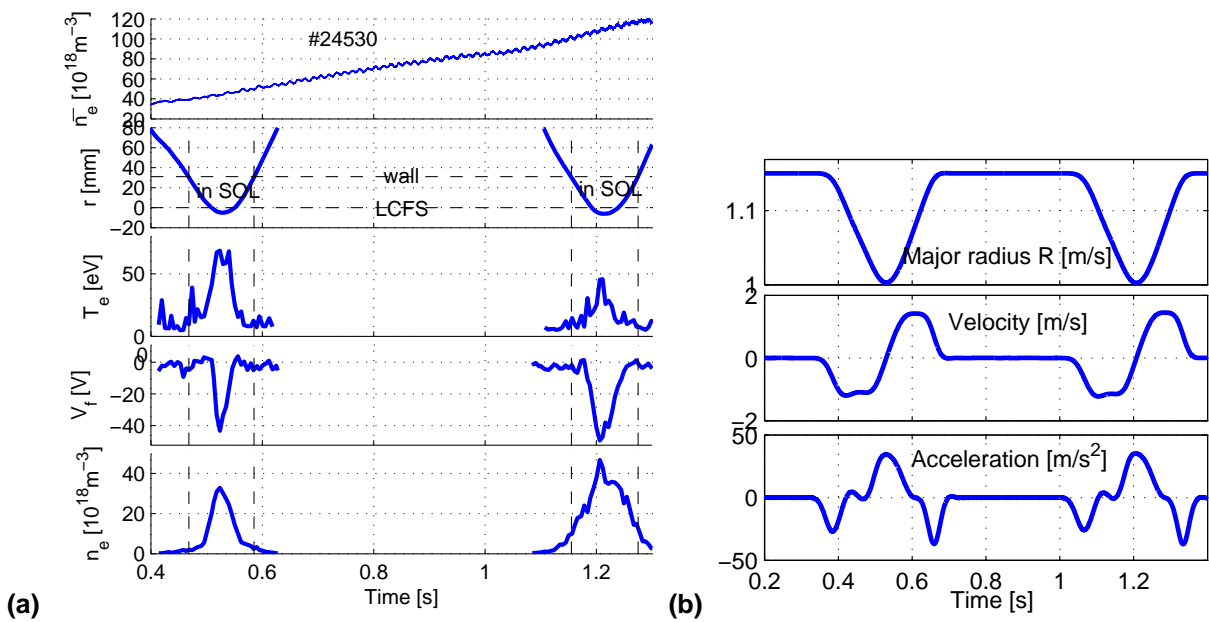


**Fig. 3.3 :** (a) Probe signals during a typical double reciprocation into a density ramp discharge; this particular L-mode ohmic discharge #24530 will be used as an example many times in this thesis because all diagnostics worked correctly and the RCP probe reciprocated exceptionally deep. Evolution (from top to bottom) of line averaged main plasma density, probe distance from separatrix, local electron temperature, floating potential and plasma density. Plasma current  $I_p = 340$  kA,  $\delta = 0.35$  and magnetic geometry in Fig. 3.1 . (b) The fast probe major radius  $R$ , velocity  $dR/dt$  and acceleration  $d^2R/dt^2$ .

float electrically. These resistors have been removed to allow Pin 3 to be used in voltage sweeping or ion saturation current mode.

### 3.2.4 Probe heads

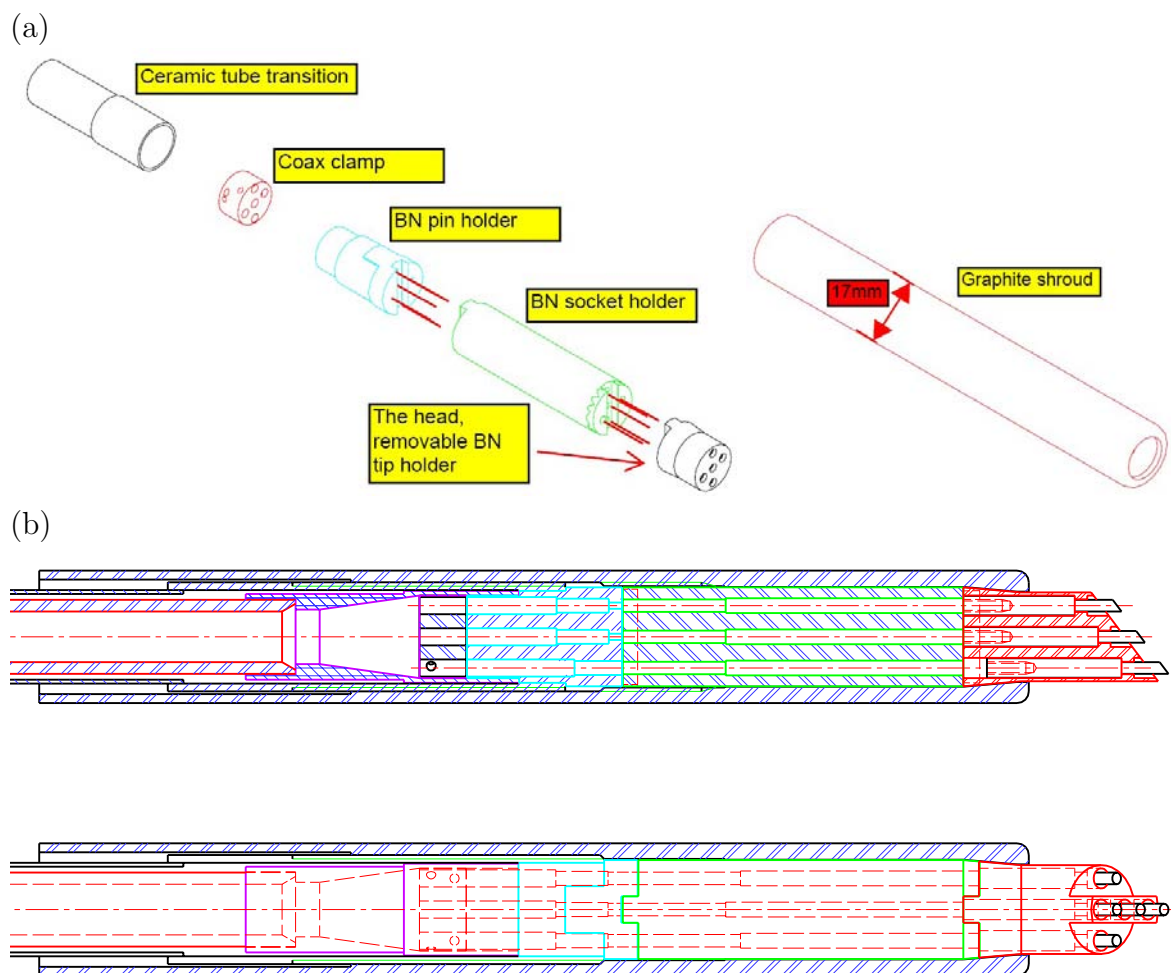
Fig. 3.5 illustrates how the probe head geometry has been varied during the course of this thesis. The original design for TEXTOR [101] is shown in Fig. 3.5 (a). To match the standard diverted equilibria on TCV at the probe position (Fig. 3.1 (a)), a new head, Fig. 3.5 (b) was designed with an oblique angle of  $37^\circ$  in the  $[r,z]$ -plane such that, at any time during the reciprocation, all 5 pins lie on a single magnetic surface, but are poloidally shifted such that no pin shields any other. To provide Mach probe capability, a central bar has been added in a later variant (Fig. 3.5 (c)) such that pins 2 and 5 form a Mach probe pair for the measurement of parallel plasma flow speed (see Section 3.10 and Chapter 6). This configuration also allows the measurement of radial gradients of density and potential using pins 3, 2 and 5 (see Section 3.8). On head (c) in particular, pins 1,3,4 are separated purely poloidally, pins 2,5 in the parallel direction and pins 2,3 and 3,5 purely radially. Note that radial here implies the cross-field, or direction perpendicular to a magnetic surface, and not the direction of major radius,  $R$ . In the context of Mach flows, dedicated experiments have been performed (see Chapter 6) during this thesis work to investigate the poloidal dependence of parallel flow strength. Yet another probe head (Fig. 3.5 (d)) was designed for this work, which required Mach flow measurements near the plasma midplane where the poloidal magnetic field is purely vertical and magnetic surfaces are flat.

## 3.3 Electronics and data acquisition

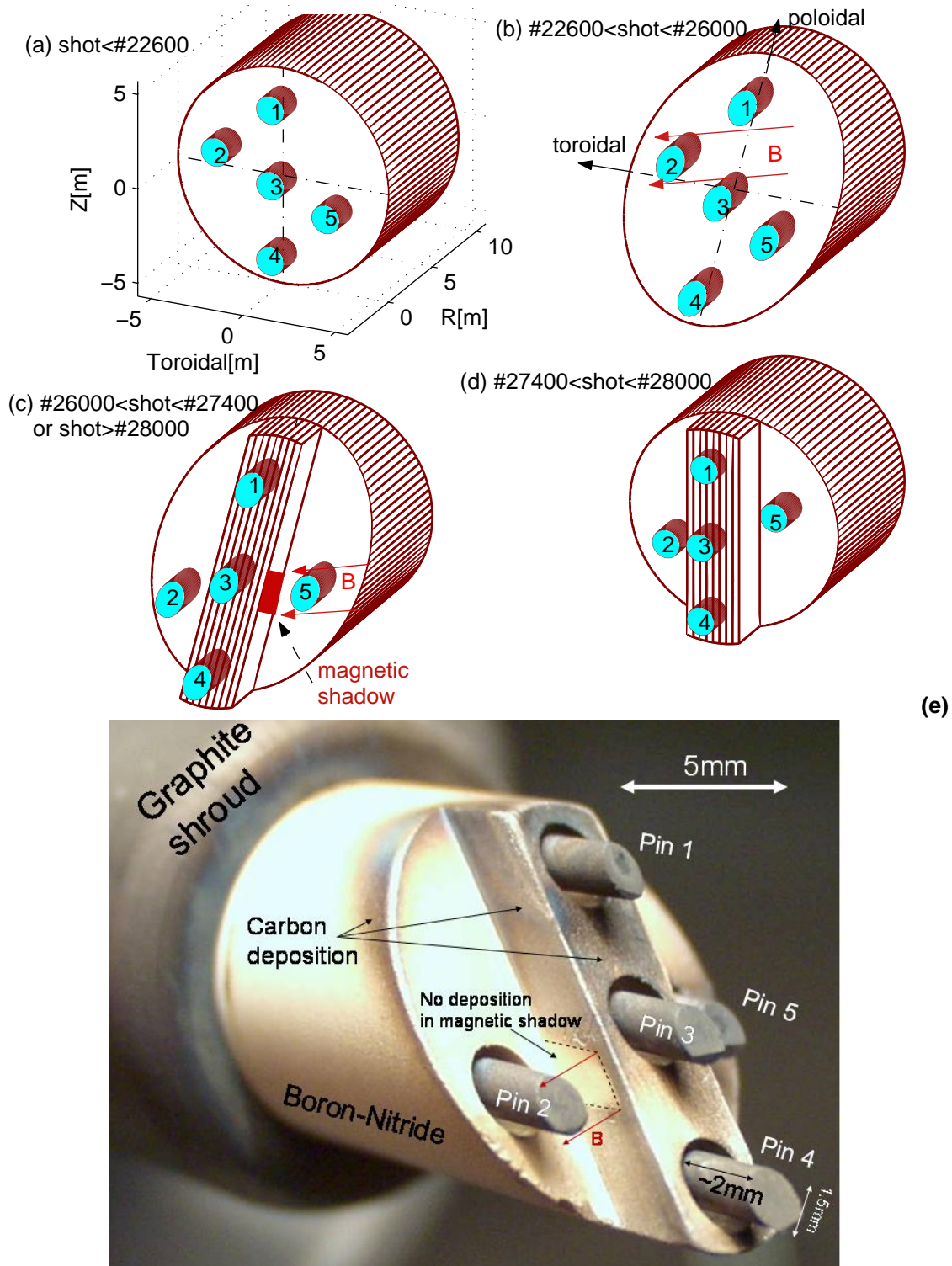
The electronics used for the fast turbulence measurement have been developed during the course of this thesis, representing an improvement on the system as first installed on TCV which was equipped only for low frequency ( $\approx 100kHz$ ) acquisition. Measurement of probe current in the range from DC to  $6MHz$  is provided by two separate electronic systems which are combined in Fourier space, following data acquisition: digital low-pass filter,  $f < 4.5kHz$  is applied to the signal acquired from low frequency to DC and a high-pass filter,  $f > 4.5kHz$  to the high-frequency data.

Fig. 3.6 (a) represents schematically the electronics and data acquisition system for a typical application in which 3 pins are configured for fast current measurements and for floating potential. In practise, any pin can be connected for ion saturation current, voltage sweeping or floating potential measurements. The low-pass current and voltage measurement is provided by APEX<sup>1</sup> amplifiers (which drive the probe current) with bandwidth from DC up to  $100kHz$  (3dB). The signal is digitized at  $125kHz$  or  $250kHz$  using the TCV standard, 6 channel TRCH ADC's. High-pass acquisition of both floating potential,  $V_{fl}$  and ion saturation current,  $I_s$  data, defined in Eq. (3.2) and Eq. (3.4), is provided by

<sup>1</sup>Avocent Inc, USA, <http://www.apex.com/>



**Fig. 3.4 :** (a) Probe head assembly showing the modular construction which allows easy head replacement. The interconnected probe head components are designed to allow a smooth transition from the coaxial cables taking signals down through the main shaft to the probe vacuum feedthrough to the graphite pins. A polycrystalline graphite shroud (b) holds the head components together and protects them from plasma fluxes. The shroud connects to the probe shaft using a multi-turn screw shroud.



**Fig. 3.5 :** Gallery of all four RCP probe heads used on TCV during the course of this thesis. The TCV discharge numbers indicate the shot ranges over which the heads have been used. **(e)** shows a photograph of the probe head **(c)** following plasma exposure. Colouring on the boron-nitride insulation surface is due to the deposition of carbon layers in regions exposed to plasma flowing along the magnetic field.

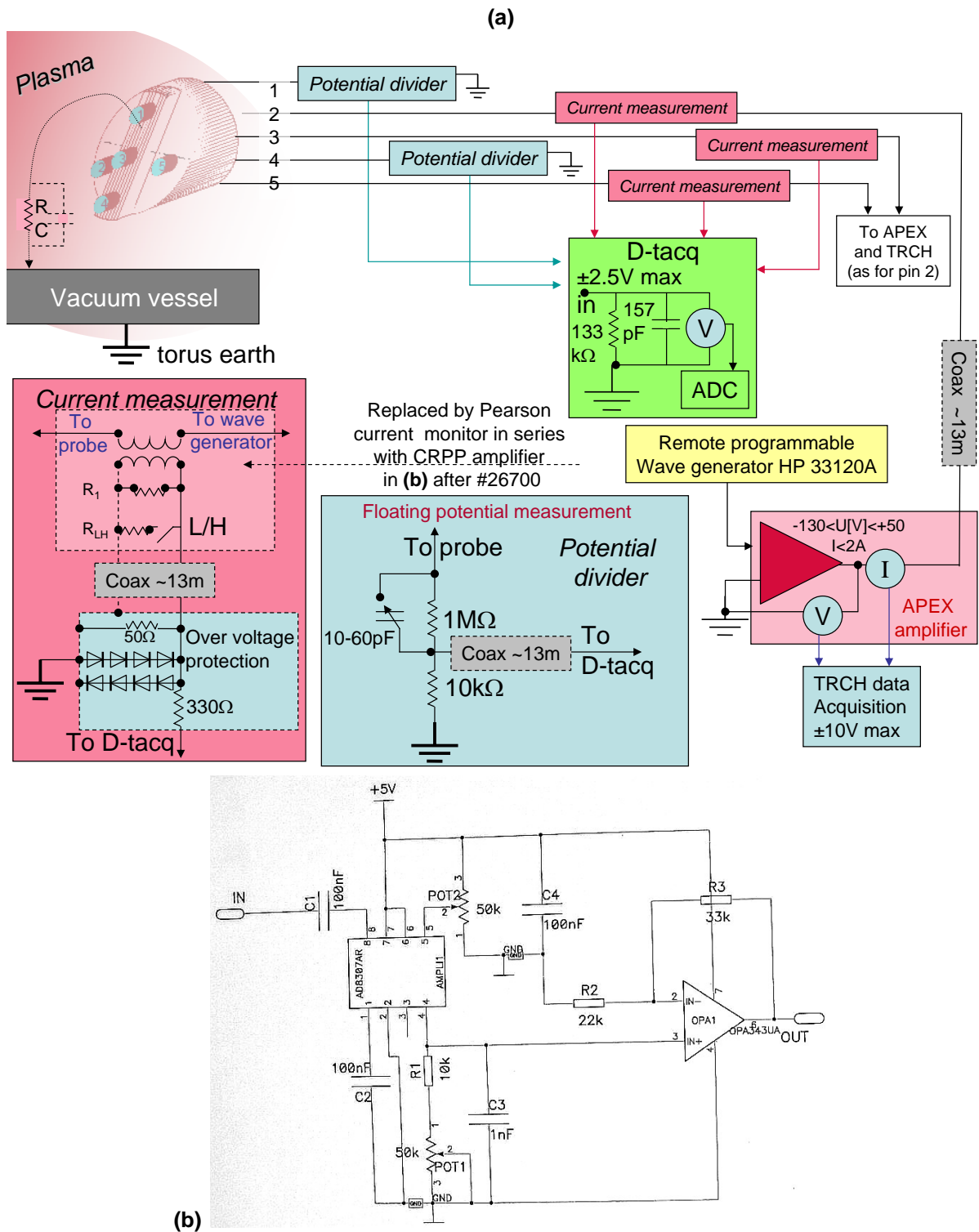


**Fig. 3.6 :** (a) Block diagram of the RCP data acquisition and electronics. Schematics of the fast  $V_H$  and  $I_s$ -measurement electronics are shown separately on the left. For TCV discharges after #26700, the CRPP-made current transformers are replaced by the Pearson current monitors in series with the fast CRPP amplifier shown in (b).

D-tAcq<sup>2</sup>: two 14bit, differential input ADC cards with 4 channels each providing acquisition of voltages in the range  $-2.5 < U[V] < +2.5$  at 6MHz standard sampling. Specific overvoltage circuitry is provided for these delicate modules. A single discharge with two reciprocations typically generates  $\sim 70MB$  of data.

In-house CRPP-made current transformers were initially used for high frequency measurements (AC only). The transfer function of the full electronics circuit from the probe to the D-tAcq acquisition is shown in Fig. 3.7 and is used for signal calibration. The amplitude is normalized to that computed from values of resistors,  $R_1^{-1} + R_{LH}^{-1} + 50\Omega^{-1}$  based on Fig. 3.6 (a), where a possibility to have high (H) or low (L) voltage/current gain is provided by (dis)connecting the  $R_{LH}$  resistor. In later experiments (for discharges after #26700), commercial current monitors<sup>3</sup> with larger bandwidth ( $1Hz < f < 20MHz$ ) have been used. This avoids the problem of summation of separate signals (TRCH + D-tAcq) in different frequency ranges which is unsatisfactory, especially during transient events like ELMs which has not been correctly understood. Concerning the ordinary plasma turbulence (outside ELM events or disruptions), the current monitors yields signal of no difference in the turbulence character as that measured with the CRPP-made current transformers combined with TRCH. Because the output voltage of these new current monitors is low (gain=0.1V/A), a 40dB high-frequency amplifier (Fig. 3.6 (b)), designed at CRPP, is used to increase the signal level to the  $\pm 2.5V$  range possible at the D-tAcq input.

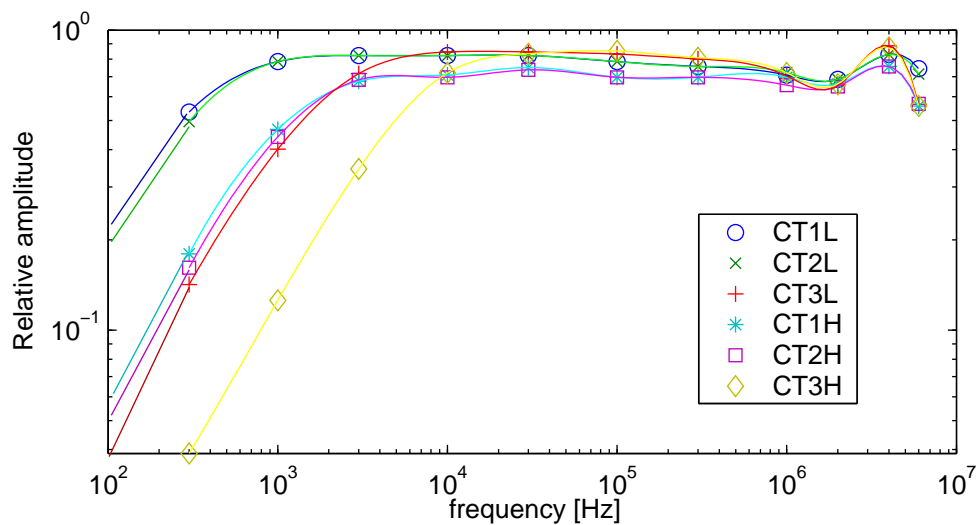


**Fig. 3.7** : Transfer functions of the full fast  $I_s$ -measurement: current transformer CT (1,2,3 at Low and High gain), 13m cables and the D-tAcq acquisition, corresponding to a high-pass filter.

The direct interaction of the probe head with plasma means that all probe electronics must be grounded with respect to the vacuum vessel and not the TCV building earth,

<sup>2</sup><http://www.d-tacq.co.uk/ACQ16PCI.htm>

<sup>3</sup>Model 411 from Pearson Electronics, Inc., USA, <http://www.pearsonelectronics.com/>.

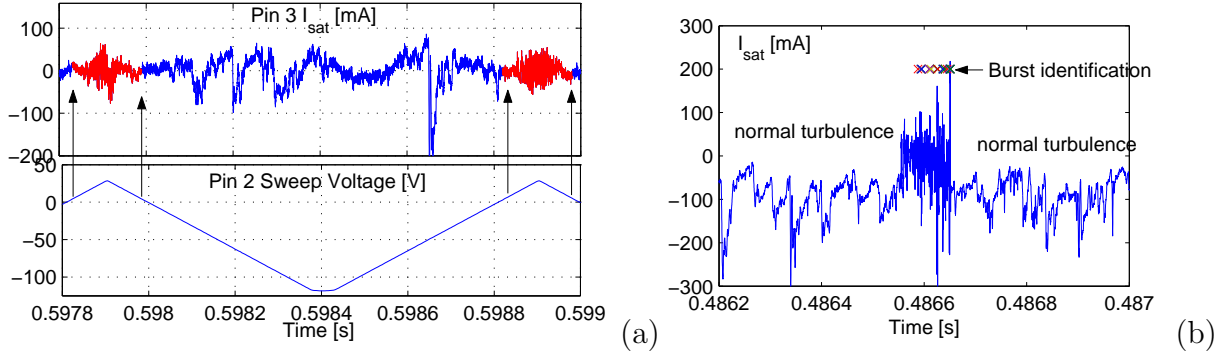


**Fig. 3.8** : Various perturbations on the  $I_s$ -signal: **(a)** Periodic perturbation on pin #3 due to a neighbouring sweeping probe #2 during electron saturation. **(b)** Large high-frequency aperiodic perturbations.

as is the case for most other diagnostics. Excursions of up to  $1kV$  between the vessel and building earths are possible during plasma operations, especially during disruptions. A special ground loop protection system is provided on TCV to detect when separate ground circuits are connected. In the case of the RCP, all the drive bellows, probe shaft, and probe head etc. are referenced to the torus potential. The entire mechanical support structure is isolated from the systems at building earth to which it is connected. The cupboards housing the electronics racks are also held at torus potential using isolation transformers to supply rack power from the main TCV hall electrical distribution network.

### 3.4 Signal processing

A variety of procedures are applied to remove noise from the acquired current and voltage data. Noise identification is based on the signal obtained before and after probe reciprocations and contain the following components:

- Perturbations can appear when electron current saturation occurs during sweeping of neighbouring pins or even divertor Langmuir probes are operating in swept mode (see Fig. 3.8 (a)).
- Perturbation of unknown origin and aperiodic is shown in Fig. 3.8 (b). It has been found that it can be reasonably identified ad-hoc by large fourth order time derivative,

$$I_s^{(4)} > \langle I_s^{(4)} \rangle + 10\sigma(I_s^{(4)}) \text{ where } I_s^{(4)} \stackrel{\text{def}}{=} |d^4 I_s / dt^4|$$

- For both  $V_{fl}$  and  $I_s$  signals, frequency peaks which are present in the signal independently of probe insertion into the plasma are identified and removed. Frequencies of these peaks can vary from one discharge to another. This procedure removes partially also perturbations with periodicity of  $8\mu s$  originating from the CRPP amplifier clock.
- The TCV Diagnostic Neutral Beam Injection (DNBI) system is also a significant noise source. Strong electromagnetic pick-up is found at  $1.43 \text{ MHz}$  which comes from

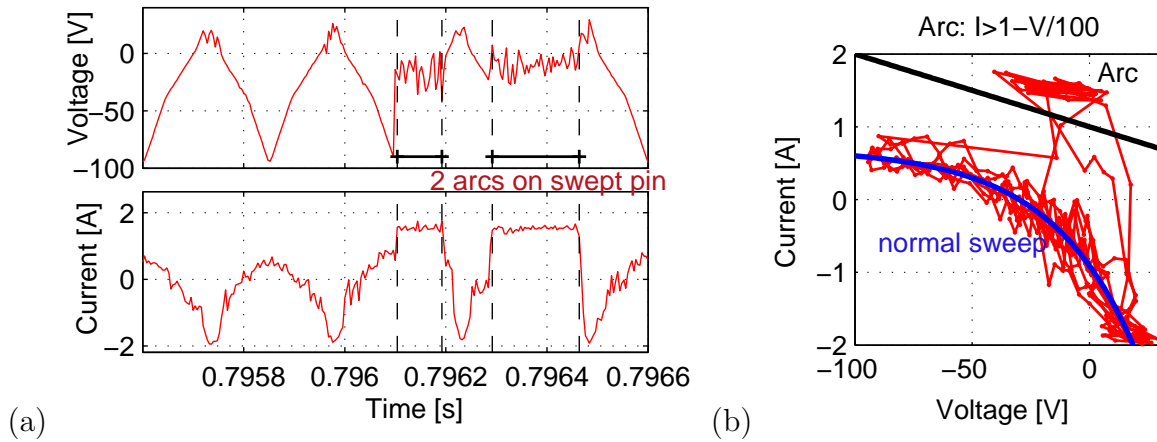


**Fig. 3.9** : (a) Demonstration of arcing on a swept pin; arcs appears only during the period when  $V < 0$ . For the same data the IV-characteristics used for arc identification is shown in (b), together with the threshold used for the automatic arc identification.

the DNBI radio-frequency generator at 4.6 MHz due to aliasing with the D-tAcq sampling frequency,  $1.43 \text{ MHz} = 6 - 4.6 \text{ MHz}$ . Whilst *low-frequency* measurements are not disturbed by this noise source, the perturbation is too strong for high frequency measurements and the DNBI must be switched-off during turbulence experiments.

- Unipolar arcs on a negatively biased pin strongly disturb the measurements, especially for deep insertion into the plasma or during an ELM event, when power fluxes are high and arcs are more easily destabilized. They are easily recognized in the signal as a sudden drop in potential and current increase up to saturation of the amplifier. Fig. 3.9 (a) shows an example in which, at the deepest point of the reciprocation, the temperature threshold for electron emission at the graphite pins is reached. The ad-hoc criteria used here for arc identification is set as  $I[\text{A}] > 1 - V[\text{V}]/100$  (see Fig. 3.9 (b)). In general, the relevant portion of the signal is removed if any of the five pins arc, since the signal on neighbouring pins is also disturbed, especially at high frequencies. Arcing does not appear to provoke any significant damage to pins or electronics, provided appropriate *fast* fuses are used to protect the APEX chip against over-current.

### 3.5 Langmuir probe theory

The Langmuir probe is one of the simplest tokamak diagnostics and is extensively used [63]. In tokamaks in its simplest form, it is usually a cylindrical pin inserted into the edge plasma and used for measuring local  $T_e$ ,  $n_e$  and  $V_{fl}$ . By applying a swept bias potential,  $V_{prb}$  to the probe and measuring the current drawn,  $I_{prb}$ , the probe voltage-current IV-characteristic is generated [107]:

$$I_{prb} = I_s(1 - \exp((V_{prb} - V_{fl})/T_e)), \quad (3.1)$$

Eq. (3.1) is in fact the IV-characteristic of the *plasma sheath* which is formed in front of surface of any material object inserted into a plasma [8] (Fig. 1.3 ). It arises as a result of the much greater mobility of electrons compared with the ions and places the object at a negative potential with respect to the plasma potential. This negative potential repels lower energy electrons such that the swept probe in fact measures only the tail of the electron energy distribution. A three parameter non-linear fit is typically applied to the experimental probe characteristics to obtain the values of  $T_e$ ,  $I_s$  and  $V_{fl}$ . Fig. 3.10 provides an example. It should be noted, however, that credibility of  $T_e$ -measurement is usually quite low. At divertor targets effect of parallel temperature gradient [108] has been found as not sufficient to explain discrepancies between experiment and theory. An attempt to account for "turbulence" effects of correlated and fluctuating  $\tilde{V}_{fl}$ ,  $\tilde{I}_s$  and  $\tilde{T}_e$  has been found negligible [109], however, the turbulence strength (fluctuation level) has been assumed unrealistically low in this study.

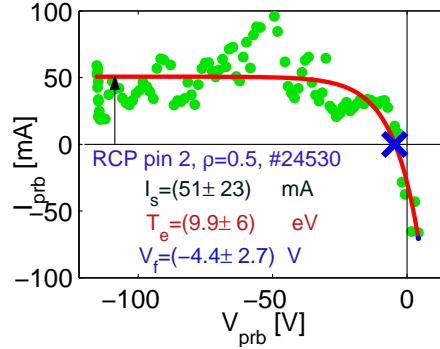


**Fig. 3.10** : Typical IV-characteristic obtained with the RCP and its corresponding fit using Eq. (3.1).

In a magnetized plasma  $I_s$  is given by

$$I_s = n_e f e A_{\perp} Z_i c_s \quad (3.2)$$

where  $c_s = \sqrt{\frac{T_e + Z_i T_i}{m_i}}$  is the plasma ion *sound speed*,  $T_i$  the ion temperature,  $m_i$ ,  $Z_i$  the ion mass and charge, respectively.  $A_{\perp}$  is the probe pin projected surface area and  $f$  is a factor describing the density depression caused by the flow acceleration to the probe-sheath interface. This is specific to strongly magnetized plasmas and is model dependent. In the isothermal fluid approximation often used in SOL physics,  $f = 1/2$  [8]. A number of alternative values for  $f$ , computed to various levels of sophistication with fluid or kinetic treatments, are also available, but differ only slightly from the isothermal fluid result [8]. The simplest estimate of  $A_{\perp}$  is given by the parallel geometric projection of the pin,  $A_{\perp} = 2dh \approx 6 \text{ mm}^2$ , which varies slightly depending on exact measurements of the pin dimensions for each of the probe heads in Fig. 3.5 . Both finite ion Larmor radius and varying  $T_i$  can affect  $A_{\perp}$ , as discussed in the following Section 3.7, but in practise, such refinements are not applied in this thesis. Instead,

$$f = 1/2, \quad Z_i = 1 \text{ or } 2, \quad A_{\perp} = 2dh, \quad T_i/T_e = 1 \quad (3.3)$$

will be assumed throughout in estimating  $n_e$  from measurements of  $T_e$  and  $I_s$  using Eq. (3.2). If value of  $T_e$  and  $T_i$  is known, correction factor in Fig. 3.13 (c) may be applied.

Since  $T_e$  is currently measured on TCV at only 3kHz, fluctuations must be assumed negligible when estimating the value of the fluctuating density. This is a frequently employed assumption in studies of this nature, even though measurements in some cases (e.g. [110]) have shown that the relative fluctuation level of  $T_e$  can be as high as that in  $I_s$ .

Taking into account the sheath potential fall,  $V_{fl}$  is related to the *plasma potential*,  $\phi$  using Eq. (1.5):

$$V_{fl} = \phi - 2.8T_e, \quad (3.4)$$

where isothermal ( $T_i = T_e$ ) fluid model for deuterium plasma has been used for evaluation. Neglecting temperature fluctuations, the fluctuations in plasma potential ( $\tilde{\phi}$ ) and density ( $\tilde{n}$ ) are therefore related to the measured quantities through:

$$\tilde{V}_{fl}(t) = \tilde{\phi}(t), \quad \tilde{I}_s(t) \propto \tilde{n}_e(t) .$$

### 3.6 Fast electron temperature measurement

There are Langmuir probe based techniques for obtaining fast  $T_e$ . A tunnel probe [62], which is supposed to yield  $T_e$  (and even  $T_i$ ) from the ratio of  $I_s$  (i.e. not sweeping) collected on two surfaces inside a tunnel, is currently tested on Tore Supra and CASTOR tokamak. An attempt to implement a harmonic method [110] for fast  $T_e$ -measurement on TCV was not successful. Therefore an alternative, much simpler technique, has been developed. It uses the classical sweeping of the pin but just much faster than usually, at 60 kHz. This frequency is the highest which the sweeping part of the electronics, literally the APEX amplifiers, can handle without significant loss of voltage amplitude; at 60 kHz the amplitude drops already to 100V from the required 130V. The measurement of the current and voltage is, however, well adapted to frequencies of 6MHz since it uses the same current monitors and potential dividers as for the fast turbulence investigation (Section 3.3). 60 kHz is on the other hand fortunately just enough to investigate  $T_e$  fluctuations of individual blobs (Fig. 5.11) which, except from permitting to study the blob physics, yields VI-characteristics that are very quiet (Fig. 3.12) and thus fitted more easily than those arising from the standard slow sweep (Fig. 3.10).

In Fig. 3.11 comparison of time-averaged profiles from two identical discharges are shown. It demonstrates that indeed sweeping at 60kHz and 2kHz results in identical time-averaged  $T_e$ ,  $n_e$  and  $I_s$  profiles. Profile of  $V_{fl}$  does not, however, seem correct due to hysteresis in the fast sweep (Fig. 3.12).

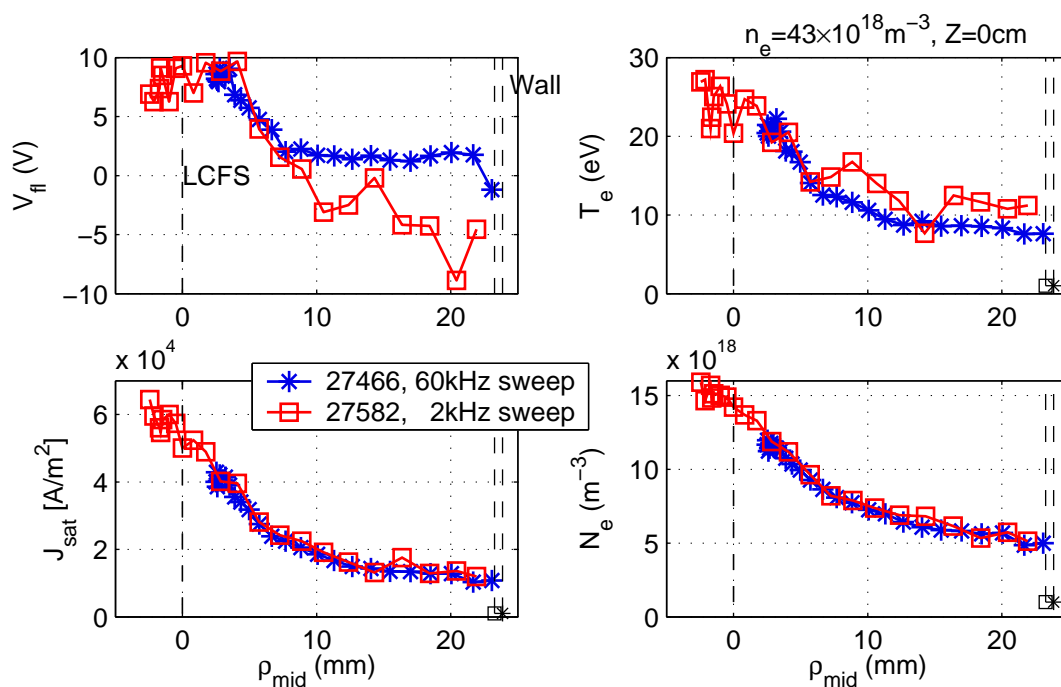


**Fig. 3.11** : Demonstration of identical  $T_e$ ,  $n_e$  and  $J_s$  profiles obtained by fast or slow sweeping. Each point correspond to an average value of many sweeps during  $\approx 2ms$ .

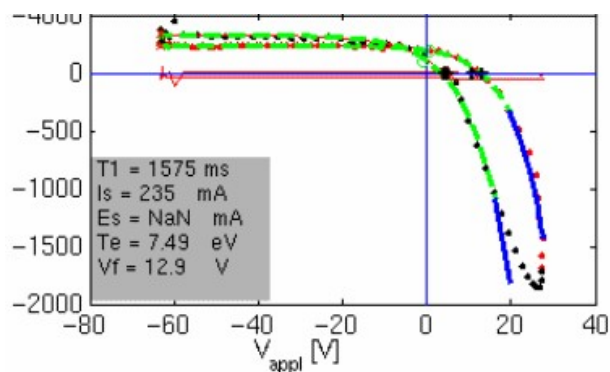


**Fig. 3.12** : Example of a Langmuir probe characteristic obtained with 60kHz sweep, i.e.  $8 + 8\mu s$  voltage ramp up+down. The hysteresis implicates that  $V_f$  is systematically shifted in sweep up with respect to sweep down, while estimation of both  $T_e$  and  $n_e$  is rather independent.

### 3.7 Probe effective collection area

To understand the probe-plasma interaction it is necessary to characterize in what state the surrounding plasma is. The TCV low-field-side SOL plasma is characterized by, as shown in Fig. 3.3 ,

$$B \approx 1.25T, \quad n_e = 0.3 - 30 \times 10^{18} m^{-3}, \quad T_e = 7 - 40eV$$

which determines the magnitude of the following parameters, computed using [2, Chap. 14.9]: the electron/ion *Larmor radius*,  $\rho_L$

$$r_{eL} = \sqrt{m_e T_e / B} \approx 10 - 20 \mu m, \quad r_{Li} = \sqrt{m_i T_i / B} = 0.5 - 1 \text{ mm}$$

The Debye length is

$$\lambda_D = \sqrt{\epsilon_0 T_e / n_e / e} = 3 - 30 \mu m.$$

The sheath thickness for the maximum  $-120V$  pin bias [64]:

$$\lambda_{sh} \approx \lambda_D |(V - \phi) / T_e|^{3/4} < 200 \mu m$$

The ion and electron mean-free-paths:

$$\lambda_i \approx \lambda_e / 2 = 0.01 - 1 \text{ m}$$

. These values implicate that in the Debye sheath region both electrons and ions travel collisionlessly, affected by the sheath electric field and electron trajectories are curved by the magnetic field. Since  $r_{Li} \approx d$ , the effective pin surface area,  $A_{\text{eff}}$ , i.e. the width of the magnetic flux tube from which ions are collected, is larger than the geometric projection,  $A_{\perp}$  of the pin onto the magnetic field.

Since the ion cloud width is expected to be roughly equal to  $r_{iL}$ , one expects to find a projected surface enhancement factor:

$$\frac{A_{\text{eff}}}{A_{\perp}} \approx \frac{d + r_{Li}}{d}. \quad (3.5)$$

A simple numerical model of the particle trajectories around the pin has been developed to estimate  $A_{\text{eff}}/A_{\perp}$  in a more appropriate way (a similar exercise has been performed in [111]). Because  $\rho_{Li} \sim d$ , the geometry of the problem is indeed 3D since an ion with centre of gyration crossing the pin can in practise avoid it on its helical trajectory. Particles are launched from a uniform distribution in the poloidal plane  $[R, z]$  and in the phase-space of the gyro-rotation. The perpendicular and parallel velocity distributions are assumed to be Maxwellian with  $T_{\perp} = T_{\parallel}$ . It is further assumed that the Boron-Nitride supporting structure neutralizes all ions hitting its surface, thereby preventing them from being collected by the pin. Fig. 3.13 (a) provides a 2D representation of guiding centres of those ions collected by the probe for  $T_i = 50eV$  and the realistic TCV probe inclined pin geometry for the probe head, shown in Fig. 3.5 (b,c); for a rectangular pin (Fig. 3.5

(a,d)) the resulting feature is similar and leads to the same (within 10%) value of  $A_{\text{eff}}/A_{\perp}$ . The result of varying  $T_i$  is shown in Fig. 3.13 (b), showing a maximum of  $A_{\text{eff}}/A_{\perp} \approx 2$  at  $T_i = 150\text{eV}$ . This  $T_i$  dependence is well matched by the simple function Eq. (3.5), demonstrating that accounting for the ion energy distribution function and 3D effects of gyro-rotation combined with parallel motion does not lead to any significant modification with respect to the intuitive estimate. Eq. (3.2) can thus be refined to account for the increased area and  $T_i/T_e \neq 1$ :

$$I_s^{\text{refined}} = n_e \frac{e}{2} 2dh \left(1 + \frac{\sqrt{2T_i M_i}}{Bd}\right) \sqrt{\frac{(T_e + Z_i T_i)}{m_i}} \quad (3.6)$$

Unfortunately,  $T_i$  is not measured on TCV. Simulations of the TCV SOL using the B2.5-Eirene code package [14, Chap. 5.3] predict  $1 < T_i/T_e < 4$  which can lead to important modifications to the density calibration factor  $I_s^{\text{refined}}/I_s$ , where  $I_s$  is computed from Eq. (3.2) and Eq. (3.3). This calibration (Fig. 3.13 (c)) is a multiplication factor that can be applied to all density measurements derived from the reciprocating probe, but since in experiment  $T_i$  is generally unknown, in this thesis this factor is not applied anywhere. It does, however, provide one possible explanation for the discrepancies often seen when comparing RCP and Thomson scattering density data (see Section 4.3.1).

### 3.8 Estimation of radial gradients

When using the Mach probe heads,  $E_r$  can be measured using signals of pins 3, 2 and 5 which are allowed to float electrically,

$$E_r = (V_{f3} - (V_{f2} + V_{f5})/2)/\Delta r \quad (3.7)$$

where the pin radial separation is  $\Delta r = 2$  mm for head Fig. 3.5 (c) and  $\Delta r = 2.5$  mm for the probe head Fig. 3.5 (d). The density gradient can be similarly estimated as

$$dn_e/dr = (I_{s3} - (I_{s2} + I_{s5})/2)/\Delta r.$$

Since  $T_e$  is measured by a single pin only, usually pin 3, and with low time resolution, correction for the temperature gradient,  $dT_e/dr$  is not possible on the fluctuation timescale. For a low frequency estimation of gradients in density or plasma potential, polynomial fits of  $\phi(\rho) = V_{f3}(\rho) + 2.5T_e(\rho)$  or  $n_e(\rho) \propto I_s(\rho)\sqrt{T_e(\rho)}$  are used, as demonstrated in Fig. 6.8 .

### 3.9 Fluctuation induced flux

A pair of probe tips 1 and 4, each measuring  $V_f$ , provides an instantaneous measurement of the poloidal electric field and hence the turbulent driven, radial ExB particle flux

$$\Gamma_r = \tilde{E}_{\text{pol}} \cdot n_e/B, \text{ where } \tilde{E}_{\text{pol}} \approx (\tilde{V}_{f1} - \tilde{V}_{f4})/\Delta_{\text{pol}} \quad (3.8)$$

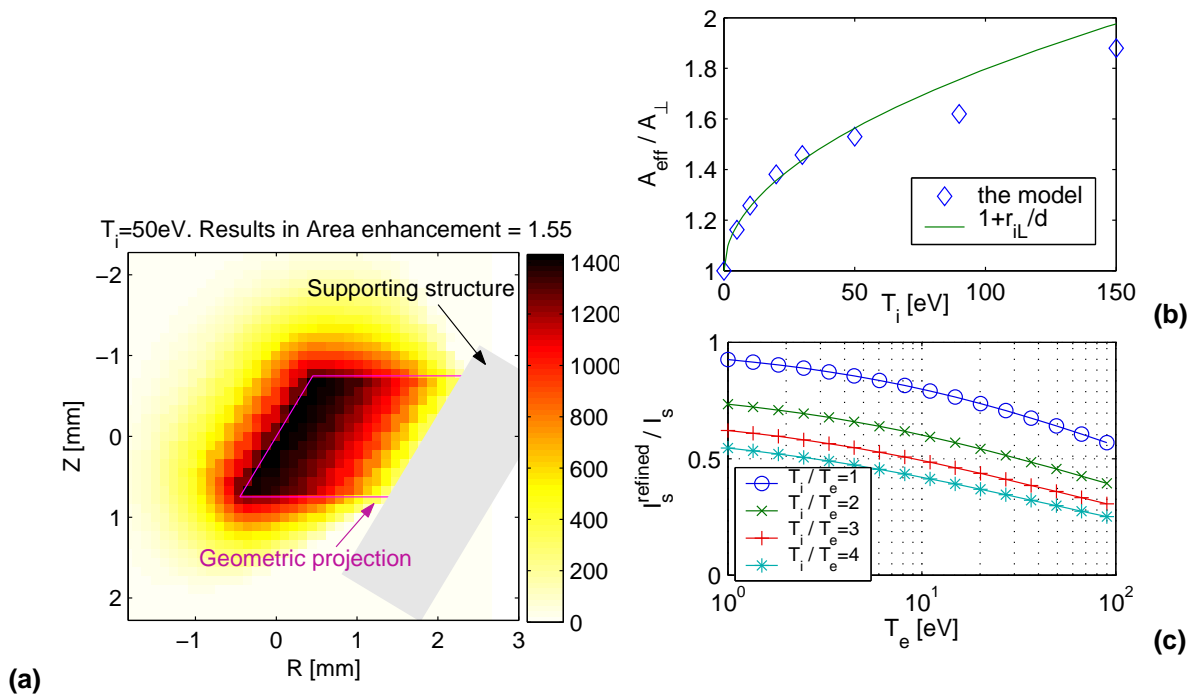


**Fig. 3.13** : Output from the simple particle trajectory model shows how the finite ion Larmor radius effect enhances the effective probe collection area with respect to the geometric projection. **(a)** The colour [a.u.] cloud shows  $[R, z]$ -region where the ions collected by the pin originate (centers of the gyro-motion). **(b)** Ion temperature scan of the collection area increase. **(c)** Only for shots above #26000, resulting density correction factor accounting for the finite Larmor radius effect (function of  $T_i$ ) and the ratio  $T_i/T_e$  which is generally unknown. The factor is the ratio of the densities computed from Eq. (3.6) with respect to Eq. (3.2) with Eq. (3.3).

assuming  $\tilde{T}_e = 0$  and where  $\Delta_{\text{pol}} = 1\text{cm}$  is poloidal separation of the pins and  $n_e = \langle n_e \rangle + \tilde{n}_e$ , with  $\tilde{n}_e$  the fluctuating component and  $\langle n_e \rangle$  the average value. The poloidal separation of  $\Delta_{\text{pol}}$  is a weak point of the flux measurement. If the poloidal space-dimension of  $\phi$  is not much longer than  $\Delta_{\text{pol}}$ , then  $E_{\text{pol}}$  computed as  $(\tilde{V}_{f11} - \tilde{V}_{f14})/\Delta_{\text{pol}}$  is not credible. Whether it is or not the case for TCV SOL is discussed in Section 5.2.6.

The time-averaged radial flux may also be expressed as

$$\langle \Gamma_r \rangle = C_{n,E} \sqrt{\langle \tilde{n}_e^2 \rangle \langle \tilde{E}_p^2 \rangle} / B \quad (3.9)$$

where  $C_{n,E}$  is the correlation coefficient between density and poloidal electric field fluctuations.

It should be emphasized that including the time averaged density  $\langle n_e \rangle$  in Eq. (3.8) does not affect  $\langle \Gamma_r \rangle$  :

$$\langle \Gamma_r \rangle = \langle \tilde{E}_{\text{pol}} \cdot n_e / B \rangle = \langle \tilde{E}_{\text{pol}} \tilde{n}_e \rangle / B + \langle \tilde{E}_{\text{pol}} \rangle \langle n_e \rangle / B = \langle \tilde{E}_{\text{pol}} \tilde{n}_e \rangle / B \quad (3.10)$$

since  $\langle \tilde{E}_{\text{pol}} \rangle = 0$ . This is why  $\langle n_e \rangle$  is not usually accounted for in computing  $\Gamma_r$ , for example in studies of particle balance. Its inclusion does, however, significantly increase the standard deviation,  $\sigma_{\Gamma_r} = \sqrt{\langle (\Gamma_r - \langle \Gamma_r \rangle)^2 \rangle}$ :

$$\sigma_{\Gamma_r} = \sigma(\tilde{E}_{\text{pol}} n_e / B) = \sigma(\tilde{E}_{\text{pol}} \tilde{n}_e) / B + \sigma(\tilde{E}_{\text{pol}}) \langle n_e \rangle / B \quad (3.11)$$

As a consequence, the flux arriving at a material surface is affected since it is proportional to the sum of all *outgoing* particles:  $\int_0^\infty \text{PDF}(\Gamma_r) d\Gamma_r$ .

It should be noted that the absolute value of  $\langle \Gamma_r \rangle$  measured by the probe may be overestimated. Recent work on Alcator C-mod using a similar reciprocating probe diagnostic has shown that the fluctuation induced radial particle flux integrated over the LCFS significantly exceeds that derived from particle balance [112], where the latter combines experimental information from the midplane probe ( $\Gamma_r$ ), divertor probe (parallel losses) and  $Ly_\alpha$  emission (ionization rate). These observations suggest that the fluctuation induced cross-field particle flux estimates derived from the probe measurements are not characteristic of transport in the unperturbed plasma. Ref. [112] demonstrates, in fact, that the measured flux is due to plasma flow into the probe presheath region which must increase above the background transport level in order to conserve plasma-neutral mass balance (ions are neutralized on the probe surface and much of the neutrals recycling on the probe will ionize outside the probe presheath). These new findings are perfectly consistent with some previous similar measurements [113] and strongly indicate that probe derived turbulent driven fluxes should be treated with caution.

Nevertheless, it has been reported by some authors [73, 78] that the fluctuation driven particle and energy flux measured by probes can be within a factor of two of that derived from global balance. It has further been noted in [92] that for small pin sizes ( $d < 2\rho_{\text{Li}}$ ), parallel currents driven by the probe should not significantly enhance the measured cross-field transport. Since the TCV probe pins are of dimension similar to  $\rho_{\text{Li}}$  and are not an integral part of a larger housing, it is not clear that their disturbance to the plasma is large enough to drive an enhanced turbulent flux. Indeed, evidence will be presented later in Section 5.2.7 that the probe does apparently measure the flux correctly.

### 3.10 Parallel Mach number

Mach number of the parallel plasma flow can be directly estimated from the ratio of ion saturation currents to separate sensors aligned with the total magnetic field and facing upstream and downstream of the flow. This is the idea behind the design of the probe heads in Fig. 3.5 (c,d), where the Mach pair consists of the two identical pins 2 and 5, physically separated by a bar. To see how the ratio of saturation currents to these separated pins can provide an estimate of the fluid flow speed, an extremely simple argument, based on reasoning in [55] (1926), can be formulated: Assuming Maxwellian velocity distributions  $\exp(\frac{-m_i(v-v_0)^2}{2k_B T}) = \exp(\frac{-(v-v_0)^2}{c_s^2})$  in the probe vicinity and a fluid drift velocity  $v_0$ , the upstream/downstream saturation current ratio may be written (using Eq. (3.2), Fig. 3.14 (a))

$$\frac{I_{sat,5}}{I_{sat,2}} = \frac{feA_{\perp}Z_i n_e \int_{-\infty}^0 \exp(-(\frac{v-v_0}{c_s})^2) dv}{feA_{\perp}Z_i n_e \int_0^{\infty} \exp(-(\frac{v-v_0}{c_s})^2) dv}. \quad (3.12)$$

Assuming the upstream and downstream far-field plasma has identical  $n_e$  and  $T_e$ , that the pins are identical in site and using the substitution  $M' = (v - v_0)/c_s$  yields

$$\frac{I_{sat,5}}{I_{sat,2}} = \frac{\int_{-\infty}^M \exp(-M'^2) dM'}{\int_M^{\infty} \exp(-M'^2) dM'} = \frac{1 + \text{Erf}(M)}{1 - \text{Erf}(M)} \quad (3.13)$$

where  $M = v_0/c_s$  is the Mach number and Erf is the error function, defined as  $\text{Erf}(x) = \frac{2}{\sqrt{\pi}} \int_0^x e^{-t^2} dt$ . Much more sophisticated models have been developed over the past 20 years,

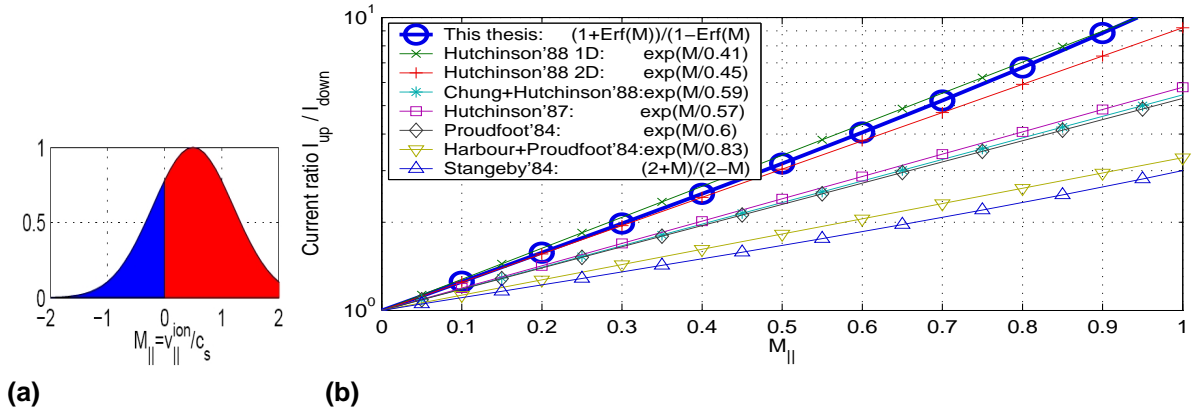


**Fig. 3.14 :** (a) Ion velocity Maxwellian PDF with  $M_{\parallel}=0.5$ . (b) Various models predict different analytic expressions for the current ratio of the parallel particle flux. The models correspond to references [114, 115, 116, 107, 117, 118].

accounting for the effect of the probe on the surrounding plasma; the interplay between cross-field transport and parallel motion, ion acceleration by the presheath and sheath electric field etc. In Fig. 3.14 (b) some of these models are compared, based on broad discussion in [115], with the result of Eq. (3.13). Despite its simplification, the latter is

extremely close to the 1D and 2D fluid result of Hutchinson [116]. It is not immediately obvious why agreement is so good and it is almost certainly at least partly coincidental. Whilst probes inserted into strong flows do not significantly perturb the upstream plasma flow, all Mach probe theories predict significant modifications to the parallel profiles of plasma parameters downstream of the probe. In assuming no perturbation at all, the simple model in Eq. (3.12) cannot capture the essential physics of the local perturbation and it is surprising that agreement with a considerably more complex and complete theory should be so good. In this thesis, the following expression has been chosen for computing the flow magnitude:

$$M_{\parallel} = 0.4 \ln\left(\frac{I_{sat,5}}{I_{sat,2}}\right) \quad (3.14)$$

## Part II

# Results of turbulence studies on TCV



# Chapter 4

## Universality of electrostatic fluctuations

This chapter presents a detailed investigation of the electrostatic fluctuation data obtained by the reciprocating probe described in the previous chapter. Elementary statistical techniques are introduced and are employed for the data analysis of a particular discharge. Following the results presented in [34, 33] a broad TCV database is described in terms of Skewness, Kurtosis, fluctuation levels and timescales of the local density and particle flux fluctuations. Finally, flux scaling with density is discussed, together with the detailed temporal wave-form of density fluctuations. The analysis described here will be used again in the following chapter, where its application to time series for quantities resulting from 2D fluid turbulence code runs provides an excellent means by which to compare code and experiment.

### 4.1 Elementary statistics

An individual measurement of any quantity of a turbulent medium evolving in time is a random variable, but a statistical description provides reproducible observables. In this thesis such statistical quantities involve time-integrals of the density fluctuations. Before describing the results of statistical analysis, some basic notions underlying the techniques used here are briefly reviewed. The random variable will be denoted by  $n$ , reflecting the tendency, in this thesis, for discussion of density fluctuations.

The *probability distribution function*, *PDF*, describes the distribution of a statistical quantity over a chosen temporal range. In general, the probability of  $n$  being within the interval  $n_a < n < n_b$  is  $\int_{n_a}^{n_b} P(n)dn$ . In practice, the PDF is approximated with a histogram comprising a limited number of measurements.

### 4.1.1 Statistical moments

It is usual to characterize a distribution by its lowest-order central *statistical moments*:

$$PDF \text{ normalization} : 1 = \int_{-\infty}^{+\infty} P(n)dn \quad (4.1)$$

$$mean = \mu = \langle n \rangle = \bar{n} = \int_{-\infty}^{+\infty} nP(n)dn \quad (4.2)$$

$$standard \ deviation(STD) = \sigma(n) = \sigma = \left[ \int_{-\infty}^{+\infty} (n - \mu)^2 P(n)dn \right]^{1/2} \quad (4.3)$$

$$Skewness = S = \int_{-\infty}^{+\infty} (n - \mu)^3 P(n)dn / \sigma^3 \quad (4.4)$$

$$Kurtosis = K = \int_{-\infty}^{+\infty} (n - \mu)^4 P(n)dn / \sigma^4 \quad (4.5)$$

$$r^{th} \text{ central moment } \forall r > 2, \quad M^{(r)} = \int_{-\infty}^{+\infty} (n - \mu)^r P(n)dn / \sigma^r \quad (4.6)$$

$$(4.7)$$

Note that the first and second moments ( $\mu, \sigma$ ) have dimensions of the quantity  $n$  while higher moments ( $S, K, M^{(r)}$ ) are dimensionless. A distribution function is *fully* determined by all the moments, but the salient features of  $P(n)$  are determined by Eq. (4.2)→Eq. (4.5). Therefore, if  $\mu, \sigma, S$  and  $K$  derived from experimental data are equal to values of a particular analytical distribution, for example those from Table 4.1, the corresponding PDF approximates the data as well. On the other hand, higher moments have large statistical errors for *limited* number of samples of the random variable. Intuitively this is because higher moments are sensitive to higher amplitude events which in physical distributions are *rare*, and thus require a very large data set. This is observed in [119] in the context of a variant of the Gamma distribution.

### 4.1.2 Various distributions

To study electrostatic turbulence in the SOL, it is convenient to concentrate on density and plasma potential fluctuations since they are directly measured by the reciprocating Langmuir probe, as discussed in detail in Chapter 3. Because of its direct link to transport, particle balance and plasma-wall interaction, the turbulent driven particle flux,  $\Gamma_r$ , is of particular importance. For electrostatic turbulence,  $\Gamma_r \propto n \nabla_{\text{pol}} \phi$ , with  $\phi$  the plasma potential and is thus a combination of the two main fluctuating quantities measured by the probe. Both  $n$  and  $\phi$  can be deduced from probe measurements only if temperature fluctuations can be assumed negligible. Various PDFs have been compared with the plasma density fluctuations in the SOL. Five of these distributions are given explicitly in Table 4.1. Each of these distributions can be uniquely characterized by just two free parameters,  $\mu$  and  $\sigma$ . The ratio  $A = \mu/\sigma$  is of particular relevance because:

name	Skewness	Kurtosis	PDF	definition
Gaussian	0	3	$\frac{1}{\sigma\sqrt{2\pi}} \exp\left[-\frac{n'^2}{2}\right]$	$n' \stackrel{\text{def}}{=} \frac{n-\mu}{\sigma}$
BHP	0.89	4.415	$\frac{2.16}{\sigma} \exp\left(\frac{\pi}{2}[n_b - e^{n_b}]\right)$	$n_b \stackrel{\text{def}}{=} -0.934n' - 0.348$
Gumbel	1.139	5.4	$\frac{\pi}{\sqrt{6}\sigma} \exp[n_g - e^{n_g}]$	$n_g \stackrel{\text{def}}{=} -\frac{\pi}{\sqrt{6}}n' - 0.577$
Lognormal	$\frac{3}{A} + \frac{1}{A^3}$	$[\lambda^4 + 2\lambda^3 + 3\lambda^2 - 3]$	$\frac{\exp[-\ln^2(n/\mu\sqrt{\lambda})/\ln\lambda^2]}{n\sqrt{2\pi\ln\lambda}}$	$\lambda \stackrel{\text{def}}{=} 1 + A^{-2}$
Gamma	$\frac{2}{A}$	$3 + \frac{6}{A^2}$	$\frac{A^2}{\mu\Gamma(A^2)} \left(\frac{A^2n}{\mu}\right)^{A^2-1} \exp\left(-\frac{A^2n}{\mu}\right)$	$A \stackrel{\text{def}}{=} \mu/\sigma$

Table 4.1: Characteristics of basic distribution functions [25, 124, 125] for a random variable  $n$  which in this thesis usually corresponds to electron density  $n_e$ .  $\Gamma(z)$  is the Gamma *function* which is a generalized factorial for non-integer  $z$ ,  $\Gamma(z) = (z-1)!$ ,  $\forall z \in \mathbb{N}$ .

1.  $A$  is the *inverted fluctuation level*, being directly computed from the density data series as  $A = \langle n_e \rangle / \sqrt{\langle (n_e - \langle n_e \rangle)^2 \rangle}$ .
2.  $A$  determines the *shape* of the Gamma and Lognormal PDFs.
3. In statistical models [30, 120, 121],  $A$  is often called the *cluster parameter* because it describes the degree of clustering - increased fluctuation level corresponds to reduced  $A$ .

#### 4.1.2.1 Fixed-shape universal PDFs

The Gaussian (or Normal) PDF is widely observed in nature. As shown with the central limit theorem, it results from the limit distribution of an infinite sum of random and independent processes [22]. A global quantity, regardless of its precise nature, therefore usually fluctuates according to a Normal distribution. However, in highly correlated systems, other limit distributions are possible [122]. PDFs with long tails characterize *rare* fluctuations in a variety of physical systems such as power fluctuations in a closed turbulent flow between counter rotating disks [123]. A feature common across such examples of correlated systems is their scale-free or self-similar characteristics [120].

The BHP [120] PDF has been suggested as a suitable distribution to describe the global energy fluctuations of a confined turbulent flow as well as the PDF corresponding to the fluctuations in a magnetized system at the critical point [126] and of a system exhibiting self-organized criticality (SOC, Section 2.2) [26] such as a numerical sandpile, or of water level fluctuations in a river [122]. In this sense, it has been suggested [124] that the BHP PDF is a hallmark of non-Gaussian statistics and SOC. The BHP distribution, and partially also the Gumbel PDF, are found in [124] to be attractors for the PDF of density fluctuations in SOL turbulence. Interpretation of the BHP, being associated with SOC, is however quite different to the Gumbel [125] distribution, which describes the probability distribution of extreme values. Both BHP and Gumbel distributions are

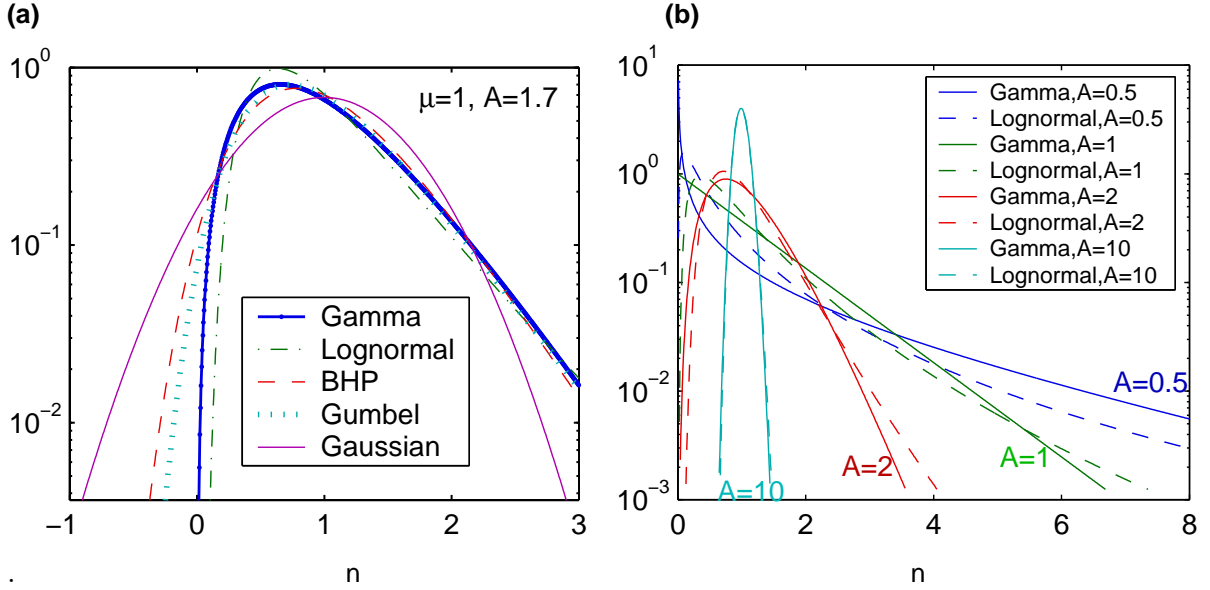


**Fig. 4.1:** (a) Gallery of normalized ( $\int P(n)dn = 1$ ) PDFs from Table 4.1. (b) Variation with  $A$  of shape of Gamma and Lognormal PDFs with fixed  $\mu = 1$ .

very similar to the Gamma distribution for  $A \approx 2.15$  and  $A \approx 1.67$ , respectively, where  $A \stackrel{\text{def}}{=} \langle n_e \rangle / \sigma$ .

#### 4.1.2.2 Variable shape PDFs

The Gamma distribution is found to describe fluctuations in systems where clustering of events is fundamental. An experimentally observed fluid example is the distribution of droplet sizes after a liquid ligament breakup [127]. Other examples include the intensity of scattered light in turbulent media [128], where the K-distribution has been used, for which the Gamma PDF is a special case. The *discrete* form of the Gamma process is central both to the development of birth-death-immigration population models [121] and to simulations of rice pile avalanching systems [30]. A rice pile is a correlated, self-organized system which conforms accurately to a family of Gamma PDFs across the entire pile, clearly exhibiting both temporal and spatial scale-free correlations up to the system size.

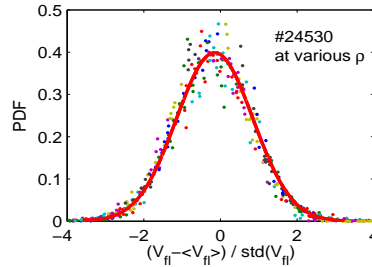


**Fig. 4.2 :** Demonstration that the floating potential, measured in the TCV SOL using the RCP, is normally distributed.

Special cases of the Gamma distribution include  $A \rightarrow \infty$ , which corresponds to the absence of clustering, and for which it can be shown that Gamma-PDF reduces to a Gaussian distribution ( $S=0, K=3$ ). Up to the 4<sup>th</sup> moment this can be seen from Table 4.1 since for  $A \rightarrow \infty$  one obtains  $S = \frac{2}{A} \rightarrow 0$  and  $K = 3 + \frac{6}{A^2} \rightarrow 3$ . For  $A = 1$ , the Gamma distribution reduces to a negative exponential distribution,  $P = e^{-n/\langle n \rangle} / \langle n \rangle$  and for  $A \rightarrow 0$  to  $P \propto n^{-1}$ . At the origin ( $P(0)$ ),  $P(0) = 0$  for  $A > 1$  whilst  $P(0) = \infty$  for  $A < 1$ .

It has been pointed out [129] that a Lognormal distribution can match density PDFs and that this form of PDF might be qualitatively expected from the basic equation of charge conservation. The plasma potential in the TCV is usually observed to be normally distributed:

$$P(\phi) \propto \exp\{-(\phi/T)^2\},$$

as demonstrated in Fig. 4.2. Assuming Boltzmann-distributed electrons that links density with potential fluctuations,

$$n_e \propto \exp(-\phi/T) \quad \text{and hence} \quad \phi \propto -T \ln n_e,$$

and the fact that  $P(\phi)d\phi = P(n_e)dn_e$ , the density PDF can be computed as [129]

$$P(n_e) = \frac{d\phi}{dn_e} P(\phi) \propto \frac{d}{dn_e} (-T \ln n_e) \exp \left[ - \left( \frac{-T \ln n_e}{T} \right)^2 \right] = -\frac{T}{n_e} \exp [-(\ln n_e)^2]$$

which is indeed, ignoring the normalization, the Lognormal PDF in Table 4.1. We note that the Lognormal PDF also depends on  $A$ .

### 4.1.3 Temporal characteristics

PDF does not contain any information concerning temporal behaviour of a statistical quantity. For this purpose e.g. the Fourier transform (FT) is a useful technique that transfers a variable from the time domain into the frequency domain. Together with the inverse transform, it is defined as

$$N(f) = \frac{1}{\sqrt{2\pi}} \int_{-\infty}^{+\infty} e^{ift} n(t) dt, \quad n(t) = \frac{1}{\sqrt{2\pi}} \int_{-\infty}^{+\infty} e^{-ift} N(f) df \quad (4.8)$$

The Fourier function  $N(f)$  uniquely identifies the original time-domain function. A widely evaluated quantity is the *power spectrum*, defined as  $P(f) = |N(f)|^2$ , ignoring any phase information. Intuitively,  $P(f)$  is in fact a histogram characterizing the appearance of a particular frequency  $f$  in the signal  $n(t)$ . In a turbulent system,  $n(t)$  is a random variable, while  $P(f)$  is usually a predictable and robust quantity. For example, the Kolmogorov's power law [23], derived in Eq. (2.3), predicts  $P(f) \propto f^{-5/3}$  for an incompressible viscous fluid with high Reynolds number. It should be noted that in the edge plasma the power spectrum obtained with a fixed Langmuir probe is a convolution of the temporal as well as its spatial characteristics given by both the global poloidal flow. In the near SOL

and inside LCFS, the poloidal movement indeed dominates and thus the power spectra is effectively an image of the spatial power spectra,  $P(\omega) = v_{pol}k_{pol}$ . This is based on observations of the plasma as a fluid in the animations in Fig. 5.6. From a discrete signal in the time domain, the discrete Fourier transform is a numerical procedure to estimate the power spectrum.

The *structure function* (SF) is defined as the standard deviation of a departure from the origin after a certain time delay [22]

$$\text{SF}(\tau) = \sqrt{\langle [n(t) - n(t - \tau)]^2 \rangle_t}. \quad (4.9)$$

Closely linked to the structure function is the *autocorrelation function* (ACF) which is useful for characterizing the timescale of a fluctuating quantity. It is defined [22] as

$$\text{ACF}(\tau) = \frac{\langle n(t)n(t - \tau) \rangle_t}{\langle n^2(t) \rangle_t}. \quad (4.10)$$

The ACF reaches a maximum for  $\tau = 0$ , for which  $\text{ACF}(0) = 1$ , and for a turbulent, non-periodic signal decays to zero for  $\tau \rightarrow \infty$ . Expanding Eq. (4.9) yields general relationship between SF and ACF:

$$\text{SF}^2(\tau) = 2(\mu^2 + \sigma^2)(1 - \text{ACF}(\tau)) \quad (4.11)$$

The expected form of the SF within a scale-free region,  $\tau \leq \tau_c$ , is

$$\text{SF}(\tau \leq \tau_c) \propto |\tau/\tau_c|^H. \quad (4.12)$$

which is the definition of the *Hurst exponent*,  $H$  for self-similar time series, described in Section 2.2.1, and  $\tau_c$  is the *correlation time* that characterizes the typical timescale of the density fluctuations. Inserting Eq. (4.12) into Eq. (4.11) yields the expected form of the ACF within a scale-free region,

$$\text{ACF}(\tau) \approx 1 - |\tau/\tau_c|^{2H}. \quad (4.13)$$

For large  $\tau$ , however, the SF for physical systems saturates to the value

$$\text{SF}(\tau \gg \tau_c) = \sqrt{2(\sigma^2 + \mu^2)} \quad (4.14)$$

In order to account for the scale-free region of the ACF (for  $\tau/\tau_c \ll 1$ ) as well as for its decay for  $\tau/\tau_c \gg 1$ , one can rather imply

$$\text{ACF}(\tau) = \exp[-|\tau/\tau_c|^{2H}], \quad (4.15)$$

which is consistent with Eq. (4.13) for  $\tau/\tau_c \ll 1$  and, through Eq. (4.11), also with the saturation in Eq. (4.14).

In general, the ACF is just the Fourier transform of the power spectrum [130, p.96]. Combining Eq. (4.13) with Eq. (4.8) leads, after some algebra, to the expected form of the power spectrum for a stationary scale-free ( $f^{-\beta}$ ) process:

$$P(f) = |\text{FT}(\text{ACF})|^2 = \frac{1}{2\pi} \left| \int_{-\infty}^{+\infty} e^{+if\tau} (1 - |\tau/\tau_c|^{2H}) d\tau \right|^2 \propto f^{-(1+2H)} \quad (4.16)$$

which therefore relates the cascade index,  $\beta$  with the Hurst exponent as  $\beta = 1 + 2H$ .

## 4.2 Detailed analysis of a single probe reciprocation

Statistical analysis is performed on data from 5 ms time windows. This choice represents a good compromise between the requirement for the reduction of statistical noise and the fact that during this time the probe moves only through a distance  $\delta\rho < 0.2$  (or 5 mm), which has to be (and is) always less than the radial density scale length (between 10 mm and 30 mm, see Fig. 4.5). Uncertainties in the absolute spatial position of the probe and the separatrix obtained from the magnetic reconstruction is below  $\sim 2$  mm, as discussed in Section 3.2.1.

A 1 kHz high-pass filter is applied to the 5 ms data series to reduce both the influence of the probe movement and the effect of sawteeth at  $\sim 100$  Hz. Such a filter does not interfere with the intrinsic local plasma fluctuations, for which the timescale, defined precisely later, is at least an order of magnitude shorter:  $1/\tau_c > 10$  kHz. It should be noted that the appearance of nonphysical negative density bursts manifested in the PDF of Fig. 4.3 (c), and even more strikingly in that of Fig. 4.11 (a), originates from both the electronics and the problematic summation of low and high pass signals discussed in Section 3.3.

The first reciprocation (at  $\bar{n}_e = 4.4 \times 10^{19} m^{-3}$ ,  $I_p = 340$  kA) in the L-mode deuterium ohmic discharge #24530 has been selected as an example. Note that the actual density limit for this particular discharge is  $n_{DL} = 1.22 \times 10^{20} m^{-3}$ , obtained as the density value at the disruption, taken into account little modification ( $n_{DL} \propto I_p$ ) [131] of the plasma current at the time of reciprocation. Its global plasma parameters are illustrated in Fig. 3.3 (a) and the plasma geometry in Fig. 3.1. As a consequence of good diagnostic coverage and the exceptionally deep probe reciprocation, data from this particular discharge #24530 is used frequently in this thesis. A typical example of the time evolution of the turbulent density measured in the TCV SOL is shown in Fig. 4.3 (a), which compiles short time traces at four radial locations marked by the corresponding symbols in Fig. 3.1 (b). The figure demonstrates clearly the qualitative change in the density fluctuation signal, showing the tendency for large, infrequent bursts with increasing  $\rho$ , where  $\rho$  is the normalized radial coordinate introduced in Fig. 3.1 (b). Useful information is extracted from these time series by applying the statistical methods introduced in Section 4.1. In particular, at all locations the signal is characterized by its auto-correlation function (Fig. 4.3 (d)), the power spectrum (Fig. 4.3 (e)) and the probability distribution function (Fig. 4.3 (c)). All three characteristics show strong variations with location in the SOL.

In the separatrix vicinity (see  $\rho = -0.1$  in Fig. 4.3 (a)), the density fluctuations are generally relatively weak. This can be quantified by noting that the parameter  $A \equiv \mu/\sigma$  is much larger than unity in this region (see the legend). The PDF has a Gaussian shape, the correlation time,  $\tau_c$  is short and both the power spectrum and structure function fall rapidly with frequency beyond a given threshold. In contrast, in the wall shadow ( $\rho = 1.4$ ), long-lived intermittent bursts clearly dominate the signal, such that  $A = 1.2$ . The PDF is highly skewed,  $\tau_c$  is higher by an order of magnitude than that at separatrix and both the power spectrum and structure function are clearly characterized by a power law (i.e.  $PS \propto f^{-\beta}$ ) extending over two orders of magnitude in frequency (Fig. 4.3 (c)).

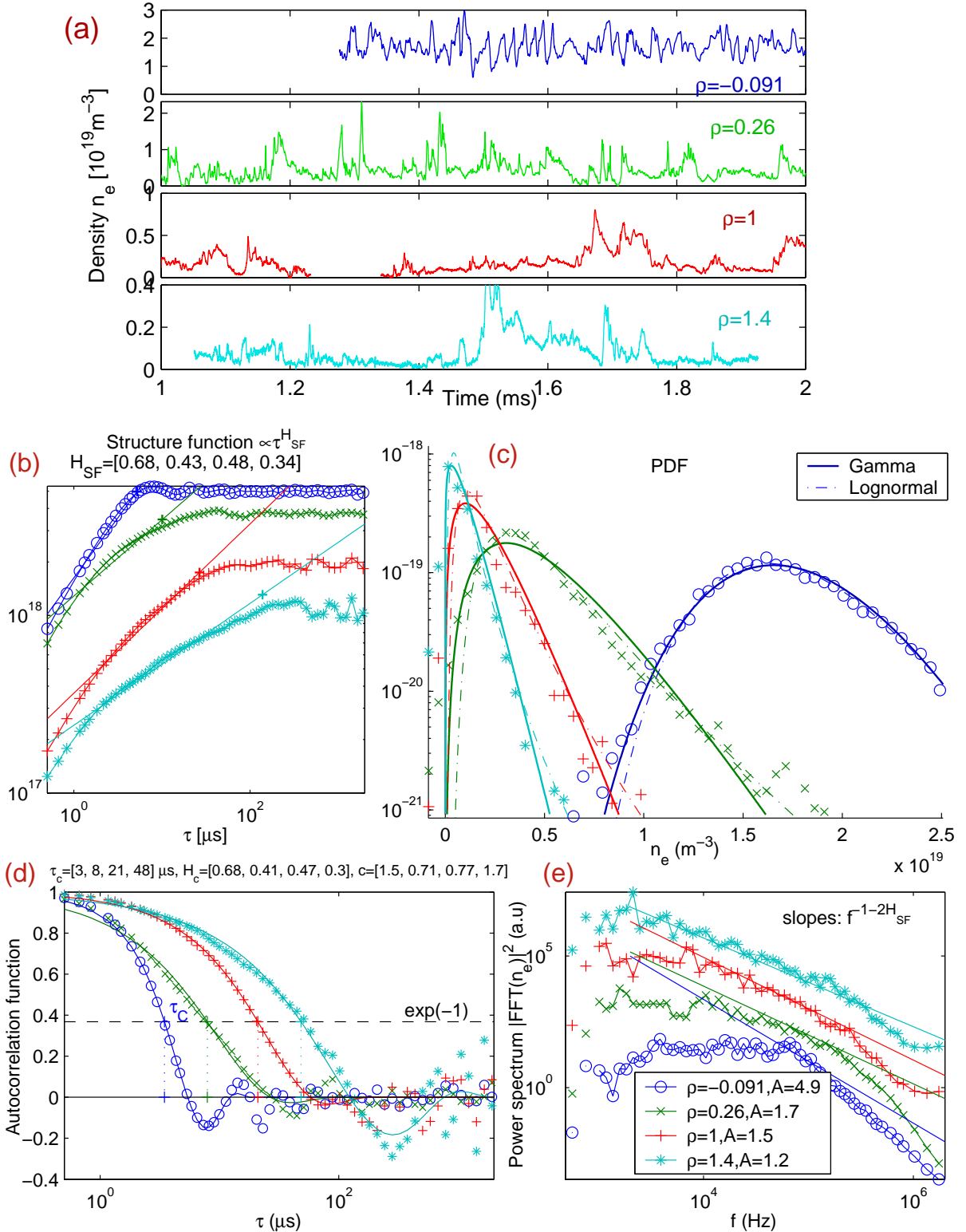


**Fig. 4.3 :** (a) Time series at four probe locations in the SOL for the first reciprocation (with  $\bar{n}_e = 4.4 \times 10^{19} \text{m}^{-3}$ ) in the L-mode ohmic discharge #24530. (b) The structure function fitted with the function  $\text{SF} \propto \tau^{H_{\text{SF}}}$  for  $\tau \leq \tau_c$ . (c) probability distribution functions in comparison with the Gamma and Lognormal distributions (defined in Table 4.1). (d) Autocorrelation functions with fits from Eq. (4.17). (e) Power spectra and comparison with scaling  $f^{-1-2H_{\text{SF}}}$ , with  $H_{\text{SF}}$  derived from the structure function fit.

This behaviour is also visible on the structure function shown in Fig. 4.3 (b).

The power spectrum in Fig. 4.3 (e) can be compared with that which would be obtained in a scale-free cascade model (defined in Section 2.1.2), for which  $P(f) \propto f^{-\beta}$ , with  $\beta$  the cascade index. It is also of note that an *inverse energy cascade* (see Section 2.1.2) in the frequency domain corresponds to  $\beta = 5/3$ , which is approximately the index measured from the power spectrum close to the wall in TCV. The power law line in the power spectra plot Fig. 4.3 (e) is derived from fitting the structure function, showing that indeed  $P(f) \propto f^{-(1+2H_{\text{SF}})}$ , except for  $\rho < 0$  where the power law is not clear.

For a stationary process within the scale-free region, the autocorrelation function is described by Eq. (4.15). Inspection of the fluctuation data considered here reveals a functional form, consistent with Eq. (4.15) when  $\tau < \tau_c$ :

$$\text{ACF}(\tau) = \exp(-|\tau/\tau'_c|^{2H}) \cos(c|\tau/\tau'_c|^{2H}) \quad (4.17)$$

where the cosine term permits the oscillations reaching negative values in the ACF to be followed. Allowing  $c$ ,  $\beta$  and  $\tau'_c$  to be free parameters results in the fitted lines in Fig. 4.3 (d) which describe well the temporal behaviour of the density fluctuations at all locations in the SOL. From Eq. (4.13), the correlation time is defined by the condition  $\text{ACF}(\tau_c) = \exp(-1)$ , as shown in Fig. 4.3 (d). In Refs. [34, 32] the value of  $c$  has been fixed to  $c = 1$  for simplicity. Allowing here  $c$  to be a free parameter permits to follow correctly the negative correlation extremes in ACF.

Fig. 4.3 (c) shows the PDFs obtained from the time series at each of the four radial locations. An important observation is that both the Gamma and Lognormal distributions, defined in Section 4.1.2, are good descriptions of the experimental PDFs across the entire SOL width. To demonstrate goodness of the PDF fits across the entire SOL region for varying PDF shape, as is the case for the Gamma and Lognormal distributions, would require many graphs. In what follows, the PDFs, determined fully by an infinite number of statistical moments  $M^{(n)}$ , will be therefore described simply by just three numbers: the cluster parameter,  $A$ , together with the lowest moments, Skewness and Kurtosis. Apart from the obvious simplifications achieved in this way, a further advantage of such an approach is that lower-order moments are relatively insensitive to rare events in a limited data-series, as discussed in Section 4.1.2.

### 4.3 Universality across various discharges

Having described in detail the fluctuating data from the probe reciprocation at medium density in discharge #24530, this section extends the discussion to analysis of a broad TCV database covering a wide range of operation under ohmic conditions. It will be demonstrated that turbulence in the TCV SOL under these conditions displays a remarkable degree of universality.

### 4.3.1 The TCV edge database description

Before presenting statistical analysis of the turbulence measurements, it is pertinent to look at the global plasma characteristics of the probed discharges. The database contains a large number ohmic discharges with  $I_p$  in the range 260-400 kA,  $B_\phi = \pm 1.2\text{T}$  (at the probe location), L and H-mode (ELM's are excluded from the analysis) and with both deuterium and helium as working gas. Line averaged densities range from the lowest operational values up to the actual discharge density limit - the case for the second probe reciprocations in both discharges #24530 and #26223.

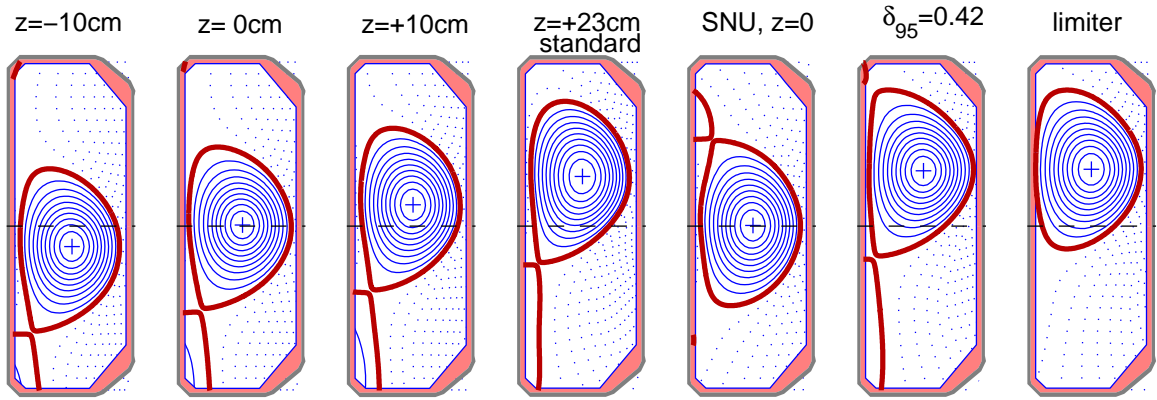


**Fig. 4.4 :** Gallery of poloidal cross-sections of the principal magnetic configurations from which the data used in this thesis were obtained. The reciprocating probe position at midplane is marked by the dashed line, and the separatrix highlighted. If not mentioned, the standard configuration is SNL,  $z=+23\text{cm}$ ,  $\delta \approx 1/3$ .

The standard magnetic equilibrium configuration corresponds to  $z = +23\text{cm}$ , single-null-lower (SNL) divertor with magnetic axis at  $z = +23\text{cm}$  (see Fig. 3.1 ) as for the discharge #24530. However, a large variety of plasma configurations can be obtained in TCV. Particularly, slightly modified in the database is the plasma triangularity,  $\delta_{95}$ , defined in Fig. 4.6 (b). To profit from this variability, the database used in this thesis also contains a vertical scan of the magnetic axis position ( $z = [-10, 0, +10, +23]\text{cm}$ ), single-null-upper (SNU) configurations and plasmas where the inner wall plays the role of a limiter, shown in Fig. 4.4 . Shifting the magnetic axis horizontally is useful to provide a poloidal scan of the SOL with the RCP which is fixed in space at  $z = 0$ . This horizontal shifting implicates, unfortunately, varying length of the outer divertor leg.

Profiles of time-averaged  $V_{\text{fl}}$ ,  $T_e$ ,  $J_s$  and  $n_e$  from the shots comprising the database are shown in Fig. 4.5 . Of particular note is the spans, by two orders of magnitude, in density across the radial position. Even at a given position, e.g. at  $\rho = 1$ , it varies by up to a factor of ten across the various discharges in the database.

The edge Thomson scattering (TS) is the only available diagnostic on TCV with which the probe measurements can be cross-check. As shown in Fig. 4.6 (a), the edge TS system [133] complements the main TS diagnostic on TCV. For the data shown here, a

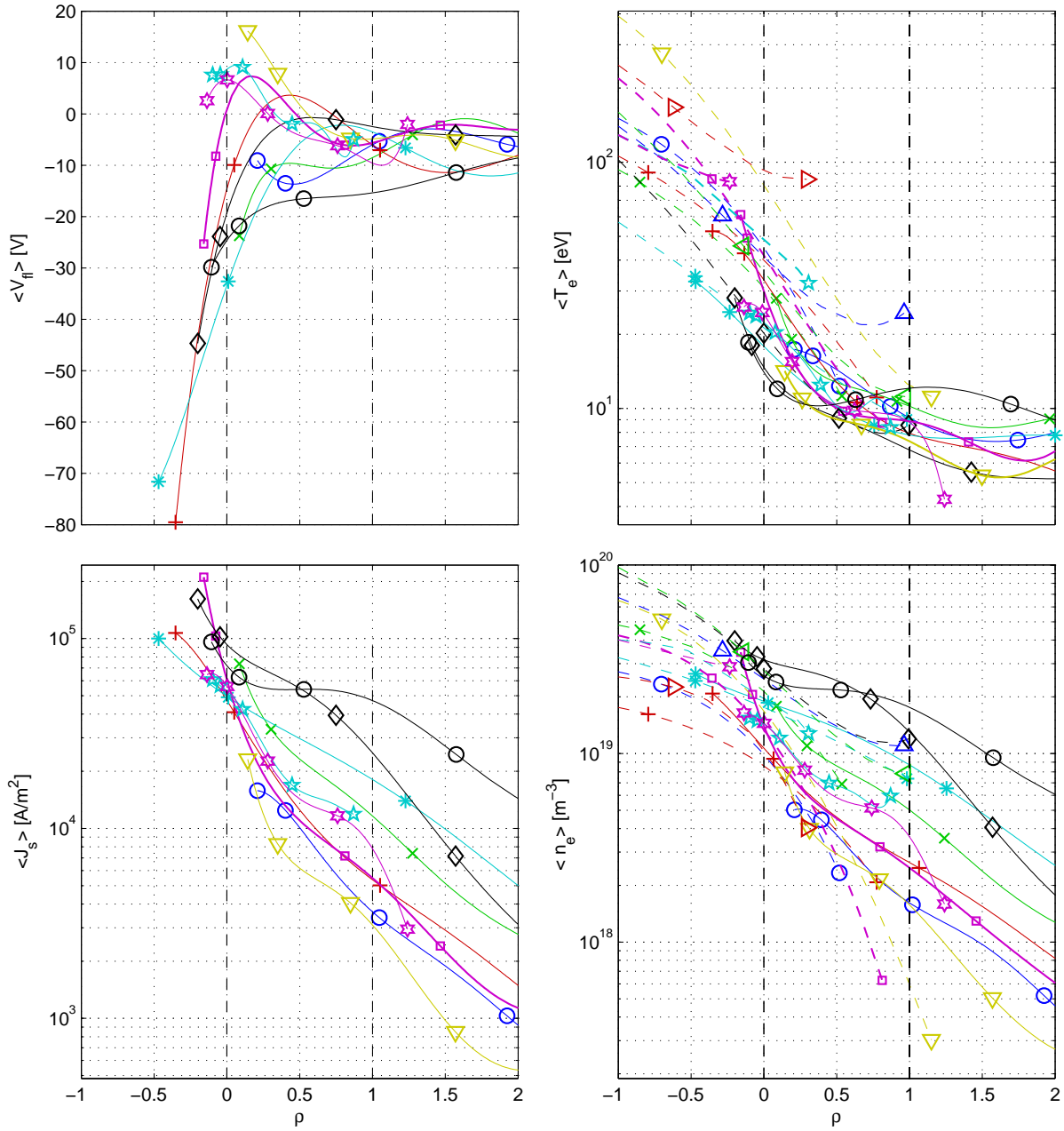


**Fig. 4.5 :** Outboard midplane mapped profiles from all discharges used in this chapter for turbulence analysis.  $V_{fl}$ ,  $T_e$ ,  $J_s$  and  $n_e$  are derived from swept Langmuir probe IV-characteristics (Fig. 3.10) and its profiles are shown for simplicity by polynomial lines fit corresponding to  $\sim 500$  data points per each line (one reciprocation). Solid lines correspond to measurements using the reciprocating probe and the dashed lines using the edge Thomson scattering. The legend in Fig. 4.9 should be used to identify the individual discharges through their symbols. The dashed and dot-dash vertical lines indicate the separatrix and wall locations.

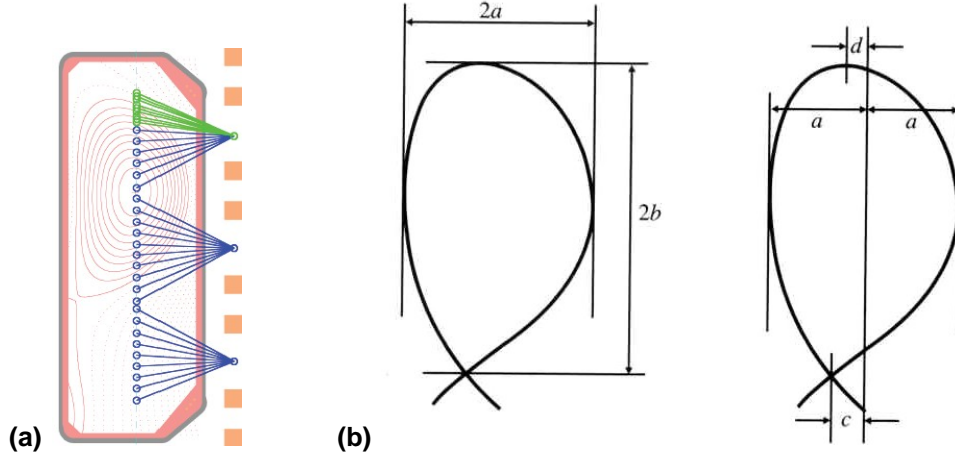


**Fig. 4.6 :** (a) Arrangement of spatial channels of the main and edge (in green) Thomson scattering diagnostic [132]. (b) Definitions of the plasma shape parameters: elongation,  $\kappa = \frac{b}{a}$  and triangularity,  $\delta = \frac{c+d}{2a}$  (from [2]).

set of polychromators, described in [134], on loan from the RFX device have been used to produce the edge profiles, allowing measurements quite deep into the SOL plasma. The edge channels are placed at the top of the machine, well adapted for the standard SNL divertor at  $z = +23\text{cm}$ . In general (Fig. 4.5)  $T_e$  and  $n_e$  from the edge TS match the RCP data well, except for the systematic observation that  $n_e$ , derived from TS, is usually lower than that obtained with the probe. This discrepancy is, however, roughly consistent with the error in the effective collecting area of the probe, as discussed in Section 3.7 - if the area correction factor from Fig. 3.13 (c) is applied to the probe measured densities, the values become quite similar to those obtained from the edge TS.

At high density, the SOL density profile flattens, as observed in other tokamaks (e.g. Alcator C-mod [18, 135] and DIII-D [136]). This is illustrated in both Fig. 4.5 and Fig. 4.7, where the SOL density e-folding length,  $\lambda_n$  for discharges in the database is plotted as a function of  $\bar{n}_e$ . Data for  $\rho > 1.5$  are excluded from the analysis due to low values of  $\langle n_e \rangle$  close to the noise threshold.

The connection length ( $L_c$ ) to the material wall determines the parallel particle loss and consequent life-time of turbulent structures, as discussed more broadly in Section 5.1.4. Precise values of  $L_c$  computed by the LIUQE magnetic reconstruction are presented in Fig. 4.8.  $L_c$  towards the bottom floor decreases slowly from the infinite value at  $\rho < 0$ .  $L_c$  in the opposite direction (i.e. upwards the central column) is affected by the sudden brake at  $\rho = 1$  corresponding to the field line hitting the outside midplane first wall since in all these discharges the probe sits below the magnetic axis, see Fig. 3.1. Presence of the upper X-point (shown in Fig. 5.2 (e)) is manifested by localized increase of  $L_c$ .

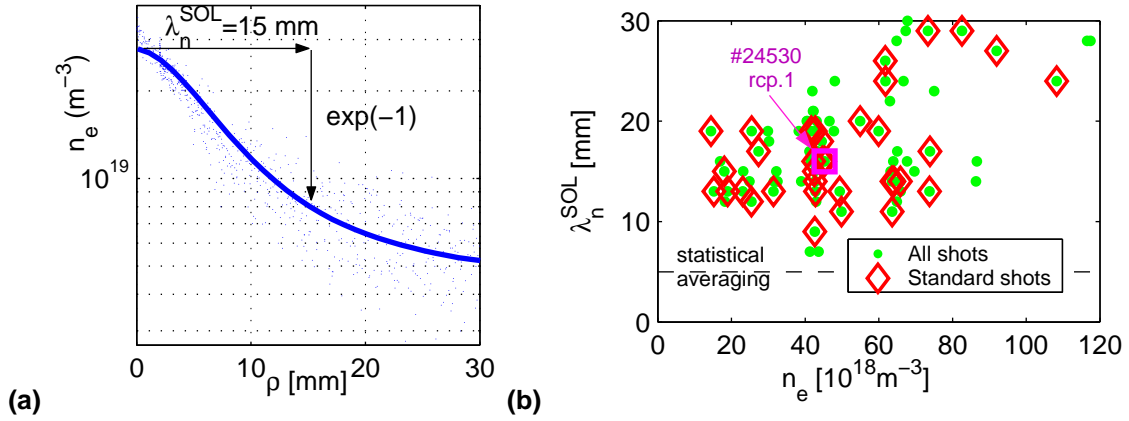


**Fig. 4.7 :** (a) Demonstration of meaning of the near SOL density width computed as e-folding length  $\lambda_n^{\text{SOL}}$  in the deepest region of a reciprocation. (b) shows that  $\lambda_n^{\text{SOL}}$  increases with  $\bar{n}_e$ .  $\lambda_n^{\text{SOL}}$  is compared with the distance ( $\leq 6$  mm) the probe travels within the standard time interval of  $5\text{ms}$  used to collect enough data for statistical averaging. Each point corresponds to one of the 76 discharges listed on page 126, amongst which the standard shots (L-mode,SNL,deuterium gas, $z \approx +23\text{cm}$ ) are emphasized.

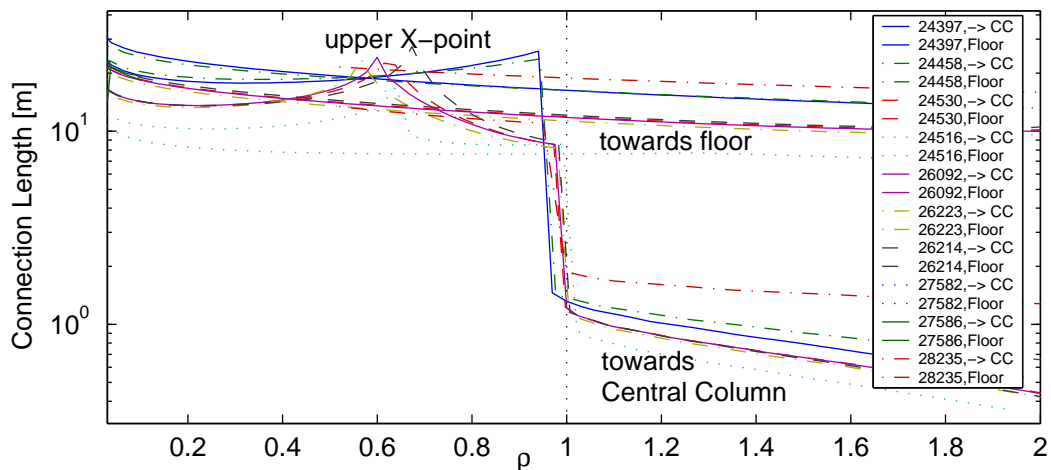


**Fig. 4.8 :** The parallel magnetic connection length from the reciprocating probe position at  $z = 0$  towards both the floor and the central column for all the discharges used in this chapter.

### 4.3.2 Universality of density fluctuations

Fig. 4.9 compiles radial profiles of the reduced (statistical) data from the database described above. The general behaviour characterized in Section 4.2 for the medium density (first reciprocation) standard shot #24530 is consistent with the behaviour found in the wider data set. With increasing distance from separatrix,  $S$ ,  $K$  and  $\tau_c$  increase and  $A$  decreases, saturating for  $\rho \geq 1$ . In the far SOL,  $0.5 < \rho < 1.5$ ,  $\langle n_e \rangle$  varies by two orders of magnitude across the database (Fig. 4.5) while the relative fluctuation level  $A \equiv \langle n_e \rangle / \sigma_{n_e}$  saturates at around  $1.7 \pm 0.3$  for all discharges (Fig. 4.9 (d)). In the same region,  $\tau_c$  varies by up to a factor of 5 (Fig. 4.9 (c)) across the differing plasma conditions. The  $\rho$  dependence of the skewness (Fig. 4.9 (b)) clearly shows how the PDFs tend systematically toward distributions with dominant positive density excursions as the wall is approached. It is interesting to note that  $A$ ,  $S$  and  $K$  remain essentially invariant to  $\tau_c$  and hence to the inter-burst time near  $\rho = 1$ , despite its wide variation. Somewhat exceptional behaviour (short  $\tau_c$  and high  $A$ ) is found in the low density helium discharge.

In the vicinity of separatrix the turbulence is close to normal, Gaussian noise (Skewness=0, Kurtosis=3). This is clearly a consequence of destruction of turbulence structures due to velocity *shear* located at separatrix (Fig. 2.5, [137]). This TCV observation that the far SOL is more turbulent than the near separatrix region is not new and has been observed elsewhere, with data from the Alcator C-Mod tokamak providing a particularly well documented example [19], The C-Mod SOL has been found to be separated into regions dominated by parallel conduction (near separatrix) and cross-field convection (in far SOL). Increasing  $\bar{n}_e$  up to the plasma density limit essentially spreads out the turbulent convection dominated region beyond the separatrix. This leads one to speculation that the limit itself may be due ultimately to a shift in the balance of cross-field transport and parallel losses [131].

As discussed earlier, the power spectrum is characterized by the power law  $P(f) \propto f^{-\beta}$  in frequency region  $f > \tau_c^{-1}$  corresponding to one decade close to separatrix up to over two decades in the wall shadow (Fig. 4.3). The cascade index,  $\beta$  (or the *Hurst exponent*  $H = (\beta - 1)/2$ , defined in Section 2.2.1) is found to be (Fig. 4.9 (e)) in between the level of the *energy cascade* process  $\beta = 5/3$  (see Section 2.1.2) and the uncorrelated *random walk*, corresponding to  $\beta = 2$ . The clear transition from *persistent* ( $\beta > 2$ ) to *anti-persistent* ( $\beta < 2$ ) behaviour corresponds interestingly to crossing the separatrix. Values of  $\beta$  have been derived by fitting the structure function in Fig. 4.3 (b) according to  $SF(\tau) \propto \tau^H$  for  $\tau < \tau_c$ . It could also be derived from the power spectra or the autocorrelation function (Eq. (4.17)) and these three methods yield similar values.

It has recently been suggested [124] that electrostatic SOL turbulence statistics tend towards the universal BHP distribution. Fig. 4.9 (a,b) clearly shows that whilst most TCV data can be described by fixed-shape PDFs in certain regions of the SOL ( $0.1 < \rho < 0.5$ ), this does *not* hold across the *entire* SOL. Approaching the wall from inside the separatrix, both  $S$  and  $K$  depart from Gaussian, cross values of the BHP and Gumbel distributions and continue to grow towards the wall shadow region.

The most convenient way of comparing these analytical distributions with the exper-

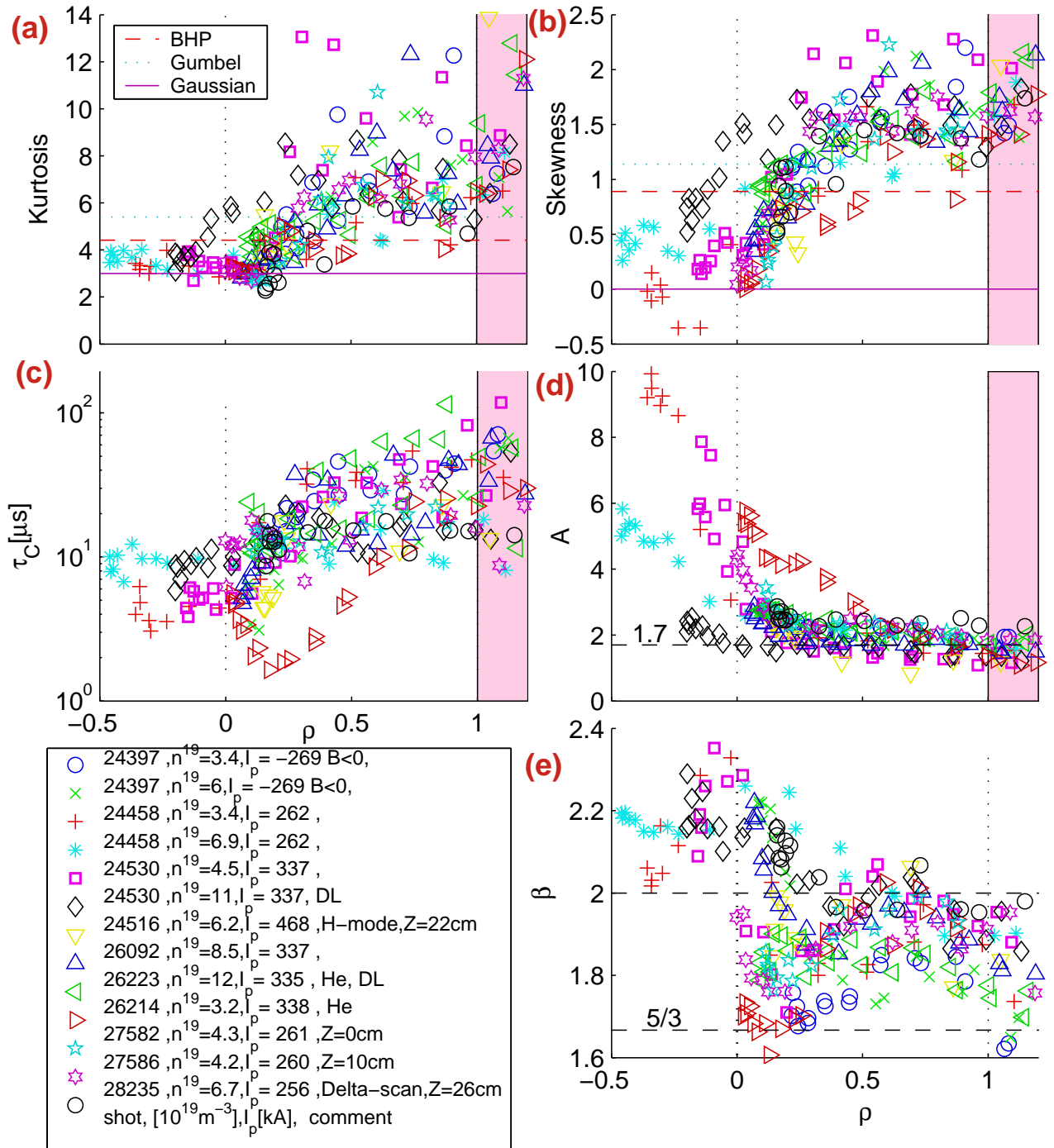


**Fig. 4.9** : Variation with normalized radius of density fluctuation statistics: **(a)** Kurtosis, **(b)** Skewness, **(c)** decorrelation time, **(d)** inverted fluctuation level and **(e)** the cascade index  $\beta$  for data from a wide range of TCV discharges (see Section 4.3.1). DL marks probe reciprocations close ( $> 95\%$ ) to the density limit of the discharge in question. Horizontal mark values of the particular PDFs (see legend in **(a)**).

imental data is to plot  $S$  and  $K$  as a function of  $A$  (using the relations in Table 4.1), independently of the probe position and plasma parameters. For all the cases considered the cluster parameter  $A$  is the key parameter characterizing the intermittent behaviour. In particular, Fig. 4.10 demonstrates that at any radial location and for all discharges, the functional dependence of  $S$  and  $K$  on  $A$  conforms reasonably well with the Gamma distribution. Fig. 4.10 also shows that the Lognormal distribution (discussed in Section 4.1.2) provides a qualitative match to the TCV data, but performs slightly less well than the Gamma distribution across the SOL whole width. The failure, noted above, the fixed shape distributions (BHP and Gumbel) to match the TCV statistics across the SOL is evident in Fig. 4.10. Chapter 5 will attempt a similar comparison for fluctuation time series derived from a 2D fluid turbulence model. In this case, the Gamma distribution will also turn out to be the best match amongst the five analytical PDFs, especially in the wall shadow.

Fig. 4.11 (a) compiles a set of density PDFs for all the database discharges, corresponding to the data points in Fig. 4.9 at  $\rho \sim 1$  (the wall radius). For comparison, both the Lognormal and Gamma distributions are plotted with  $A=1.7$ , the average value of  $\langle n_e \rangle / \sigma_{n_e}$  at the wall. The very clear data collapse demonstrates that the PDF shape (thus  $S$ ,  $K$  and  $A$ ) is similar for all discharges at  $\rho = 1$  and conforms well (within the scatter) to both the Gamma and Lognormal distributions.

To facilitate transfer of these observations to data from other tokamaks, an empirical scaling has been performed (Fig. 4.12) for  $A$  as a function of two general parameters,  $\rho$  and  $\bar{n}_e$ . This scaling, together with knowledge of local  $\langle n_e \rangle$  and the assumption that the density PDF is Gamma, or Lognormal-distributed, permits generation of an approximate distribution function everywhere in TCV edge for any discharge.

### 4.3.3 Universality of cross-field flux

The observed invariance of  $A$  for the density fluctuations in the far SOL has consequences for another important fluctuating quantity of interest. This is the turbulent driven radial particle flux,  $\Gamma_r$ , which is directly derived from the probe data using Eq. (3.8). In analogy to Fig. 4.9 for the density, Fig. 4.13 illustrates the radial variation of the  $\Gamma_r$ -statistics. Since the time-averaged value of the flux,  $\langle \Gamma_r \rangle$  is dominated by the averaged density (see below), there is a variation of over two orders of magnitude in the data set. In the separatrix vicinity,  $\langle \Gamma_r \rangle$  is even observed to reverse direction from outward to inward. Whether inward fluxes really exist, or simply that they are an artifact of an incorrect flux measurement has been discussed in Section 3.9. Nevertheless it is important to note that the flux skewness is higher than that of density, as expected from the discussion in Section 2.6.1.

The averaged flux can be expressed in terms of a correlation coefficient between the radial velocity, estimated from the poloidal electric field measurement,  $v_r = E_{\text{pol}}/B$ , and density fluctuations (Fig. 4.13 (f)):

$$C_{v,n} \stackrel{\text{def}}{=} \frac{\langle \tilde{v}_r \cdot \tilde{n}_e \rangle}{\sqrt{\langle \tilde{v}_r^2 \rangle \langle \tilde{n}_e^2 \rangle}} = \frac{\langle \Gamma_r \rangle}{\sigma_v \sigma_n}. \quad (4.18)$$

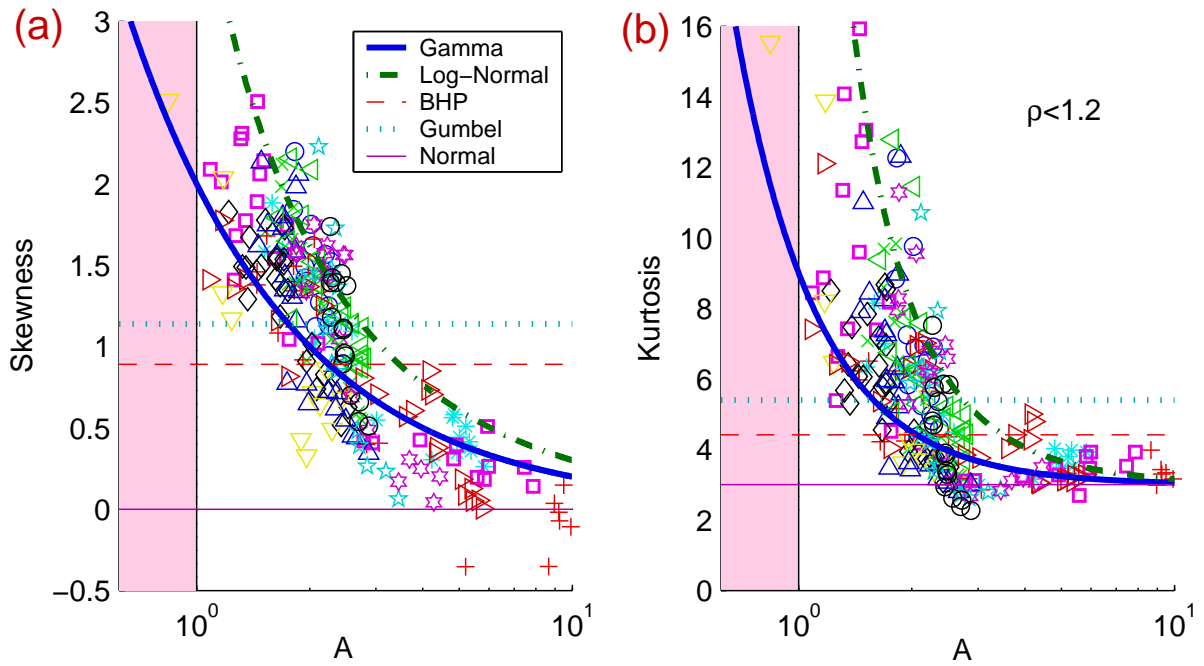


**Fig. 4.10** : Variation of (a) Skewness and (b) Kurtosis with  $A$  showing that whilst Gamma and Lognormal PDFs describe the data well across the entire SOL, other candidate fixed-shape distributions fail to capture the full radial variations. See the legend of Fig. 4.9 for the symbols.

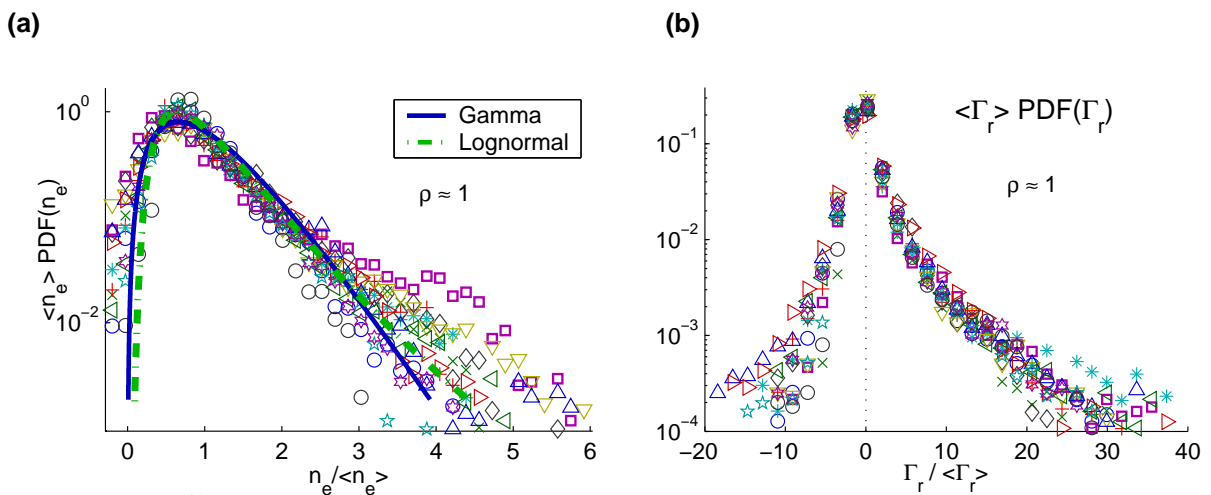


**Fig. 4.11** : Universality of PDF at wall for density (a) and radial particle flux (b). The local density  $\langle n_e \rangle$  varies by factor of  $\sim 10$  across the discharge database (see Fig. 4.9 for meaning of symbols).

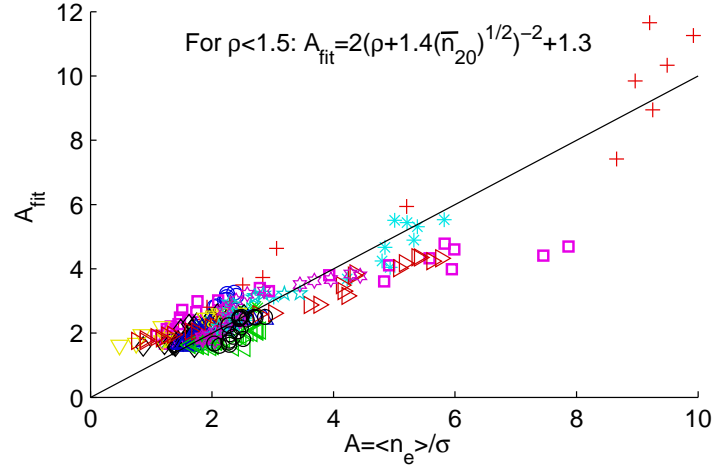


**Fig. 4.12** : Empirical scaling of  $A = \mu/\sigma$  with generic parameters:  $\rho$  and the line averaged density [ $10^{20} m^{-3}$ ]. See the legend of Fig. 4.9 for the symbols.

It is interesting then to observe in Fig. 4.13 (d,f) that the correlation coefficient is approximately equal to the relative fluctuation level of the flux,

$$C_{v,n} \approx A_{\Gamma} \stackrel{\text{def}}{=} \langle \Gamma_r \rangle / \sigma_{\Gamma_r}, \quad (4.19)$$

which, using Eq. (4.18), implies that

$$\sigma_{\Gamma_r} \approx \sigma_v \sigma_n. \quad (4.20)$$

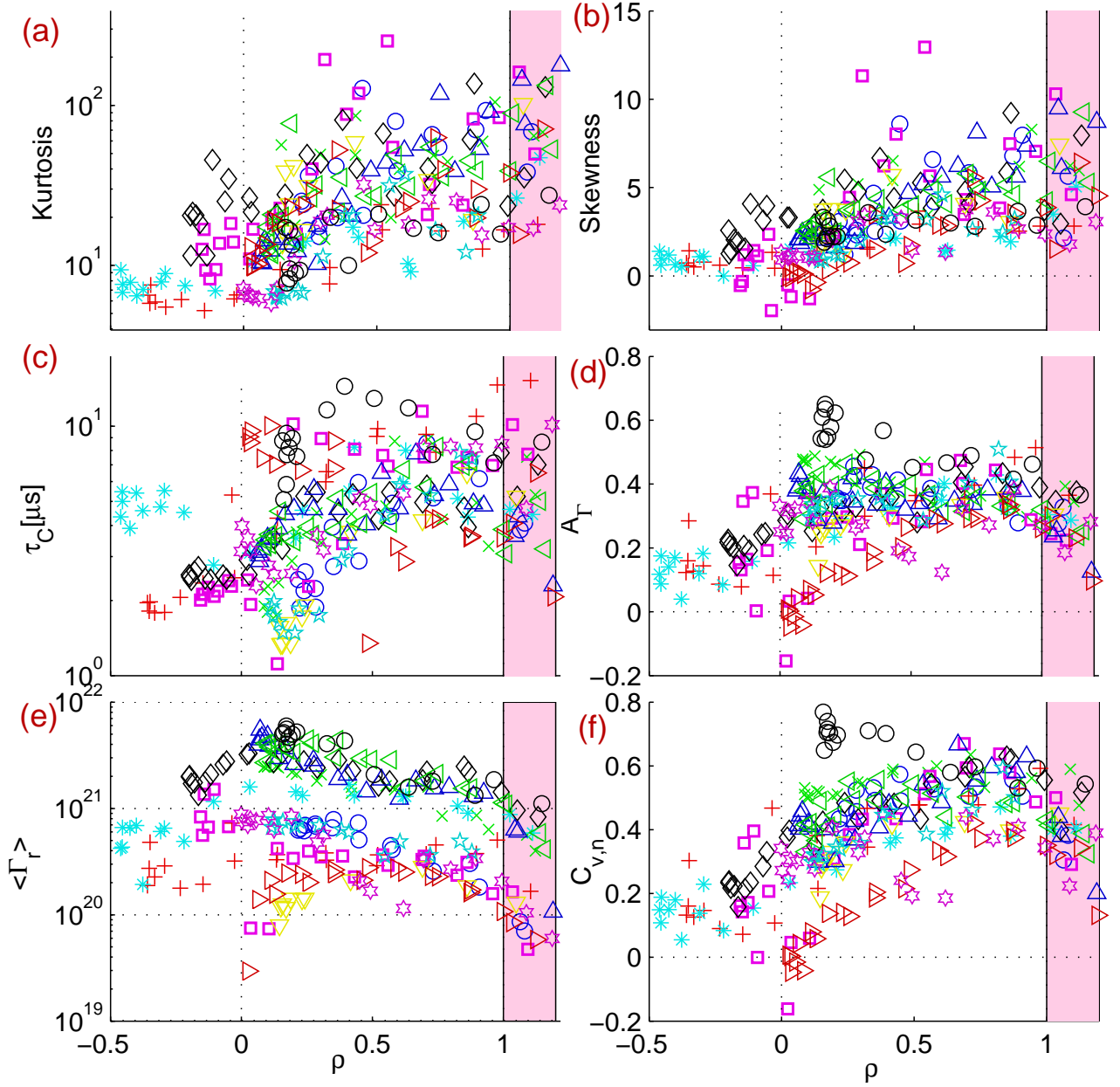
It has been reported that in the edge region of both the JET tokamak and the TJ-II stellarator, the PDF for the flux,  $P(\Gamma_r)$ , has a universal form upon rescaling [80] as  $\sigma_{\Gamma} P(\Gamma_r) = P(\Gamma_r/\sigma_{\Gamma})$ . Data collapse upon this rescaling requires  $\langle \Gamma_r \rangle = A_{\Gamma} \sigma_{\Gamma}$ , with  $A_{\Gamma}$  a constant. That the shape (skewness, kurtosis etc) of the distribution does not change requires that the correlation,  $C_{v,n}$  be invariant. Since both <sup>1</sup>  $A$  and  $A_{\Gamma}$  are approximately constant near the wall radius (Fig. 4.9 (d) and Fig. 4.13 (d)), it is clear that  $\langle \Gamma_r \rangle \propto \langle n_e \rangle \sigma_v$  and therefore  $\sigma_{\Gamma_r} \propto \langle n_e \rangle \sigma_v$ . The normalized flux PDF is shown in Fig. 4.11 (b), showing indeed a universal character across the various discharges, independently of normalization by  $\sigma_{\Gamma_r}$  or  $\langle \Gamma_r \rangle$ .

Figure 4.14 plots  $\langle \Gamma_r \rangle$  and  $\sigma_{\Gamma_r}$  as a function of the local mean density for the range of discharges used in Fig. 4.9 and over a radial interval approximately centered on the wall. The following scaling may be derived:

$$\langle \Gamma \rangle \propto \langle n_e \rangle^{1.1} \quad \text{and} \quad \sigma_{\Gamma} \propto \langle n_e \rangle^{1.1}. \quad (4.21)$$

This observation is consistent with the analysis in [19] of particle balance in the SOL, which demonstrates an increased level of cross-field transport as the density is raised.

<sup>1</sup>Note that  $A$  is a symbol for density inverted relative fluctuation,  $A \equiv A_n$ .



**Fig.** 4.13 : Variation with  $\rho$  of the local turbulent driven radial **particle flux** statistics: Kurtosis **(a)**, Skewness **(b)**, decorrelation time  $\tau_c$  **(c)**, inverse fluctuation level **(d)**, mean flux **(e)** (note strong increase of  $\langle \Gamma_r \rangle$  in higher density shots) and correlation between  $v_r = E_{\text{pol}}/B$  and  $\tilde{n}$  **(f)**. See legend in Fig. 4.9 for meaning of the symbols.

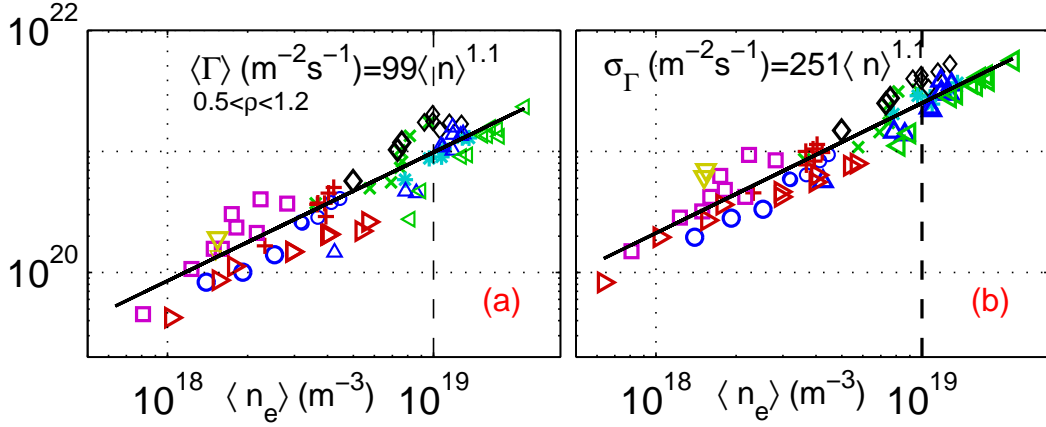


**Fig. 4.14** : Variation of  $\langle \Gamma_r \rangle$  (a) and  $\sigma_{\Gamma_r}$  (b) with respect to the local mean density  $\langle n_e \rangle$  in the wall vicinity  $0.5 < \rho < 1.2$ .

Eq. (4.21) provides the empirical form for this dependence in TCV over nearly two orders of magnitude in density, where we note that the scaling follows from the universal nature of both the density and flux PDF near the wall. The deviation of the exponents from unity results principally from a weak dependence of the radial velocity fluctuations on density. Put another way, this means that the variation in  $\langle \Gamma_r \rangle$  and  $\sigma_{\Gamma_r}$  across discharges is dominated by the value of local density  $n_e$ , whilst variations of the correlations,  $C_{v,n}$ , and the magnitude of the radial velocity,  $\sigma_v$ , play only a minor role.

#### 4.3.4 Diffusion versus convection

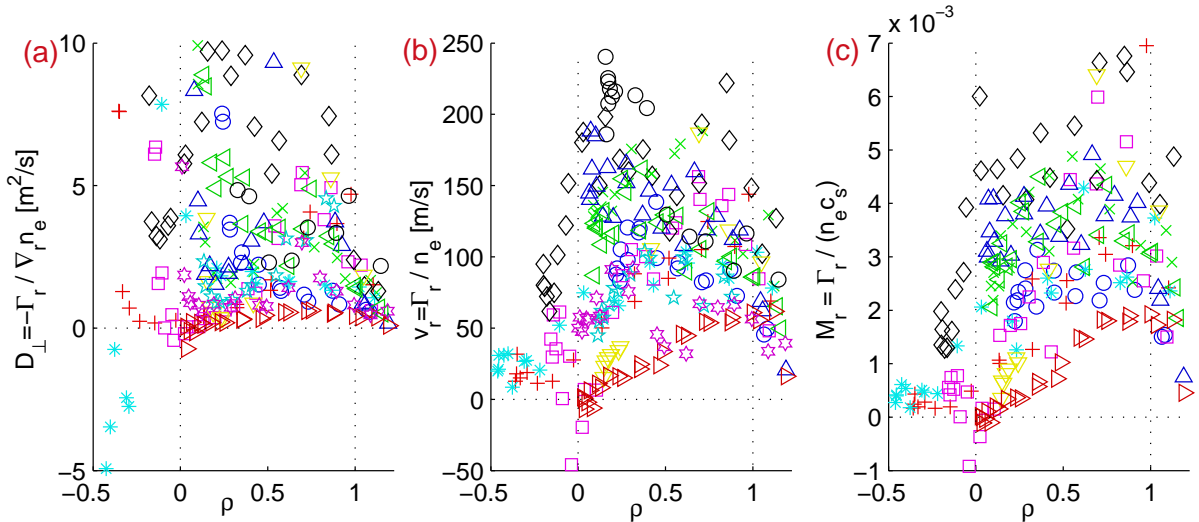


**Fig. 4.15** : (a) Time-averaged radial variation of the cross-field diffusion coefficient, (b) effective radial velocity and (c) effective radial Mach number.

Section 1.3.2 has already pointed out that the diffusion coefficient derived from experimental data,  $D_{\perp} = -\langle \Gamma_r \rangle / \nabla \langle n_e \rangle$ , is 2-3 orders of magnitude higher than that expected from first principles theory based on particle collisions (Eq. (1.8)). Despite this large discrepancy, the diffusive ansatz is still widely used in non-turbulent SOL models with  $D_{\perp}$  simply chosen to match the experimental profiles but without any physical justification. The transport can, however, equally be viewed as convective,  $\langle \Gamma_r \rangle = v_r \langle n_e \rangle$ . Indeed, Section 5.2.6 will demonstrate that radial convection driven by the interchange turbulence is in agreement with experimental data from TCV. Fig. 4.15 compiles estimates of the diffusion coefficient, effective radial velocity and corresponding radial Mach number from the TCV database. Within the large scatter in the database, the values are comparable to those found elsewhere: C-Mod [19, 18], T-10 tokamak [40], the Bohm scaling (Eq. (1.15)) and even in modelling of impurity diffusion [138].

The radial Mach number,  $M_r$  offers a convenient tool for comparing the parallel and cross-field fluxes: For convective motion, a single particle will, on average, reach the wall at the midplane in a time,  $d_{\text{wall}}(1 - \rho)M_r c_s$ . In the parallel direction, the time to reach the divertor target from the midplane is typically  $L_{\parallel}/c_s$ . Therefore, if

$$M_r > d_{\text{wall}}/L_{\parallel} \approx 3\text{cm}/15\text{m} = 2 \times 10^{-3}, \quad (4.22)$$

particles reach the main chamber walls before the divertor targets. Interestingly, the critical  $M_r$  for ITER is similar to that of TCV,  $d_{\text{wall}}/L_{\parallel} \approx 8\text{cm}/100\text{m} = 10^{-3}$ .

### 4.3.5 Scaling with line-averaged density

As discussed in on page 23, the *main chamber recycling* (MCR) regime enhances nonlinearly the wall bombardment which is a result of two effects: (1)  $n_e$  midplane separatrix density increase is roughly proportional to  $\bar{n}_e$ , (2) the mean-free-path of neutrals backscattered from the wall is inversely proportional to  $\bar{n}_e$ . The net result is a total ion outflux,  $\phi_{\text{total}}$  from the core plasma which scales as:

$$\phi_{\text{total}} \propto \bar{n}_e^2 \quad (4.23)$$

Such a scaling has been found experimentally on Alcator C-Mod and other tokamaks (Fig. 4.16) and is actually a result of the simple *Engelhardt model* [139] describing diffusive outward transport and neutral recycling. Identifying  $\langle \Gamma_r \rangle$  with  $\phi_{\text{total}}$ , Fig. 4.17 demonstrates that the Engelhardt scaling, Eq. (4.23) is also satisfied for TCV. The absolute values of  $\langle \Gamma_r \rangle$  are  $\sim 70\%$  higher than those corresponding to the dashed line in Fig. 4.16. This discrepancy maybe partially corrected by applying the calibration coefficient (Fig. 3.13 (c)) for the probe effective collection surface area and is also likely to large extent due to different poloidal location of the RCP.

### 4.3.6 Conditionally averaged waveform

This final section examines the detailed temporal behaviour of the density bursts. Individual events are extracted from the full data series,  $n_e(t)$  using the technique of *conditional averaging*. For the TCV data, this is performed by identifying individual bursts

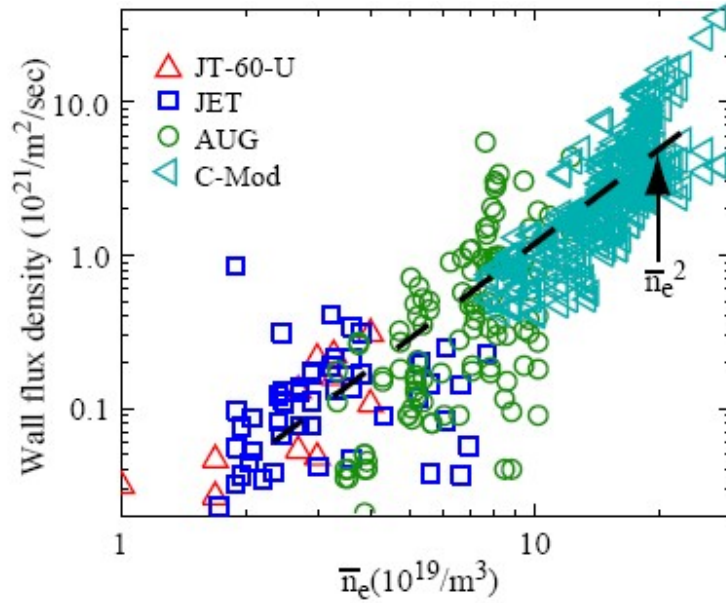


Fig. 4.16 : Scaling of the particle flux density at the wall for 4 divertor tokamaks. From [135].

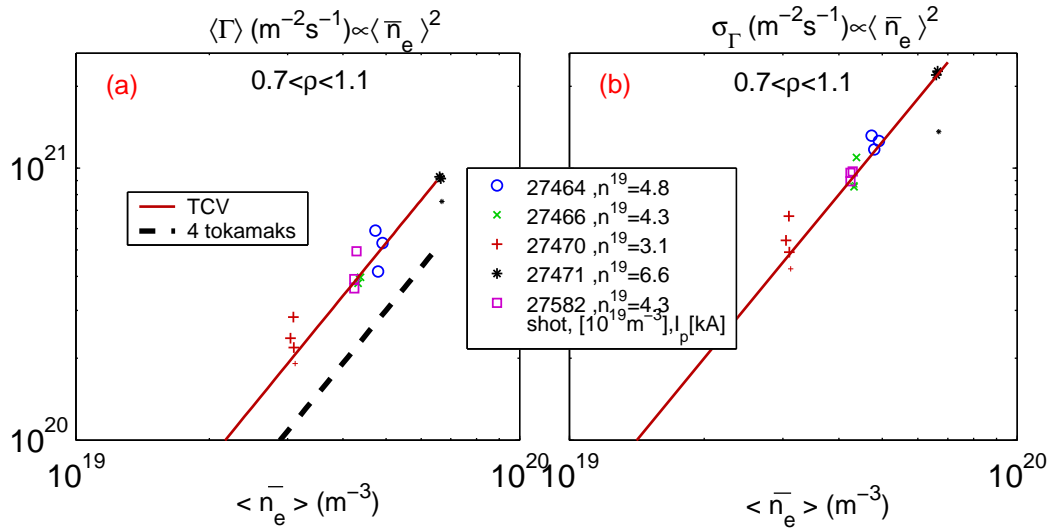
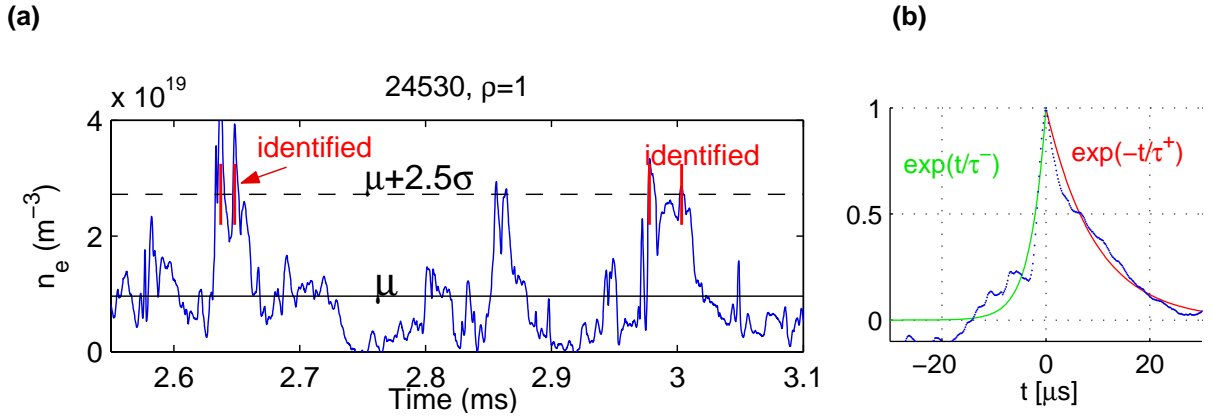
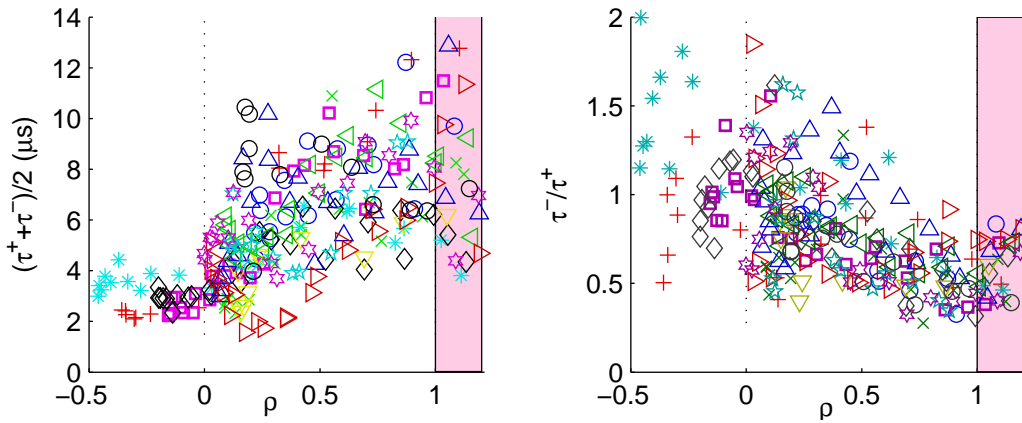


Fig. 4.17 : Line averaged density scan of the fluctuation driven radial particle flux,  $\langle \Gamma_r \rangle$  and its standard deviation,  $\sigma_{\Gamma_r}$  at the wall in TCV, demonstrating the square law dependance. The absolute level is compared with the scaling from those four tokamaks in Fig. 4.16 . The data are extracted from a set of discharges at  $z = 0$  (see Fig. 4.4 ) with  $I_p = 260$  kA.



**Fig. 4.18 :** (a) Large bursts are identified in the TCV time series as those with  $n_e > \langle n_e \rangle + 2.5\sigma$ , persisting longer than  $1\mu s$  and separated from a neighbouring burst by more than  $8\mu s$ . (b) Averaging and normalizing all such events generates a conditional waveform to which exponential growth and decay times are fitted ( $e^{t/\tau^-}$ ,  $e^{-t/\tau^+}$ ).



**Fig. 4.19 :** Temporal characteristics of density bursts. (a) radial profile of the burst timescale. (b) ratio of the growth/decay timescale. Symbols refer to discharges described in Fig. 4.9 .

as  $n_j(t) = n_e(t_j + t)$  at high density events  $t_j$  found as  $n_e(t_j) > \langle n_e \rangle + 2.5\sigma_n$ , over the time interval  $-30 < t[\mu s] < +30$  around each burst. If necessary, a small shift is applied to  $t_j$  to satisfy  $n_e(t_j) = \max_t(n_e(t_j + t))$ . An example of this burst identification within a density time series is demonstrated in Fig. 4.18 (a). Once extracted, the  $N$  bursts from each time series are normalized and averaged to produce a conditionally averaged waveform for any given  $\rho$ :

$$n_{av}(\rho, t) = \frac{1}{N} \sum_{i=1}^N n_e(t_j + t)/n_e(t_j)$$

Assuming simple exponential growth and decay, time averaged burst timescales can be obtained by fitting:

$$n_{av}(t) = \exp(+t/\tau^-) \text{ for } t < 0, \quad n_{av}(t) = \exp(-t/\tau^+) \text{ for } t > 0$$

where  $\tau^-, \tau^+$  are the burst *growth* and *decay* times, respectively.

The results, presented in Fig. 4.19 for the full shot database show that the bursts live typically  $\sim 3\mu s$  and are time-symmetric ( $\tau^-/\tau^+ \approx 1$ ) in the separatrix vicinity, consistent with uncorrelated Gaussian distributed random noise [137]. At the wall, however, the bursts are longer ( $\tau = 7 \pm 3\mu s$ ), consistent with the previously observed longer  $\tau_c$  at this location (Fig. 4.9 (c)). The bursts are also strongly asymmetric in time in the wall vicinity, growing rapidly and decaying slowly, such that  $\tau^-/\tau^+ \approx 0.4$ . This behaviour is again reasonably universal across the various discharges in the database. The fact that both  $\tau^-$  and  $\tau^+$  are shorter than  $\tau_c$  demonstrates that the lifetime of large bursts is less than that of the 'average' background fluctuations.

Turbulent structures with a sharp front and a trailing wake is a characteristic seen elsewhere experimentally in many tokamaks and linear devices [68, 12, 140]. It is also expected on the basis of a recent theory of blob evolution [86]. The code-experiment comparisons presented in Section 5.2.8 will demonstrate unequivocally that the measured burst characteristics presented in Fig. 4.19 are quantitatively reproduced in the numerical model (Section 5.1).

# Chapter 5

## Understanding TCV SOL turbulence: interchange motions

Direct comparison between TCV experimental data and a 2D fluid turbulence model is investigated, following and pushing ahead the results presented in [32,141]. This chapter will demonstrate that the fluctuation statistics of a typical diverted, ohmically heated, high density TCV plasma seem to be quantitatively obeyed by the output time series of 2D fluid turbulence simulations adapted as closely as possible to the experimental situation (within the constraints of the physics and geometry currently included in the numerical model). Using a simple description of the transition between open and close field lines, the simulations naturally generate radially advecting plasma filaments or blobs, the time series of which at any single spatial sampling part lead to asymmetric conditional waveforms and skewed and flattened PDFs. The radial advection mechanism for isolated plasma blobs has been elucidated in separate investigations [84,86], briefly introduced in Section 2.7.1, and yields profound insight into the statistical properties derived from the turbulence simulations and experimental measurements. The favourable agreement provides strong evidence that density fluctuations and cross-field transport in the tokamak SOL are due to turbulent driven in the region of closed field lines, spreading intermittently into the region of open field lines, and subsequently governed by non-linear interchange motions. The radial advection of these structures provides an explanation for the commonly observed large fluctuation levels and broad SOL density profiles presented in Chapter 4.

This chapter has the following structure. The physics basis and the governing equations of the fluid model are first described. Two dimensional turbulent structures resulting from the model are then presented. Finally, the model is compared with experiment using zero-dimensional time traces corresponding to the  $I_s$ ,  $T_e$  and  $V_{fl}$  measurements obtained experimentally with the reciprocating probe. The statistical techniques used have already been introduced in Section 4.1 and used in the entire Chapter 4.

## 5.1 Description of the ESEL model

### 5.1.1 Model equations

The ESEL (edge-SOL electrostatic) code, has been developed in the Risø National Laboratory in Denmark by V. Naulin, O.E. Garcia, A.H. Nielsen and J. Juul Rasmussen, [142,49]. ESEL solves a set of equations describing a two-dimensional interchange model (explained in Section 2.5.1) in which magnetic field curvature and density gradient drive turbulence through the interchange instability. It is a reduced fluid model for the self-consistent time evolution of edge plasma density, temperature and vorticity. The cross-field collective dynamics is fully modelled in a 2D poloidal plane appropriate to a small region of the tokamak boundary centred on the outboard midplane (Fig. 3.1 (b)). The loss of particles, energy and vorticity  $\Omega$  in the parallel direction is modelled simply by linear damping of all fields in the SOL and wall shadow, separately, corresponding to the parallel flows and currents. Finite Larmor radius effects and ion heat dynamics are neglected.

The fluid equations for low-frequency (i.e. below the ion Larmor frequency,  $\omega_{ci}$ ) dynamics in magnetized plasmas are simplified using the *drift approximation* (i.e. averaging over ion Larmor orbits), whereby the momentum equation for each charged particle species is reduced to an algebraic expression for the fluid drifts in terms of scalar fields ( $n, T, \Omega$ ). A full derivation is given in [49], only the basic steps of which are outlined here. An implicit expression is first derived for the cross-field fluid drift of any particle species with charge  $q$  and mass  $m$ ,

$$\mathbf{v}_{\perp} = \overbrace{\frac{1}{B} \mathbf{b} \times \nabla \phi}^{\text{ExB drift}} + \overbrace{\frac{1}{qnB} \mathbf{b} \times \nabla p}^{\text{diamagnetic drift}} + \overbrace{\frac{m}{qB} \mathbf{b} \times \left( \frac{\partial}{\partial t} + \mathbf{v} \cdot \nabla \right) \mathbf{v}}^{\text{polarization drift}}, \quad (5.1)$$

where  $\mathbf{b} = \mathbf{B}/B$  denotes the unit vector along the magnetic field, the pressure  $p$  is taken as scalar and only electrostatic perturbations are considered through the electric potential,  $\phi$  i.e.  $|\tilde{B}/\bar{B}| \ll 1$ . Augmented with the particle continuity equation for each species,

$$\frac{\partial n}{\partial t} + \nabla \cdot (n\mathbf{v}) = 0, \quad (5.2)$$

and the temperature equation by introducing a closed form of the cross-field heat flux  $\mathbf{q}_{\perp}$ ,

$$\frac{3}{2}n \left( \frac{\partial}{\partial t} + \mathbf{v} \cdot \nabla \right) T + nT \nabla \cdot \mathbf{v} + \nabla \cdot \mathbf{q}_{\perp} = 0, \quad (5.3)$$

a closed model in terms of scalar fields is then obtained by an iteration procedure of inserting and combining Eq. (5.1), Eq. (5.2) and Eq. (5.3) all together. This procedure leads to explicit expressions for  $n, T, \Omega$  only if some lowest order terms on the right-hand side of Eq. (5.1) are neglected. More details of the meaning of this "lowest order" assumption can be found in [142,49]. The importance of avoiding the isothermal assumption is further discussed in [90].

The terms on the right-hand side of Eq. (5.1) are the familiar  $\mathbf{E} \times \mathbf{B}$  drift  $\mathbf{v}_E$ , *diamagnetic drift*  $\mathbf{v}_d$  and *polarization drift*, defined, respectively, by

$$\mathbf{v}_E = \frac{1}{B} \mathbf{b} \times \nabla \phi = \frac{\mathbf{E} \times \mathbf{B}}{B^2}, \quad \mathbf{v}_d = \frac{1}{qnB} \mathbf{b} \times \nabla p, \quad \mathbf{v}_p = \frac{m}{qB} \mathbf{b} \times \left( \frac{\partial}{\partial t} + \mathbf{v} \cdot \nabla \right) \mathbf{v}. \quad (5.4)$$

The second term comprises diamagnetic effects due to the particle gyration as well as the fluid motions corresponding to guiding centre drifts in the presence of a non-uniform magnetic field. The divergence of the electric drift consists of two terms,

$$\nabla \cdot \mathbf{v}_E = \overbrace{\nabla \left( \frac{1}{B} \right) \cdot \mathbf{b} \times \nabla \phi}^{(1)} + \overbrace{\frac{1}{B} \nabla \times \mathbf{b} \cdot \nabla \phi}^{(2)} = \mathcal{C}(\phi), \quad (5.5)$$

which, for low pressure plasmas, are equal and in which the *curvature operator*,  $\mathcal{C}$  is introduced.

The *thin layer approximation* is commonly invoked in the derivation of reduced fluid models as well as in ESEL. This condition assumes that the relative change in the particle density and temperature is small in the domain under consideration, a condition which is rarely satisfied in reality. One motivation for this simplification is that it allows variations in the particle density to be neglected in the compression of the lowest order drifts, and thus significantly reduces the necessary computational resources for numerical solutions. The term that is neglected corresponds to plasma advection by the polarization drift. Since the transport by the electric drift usually dominates over the polarization drift (in Eq. (5.1)), this approximation is also commonly applied in other models (see e.g. [49, 90, 91, 92, 24]). More details can be found in [143] (under local approximation).

### 5.1.2 Reduced model equations

It can be shown that the diamagnetic drift does not contribute to plasma and heat advection, an effect known as *diamagnetic cancellation* [49]. This is essentially because the diamagnetic motion does not by itself involve the transport of heat or particles over macroscopic distances. In magnetized plasmas the assumption of quasi-neutrality allows the direct role of space charge advection in current creation to be neglected. Since the  $\mathbf{E} \times \mathbf{B}$  drift is the dominant contribution to the plasma motion, as discussed in Section 2.6.1, the plasma *vorticity*, defined as  $\Omega \stackrel{\text{def}}{=} \nabla \times \mathbf{v}$ , is directly linked to the plasma potential

$$\Omega = \nabla \times \mathbf{v}_E = B^{-2} \nabla \times (\mathbf{B} \times \nabla \phi) = \nabla_{\perp}^2 \phi. \quad (5.6)$$

where the proper mathematical derivation is provided in Appendix A. In the coordinate system with  $x, y$  denoting the radial and poloidal model coordinates,  $\rho$  the normalized SOL coordinate, the so-called *Bohm normalization* (with  $x = 50$  at separatrix) relates the model coordinates to the real space:

$$\omega_{ci} t \rightarrow t, \quad \frac{\rho}{\rho_s} = x + 50, \quad \frac{y}{\rho_s} \rightarrow y, \quad \frac{e\phi}{T} \rightarrow \phi, \quad \frac{n}{N_0} \rightarrow n, \quad \frac{T}{T_0} \rightarrow T. \quad (5.7)$$

where  $\rho_s = \sqrt{\rho^*} = c_s/\omega_{ci}$  is the hybrid thermal Larmor radius, that is identical to  $\rho_{Li}$  with thermal velocity computed using the electron temperature.

This was the final step leading to the reduced model equation set,

$$\frac{dn}{dt} + n\mathcal{C}(\phi) - \mathcal{C}(nT) = \Lambda(n) \quad (5.8)$$

$$\frac{dT}{dt} + \frac{2T}{3}\mathcal{C}(\phi) - \frac{7T}{3}\mathcal{C}(T) - \frac{2T^2}{3n}\mathcal{C}(n) = \Lambda(T) \quad (5.9)$$

$$\frac{d\Omega}{dt} - \mathcal{C}(nT) = \Lambda(\Omega) \quad (5.10)$$

where the advective time derivative,  $d/dt$ , curvature operator ( $\mathcal{C}$ ), non-dimensional inhomogeneous magnetic field,  $B(x)$  and the sink operator,  $\Lambda$  are defined as

$$\frac{d}{dt} = \frac{\partial}{\partial t} + \frac{\mathbf{z} \times \nabla\phi \cdot \nabla}{B}, \quad \mathcal{C} = -\frac{\rho_s}{R_0} \frac{\partial}{\partial y}, \quad \frac{1}{B(x)} = 1 + \frac{a + \rho_s x}{R_0}, \quad \Lambda = D\nabla_{\perp}^2 - \frac{1}{\tau_{\parallel}}. \quad (5.11)$$

All the equations in this section, Eq. (5.6)→Eq. (5.11), are the complete and self-consistent reduced set of equations solved by the ESEL code. The influence of particle collisions and parallel motions is described by the operator  $\Lambda$ , where  $D$  is the collisional diffusion coefficient and  $\tau_{\parallel}$  represents particle loss time due to transport along open magnetic field lines.  $D$  and  $\tau_{\parallel}$  are generally called the *transport coefficients*.

### 5.1.3 Transport coefficients

The fluctuations measured by the RCP and seen in the 2D turbulence simulations are in reality plasma "filaments" elongated along the total magnetic field with finite parallel correlation length. This is in fact limited by the connection length,  $L_c$  along the field, from the point of origin of the structure and the divertor targets. On TCV,  $L_c(\rho)$  (shown in Fig. 3.1) is computed from the LIUQE magnetic equilibrium reconstruction, introduced in Section 3.2.1. With  $L_c \sim 16\text{m}$  to the end plates and a parallel velocity given by the average thermal velocity  $\sqrt{\langle v^2 \rangle} \sim c_s = \sqrt{T/m_i} \sim 60\text{km/s}$ , the parallel loss time is

$$\frac{\tau_{\parallel}}{\omega_{ci}} \sim \frac{L_c}{c_s} \sim 250\mu\text{s} \quad \text{so that} \quad \tau_{\parallel}^{-1} \sim 7 \times 10^{-5}.$$

Combining Eq. (5.8) with Eq. (5.11) and neglecting the cross-field diffusion leads to  $\frac{dn}{dt} + \frac{n}{\tau_{\parallel n}} = 0$  with solution

$$n(t) \propto \exp\left(-\frac{t}{\tau_{\parallel n}}\right), \quad (5.12)$$

which associates  $\tau_{\parallel}$  with the typical life-time of the turbulent structures. Much more rigorously than this simple approach, for the ESEL simulations performed for TCV, the loss times  $\tau_{\parallel n}, \tau_{\parallel T}, \tau_{\parallel \Omega}$  and the transport coefficients  $D_n, D_T, D_{\Omega}$  have been estimated [88] on the basis of first principles expressions using the neoclassical cross-field transport (Pfirsch-Schlüter collisional diffusion) and classical parallel transport (sub-sonic advection and

Spitzer-Härm diffusion). Classical diffusion due to particle collisions has been introduced already in Eq. (1.8). For the high-density 2nd reciprocation of discharge #24530, which is used exclusively in this chapter for the model-experiment comparison, these estimates yield the following values for the dimensionless coefficients [88]:

$$\begin{aligned} D_n &= 0.9(4.5)^{\text{used}} \times 10^{-3}, & D_T &= 1.0 \times 10^{-2}, & D_\Omega &= 2.5 \times 10^{-2}, \\ \tau_{s||n}^{-1} &= 3.1 \times 10^{-5}, & \tau_{s||T}^{-1} &= 1.8 \times 10^{-4}, & \tau_{s||\Omega}^{-1} &= 3.1 \times 10^{-5}. \end{aligned} \quad (5.13)$$

Note the subscript  $_s$  states for values in the SOL;  $D_n, D_T, D_\Omega$  are usually called the particle and heat diffusion coefficients and viscosity, respectively. The value of  $D_n$  actually used in the simulations is  $5 \times$  higher than the neoclassical transport estimate. Using the low value ( $D_n = 0.9 \times 10^{-3}$ ) would be too demanding for the numerical grid resolution. A short test run at half this value ( $D_n = 2.2 \times 10^{-3}$ ) has confirmed that similar results are obtained. In Section 5.2.7 this inconsistency is proposed as a possible explanation for the mismatch in poloidal structure size found in this model-experiment comparison.

For simplicity,  $D$  and  $\tau_{||}$  are taken as *constants* in the whole simulation region with a crude, but important, variation of the parallel loss times:

$$\tau_{||} = \infty \text{ for } \rho < 0, \quad \tau_{||} = \tau_{s||} \text{ for } 0 < \rho < 1, \quad \tau_{||} = \tau_{s||}/10 \text{ for } \rho > 1. \quad (5.14)$$

This constitutes an approximate attempt to account for the variation in parallel connection length across the edge. In the confined plasma, field lines are closed and thus  $L_c \rightarrow \infty$  is assumed. In the main SOL (up to the wall radius),  $L_c$  and thus  $\tau_{||}$  is assumed constant. Whilst  $L_c$  is roughly symmetric from midplane to inner and outer targets in the main SOL, it is substantially shorter in the wall shadow region in the direction towards the inner target from the probe location. Here field lines terminate on the outside midplane wall (Fig. 3.1), a distance of only  $\sim 1\text{m}$ . In the direction towards the outer target  $L_c$  decreases from  $\sim 20\text{m} - 10\text{m}$  across the wall shadow region. This asymmetry of the connection lengths cannot yet be accounted for in ESEL and so a value of the damping coefficient is chosen which gives stronger weight to the short connection length side. This inclusion in ESEL model of a region of no damping inside the separatrix, in contrast to the model in [91] with constant finite damping everywhere, is an important ingredient since it appears to be this transition region from zero to finite damping where the interchange instability develops.

These transport coefficients and loss times strongly vary with the plasma parameters  $n, T$ . Since the SOL turbulence is collisional,

$$\nu^* = L_{||}/\lambda_{ee} = 10^{-16} L_{||} n_e T_e^{-2} \sim 50 \gg 10 \quad \text{in SOL} \quad (5.15)$$

and assuming  $T_i = T_e$  yields [88]:

$$D_n \propto D_T \propto D_\Omega \propto n T^{-1/2}, \quad \tau_{||\Omega} = \tau_{||n} \propto T^{-1/2}, \quad \tau_{||T} \propto n T^{-5/2}. \quad (5.16)$$

Combining Eq. (5.13) (at  $\rho = 0.3$ ) with Eq. (5.16) and the profiles  $n(\rho), T(\rho)$  from shot #24530 in Fig. 4.5, the radial variations of these coefficients is illustrated in Fig. 5.1.

Note that the parallel damping of vorticity is assumed identical to that of particle density. Imposing these coefficients as constants within the ESEL model is certainly a significant simplification, especially for lower density plasma (for example corresponding to the first of the two reciprocations in shot #24530). To introduce a variation with  $\rho$  is a significant challenge for future model development [144].

### 5.1.4 Effect of connection length

The parallel connection length from the probe at midplane to the targets would be expected to exert an important influence on the blob amplitude since it determines the upper limit to its life-time (Eq. (5.12)) through parallel particle loss. This is demonstrated experimentally in Fig. 5.2. For a plasma of circular cross-section,  $L_c \approx 2\pi Rq$ , where  $q \approx \frac{aB_T}{RB_{\text{pol}}}$  and  $B_{\text{pol}}(a) \approx \frac{\mu_0 I_p}{2\pi a}$ , so that

$$L_c = \frac{(2\pi a)^2 B}{\mu_0 I_p} = \frac{2.4\text{MA}}{I_p} \text{m} \quad (5.17)$$

If instead the full equilibrium magnetic reconstruction is used to compute the connection length (see Section 3.2.1),  $L_c$  in the diverted configuration of #24530 is about a factor of 2 longer due to the plasma shape and the presence of a lower X-point. Nevertheless,  $L_c \propto I_p^{-1}$  still applies. Fig. 5.2 (a) shows the radial variation of  $L_c$  for three discharges differing only in the magnitude of  $I_p$ . Fig. 5.2 (b) demonstrates qualitatively that the density gradient  $dn_e/d\rho$  is smaller for discharges with longer  $L_c$ . One interpretation of this observation could be that the blob lifetime increases since the parallel loss times increase (due to Eq. (5.12)) and the blob can propagate radially further into the SOL ( $\tau_{\parallel} \propto L_c$ ).

Even though the equilibrium of #24530 is SNL, upper X-point is also present, just outside the vacuum vessel (Fig. 5.2 (e)). At  $\rho \sim 0.4$  Fig. 5.2 (a) shows that this second X-point increases  $L_c$  sharply. Interestingly, it appears that the enhanced magnetic shear in the vicinity of the X-point destroys the blobs. Indeed, the turbulence level ( $1/A$ , Fig. 5.2 (c)) decreases in the radial region beyond the X-point. Since  $S \approx 2/A$ , the Skewness also flattens in this region (Fig. 5.2 (d)). The mechanism driving this effect is presently unknown. Seeking an explanation using the ESEL simulations is presently impossible since the code does not account for changes in the magnetic topology.

### 5.1.5 Boundary conditions

The ESEL code models only a small part of the tokamak poloidal cross-section centred on the outboard midplane. An essential question is therefore what to assume at the boundaries of the simulation domain. In order to control the collective and collisional fluxes of particles and heat through the boundaries, the following *boundary conditions* are

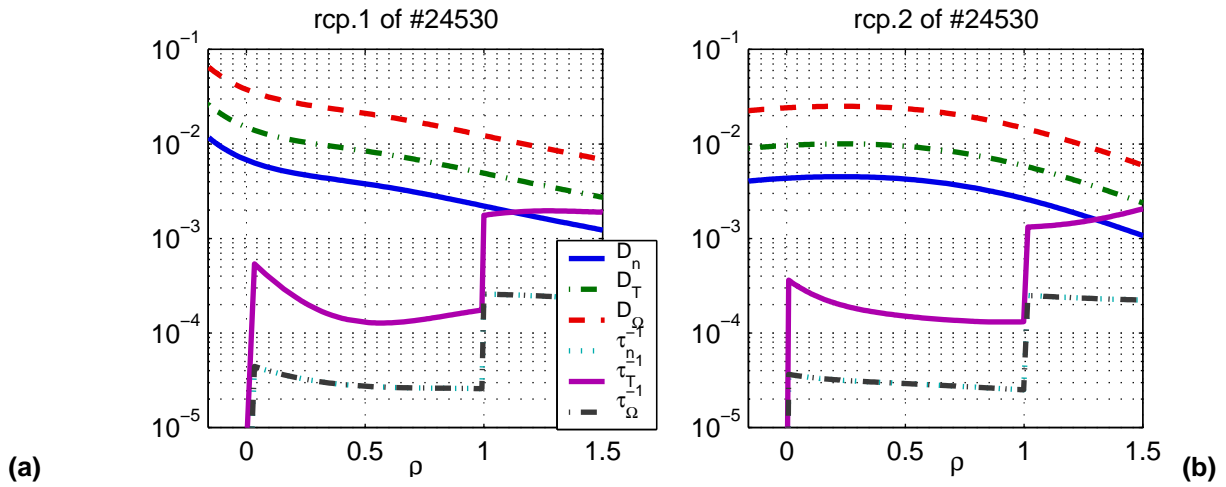


**Fig. 5.1 :** Demonstration of how much the diffusion coefficients and parallel loss times vary across the SOL for medium (1) and high (2) density reciprocations in shot #24530. In the code the coefficients are assumed constant, accounting only for the changes in  $\tau^{-1}$  at  $\rho = 0$  and  $\rho = 1$  (Eq. (5.14)).

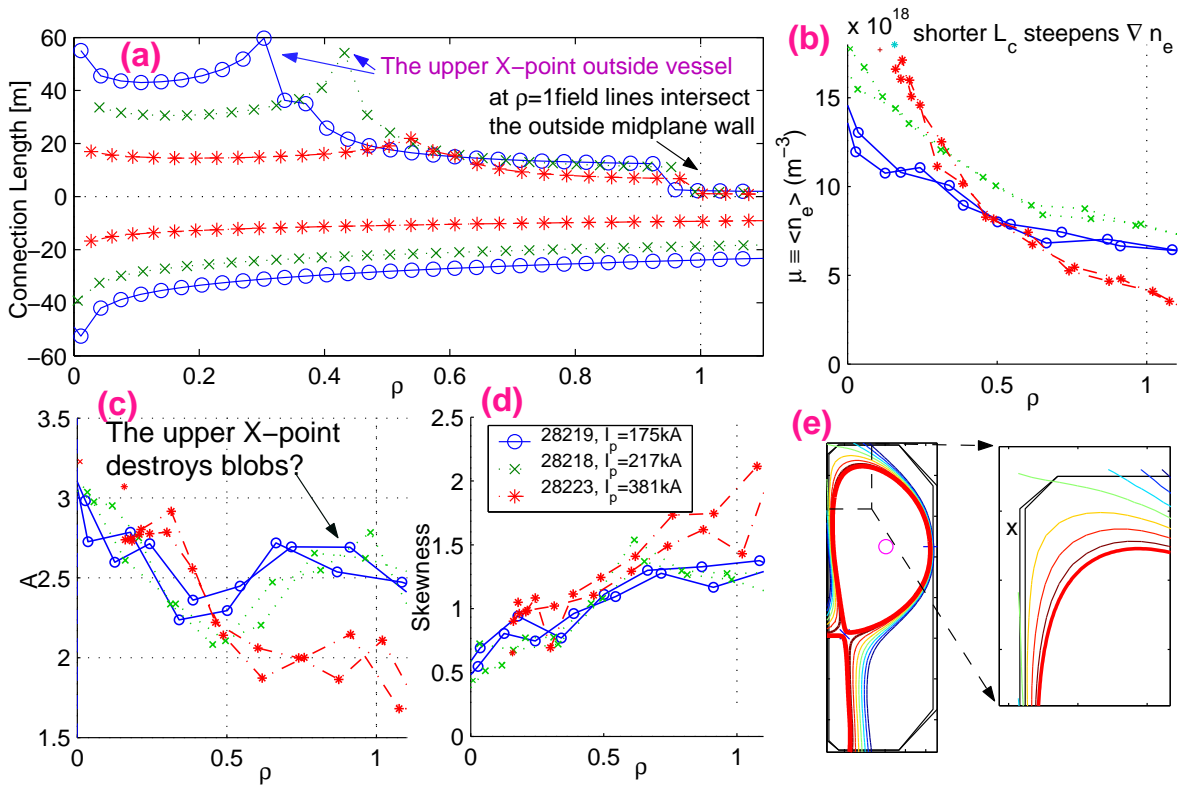


**Fig. 5.2 :** Illustrating the influence of connection length on SOL density fluctuations for three discharges differing only in the magnitude of  $I_p$  with  $\bar{n}_e \approx 4.2 \times 10^{19} \text{m}^{-3}$ . **(a)**  $L_c$  towards the inner ( $L_c > 0$ ) and outer ( $L_c < 0$ ) targets. **(b)** demonstrates that  $dn_e/d\rho$  is steeper for shorter  $L_c$ . The effect of the upper X-point on the fluctuation level is shown in **(c)** and on Skewness in **(d)**. **(e)** The magnetic configuration with expanded region around the upper X-point.

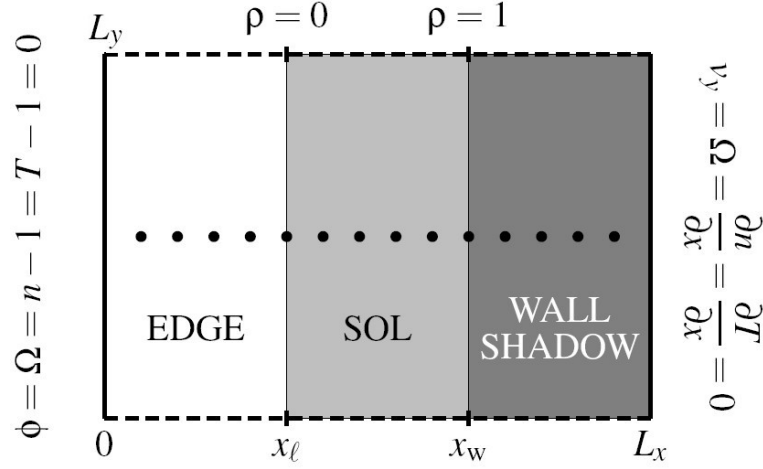


**Fig. 5.3 :** Geometry of the ESEL simulation domain illustrating the position of test probes (the  $\bullet$  symbols), regions of confinement (edge) and damping (in SOL and wall shadow) and boundary conditions. The box dimensions are  $L_x = 200\rho_s$  (radial) and  $L_y = 100\rho_s$  (poloidal) with  $\rho_s \approx 0.7$  mm. In experiment, this geometry corresponds to the small rectangle shown in Fig. 3.1 (b). Parallel damping strengths are proportional to  $1/L_c$  (Fig. 3.1 (c)).

applied (see Fig. 5.3 ):

$$\text{poloidal periodic : } q(x, 0, t) = q(x, L_y, t), \quad \text{for } q \in \{n, T, \Omega, \phi\}, \quad \forall x, t \quad (5.18)$$

$$\text{inner boundary } (x = 0) : \quad \phi = \Omega = T - 1 = n - 1 = 0 \quad (5.19)$$

$$\text{outer boundary } (x = L_x) : \quad \frac{\partial \phi}{\partial x} = \Omega = \frac{\partial T}{\partial x} = \frac{\partial n}{\partial x} = 0 \quad (5.20)$$

Imposing a periodic boundary condition in the *poloidal* direction is a reasonable approach since the poloidal extent of the computational region,  $L_y$  is much shorter than the outer TCV midplane region  $\sim 30$ cm (see Fig. 3.1 (b)). This region can therefore be assumed to be statistically homogeneous in the poloidal direction. In a real tokamak, of course, blobs do not periodically cross this artificial upper boundary only to reappear again at the lower boundary. It is thus important to check that the typical poloidal extension of structures is short enough in comparison with  $L_y$  in order to avoid unphysical situation where a structure bottom interacted with itself top. Mathematically this can be expressed by imposing a condition that the fluctuations must be uncorrelated across half the poloidal extension of the simulation domain:

$$\left| \frac{\langle q(x, 0)q(x, L_y/2) \rangle}{\langle q^2(x, 0) \rangle} \right| \ll 1, \quad \forall x, q \in \{n, T, \Omega, \phi\}.$$

where also obviously  $\langle q(x, 0) \rangle = \langle q(x, L_y/2) \rangle$ . These two constraints can be expressed as  $L_{y, \text{blob}} \ll \rho_s L_y \ll 30$ cm, which is roughly satisfied by the choice of  $L_y = 100 \approx 7$ cm/ $\rho_s$  used in the simulations. Such post-run checks have not been yet performed but, based on

observations of the resulting turbulence structures (Fig. 5.6), the above criteria appear to be roughly satisfied.

The outer boundary ( $x = L_x$ ) implies reasonable assumptions of zero vorticity,  $E_r = 0$  and thus zero poloidal velocity. No diffusive flux is implied through this boundary, which is a reasonable assumption as far as the simulation domain is large enough for the fields  $T, n$  to be damped strongly before the plasma is advected to this boundary. These radial boundary conditions have been significantly *modified* with respect to the most recent ESEL publication [49], in which the following boundary conditions were assumed:

$$\phi = \Omega = \frac{dn}{dx} = \frac{dT}{dx} = 0 \text{ at } x = 0, \quad \phi = \Omega = n - 1 = T - 1 = 0 \text{ at } x = L_x. \quad (5.21)$$

The new conditions (5.19,5.20) assumed here permit orders of magnitude variation in the  $\langle n(\rho) \rangle$  and  $\langle T(\rho) \rangle$  profiles where previously the variation was at most 40%. The turbulence level,  $\sigma/\mu$  is also much higher with the new boundary conditions and thus correspond more closely to experiment.

The model-experiment comparison also improved with regard to the magnitude of  $v_{\text{pol}} = E_r/B$  in the wall-shadow region as a consequence of modification to the electric potential boundary condition. Eq. (5.21) implies that  $\phi(0) = \phi(L_x)$  and thus that the radial electric field averaged over  $x$  vanishes since

$$0 = \phi(0) - \phi(L_x) = \int_0^{L_x} \frac{d\phi}{dx} dx = - \int_0^{L_x} E_r dx = \langle E_r \rangle_x.$$

Inside separatrix the *tilting instability* generates a poloidal velocity shear (or zonal flow) layer and, as a result  $E_r < 0$  [145]. In the SOL,  $E_r > 0$  for to compensate  $\langle E_r \rangle_x$  to zero, with consequent large poloidal velocity. The new boundaries force  $E_r = v_{\text{pol}} = 0$  at the outer boundary which is demonstrated in Fig. 5.4, where also comparison with  $v_{\text{pol}}$  in TCV is provided; mind that the technique to measure  $v_{\text{pol}}$  in TCV is only approximative.  $v_{\text{pol}}$  strongly affects the fluctuation time-scales obtained by a single-point measurements. In the entire SOL,  $\tau_c$ , estimated from the simulation time series, was dominated by the fast poloidal movement of the structures for the old boundary condition on  $\phi$ . The modified assumption now implicates that it is all the blob lifetime,  $\tau_{\parallel}$ ,  $v_{\text{pol}}$  and the radial advective velocity,  $v_{\text{rad}}$  that all determine  $\tau_c$  in the far SOL. This can be expected also from the analytic relation [78, p.38]

$$\tau_c^{-2} = \tau_{\parallel}^{-2} + \frac{v_{\text{pol}}^2 + v_{\text{rad}}^2}{\lambda^2}.$$

The single point correlation time becomes thus much longer and thus closer to the experimental probe measurements with the modified boundary condition on the space potential.

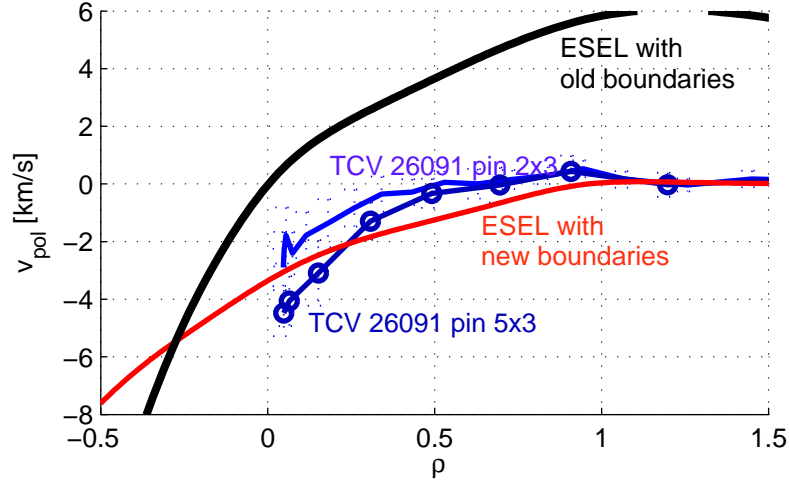


**Fig. 5.4** : Poloidal velocity profile from the ESEL model with old (Eq. (5.21)) and new (Eqs.(5.19,5.20)) outer boundary conditions. The phase velocity from experiment is also shown, using the approximate cross-correlation technique based on [78] on pins [2,3] and [5,3].

## 5.2 Model-experiment comparison

### 5.2.1 Parameter settings

The interchange model described in the previous section is a highly simplified description of the plasma boundary region. A true quantitative agreement between experiment and simulations must therefore be limited. Details of drift wave dynamics, finite Larmor radius effect, divertor geometry, particle sources due to ionization within SOL and impurities are all neglected, as are parallel dynamics (since the model is purely 2D) which are modelled according to a reasonable SOL model [88] (parallel loss times), neglecting the radial variations of  $n$  and  $T$ . Within these constraints, which are a challenge for future code development [144], all model parameters for the code-experiment comparison described here have been set to those corresponding as closely as possible to the situation in the TCV SOL plasma (Eq. (5.13)). The particle density is normalized to  $N_0 = 10^{20}\text{m}^{-3}$ , the temperature is normalized to  $T_0 = 80\text{eV}$ . These values were arbitrarily chosen such that then absolute values at separatrix match those in experiment,  $n_e^{\text{TCV}} = N_0 n^{\text{ESEL}}$ ,  $T_e^{\text{TCV}} = T_0 T^{\text{ESEL}}$ . The model equations (Section 5.1.2) are independent of any such normalization on both density and temperature. The fact, that the experimentally observed turbulence level varies significantly with the line-averaged density, is modelled through the dependence of the diffusion and damping coefficients on  $N_0$  and  $T_0$  (Eq. (5.16)). Note that the values in Eq. (5.13) for the diffusion and damping coefficients have been estimated on the basis of *characteristic* densities and temperatures in the SOL, i.e.  $n_e^{\text{SOL}} \sim 10^{19}\text{m}^{-3}$ ,  $T_e^{\text{SOL}} \sim 20\text{eV}$ . The *Bohm normalization* (Eq. (5.7)) introduces the temporal scale in units of the ion Larmor frequency  $t \rightarrow t\omega_{ci} = eB/m_i = 58.5\text{MHz}$  (for  $B = 1.2\text{T}$ ), whilst the spatial coordinates,  $x = \rho/\rho_s$  and  $y = z/\rho_s$  are in units of the hybrid thermal ion Larmor radius,  $\rho_s = \sqrt{2m_i T_e^{\text{SOL}}/B} = 0.75\text{mm}$ , assuming  $T_e = T_i$ .

For statistical comparison with the data from TCV, a series of time traces from a set of "test probes" are used. At each of these points, the relevant fields are averaged over realistic probe size with dimensions  $\delta x = 3$ ,  $\delta y = 3$ , corresponding roughly to  $2\text{mm} \times 2\text{mm}$  - the approximate dimension of the TCV reciprocating probe pin. As demonstrated by the time traces in Fig. 5.5, however, the effect of choosing a finite "probe size" is found to be insignificant. Over an order of magnitude in assumed probe dimension, the simulated ion saturation current time series, and hence the relative fluctuation level,  $A$  are largely unchanged.

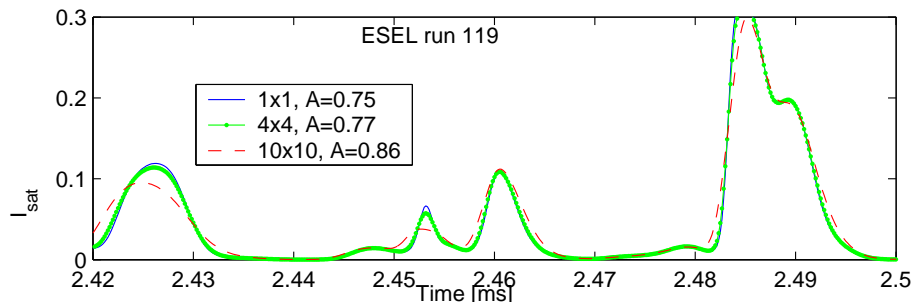


**Fig. 5.5 :** Time traces of simulated ion saturation currents,  $I_s \propto n_e \sqrt{T_e}$ , demonstrating the effect of probe size. The probe is modelled simply by averaging the code output over a square with size  $\delta x = \delta y = [1, 4, 10]$ . Values of the inverted relative fluctuation level,  $A$  are given in each case.

### 5.2.2 Characterization of the 2D time evolution

With the boundary conditions, transport and damping coefficients described above, the numerical simulations saturate into a statistically steady state after  $\sim 100\mu\text{s}$ , with a steep pressure gradient driving turbulence in the edge region [141]. Due to profile relaxations, the edge layer intermittently erupts plasma blobs into the SOL, which may transport deep into the wall shadow [49]. An example of the code output, in the form of time frames of 2D structures, is shown in Fig. 5.6. Associated with the mushroom-like shape of the blob front is a dipolar vorticity field with a large radial velocity component, which is typically a substantial fraction of the acoustic speed [49, 84]. The fast radial advection of blob structures leads to large relative fluctuation levels and contributes significantly to the local time-averaged plasma density profile throughout the SOL.

As reported already in [49], the intensity of the fluctuating motions show irregular oscillations with pronounced bursts. The formation of blob structures takes place during such burst events in the kinetic energy of the fluctuating motions. Whenever this fluctuation level is sufficiently large, there is a rapid growth of the energy in the sheared poloidal flows (Fig. 5.7). This is essentially a demonstration of *zonal flows* generation due to the *tilting instability*, described in Section 2.4. These bursts are followed by a suppressed

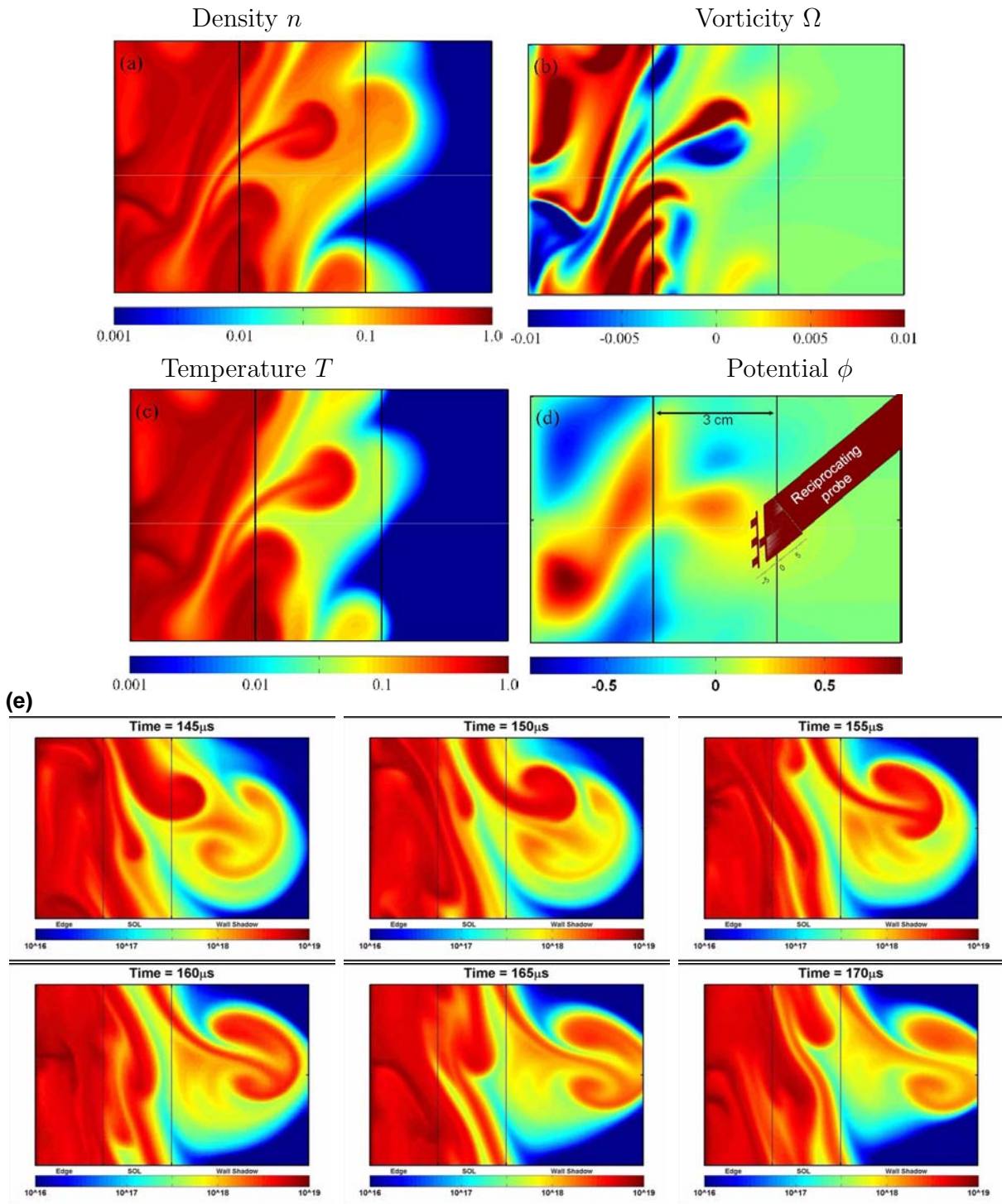


**Fig. 5.6** : Typical outputs  $n, \Omega, T, \phi$  for the fields (a-d) of from the ESEL model (the geometry is described in Fig. 5.3). The Bohm normalization Eq. (5.7) should be used to transform into SI-units real space. The probe head with the poloidal row of three pins is shown schematically for comparison of real sizes. In (e) density perturbation of a propagating plasma blob forming a mushroom-like shape is shown in six time frames separated by  $5\mu\text{s}$ . To see the dynamics, it is strongly suggested to look at the corresponding animations on <http://go.to/horacek/phd>.

level of fluctuating kinetic energy, while the flow energy is slowly damped, resulting in quasiperiodic relaxation oscillations of the latter. Such dynamical regulation is a result of kinetic energy transfer directed from the fluctuating motions to the sheared flows, with viscous damping of the latter on a slow timescale. This is in fact a self-organizing mechanism such that the system may be labelled as a *self-organized criticality* system, as discussed in Section 2.2.2 and reported in [42, 39].

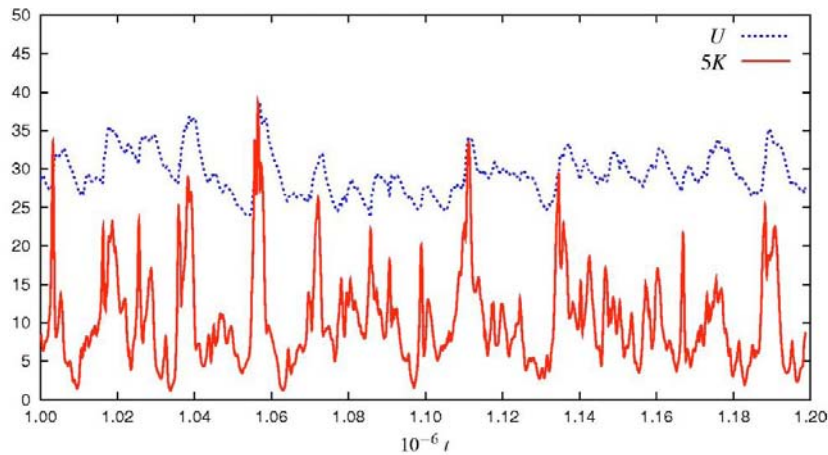


**Fig. 5.7** : Temporal evolution of the kinetic energy transferred between the fluctuating motions,  $K$ , and the sheared poloidal flows,  $U$ . Courtesy of [49].

The following section will demonstrate that the statistical behaviour of density time-series produced by the ESEL simulation adapted for TCV agree both qualitatively and quantitatively with experiment. As a consequence, the turbulent character described above can be considered as a realistic representation of the tokamak SOL turbulence. More importantly, it will also become clear that this interchange model provides excellent agreement with experimental measurements of turbulent *transport* perpendicular to the magnetic field.

Statistical analysis of time-sequences with 5 ms duration is performed in exactly the same way on data from both experiment and code. The main statistical characteristics of three identical TCV discharges #[24529,24530,24532] from both reciprocations (at medium and high density) are compared in the next subsections with the results of a single ESEL run (116) in terms of density, temperature, particle flux, potential spatial dimensions and detail waveforms. Section 4.2 has already provided a detailed experimental description of discharge #24530. The diffusion and damping coefficients (Eq. (5.13)) correspond to the plasma conditions of the 2nd reciprocation (high density) #24529-32. To illustrate variations with  $\bar{n}_e$ , data from the first (medium density) reciprocation will be also shown, even though it is not expected to match the simulation data. At high density, the SOL profiles of  $T_e$  and  $n_e$  are rather flat so that the assumption, in the simulation, of constant coefficients in Eq. (5.13) is less severe than for the medium density case (demonstrated in Fig. 5.1).

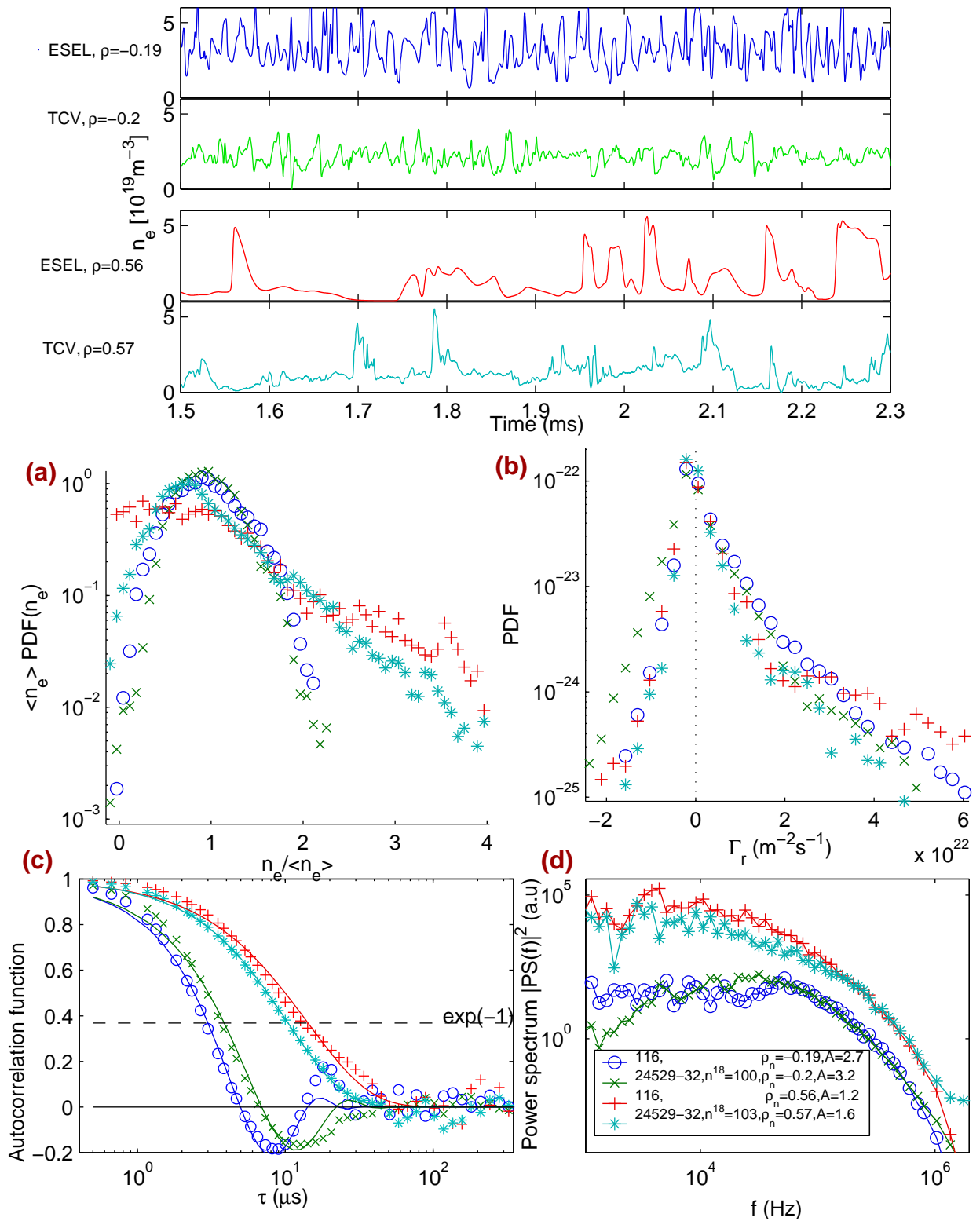


**Fig. 5.8 :** Top: Raw **density** time evolution at two positions: ( $\rho = -0.2$ ) and  $\rho = 0.57$  for ESEL model run 116 and for the TCV 2nd (high density) reciprocation in discharges #24529-32. The corresponding PDFs **(b)**, autocorrelation functions **(c)** and power spectra **(d)**. **Flux** PDF is also shown for comparison in **(b)**.

### 5.2.3 Particle density

Examples of fluctuating density time traces at radial locations inside the separatrix and in the centre of the main SOL are shown at the top of Fig. 5.8 for both TCV and ESEL. The key experimental observation, that the fluctuation level in density increases with  $\rho$  (see Section 4.2 and e.g. [19]), is reproduced by the ESEL time series. Using the statistical analysis techniques described in Section 4.1, reveals that the corresponding PDFs of both model and experiment are Gaussian in the confined region, but skewed in the main SOL (Fig. 5.8 (a)). The autocorrelation function (Fig. 5.8 (c)) is well described by Eq. (4.17) with the three free parameters  $[\tau_c, H, c]$  for both TCV and ESEL data.

The power spectra (Fig. 5.8 (d) in arbitrary units) also show certain similarity, with the caveat that power at the highest frequencies ( $f > 1\text{MHz}$ ) is missing in the ESEL output. This may be explained both by the lack of fine spatial structures in the model due to the unrealistically high particle diffusion coefficient in Eq. (5.13) and limited spatial grid in the simulation. Code runs with higher spatial resolution are not yet finished at time of writing. In addition, in experiment it is likely the electromagnetic noise dominates the signal for  $f > 1\text{MHz}$ .

The density fluctuations statistics, shown in Fig. 5.9 (a,b,d,e), contain several important features. Within the somewhat arbitrary scalar normalization factor  $N_0$ , the radial density profiles from code and experiment are in reasonable agreement. The absolute values of the inverted relative fluctuation level,  $A = \langle n_e \rangle / \sigma_n$  are comparable over the entire radial region over which experimental data exist. The fluctuation level ( $1/A$ ) increases with  $\rho$ , particularly in the wall shadow, where code results are available but in which the experimental signal level is too low for reliable measurements. It should be recalled that it is the radial boundary condition modification, from the original Eq. (5.21) (used in [49, 142]) to those in Eqs.(5.20,5.19), which leads to increased values of  $A$ ,  $\frac{1}{n} \frac{dn}{dr}$  and the fluctuation timescale (Fig. 5.9 (c)) by an order of magnitude and hence favourable in comparison with experiment. Even though the ESEL power spectra do not show a distinct power law  $PS(f) \propto f^{-\beta}$ , it is still possible to assign some value of  $\beta$  which is, again, close to that found from the TCV data. For the sake of academic interest, at the model inner boundary,  $\rho = -1$  (which in principle is not considered physically relevant),  $\beta$  is found to be  $\beta = 1 + 2H \sim 1$ , a manifestation of a totally uncorrelated random noise.

The shape of the density PDF is quantified by the Skewness (S) and Kurtosis (K), allowing straightforward comparison with the known analytical distribution functions (Table 4.1). The experimental observation, presented already in Fig. 4.10, that the TCV data are described by Gamma and Lognormal PDFs is also valid for ESEL. As shown in Fig. 5.10, the model output statistics conform best to the Gamma distribution and indeed approximate it even more closely than in experiment, especially for  $A < 1$ , corresponding to the wall shadow region. Without this Gamma distribution paradigm, the model-experiment match would be less striking because the model tends to have significantly higher turbulence level in the SOL ( $A < 1$ ) than that found in experiment ( $A > 1$ ). Especially, the Gamma distribution, and so thus the PDF shape from ESEL, changes significantly at  $n_e \rightarrow 0$ : for  $A = \mu/\sigma < 1$ , PDF diverges ( $P_\Gamma(0) = \infty$ ) at  $n = 0$ ,

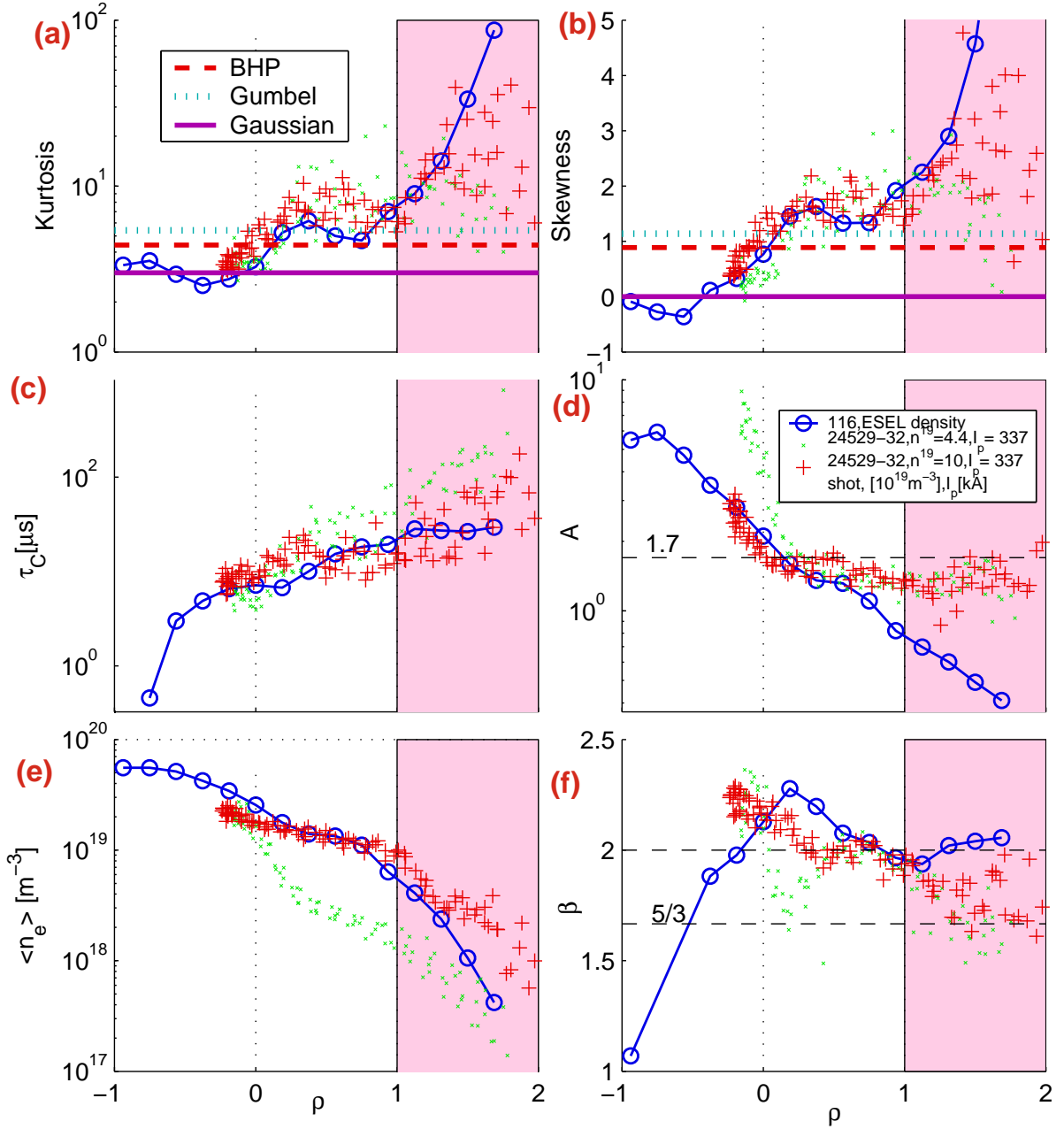


**Fig. 5.9** : Statistics of **density** fluctuation variation with respect to normalized probe position ( $\rho$ ). **(a)** Kurtosis, **(b)** Skewness, **(c)** autocorrelation time, **(d)** inverted relative fluctuation level,  $A$ , **(e)** density profile and **(f)** power-law exponent,  $\beta$ . Data from ESEL model 116 are compared with the TCV discharges #24529-32. Note that magnitude of the ESEL density  $n_e = N_0 n$  is fixed by the arbitrary scalar value of  $N_0$ .

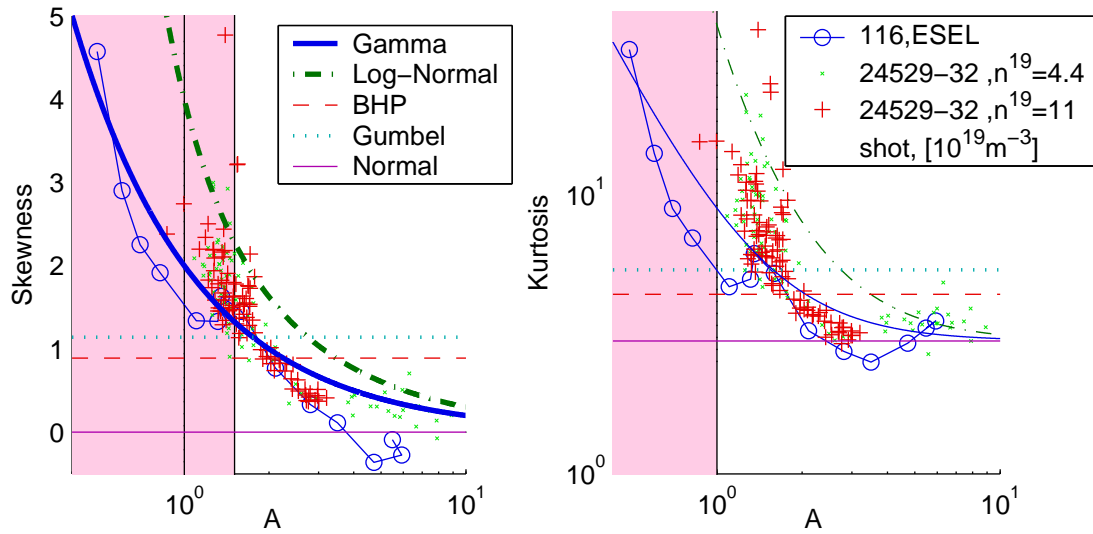


**Fig. 5.10 :** For **density** fluctuations the dependence of (a) Skewness and (b) Kurtosis on the fluctuation level  $A$  demonstrates a good match with Gamma distributed statistics for both the medium and high density ( $\bar{n}_e$ ) reciprocations in discharges #[24529,24530,24532] and with the ESEL model.

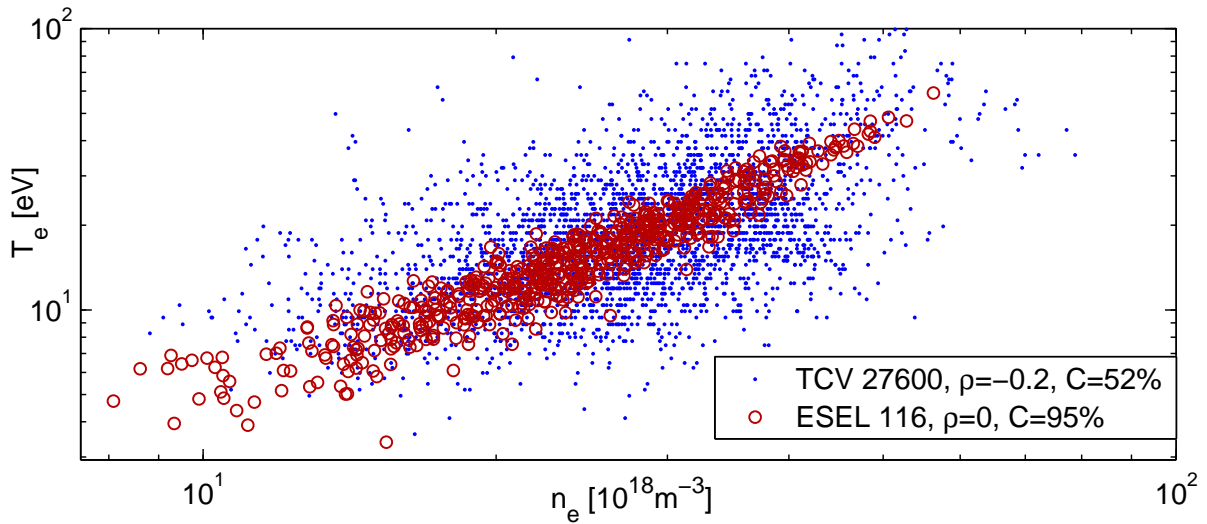


**Fig. 5.11 :** Demonstration of high correlation between  $T_e$  and  $n_e$  fluctuations at a single position measured by the RCP every  $\delta\mu s$ , and obtained from the ESEL model. The TCV measurements were performed in a different discharge than that the ESEL is adapted for and in a slightly different position.

whilst  $P_{\Gamma}(0) = 0$  for  $A > 1$  (see Fig. 4.1 (b)). Therefore, although the model PDFs do not match with the experiment in the wall-shadow region, it is because the value of  $A$  is different, but still both conform well to the Gamma distributed statistics. The disagreement in the value of  $A$  is likely to be caused by the neglect of impurities and neutrals in the ESEL model, as well as the strongly asymmetric connection lengths in this region.

### 5.2.4 Electron temperature

The ESEL model provides also naturally output data for the plasma temperature ( $T$ ) fluctuations. This section should be, however, taken with reserves since the temperature parallel damping of  $T$  is not described in the model as good as the particle density is [88]. In particular it must be assumed that the electron and ion heat channels are strongly coupled due to collisions which is likely true since the collisionality is high (Eq. (5.15)). ESEL as a *fluid* model a priori assumes the velocity distribution function be Maxwellian even though the distribution tail is emptied since the higher energy electrons leave the plasma faster. Modelling particle density is simpler since it does not rely on these assumptions.

Perhaps because the governing model equation Eq. (5.8) for density is so similar to that of temperature Eq. (5.9), the resulting temperature fluctuations are highly correlated to those in the density. This is demonstrated by the ESEL output in Fig. 5.6 (a,c), where the 2D fluctuation pattern is similar for  $T$  and  $n$  and also directly in Fig. 5.11 where, for a given position,  $T$  is highly correlated ( $C > 90\%$ ) with  $n$ . This is a consequence of a high density and temperature blob (since they originate inside the separatrix) propagating across the SOL faster than the timescale for cooling down.

Very fast sweeping of the RCP at 60kHz allows  $T_e$  to be measured on a timescale of  $1/(2 \cdot 60\text{kHz}) = 8\mu\text{s}$ , just sufficient to obtain  $T_e$  during a blob given that the duration of a typical burst is  $5 < \tau_c[\mu\text{s}] < 12$  (shown later in Fig. 5.12 (c)). A correlation is found experimentally between  $n_e$  and  $T_e$ , but the level of correlation is weaker ( $\sim 50\%$ ) than from ESEL, a result that can be likely ascribed to the fact that the probe electronics are far from optimized for fast sweeping, as discussed in Section 3.6.

For TCV shot #24530, similar statistical analysis as for the density is performed for the temperature (Fig. 5.12). The high correlation between  $n$  and  $T$  yields an unsurprising degree of similarity between the density and temperature statistics. On TCV the edge diagnostics (Thomson scattering and RCP) measured  $T_e$  in this particular discharge with sampling rate much slower than the typical blob-timescale. Only the average  $T$ -profiles from ESEL (shown in Fig. 5.12 (a)) can therefore be used for the model-experiment comparison. The ESEL model is independent from the normalization (Eq. (5.7)) by the somewhat arbitrary scalar factor,  $T \rightarrow T \cdot T_0$  and therefore the absolute level is not relevant for the model-experiment comparison, exactly as it is the case for the density. Nevertheless, Fig. 5.12 (a) shows that ESEL SOL  $T$ -profile shape is close to that obtained from both the Thomson scattering and RCP, with the exception of the wall-shadow region where ESEL  $T$  drops to very low values ( $T < 1\text{eV}$ ) due to strong parallel damping (Fig. 5.1 (b)). This strong damping also yields strong fluctuation level, high Skewness,

Kurtosis and  $1/A_T$ , consistent with the picture of a blob carrying high temperature plasma ( $T > 20\text{eV}$ ) propagating fast from inside the separatrix to the wall shadow. There the blob temperature is damped to values  $T < 1\text{eV}$  well before another blob arrives, as demonstrated by the time trace at  $\rho = 1.1$  in Fig. 5.12. The inverse fluctuation level  $A_T \stackrel{\text{def}}{=} \langle T \rangle / \sigma_T$  profile is similar to that of density and also to that shown in Fig. 5.13 obtained in an experiment on TEXTOR using the fast harmonic probe sweeping technique [110].

The temperature damping in ESEL run 116 has been set to  $5\times$  stronger than that for density. This was based on arguments in [88] that the particle energy is strongly damped preferentially at the *tail* of the energy distribution function, because the energetic particles travel faster along the field lines to the material surfaces. The plots in Fig. 5.12 would appear to imply that the chosen value of  $D_T$  is too high to describe the experimental data.

Interestingly,  $S(A_T)$  and  $K(A_T)$  in Fig. 5.12 (e,f) demonstrate that  $PDF(T)$  is, like the density, well described by the Gamma distribution. Since  $A_T$  reaches much lower values compared with  $A$ , this can be confirmed over two orders of magnitude in  $A_T$ . Unfortunately, systematic experimental investigation has not yet been performed.

### 5.2.5 Spatial dimensions of potential

The spatial dimensions of the turbulent structures can be estimated in a crude way by comparing correlations between poloidally or radially separated probe pins. Unfortunately, in all the discharges ever performed on TCV, these pins were always in the floating potential mode and thus similar comparison for the density spatial dimensions is not yet possible. An example for the poloidal correlations in floating (or plasma) potential are shown in Fig. 5.14. Surprisingly, the poloidal correlation between the floating potentials on the TCV probes pins is  $\sim 1/2$ , decreasing to  $\sim 1/3$  at  $\rho = 1$  whilst for ESEL it is nearly unity, whether or not  $T_e$ -fluctuations are included. Throughout the SOL, the ESEL structure size is therefore much larger than that observed in experiment, at least in so far as potential fluctuations are concerned. It should be recalled, however, that this ESEL run 116 uses  $5\times$  higher values of the density diffusion coefficient than estimated with Eq. (5.13) with the aim to significantly shorten the code computational time. It would be expected, however, to yield finer scale structures and thus perhaps explain this size mismatch.

An estimate of the radial correlation length and a full statistical analysis of the potential have not yet been performed. Fig. 5.14 (d) compares the fluctuation level of the floating potential,  $\sigma_{Vf}$  from TCV and ESEL, for the latter with and without including temperature fluctuations. In the separatrix vicinity,  $\sigma_{Vf} \sim 1/2T_0/e = 10\text{V}$  remaining roughly constant in ESEL across the SOL but falling in experiment. Conclusively, the potential structure sizes and fluctuation amplitude differ significantly from the experimental values. This is clearly a weak point of this model-experiment comparison, however, it is actually the only one.

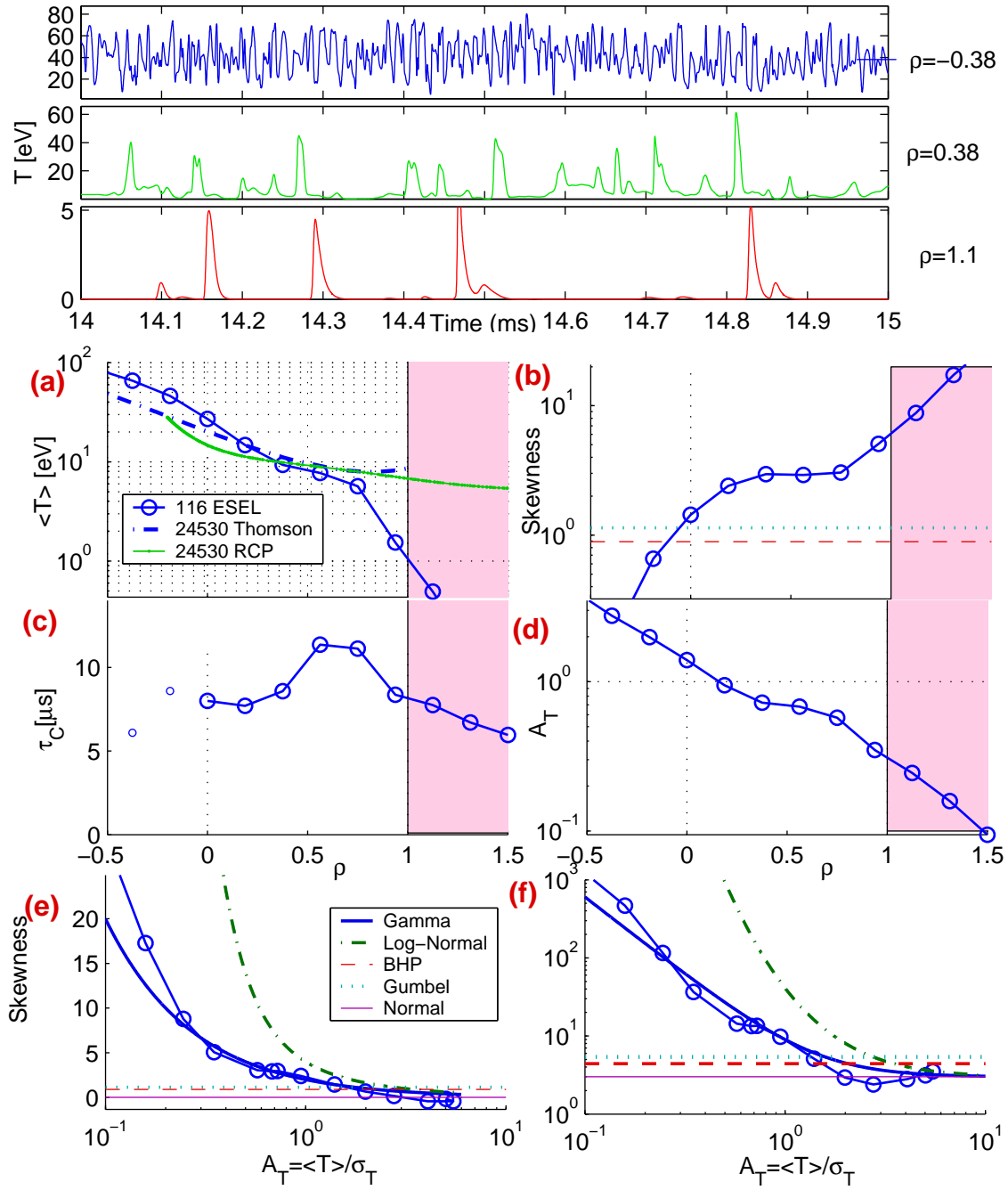


**Fig. 5.12** : Top: **Temperature** fluctuation time series predicted by ESEL (run 116) at three different radial locations. **(a)** Average  $T$  from ESEL in comparison with Thomson scattering and the RCP probe (#24530, 2nd reciprocation), **(b)** Skewness and **(c)** correlation time, **(d)**  $A_T = \langle T \rangle / \sigma_T$ . **(e,f)**  $S(A_T)$  and  $K(A_T)$  demonstrating that  $PDF(T)$  is Gamma distributed. A number of additional analytic PDFs are also given for reference.

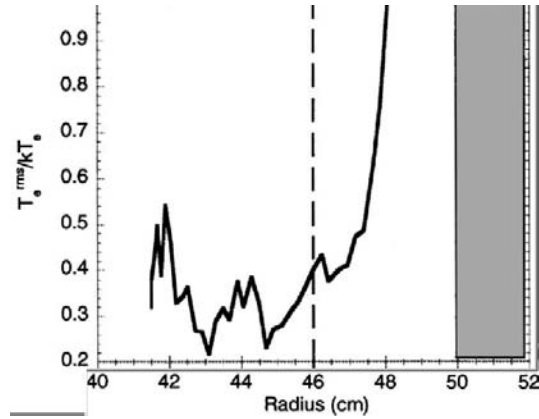


**Fig.** 5.13 : Profile of the **temperature** relative fluctuation level,  $\sigma_T / \langle T \rangle$  measured by fast (200kHz) harmonic probe sweeping technique on TEXTOR [110], to be compared with  $A_T^{-1}$  obtained from the ESEL model (Fig. 5.12 (d)). Even though not shown, the TEXTOR data grows up to  $T_e^{\text{rms}} / kT_e \sim 2.5$  at Radius=50cm.

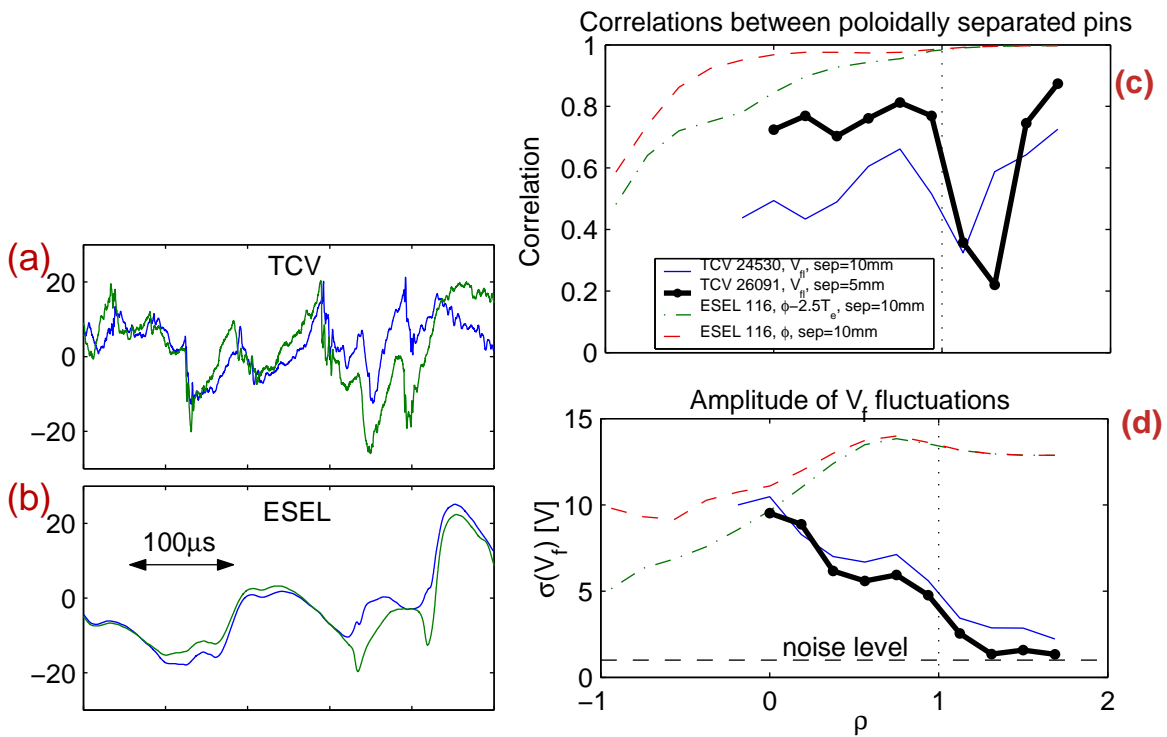


**Fig.** 5.14 : Correlations between pins separated poloidally by  $14\rho_L = 1\text{cm}$  in floating (or plasma) **potential** for both TCV (#24530) and ESEL (run 116). Short time traces of  $V_f$  from the RCP (pins 1 and 4, see Fig. 3.5 ) are shown for (a) TCV and (b) ESEL at  $\rho = 0.93$ , demonstrating that ESEL output has comparatively much higher correlation. In (c) the level of correlation of these two probes is shown across the entire SOL region on TCV and from ESEL, including (x symbols) and not including (+ symbols)  $T_e$ -fluctuations. The standard deviation of the amplitude of potential fluctuations is shown in (d).

### 5.2.6 Radial particle flux

The most important quantity with regard to the influence of turbulent transport is the fluctuation driven radial particle flux Eq. (3.8),  $\Gamma_r = n_e v_r = n_e E_{\text{pol}}/B$ . In contrast to the two-point estimate obtained experimentally through Eq. (3.8), the simulation data result from an exact single-point calculation of  $\Gamma_r$ . The estimated sizes of blob structures are generally reported to be in excess of 1 cm in the main SOL [75, 12, 69]. In fact, when the radial electric drift is estimated in ESEL using the same two-point technique as in the experiment, the results for the main SOL are similar to those obtained from the single-point calculation,

$$\Gamma_r = nB^{-1}E_{\text{pol}} \approx n(x, y, t)B^{-1}(\phi(x, y - 7, t) - \phi(x, y + 7, t))/14 \quad (5.22)$$

where time traces from two points, poloidally separated by  $14\rho_s \approx 1\text{cm}$ , have been used. This result is a consequence of the high correlations found between the potential time traces in Fig. 5.14 (c). In contrast, *in experiment* this correlation is significantly lower. In addition, as discussed in Section 3.9, LaBombard [112] has recently speculated that in the presence of probe acting as a sink for plasma particles, local cross-field transport rates might be expected to increase (and hence the turbulent driven fluxes) in order to compensate. Measured fluxes may thus be higher than would be expected if a non-perturbing technique were used.

To check this, normalized (to standard deviation) experimental and code generated flux PDFs at the wall radius ( $\rho = 1$ ) are compared in Fig. 5.8 (b). In both cases the flux distribution is highly skewed: more events propagate outwards than inwards. Agreement between code and experiment is extremely encouraging.

In the same way as has been performed for  $n$  and  $T$  fluctuations, statistical comparison of ESEL with TCV (#24529-32) is presented in Fig. 5.15. Fig. 5.15 (e) demonstrates that in the main SOL, experimental fluxes compare favourably in both magnitude and radial variation with those. As for both  $n$  and  $T$ , deviations between code and experiment are found inside LCFS and in the wall shadow. Agreement can also be considered excellent for the statistical moments (Fig. 5.15 (a,b,d)) as well as the temporal characteristics (Fig. 5.15 (c,f)). The strongly intermittent nature of the turbulent particle flux is, as expected, manifest in the very large fluctuation levels and high skewness and kurtosis.

### 5.2.7 Absolute magnitude of the flux

It should be emphasized that the particle fluxes from both the experiment and the ESEL simulations have no arbitrary free scaling factor once the density normalization factor  $N_0$  (which determines also the level of the flux) has been fixed by matching the ESEL *density* profile with that from TCV. The fact that  $\langle \Gamma_r \rangle$  from ESEL and TCV are in very good agreement (Fig. 5.15 (e)) is therefore an extremely significant result. The implication is that, at least for the TCV case here, the probe does appear to offer a reliable measure of the turbulent flux and is thus non-perturbing, diminishing the general fears about probes not measuring correctly discussed in Section 5.2.6. This is also interesting in the light of the apparent poor experimental correlations for  $V_{\text{fl}}$  between separated pins.

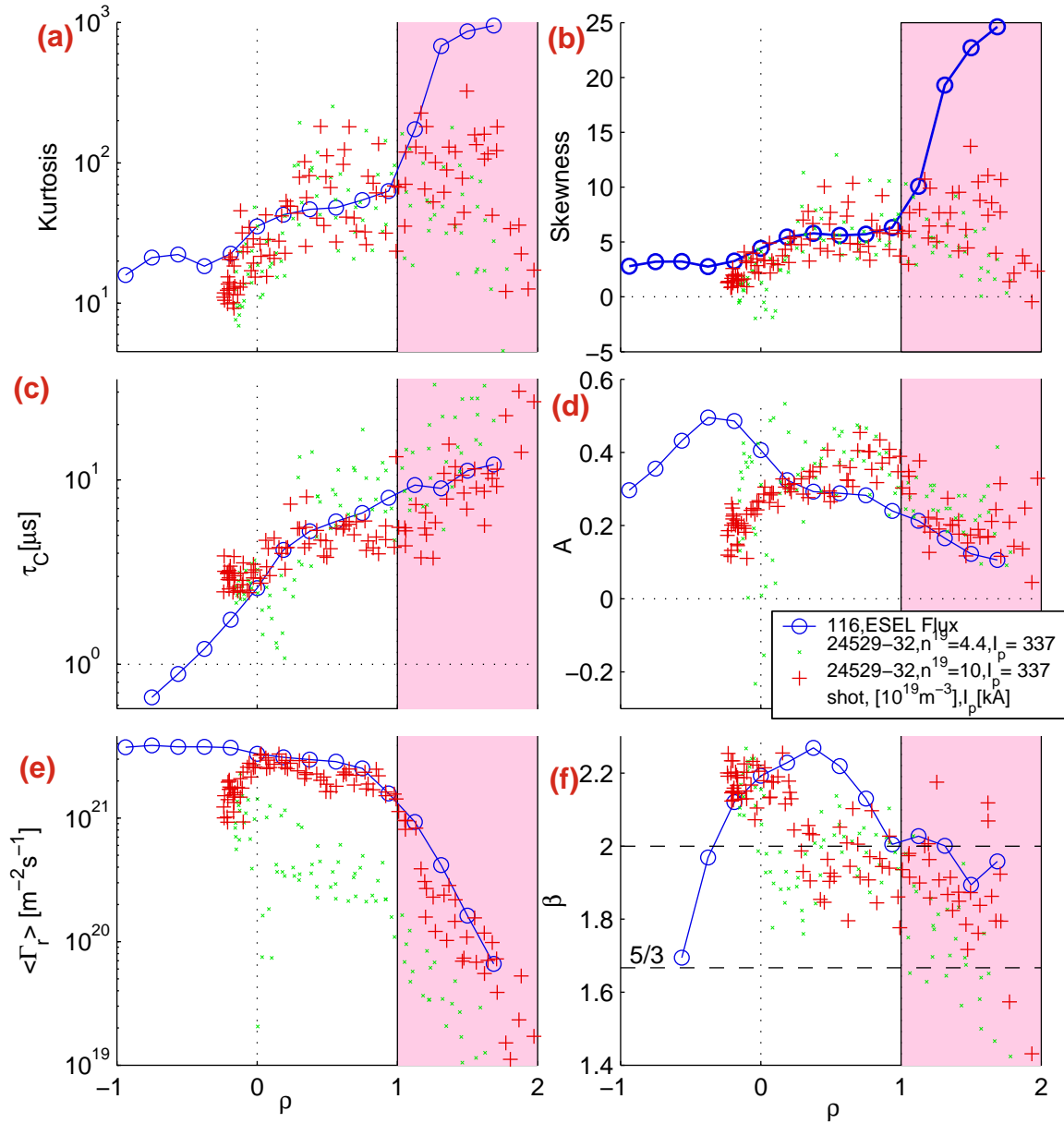


**Fig. 5.15** : Fluctuation driven **radial particle fluxes** obtained from experiment (#24529-32) at  $\bar{n}_e = 10 \times 10^{19} \text{ m}^{-3}$  match well with the ESEL model (run 116) statistical characteristics (as functions of  $\rho$ ) of (a) Kurtosis, (b) Skewness, (d) fluctuation level  $\langle \Gamma_r \rangle / \sigma_{\Gamma_r}$  and (e) mean, together with (c) timescales and (f) spectral power low coefficient  $\beta$ .

Independently of any normalization factor, the flux can be expressed in three ways: through a diffusion coefficient, an effective radial velocity and Mach number, as shown in Fig. 5.16. The TCV high density (#24529-32, 2nd reciprocation) discharges agree well in all these characteristics with the ESEL run 116. Even though the particle transport derived from the ESEL model, as well as likely in experiment, is far being called "diffusive", it is the usual way the transport is discussed in the literature and thus the effective diffusion coefficient is shown in Fig. 5.16 (a).  $D_{\perp}$  rises sharply through the main SOL, similar to what has been found elsewhere (e.g. Fig. 1.6). The values are comparable, even though quite a bit higher, to those obtained from the empirical *Bohm scaling* (Eq. (1.15) [17] in 1949).

The effective radial convective velocity,  $v_r \stackrel{\text{def}}{=} \langle \Gamma_r \rangle / \langle n_e \rangle$ , is shown in Fig. 5.16 (b). These values in far SOL of  $\sim 200\text{ms}^{-1}$  have also been reported also from both Alcator C-mod and DIII-D tokamaks [136]. The effective cross-field Mach number,

$$M_r \stackrel{\text{def}}{=} \frac{\langle \Gamma_r \rangle}{\langle n_e \rangle c_s}, \quad (5.23)$$

shown in Fig. 5.16 (c), characterizes the typical radial propagation velocity, normalized to the local sound speed. Such characterization is worthwhile for model-experiment comparison being a dimensionless quantity independent from both the density and temperature normalization factors,  $N_0, T_0$ . Discussion about how this "average" velocity is linked to velocities of individual blobs continues on page 122.

It is also interesting to observe that the effective velocity of the turbulent structures decreases beyond a certain distance from the separatrix. This might be explained by the following qualitative arguments. The principal driving mechanism for blob radial propagation is that poloidal charge separation within the blob due to  $\nabla B \times \mathbf{B}$  drift leads to a poloidal electric field which, via the  $E_{\text{pol}} \times B_T$  drift, pushes the blob radially outwards (see Section 2.7.1 or [84, 87, 86]). As the blob propagates, its shape evolves into a mushroom-like structure which later splits into two smaller blobs of opposite vorticities (see Fig. 5.6). If the blob vortex turnover time is shorter than the charge separation time inside the blob,  $E_{\text{pol}}$  is damped and consequently the radial propagation mechanism disappears; this suggestion requires, however, further investigation. Additional mechanisms that decelerate the structure radial advection are the non-linear mixing and the parallel particle loss which decreases number of particles inside a blob which, due to Eq. (2.13), slows it down.

### 5.2.8 Conditional averaged waveform

The technique of generating and analyzing the conditional waveform has been described in Section 4.3.6, together with a description of the universal behaviour observed on TCV. As in Section 4.3.6, density is chosen for comparison of the ESEL and experimental waveforms. At the wall radius, the waveform, presented in Fig. 5.17 (d), demonstrates that the turbulence simulations quantitatively reproduce both the experimental mean timescales and the shape of asymmetric bursty events. The latter are characterized by

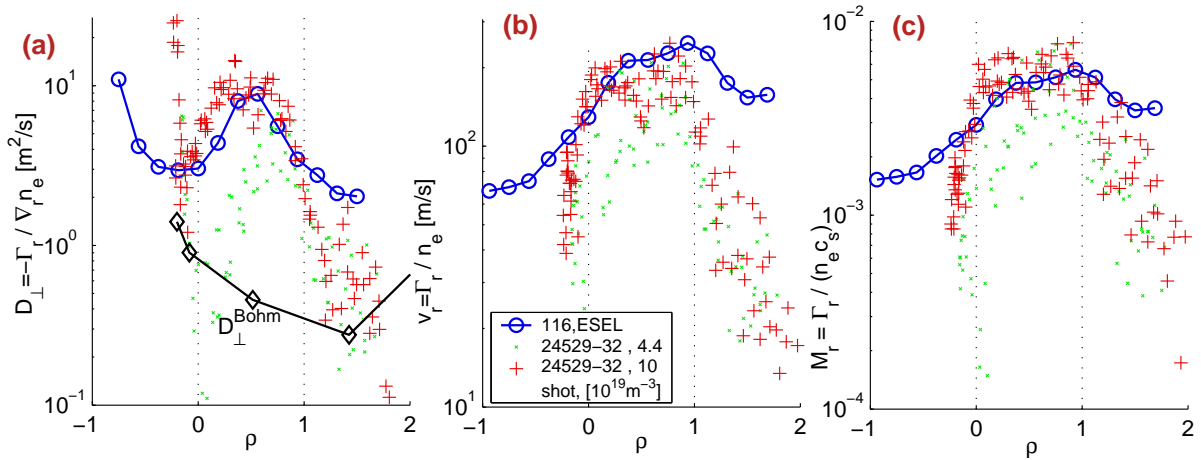


**Fig. 5.16** : Computed values from experiment and ESEL code of **(a)** the effective particle diffusion coefficient, compared with the empirical *Bohm scaling* (Eq. (1.15)) using  $n_e, T_e$  data from the 2nd reciprocation. **(b)** effective radial velocity and **(c)** Mach number.

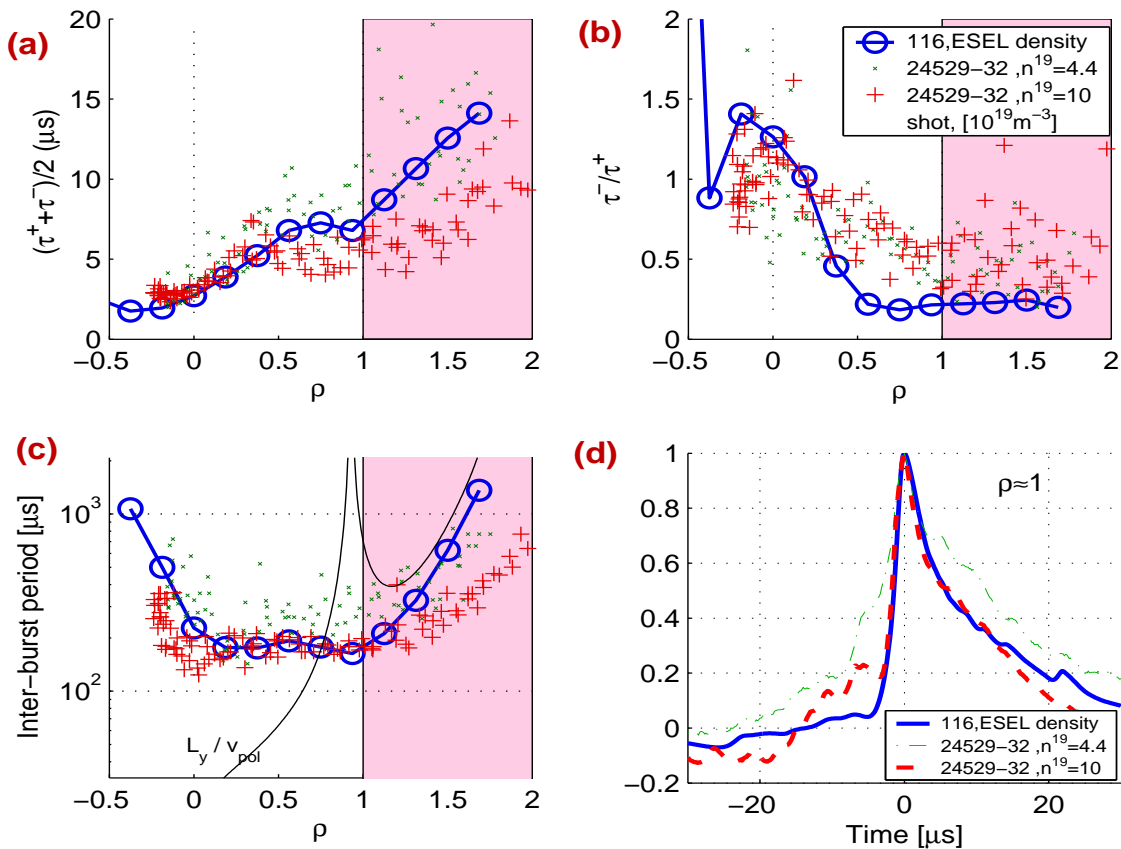


**Fig. 5.17** : Comparison of ESEL (116) and experimental (#24529-32) temporal characteristics by a density conditional waveforms. **(a)** SOL profile of the mean burst timescale. **(b)** time asymmetry evaluated as the ratio of the growth over damping timescales. **(c)** The average inter-burst time period match the high-density TCV with ESEL. In region where it follows the solid line ( $\rho > 1.5$ ), it could be an artifact of the ESEL poloidal boundary periodicity. **(d)** the full conditional waveforms at the wall radius.

a steep front and a *trailing wake* observed in several experiments [75, 12] or manifest as a non-zero skewness of the time derivative [137], and also predicted by a class of blob evolution models [84, 86].

In Fig. 5.17 (a,b) ESEL simulation data for run 116 is compared with experiment in terms of the mean burst timescale and the time asymmetry ( $\tau^-/\tau^+$ ) across the entire SOL. The combination of parallel transport, vorticity generation and mixing gives rise to a deceleration of the radially advected filamentary structures, which in turn yields the radially increasing timescales seen in Fig. 5.17 (a). The burst decay rate is well matched, although the growth rate is systematically higher in the ESEL far SOL. As a consequence, the ratio  $\tau^-/\tau^+$  is lower in the simulation than that found on TCV.

Fig. 5.17 (c) shows the average inter-burst time, defined as the average time period between two successive bursty events. The typical values of  $\sim 200\mu\text{s}$  agrees well with that reported from the MAST tokamak [146]. An excellent match is again found between data from the high-density TCV discharge #24530 and the ESEL run, suggesting that even the *blob formation* mechanism is perhaps correctly modelled in ESEL. Such agreement is indeed a surprise because the left boundary, where these blobs/bursts are formed, is not treated properly: within the model framework there is no drift wave instability nor geodesic acoustic modes that are usually considered as candidates for the blob formation.

Verification has been performed that the inter-burst time is not an artefact of the periodic boundary conditions assumed in ESEL. Although, the blobs do indeed travel repeatedly in the poloidal direction throughout the computational space, the inter-burst time is unaffected since during this poloidal turn-over time the blob usually escapes radially. This is demonstrated in Fig. 5.17 (c) by the solid line corresponding to  $t_{period} = L_y/v_{pol}$ , where  $L_y = 100\rho_s \sim 7\text{cm}$  and  $v_{pol}$  is a result from the ESEL simulation. If the ESEL inter-burst time were dominated by the unphysical poloidal boundary, it would follow the solid line  $t_{period}$ , which is not the case, apart perhaps in the deep wall shadow.

Blob radial velocities are not measured in TCV but velocities of the order of  $v_r^{blob} \sim 1\text{kms}^{-1}$  have been observed in both experiment [68, 69] (see Section 2.6) and the ESEL model (Fig. 5.6 (e)). The typical radial velocity of an individual blob is, however, significantly larger than the "average" velocity,  $\Gamma_r/\langle n_e \rangle \sim 200\text{ m/s}$  observed in Fig. 5.16 (b), which is expected because the blobs are very rare in both space and time. The blobs occur at a single point (Langmuir probe) typically at only  $\frac{\tau^- + \tau^+}{\text{inter-burst time}} = 6\%$  of the time, computed from ratio of the burst time over the inter-burst time Fig. 5.17 (a,c). They carry, by definition (Fig. 4.18 (a)), at least  $\mu + 2.5\sigma = (1 + 2.5A^{-1})\mu = 2.5\times$  the average density (for  $A \approx 1.7$  at  $\rho = 1$ ), which in total yields

$$\frac{2.5 \cdot 6\% \cdot 1\text{kms}^{-1}}{\Gamma_r/\langle n_e \rangle} = \frac{150\text{ms}^{-1}}{200\text{ ms}^{-1}} = 75\%, \quad (5.24)$$

interpreted such that the big blobs, occurring at only 6% of the time, do carry 75% of the entire radial particle flux, and the rest is carried by smaller blobs occurring more often. Similar values are reported e.g. in [76].

# Chapter 6

## Parallel SOL flows

In a slight departure from the main theme of this thesis work, some effort has been devoted to an investigation of the link between SOL turbulence and the ubiquitous flows seen in the tokamak SOL. This is a result of the recent upsurge of interest in these flows, particularly parallel flows, which are often seen to be anomalously high, and for which explanations in terms of accepted drift physics are not always successful. The same Mach probe measurements can also be combined with simultaneous data for the cross-field turbulent flux to study the relationship, if any, between anomalous radial transport and parallel flow generation. The parallel flow measurements presented here constitute the first of their kind ever performed on TCV. They will be presented in a paper [147] to the 17<sup>th</sup> International conference on Plasma-Surface Interactions in Controlled Fusion Devices to be held in Hefei, China, May 2006. Much of the flow data shown in this chapter has been recently presented to the SOL and Divertor ITPA expert group as [148].

### 6.1 Introduction

Understanding SOL plasma flows is a critical issue for next step tokamak devices like ITER. It is thought that the strong parallel flows which are observed in all tokamak SOLs [149, 150, 151] provide one mechanism for impurity migration [105]. Impurities released from the first wall and divertor targets can be convected by these global flows to regions far from the point of release, leading to accumulation of material which is projected to be in the range of tons per year for ITER [105]. Such migration is of no serious operational consequence for present-day tokamaks however. Despite the perceived importance of SOL flows, they are far from being completely understood at the time of writing.

Parallel SOL flow is generated as a result of poloidal asymmetries in the toroidal magnetic field, radial and parallel pressure gradients, poloidal and radial electric fields [152], ballooning like diffusive particle transport [149, 153] and even perhaps the perturbing effect of the probes which are invariantly used to measure it [150] due to radiation from released impurities. In the ideal, or simple SOL (i.e. without ionization [8]), much of the edge plasma is stagnant, with strong flow up to  $M_{\parallel} = 1$  (Fig. 1.3 ) developing

only as solid targets, limiters or divertors, are approached. In reality, particle drifts ( $\mathbf{E} \times \mathbf{B}$ ,  $\nabla p \times \mathbf{B}$ ,  $\nabla B \times \mathbf{B}$ ) lead to strong poloidal fluxes which must be compensated by return parallel flows, as depicted in Fig. 6.1. In the classical picture only these drifts are present and can be described by known analytical relations [154]. They lead, for example, to Pfirsch-Schlüter parallel flows which will be discussed in more detail in Section 6.3. The situation is, however, more complex in reality: the large fluid Monte Carlo coupled edge code packages such as B2.5-Eirene [155] and EDGE2D-Nimbus [153] contain all the physics in the fluid equations but fail systematically to reproduce the strong flows measured experimentally in most tokamak SOLs. Although they can qualitatively reproduce the observed poloidal flow pattern, the predicted magnitude is apparently too low to produce any significant migration [156, 150, 152]. On the other hand, the simple analytical expression given in Section 6.3 (Eq. (6.2)) for the Pfirsch-Schlüter flow is found to be consistent with data from Mach probe measurements on JT-60U [157] and also with TCV, as will be demonstrated in Section 6.3. On Alcator C-Mod strong flows have recently been observed on the inboard midplane and are seen to remain unchanged upon field reversal [149]. This is inconsistent with the Pfirsch-Schlüter flow and implies that some physics is missing. Interest has been focussing of late on the possible contribution of strong outboard, ballooning-like transport as a mechanism for driving parallel flow [149, 153]. The excess particle flux entering the SOL in this way would create local pressure increases which would be relieved by parallel flow along SOL flux tubes to limiter or target plates. Some evidence for this phenomena has been seen in the TCV experiments discussed later. A simple estimation of this ballooning component on the basis of the level of pressure fluctuations has been derived in Ref. [88] as

$$\langle M_{\parallel}^{\text{turbulence}} \rangle \approx \langle M_{\parallel} \rangle \frac{t(p > 2\langle p \rangle)}{\Delta t} \quad (6.1)$$

corresponding to a time-fraction during which the local pressure significantly exceeds the average value, and  $\langle M_{\parallel} \rangle$  is Mach number of the non-turbulent flow. Typically the values obtained are of the order of  $M_{\parallel}^{\text{turbulence}} \leq 0.1$ , comparable to that obtained in experiment, see later Fig. 6.4 (b).

The possible coupling of cross-field turbulent particle transport to parallel flows has also recently been suggested and evidence presented from JET [44]. The proposed mechanism is momentum coupling by Reynolds stress, but results presented here in Section 6.4 from TCV do not support these JET findings.

## 6.2 Experiment in forward and reversed magnetic field

The bulk of the parallel flow measurements in TCV have been performed in the standard SNL configuration which has been extensively employed for the turbulence analysis presented in Chapter 4. A sizeable database has been accumulated, almost exclusively in ohmic, L-mode plasmas but containing carefully matched forward and reversed toroidal

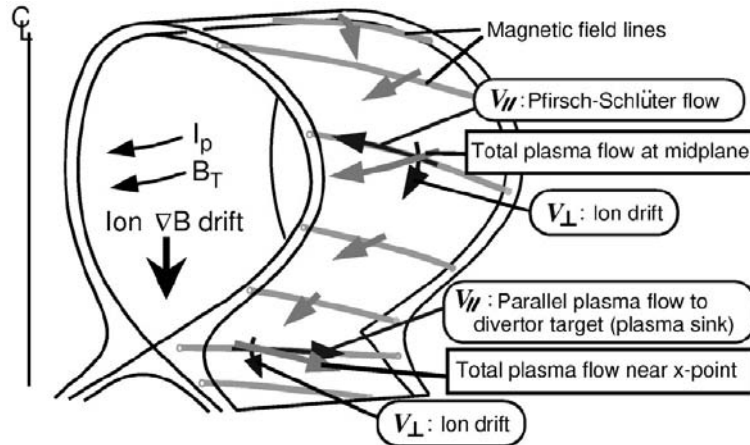


**Fig. 6.1** : Schematic view of the poloidal ion drift and Pfirsch-Schlüter flow at the midplane SOL and near the X-point as measured in JT-60U (flow driven by parallel pressure gradient) for the case  $B_T < 0$ . For  $B_T > 0$  (the usual field direction in TCV), all drift driven parallel flows reverse (divertor sink flow remains unchanged). Total plasma flow pattern is illustrated by grey arrows; long arrows indicate large velocity of the flow or drift. Extracted from [157].

field discharges in which the direction of  $I_p$  is also reversed to preserve the direction of magnetic helicity.

The large number of often similar shots means that an efficient method of presenting the data which combines clarity and good statistics has been sought. Similar discharges, characterized by similar values of  $I_p$ ,  $\bar{n}_e$ , toroidal field direction, magnetic configuration and gas fuelling type, have been combined into *discharge groups*, denoted  $G\#$  in the figures shown here and listed on page 126. The normalized, midplane mapped radial coordinate is used here, as in earlier chapters, with  $\rho = 0$  at separatrix and  $\rho = 1$  at the wall contact point at the plasma midplane (see Fig. 3.1 (b)). The probe reciprocation is typically divided into  $5ms$  time intervals that correspond, given the probe reciprocation velocity, to normalized radial bands of width of  $|\delta\rho| \leq 0.2$ . The measured Mach flow and other radial profile quantities (e.g.  $T_e$ ,  $V_{fl}$ , etc.) are averaged across each narrow strip. The results from each strip for similar discharges are then combined to produce a single value associated with a statistical error from the averaging process. The level of fluctuations around an averaged point,  $\langle M_{||} \rangle$ , are usually not shown for clarity, but lie in the range  $0.1 < M_{||} < 0.2$ , as demonstrated in Fig. 6.2. Profiles of  $\langle M_{||} \rangle$  are extremely reproducible from shot to shot with an error of  $\sim 0.02$ . Flow directions are defined according to the convention in [152, 150] which defines negative flow ( $M_{||} < 0$ ) in the clockwise poloidal direction, i.e. *downwards* at the probe position, corresponding to the direction from inner to outer targets in SNL plasmas. Flows are measured, using Eq. (3.14), from current ratios on pins 2 and 5 on the Mach probe head (see Fig. 3.5 (c,d)).

An example, for  $B_T > 0$  (for the B-field convention see Section 3.2.1) is shown in Fig. 6.3. This field direction, which places the ion  $\nabla B \times \mathbf{B}$  drift away from the lower

Group	discharges	Description
G01	26082 26084 26085 26086	$D, I_p = 337kA, n_e^{18} = 48.1m^{-3}, \kappa = 1.57, \delta = 0.353$
G02	26058 26059 26060 26061 26062 26063 26064 26065 26066	$D, I_p = 336kA, n_e^{18} = 65m^{-3}, \kappa = 1.57, \delta = 0.359$
G03	26054 26055 26056	$D, I_p = 336kA, n_e^{18} = 72.6m^{-3}, \kappa = 1.56, \delta = 0.36$
G04	26092 26093 26094	$D, I_p = 337kA, n_e^{18} = 84.2m^{-3}, \kappa = 1.54, \delta = 0.357$
G05	26091 26096 26097	$D, I_p = 335kA, n_e^{18} = 90.9m^{-3}, \kappa = 1.52, \delta = 0.35$
G06	26386 26387 26388 26389 26390 26391 26392 26393	$D, ELMs, z = 22cm, I_p = 418kA, n_e^{18} = 66m^{-3}, \kappa = 1.65, \delta = 0.425$
G07	26212 26213 26214	$He, I_p = 339kA, n_e^{18} = 32.3m^{-3}, \kappa = 1.56, \delta = 0.352$
G08	26207 26209 26210 26211	$He, I_p = 337kA, n_e^{18} = 64.9m^{-3}, \kappa = 1.56, \delta = 0.361$
G09	26206 26226	$He, I_p = 337kA, n_e^{18} = 76.6m^{-3}, \kappa = 1.56, \delta = 0.362$
G10	26216 26217 26218	$He, I_p = 338kA, n_e^{18} = 86.5m^{-3}, \kappa = 1.56, \delta = 0.369$
G11	26215	$He, I_p = 338kA, n_e^{18} = 98.5m^{-3}, \kappa = 1.55, \delta = 0.369$
G12	26221 26222 26223	$He, I_p = 336kA, n_e^{18} = 118m^{-3}, \kappa = 1.52, \delta = 0.364$
G13	26792 26794 26795 26796 26797 26799 26800	$D, I_p = -269kA, n_e^{18} = 42.2m^{-3}, \kappa = 1.6, \delta = 0.302, B < 0$
G14	26812 26813 26814	$D, I_p = -269kA, n_e^{18} = 72.6m^{-3}, \kappa = 1.55, \delta = 0.295, B < 0$
G15	26826 26827 26828	$D, I_p = -270kA, n_e^{18} = 25.5m^{-3}, \kappa = 1.61, \delta = 0.291, B < 0$
G16	26868 26869 26870	$D, I_p = -270kA, n_e^{18} = 16.7m^{-3}, \kappa = 1.61, \delta = 0.288$
G17	26875 26876	$D, I_p = -270kA, n_e^{18} = 61.8m^{-3}, \kappa = 1.58, \delta = 0.305, B < 0$
G18	26882	$D, I_p = -269kA, n_e^{18} = 42.3m^{-3}, \kappa = 1.64, \delta = 0.336, B < 0, SNU$
G19	26951 26952 26953 28215 28216 28217	$D, I_p = 258kA, n_e^{18} = 41.5m^{-3}, \kappa = 1.57, \delta = 0.337$
G20	26954 26955	$D, I_p = 258kA, n_e^{18} = 19.6m^{-3}, \kappa = 1.58, \delta = 0.327, FSsw$
G21	26957	$D, I_p = 258kA, n_e^{18} = 16.9m^{-3}, \kappa = 1.57, \delta = 0.322$
G22	26958 26960 26961	$D, I_p = 259kA, n_e^{18} = 74m^{-3}, \kappa = 1.49, \delta = 0.328, Bursts$
G23	26964 26965	$D, I_p = 258kA, n_e^{18} = 62.9m^{-3}, \kappa = 1.5, \delta = 0.327, Bursts$
G24	26967 26974	$D, I_p = 258kA, n_e^{18} = 25.3m^{-3}, \kappa = 1.58, \delta = 0.331$
G25	26977 26978 26979 26980	$D, I_p = 340kA, n_e^{18} = 31.4m^{-3}, \kappa = 1.57, \delta = 0.356$
G26	26983	$D, I_p = 258kA, n_e^{18} = 38.9m^{-3}, \kappa = 1.61, \delta = 0.334, SNU$
G27	26984	$D, I_p = 259kA, n_e^{18} = 24.9m^{-3}, \kappa = 1.62, \delta = 0.328, SNU$
G28	27002 27003 27004 27005 27006 27007 27008 27009 27012 27014 27015 27016 27017	$D, ELMs, I_p = 424kA, n_e^{18} = 64.2m^{-3}, \kappa = 1.65, \delta = 0.433$
G29	27466 27582	$D, z = 0cm, I_p = 260kA, n_e^{18} = 42.7m^{-3}, \kappa = 1.51, \delta = 0.339, FSsw$
G30	27469 27470	$D, z = 0cm, I_p = 259kA, n_e^{18} = 30m^{-3}, \kappa = 1.52, \delta = 0.336$
G31	27471	$D, z = 0cm, I_p = 261kA, n_e^{18} = 66.7m^{-3}, \kappa = 1.44, \delta = 0.316$
G32	27583 27585 27586	$D, z = 10cm, I_p = 260kA, n_e^{18} = 41.5m^{-3}, \kappa = 1.51, \delta = 0.321$
G33	27587 27588	$D, z = -8cm, I_p = 260kA, n_e^{18} = 41.4m^{-3}, \kappa = 1.51, \delta = 0.331$
G34	27590 27591 27592	$D, z = 0cm, I_p = 256kA, n_e^{18} = 66.6m^{-3}, \kappa = 1.46, \delta = 0.282, SNU$
G35	27589 27593	$D, z = 1cm, I_p = 257kA, n_e^{18} = 40.7m^{-3}, \kappa = 1.54, \delta = 0.302, SNU$
G36	27597	$D, z = 1cm, I_p = 340kA, n_e^{18} = 41.6m^{-3}, \kappa = 1.56, \delta = 0.368$
G37	27461 27462 27463 27464	$D, z = 0cm, I_p = 260kA, n_e^{18} = 48.2m^{-3}, \kappa = 1.5, \delta = 0.337$
G38	28218	$D, I_p = 217kA, n_e^{18} = 40.4m^{-3}, \kappa = 1.56, \delta = 0.316$
G39	28219	$D, I_p = 175kA, n_e^{18} = 43.4m^{-3}, \kappa = 1.54, \delta = 0.293$
G40	28220 28221	$D, I_p = 299kA, n_e^{18} = 42.6m^{-3}, \kappa = 1.59, \delta = 0.35$
G41	28222	$D, I_p = 340kA, n_e^{18} = 44.5m^{-3}, \kappa = 1.6, \delta = 0.364$
G42	28223	$D, I_p = 381kA, n_e^{18} = 44.7m^{-3}, \kappa = 1.61, \delta = 0.372$
G43	28224 28225 28226	$D, z = 26cm, I_p = 258kA, n_e^{18} = 47.6m^{-3}, \kappa = 1.44, \delta = 0.339, limiter$
G44	28227	$D, z = 26cm, I_p = 258kA, n_e^{18} = 63m^{-3}, \kappa = 1.4, \delta = 0.299, limiter$
G45	28228	$D, z = 26cm, I_p = 259kA, n_e^{18} = 32.2m^{-3}, \kappa = 1.44, \delta = 0.31, limiter$
G46	28229	$D, z = 26cm, I_p = 257kA, n_e^{18} = 38.3m^{-3}, \kappa = 1.68, \delta = 0.309$
G47	28230 28232	$D, z = 26cm, I_p = 257kA, n_e^{18} = 42.6m^{-3}, \kappa = 1.55, \delta = 0.453$
G48	28235	$D, z = 26cm, I_p = 256kA, n_e^{18} = 69.6m^{-3}, \kappa = 1.45, \delta = 0.411$
G49	29192 29194 29196 29198	$D, I_p = 316kA, n_e^{18} = 61.1m^{-3}, \kappa = 1.56, \delta = 0.336$
G50	29202 29203 29204 29205 29206 29207 29208 29209 29210 29212 29213 29214	$D, I_p = 318kA, n_e^{18} = 62.5m^{-3}, \kappa = 1.59, \delta = 0.314$
G51	30321 30322 30331	$He, I_p = 340kA, n_e^{18} = 36m^{-3}, \kappa = 1.54, \delta = 0.313, NoVf1$

Table 6.1: List of Mach probe *Groups of shots*, grouped on the basis on main plasma parameters, with possibly variable probe setting. Assuming both reciprocations are identical, density ramp shots are excluded. The group description contains gas, ELMs (if not L-mode),  $z$  (if not  $z \sim 23cm$ ), plasma current  $I_p$ , line-average density [ $10^{18}m^{-3}$ ], triangularity  $\delta$  and elongation  $\kappa$  (defined in Fig. 4.6 (b)), magnetic field direction (if not  $B_T > 0$ ) and magnetic configuration (if not SNL, Fig. 4.4 ).

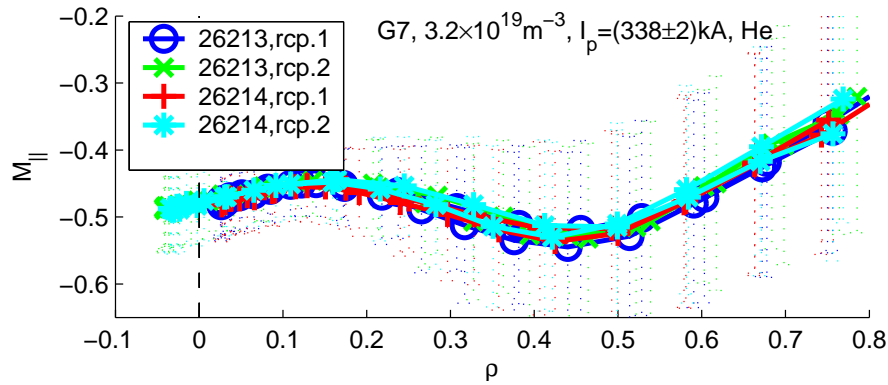


**Fig. 6.2 :** Demonstration of good reproducibility of average value  $\langle M_{\parallel} \rangle$  and fluctuation level  $\sigma(M_{\parallel})$  in two identical discharges and four reciprocations.

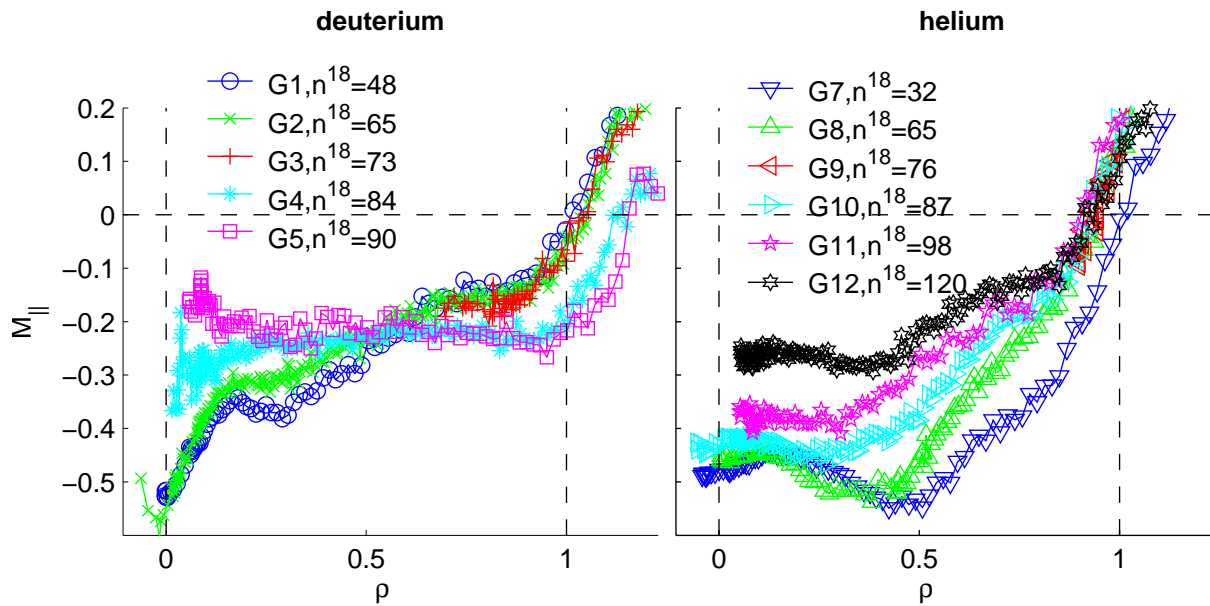


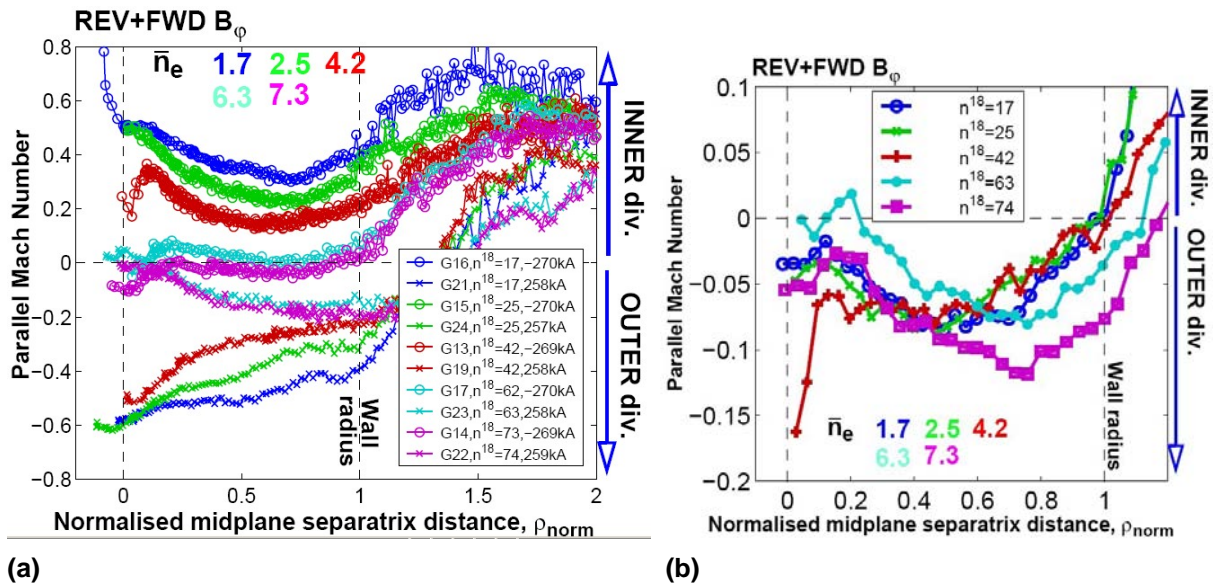
**Fig. 6.3 :** Midplane mapped, averaged SOL radial profiles of  $M_{\parallel}$  for various densities from shot groups G# in deuterium (left) and helium (right) plasmas for positive toroidal field direction (ion  $\nabla B \times \mathbf{B}$  drift upwards), ohmic discharges at  $I_p = 340$  kA. The normalized radial coordinate is the same as that used throughout this thesis (see Fig. 3.1 (b)). Negative flow corresponds to the direction from inner to outer divertor target, i.e. downwards at the outside midplane. The line averaged density (in units of  $10^{18} m^{-3}$ ) for each discharge is given in the legend. Shot groups G5 and G12 are at densities very close to the density limits in these plasmas.

X-point, is the standard configuration for TCV and is generally used to avoid transition to ohmic H-mode at reasonable  $I_p$  values. Fig. 6.3 demonstrates that strong inner to outer divertor parallel flow is seen below the outside midplane in matched deuterium (D) and helium (He) plasmas across much of the SOL and at various densities. Profile shapes differ between He and D plasmas but are of similar magnitude. The origin of these differences is unknown, but may be related to the strong differences in neutral recycling between He and D. Flows are highest at lowest densities (this is expected on the basis of simple arguments for the magnitude of drift effects [152,154]) with the profiles tending to flatten at the highest plasma densities. For  $\rho > 1$  (i.e. in the wall shadow), the abrupt change of flow direction may be attributed to the strong wall sink in a region of short connection length and low ionization. The differences between He and D in this region point further towards very different behaviour of neutral dynamics since the discharges are otherwise extremely similar.

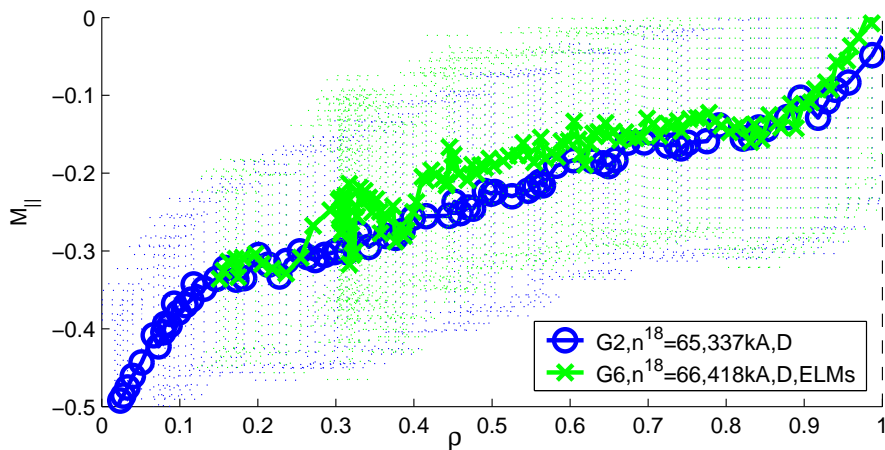
### 6.2.1 Influence of ballooning and wall sink

Fig. 6.4 compiles profiles of  $M_{\parallel}$  for deuterium plasmas with  $I_p = 260$  kA in closely matched discharges with forward and reversed  $B_T$ . Since all classical drift terms reverse with the direction of  $B_T$ , such comparisons allow to separate contributions of drift effects to the total parallel flow. That this is indeed the case is clearly shown in Fig. 6.4 (a) where parallel flows are seen to reverse direction (i.e. in the direction from outer to inner divertor) with  $B_T$  reversal. In TCV, the flow direction in the outboard SOL for  $B_T < 0$  is as observed elsewhere [JET, JT-60U, C-Mod] in ohmic and L-mode discharges. For any given density, both the flow profile and absolute magnitude are similar for each field direction, with a possible slight negative offset in favour of flow towards the outer target. This is shown in more detail in Fig. 6.4 (b) where the  $M_{\parallel}$ -profiles for forward and reversed field have been averaged in simple attempt to isolate any field-independent offset. The offset appears to be approximately density independent, though with some radial structure. Since the probe is localized below the midplane, any ballooning component to the radial transport (which is expected to be maximized on the outside midplane), together with a possible contribution from the divertor sink action would slightly strengthen parallel flows to the outer target and thus reinforce the flow measured by the probe for reversed  $B_T$ . Unfortunately, the magnitude of the offset can be to some extent explained by the divertor sink action. In this rather unconventional TCV SNL geometry, relatively strong parallel  $T_i$  gradients are predicted (though have not been measured) to occur in the main SOL using SOLP5 simulations [14] even at relatively low density. Such gradients drive parallel flows which are in the range  $0.05 < M_{\parallel} < 0.1$  and are thus able to explain a good fraction of the offset observed in Fig. 6.4. The plasma height scan described below does, however, provide further evidence for a "ballooning" component to the parallel flow.

The influence of H-mode conditions on the  $M_{\parallel}$ -profile and magnitude is illustrated in Fig. 6.5. Compared with an L-mode reference (group G2), the H-mode equivalent (Type III ELMing plasma) shows virtually no difference for the same magnetic equilibrium but at higher current (420 kA cf. 340 kA). Similar findings have been reported from JET for



**Fig. 6.4 :** (a) Density scan for  $B_T > 0$  discharges carefully matched with  $B_T < 0$  showing that flow reverses direction with toroidal magnetic field direction as would be expected on the basis of the Pfirsch-Schlüter flow. (b) The average of the flows for the two field directions ( $(M_{\parallel}^{B_T < 0} + M_{\parallel}^{B_T > 0})/2$ ) at each density shows a small  $B_T$ -independent offset consistent with a contribution from the outer target divertor sink and/or a component due to excess outboard radial transport. The fixed location of the probe below the outboard midplane makes it impossible to decouple these two contributions.



**Fig. 6.5 :** L/H-mode comparison of  $M_{\parallel}$ -profile from discharges with closely matched density reveals negligible difference, certainly within the fluctuation level,  $\sigma_M$  shown by the error bars. The H-mode points (Group G6) are taken from a Type III ELMing ohmic H-mode at  $I_p = 420$  kA. Both discharges have  $B_T > 0$ .

Type I ELMing H-mode [150].

To investigate any poloidal variation of  $M_{\parallel}$ , several identical discharges have been performed with varying plasma height, with the magnetic axis position ( $z$ ) being varied from  $z = -10\text{cm}$  to  $z = +10\text{cm}$ . Fig. 6.6 shows that the height of the magnetic axis can be easily varied in TCV, allowing the probe position, which is fixed at  $z = 0$ , to be shifted relative to the plasma centre. The difference in the flow profiles for these three probe positions relative to the magnetic axis supports a small contribution of the order of  $M_{\parallel} \sim 0.05$  from excess, ballooning-like radial transport if the effect of the divertor sink can be assumed to remain unchanged, at least for the probe positions at or below the midplane. For the probe above the midplane, the outboard divertor sink action must be essentially absent. No estimate (from SOLPS5 simulations) of the strength of any sink action is available. Fig. 6.6 also shows how the three discharges have closely matched edge profiles, demonstrating that any differences due to Pfirsch-Schlüter flow should be attributable only to variations in poloidal angle (see Eq. (6.2)).

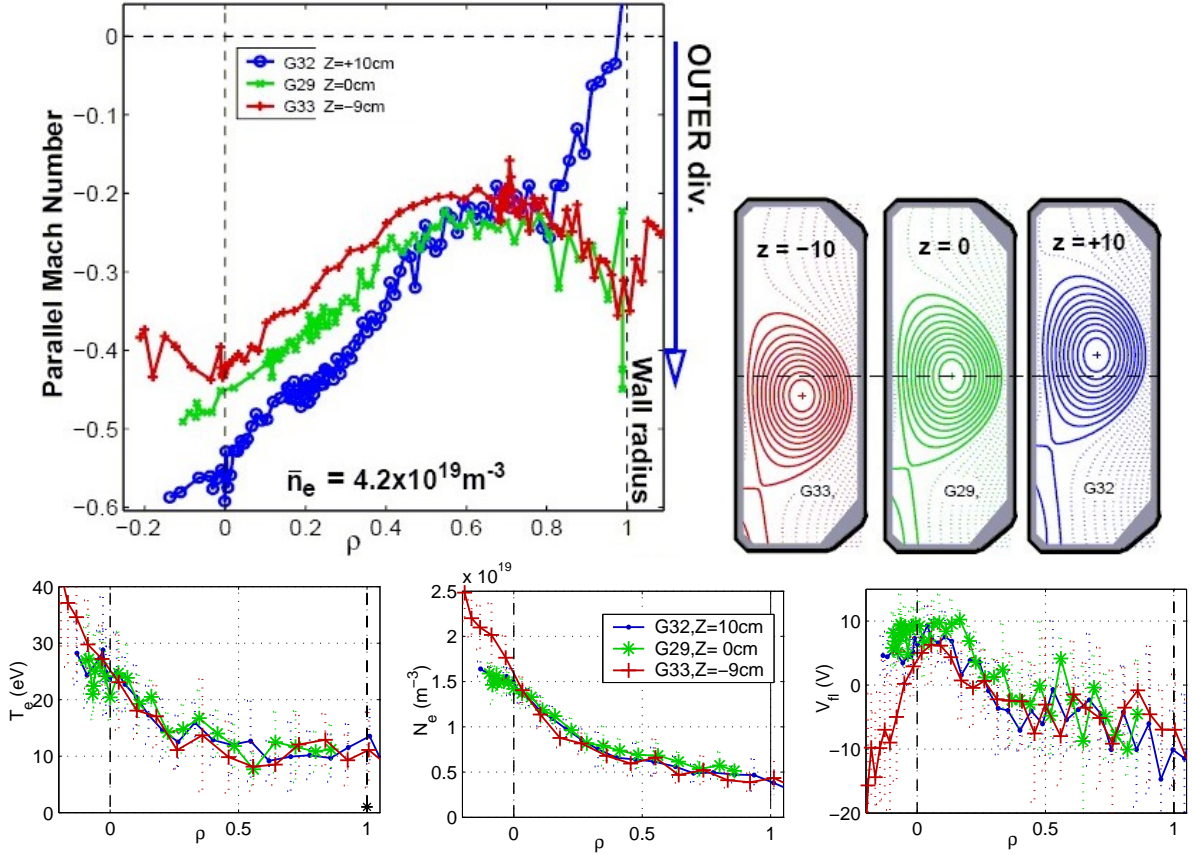


**Fig. 6.6** : Plasma height scan of otherwise identical discharges (260 kA,  $B_T < 0$ ) reveals poloidal variation of  $M_{\parallel}$ . The corresponding TCV plasma equilibria are shown on right. Demonstration that  $n_e$ ,  $T_e$ ,  $V_{\parallel}$ -profiles are identical is presented in bottom plots. Note that the "flat" Mach probe head (shown in Fig. 3.5 (d)) was used to obtain these measurements.

The influence of the divertor target sink has been investigated experimentally using

the flexibility of TCV to create SNU plasmas having the same main plasma shape but with the divertor now located at the top of the machine. As shown in Fig. 6.7, forward and reversed field discharges at fixed  $\bar{n}_e$  in SNL and SNU equilibria reveal a field independent offset which is slightly negative ( $M_{\parallel} \sim -0.07$ ) for the SNL plasmas compared with the SNU equivalents. In the case of the SNU plasmas, not only is the lower outer target now absent, but the probe is located on the lower side of the plasma midplane and thus should not feel the influence of any flow to the upper outer target. This appears to be confirmed by the mean flow in the SNU case, which is close to zero throughout most of the profile.

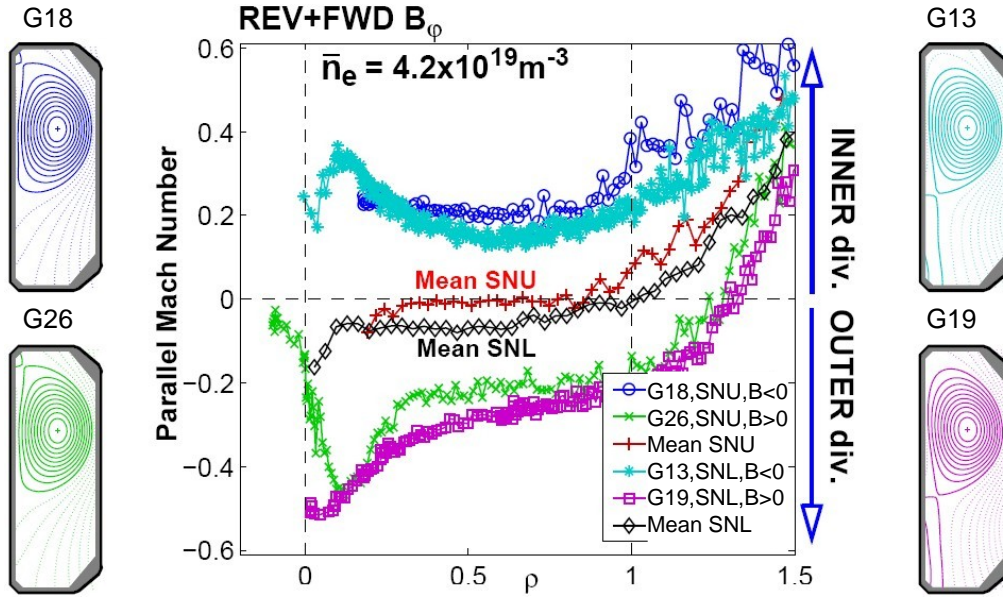


**Fig. 6.7** : Effect of the divertor sink action on  $M_{\parallel}$ . Comparing B-field-independent component of  $M_{\parallel}$  for lower and upper divertor. The B-field-dependent drift terms are removed by averaging  $M_{\parallel}$  with positive and negative magnetic field. The data colour-coded such that the TCV equilibria corresponding to each  $M_{\parallel}$ -profile can be readily identified.

### 6.3 Comparison with Pfirsch-Schlüter flow

In the toroidal geometry of the tokamak, the non-uniform and curved magnetic fields lead to almost vertical curvature and  $\nabla B$  drifts (Eq. (1.4)) which have charge dependent directions and therefore lead to charge separation (vertical electric field)<sup>1</sup>. This in turn drives parallel ion and electron flows, the former being directly measurable with a Mach probe. It can be shown [8, 154, 54] that when diamagnetic effects due to gyration of charged particles are accounted for (the so-called magnetization flux), the microscopic (single particle) and macroscopic (fluid) pictures can be exactly reconciled, such that the poloidal diamagnetic and  $\mathbf{E} \times \mathbf{B}$  fluid drifts are seen to drive a return parallel ion flow (and

<sup>1</sup>The same charge separation also drives the radial movement of the turbulent blobs described in Section 2.7.1

current) known as Pfirsch-Schlüter flow. This parallel flow has a poloidal distribution, closing at the top and bottom of the cross-section and reaching (positive and negative) maxima at the inner and outer midplanes, respectively. Since the flow closes on itself in the main SOL it cannot, in principle, be responsible for the transport of impurities between divertor legs (at least through the main SOL). In the cylindrical approximation, the Mach number of this *Pfirsch-Schlüter flow* may be written [8, eq.(18.85)],

$$M_{\parallel}^{\text{PS}} = \frac{2q \cos \theta}{c_s} \frac{\mathbf{B}}{B^2} \left( E_r - \frac{1}{n_e e} \frac{dp_i}{d\rho} \right) \quad (6.2)$$

with  $q = \frac{rB_T}{RB_{\text{pol}}}$  the cylindrical safety factor (which may significantly differ from  $q_{95}$  due to non-cylindrical geometry) and  $\frac{dp_i}{d\rho}$  is the radial ion pressure gradient and is computed, assuming  $T_i = T_e$ , from the measured  $n_e, T_e$ -profiles. Using Eq. (3.4) without the presheath field, the radial electric field,  $E_r = -\nabla\phi = -\frac{dV_f}{d\rho} - 2.8\frac{dT_e}{d\rho}$  and  $\theta$  is poloidal angle with  $\theta = 0$  defined at the outer midplane. An analytic form for this equation does not exist for non-circular plasmas and the only possibility to derive the parallel flows for shaped plasmas such as those used in the TCV experiment is to use code simulations (e.g. SOLPS5) on the real magnetic equilibrium. This has not been performed here. Instead, recognizing its approximate nature, Eq. (6.2) has been used to compare with TCV flow data. The flow is weaker inside the separatrix since  $E_r$  is in opposite direction with respect to  $-\nabla p$ , but is reinforced in the SOL where both  $E_r$  and  $-\nabla p$  are directed outwards. Its direction reverses with toroidal magnetic field reversal. Such flows have been found to be consistent in direction and to some extent in magnitude with extensive experimental measurements on the JT-60U tokamak [156, 157].

To compare the measured flow with that expected on the basis of Eq. (6.2), gradients of  $E_r$  and  $\nabla p$  must be estimated from the reciprocating Langmuir probe data. An example of how this is performed is shown in Fig. 6.8, which compiles  $n_e, p_e, V_{\text{fl}}, T_e$  profiles for a single probe reciprocation into a high density deuterium discharge. Gradients of  $E_r$  and  $\nabla_r p_e$  are obtained by derivation of linear fits to the profile data, yielding also simple error-estimations for the gradients. Note again that the calculation of  $c_s$  and  $\nabla p_i$  requires that  $T_i = T_e$  be assumed since  $T_i$  is not measured. This is likely to be a good approximation at medium to high density, but may not be valid at the lowest densities, when experimental Mach numbers are highest.

### 6.3.1 Theory-experiment comparison: restricted database

Before studying the full database of experimental measurements, Fig. 6.9 compares the experimentally measured Mach numbers ( $M_{\parallel}^{\text{exp}}$ ) with that predicted from Eq. (6.2) ( $M_{\parallel}^{\text{PS}}$ ) for a density scan of the SNL standard divertor discharges in which the bulk of experiments reported in this thesis have been obtained (see Fig. 3.1 (a)). To provide more accurate estimates of pressure gradient and electric field, the profiles have been split into three separate radial regions and the Pfirsch-Schlüter flow is estimated at the centre of each region (shown in the  $M_{\parallel}(\rho)$ -plot in Fig. 6.8).

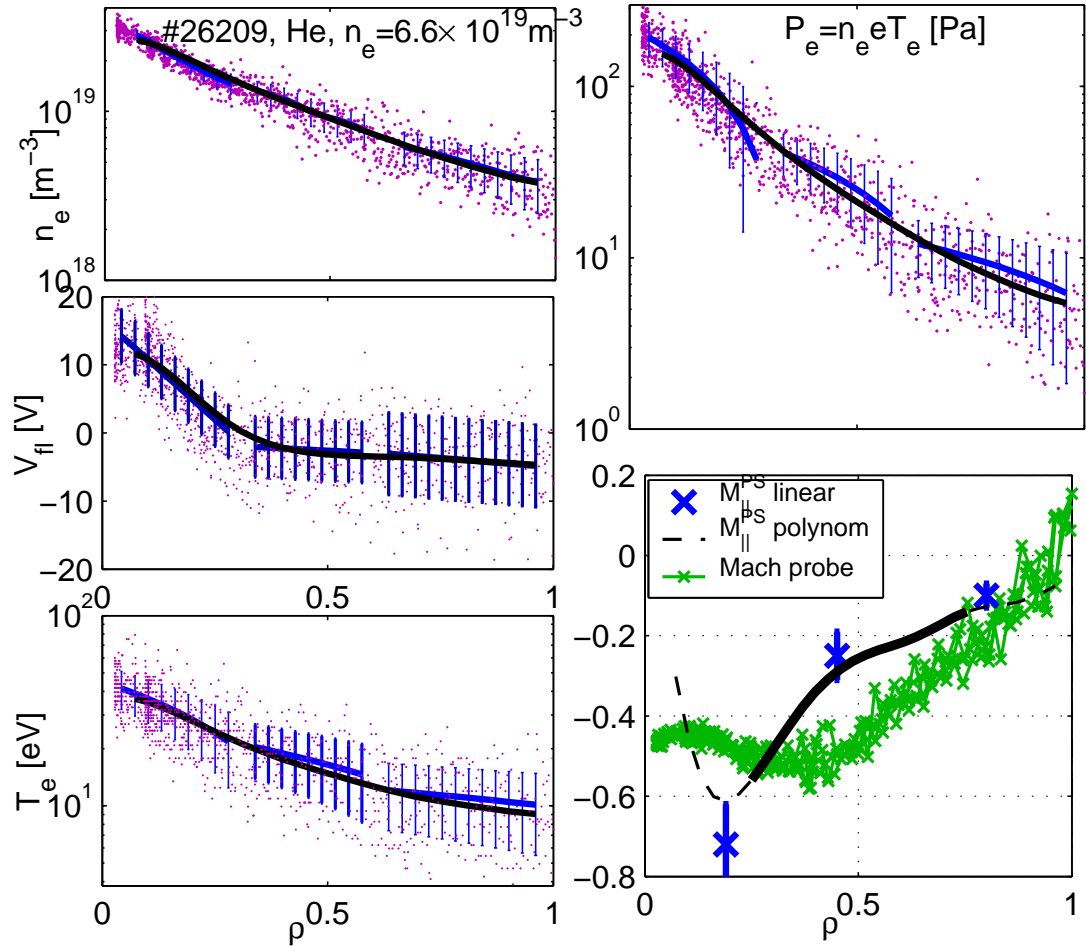


**Fig. 6.8** : Demonstration of how  $M_{\parallel}^{\text{PS}}$  is computed from experimental data. Polynomial or linear fits to the experimental profiles of  $n_e$ ,  $T_e$  and  $V_{\parallel}$  are used to estimate  $E_r$  and  $\nabla_r p_e$ . For comparison within a restricted group of standard SNL discharges in Section 6.3.1, flow measured by the Mach probe is finally compared with the expected Pfirsch-Schlüter flow (Eq. (6.2)) in three separate radial regions throughout the main SOL profile. For comparison with all available discharges and wide SOL region in Section 6.3.2, the polynomial fit is used to estimate the Pfirsch-Schlüter flow.

In general, given the approximate nature of Eq. (6.2) with regard to the real experimental situation, the Pfirsch-Schlüter flow would appear to be a reasonable description of experimental measurement in these TCV ohmic discharges. Agreement is good in both magnitude and direction and there is evidence, at least deeper in the SOL, for a field-independent offset to the flow in the direction to the outer divertor. This reflects, of course, the offset found in Fig. 6.4 (b), with a non-monotonic profile shape.

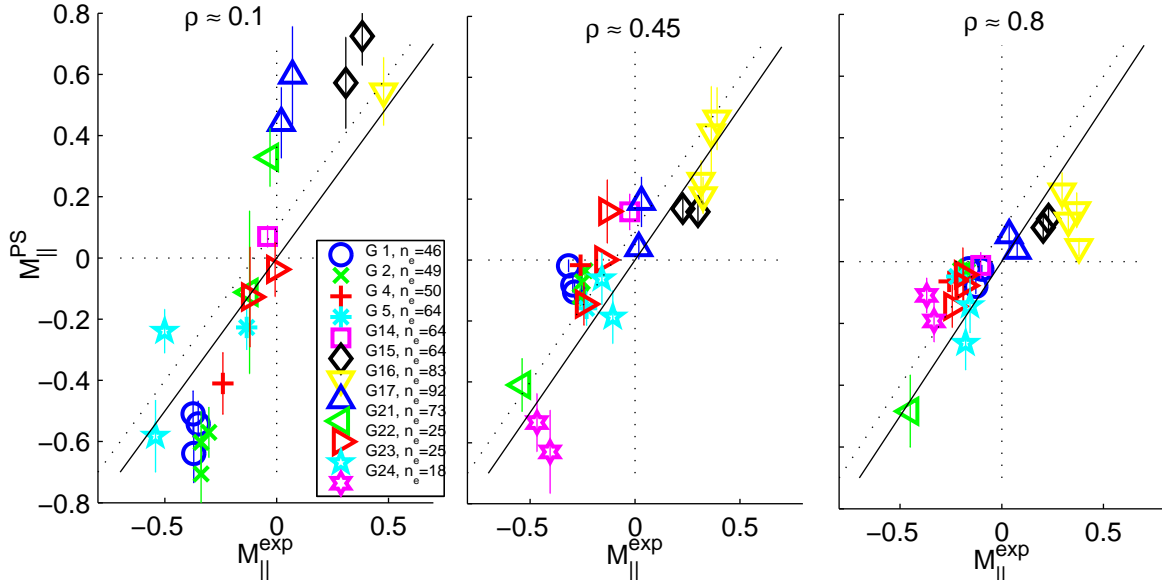


**Fig. 6.9 :**  $M_{\parallel}^{\text{PS}}$  computed from Eq. (6.2) is compared with  $M_{\parallel}$  from Mach probe Eq. (3.14). Compilation of the standard TCV equilibrium in L-mode, D gas at varying densities and both  $B_T$  directions. The SOL is split into 3 regions per window. Error bars come from error propagation within Eq. (6.2) of linear fits to experimental data. The diagonal dotted line corresponds to a flow offset of  $M_{\parallel} = -0.07$  found already in Fig. 6.4 (b). Various symbols correspond to shot-groups (listed on page 126) and the line-averaged density ( $\bar{n}_e [10^{18} m^{-3}]$ ) is mentioned in the legend.

### 6.3.2 Theory-experiment comparison: extended database

Fig. 6.10 (a) compiles the full available TCV database to provide a wider comparison of  $M_{\parallel}^{\text{exp}}$  with  $M_{\parallel}^{\text{PS}}$  for data across the entire SOL for the 77 discharges (described on page 126) in which Mach probe measurements are available. In addition to the previous section, the database contain helium plasmas, plasma height scan, current scan, H-mode and variations in plasma geometry. Polynomial fits are applied across the profiles in case, computing the required gradients at multiple radial positions. However, noise on the data often makes the gradients difficult to estimate, especially at the profile extremities. Data are therefore included in Fig. 6.10 only for the restricted radial extent encompassed by  $\min(\rho) + 0.2 < \rho < 0.8$ , where the maximal probe insertion point,  $\min(\rho)$  varies from discharge to discharge and  $\rho < 0.8$  is chosen to avoid also the effect of the midplane

wall sink. For positive definite quantities like  $n_e$ ,  $T_e$  and  $p_e$ , a logarithmic scale is used,  $n_e^{fit} = \exp[fit(\log(n_e))]$ , to avoid problems of obtaining negative values in the fit.

In Fig. 6.10 (b), the data for all radial positions and discharge conditions are shown in comparison with the following semi-empirical scaling relation:

$$M_{\parallel}^{\text{exp}} = M_{\parallel}^{\text{PS}}(\rho) + M_{\parallel}^{\text{balloon}}\left(\frac{\bar{n}_e z}{a}\right) + M_{\parallel}^{\text{config}} + M_{\parallel}^{\text{residual}}(\rho, \frac{L}{H} \text{ mode}, \delta, \text{gas}, \dots),$$

where  $M_{\parallel}^{\text{balloon}}$  is a possible ballooning contribution, Ballooning is supposed to change sign with  $z$  and increase with density because the turbulence level increases, as demonstrated in Chapter 4. The quantity  $z/a$  is the magnetic axis height normalized to the minor radius.  $M_{\parallel}^{\text{config}}$  is an offset corresponding to the magnetic configuration and can take three values for diverted SNU, SNL and limiter discharges. This multi-parameter empirical fit is shown in Fig. 6.10 (b) with the solution,

$$M_{\parallel}^{\text{scaling}}(\rho) = M_{\parallel}^{\text{PS}}(\rho) - \overbrace{0.2 \frac{z}{a} \left[ \frac{\bar{n}_e}{10^{20} \text{m}^{-3}} \right]^{0.5}}^{\text{ballooning}} + \begin{cases} +0.13 & \text{for SNU} \\ +0.07 & \text{for SNL} \\ -0.13 & \text{for limiter} \end{cases} \quad (6.3)$$

The data collapse is now better than that for only the Pfirsch-Schlüter flow, as characterized by the residual  $\sigma(M_{\parallel}^{\text{exp}} - M_{\parallel}^{\text{scaling}}) = 0.096$ , compared with  $\sigma(M_{\parallel}^{\text{exp}} - M_{\parallel}^{\text{PS}}) = 0.13$  when only Pfirsch-Schlüter flow is accounted for. Since more free parameters are used, the data collapse has to be inevitably better; the Bayesian analysis can be further used to judge its credibility and usefulness. As seen also in Fig. 6.9, the dominant term is clearly the first,  $M_{\parallel}^{\text{PS}}$ . The influence of the remaining terms can be estimated from the differences between lowest and highest values across the database. On this basis the  $M_{\parallel}^{\text{PS}}$ -term modifies  $M_{\parallel}$  by  $\pm 0.6$ . The second term, interpreted as due to a ballooning driven flow component, is consistent with that already identified in Fig. 6.6 and Fig. 6.4. Ballooning component is, by definition, directed downwards for  $z > 0$  i.e. probe below the plasma midplane (whilst upwards for probe above the midplane). The ballooning modifies  $M_{\parallel}$  by  $\pm 0.15$  at maximum poloidal shifts in the database. The last term, concerning the plasma magnetic configuration, is found to have strong effect, especially for the limiter configuration which, for otherwise fixed plasma parameters, decreases  $M_{\parallel}$  by 0.26 and 0.2 with respect to the SNU, SNL configuration, respectively. The difference  $M_{\parallel}^{\text{SNU}} - M_{\parallel}^{\text{SNL}} = 0.06$  is consistent with the observation in Fig. 6.7. Remaining parameters, such as triangularity  $0.29 < \delta_{95} < 0.45$ ,  $175 < |I_p[\text{kA}]| < 424$ , L/H-mode and  $[D|He]$  gas do not reveal (within these limits) any obvious additional functional dependence. The fact that profiles of  $M_{\parallel}$  using the deuterium fuelling are different from that in helium, as observed in Fig. 6.3, is obviously accounted by an appropriate modification of  $n_e, T_e, V_{\text{H}}$ -profiles within the Pfirsch-Schlüter flow in Eq. (6.2). In summary, the Pfirsch-Schlüter flow Eq. (6.2) is found to dominate the experimentally observed TCW midplane flows and, together with small ballooning ( $\sim 0.1$ ) and divertor sink ( $\sim 0.06$ ) components, describe most of the flows, quantified by Eq. (6.3).

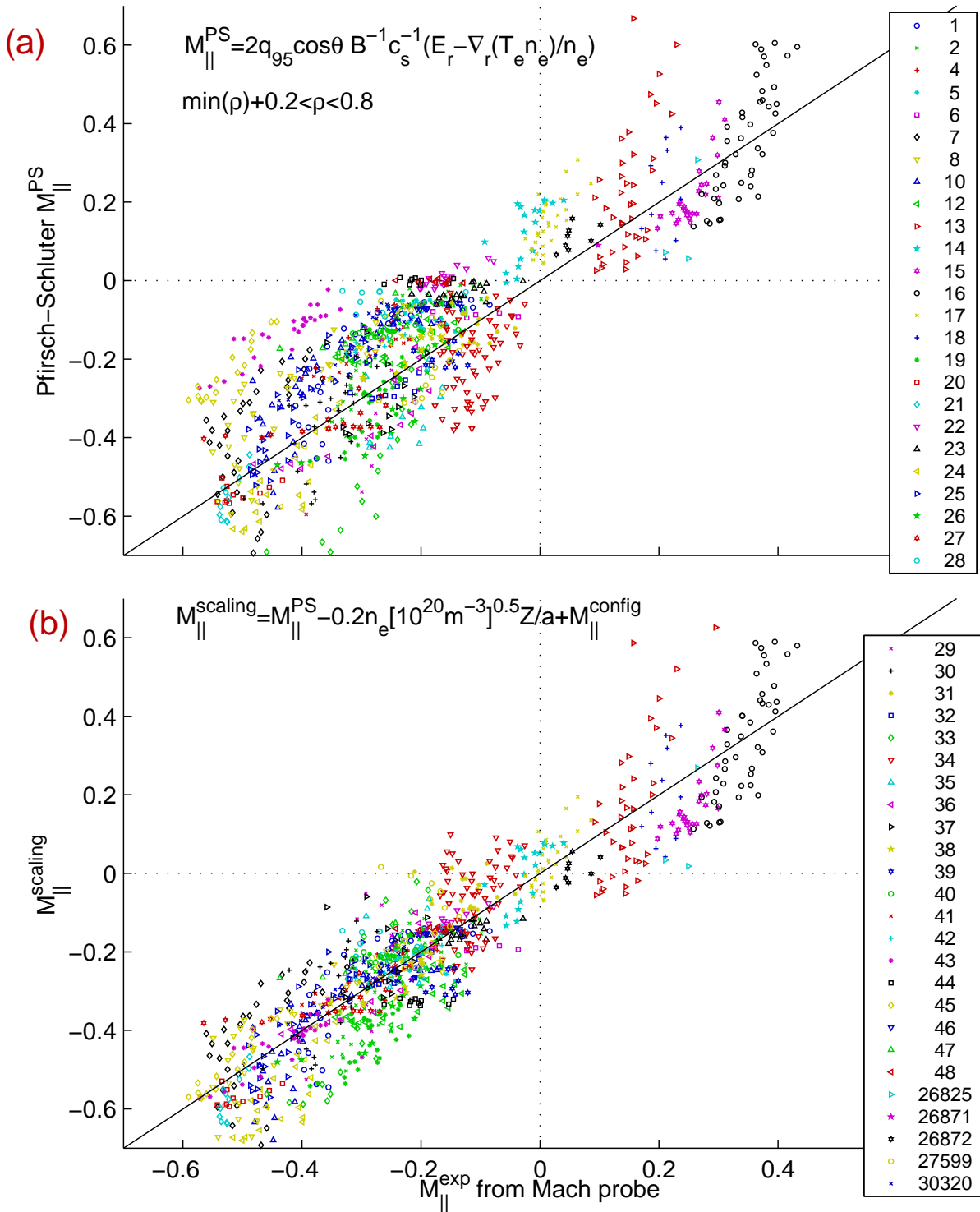


**Fig. 6.10** : Compilation of data from all TCV discharges in the entire SOL in which Mach flow measurements are available. Pfirsch-Schlüter flow computed from Eq. (6.2) is compared in (a) with  $M_{\parallel}^{\text{exp}}$  obtained by the Mach probe using Eq. (3.14). In (b) the semi-empirical scaling Eq. (6.3) is used to fit  $M_{\parallel}^{\text{exp}}$ . Various symbols correspond to shot-groups listed on page 126.

## 6.4 Dynamical interplay between turbulent transport and parallel flow

### 6.4.1 Motivation

An increasing body of evidence is being assembled through experimental measurements that parallel particle flows in the tokamak SOL are too high to be explained by (neo)classical drift theory [152]. Measurements of Mach flow at JET have found strong flows at the top LFS of the poloidal cross-section in a region where the Pfirsch-Schlüter flow should be smaller (since  $\cos\theta \approx 0$  in Eq. (6.2)) [150]. It has recently been demonstrated however, that at the same poloidal location,  $\Gamma_r$  and  $M_{||}$  are correlated in the SOL [44]. Such correlations have therefore been proposed as an interesting possible mechanism by which the energy in cross-field turbulence might drive parallel flows (via the *Reynolds stress*, defined in Section 2.3), thus perhaps accounting for some of the anomalously high measured  $M_{||}$ . Similar analysis is presented in the following for data from the TCV midplane probe where such a turbulent driven component of  $M_{||}$  is, however, not expected to be large because, as it has been demonstrated in Fig. 6.10, the measured  $M_{||}$  on TCV is already consistent with a sum of Pfirsch-Schlüter flow, ballooning and divertor sink action.

Experimental data has been chosen from a discharge in group G24, also shown in Fig. 6.4 (a), with geometry as in Fig. 3.1 (a),  $I_p = 260$  kA,  $\bar{n}_e = 2.3 \times 10^{19} m^{-3}$ ,  $B_T > 0$ . An example of time-averaged  $M_{||}$  and  $\Gamma_r$  profiles, together with the fluctuating data-points, is shown in Fig. 6.11 (a). In this case the flow reaches  $M_{||} \approx -0.5$  at the separatrix. Following the approach in [44], correlations between  $\Gamma_r$  and  $M_{||}$  are sought by computing the *expectation value*,  $E[M_{||}, \Gamma_r]$  for a measurement of  $M_{||}$ , given a simultaneous measurement of  $\Gamma_r$ .

It must be noted, as also discussed in Section 3.9, that  $\Gamma_r$  cannot be estimated with confidence where the poloidal size ( $\lambda$ ) of the turbulent structures is of the order of, or shorter than, the 10 mm pin separation (corresponding to the range of normalized radius  $\rho \leq 0.2$ ). This is demonstrated in Fig. 6.11 (a) where the radial profile of  $\lambda$  has been estimated using a cross-correlation technique that suggests that only in the main SOL is the structure size really compatible with the fixed pin separation.

### 6.4.2 Joint probability

To compute  $E[M_{||}, \Gamma_r]$  from a set of time traces of  $M_{||}$  and  $\Gamma_r$ , the joint probability,  $P^{(m\gamma)} = P(M_{||}^{(m)}, \Gamma_r^{(\gamma)})$ , shown in Fig. 6.11 (b), is first established. It is a two-dimensional PDF, a probability of *simultaneous* occurrence of  $M_{||}$  and  $\Gamma_r$  in regions close to given values,  $M_{||}^{(m)}$  and  $\Gamma_r^{(\gamma)}$ . The expected value of  $M_{||}$  at a given value  $\Gamma_r^{(\gamma)}$ , is then defined as

$$E[M_{||}, \Gamma_r^{(\gamma)}] = \frac{\sum_m P^{(m\gamma)} M_{||}^{(m)}}{\sum_m P^{(m\gamma)}}. \quad (6.4)$$

In this notation, the probability distributions of  $M_{||}$  and  $\Gamma_r$  are written:  $PDF(M_{||}(m)) = \sum_{\gamma} P^{(m\gamma)}$  and  $PDF(\Gamma_r(\gamma)) = \sum_m P^{(m\gamma)}$ , respectively. In Fig. 6.11 (b),  $E[M_{||}, \Gamma_r]$  is overlaid on the full 2D joint probability distribution, since it intuitively corresponds to a 'centre of gravity' of  $P^{(m\gamma)}$ . The value of  $E[M_{||}, \Gamma_r]$  at four separate radial position ranges, marked in Fig. 6.11 (a), is shown in Fig. 6.11 (c). Close to the separatrix, where  $\langle M_{||} \rangle$  is highest,  $E[M_{||}, \Gamma_r]$  is independent of  $\Gamma_r$ , implying the absence of any coupling between  $M_{||}$  and  $\Gamma_r$ , if this probability description can really be assumed to be a reliable indicator of such coupling. Deeper in the SOL,  $E[M_{||}, \Gamma_r]$  appears to increase for large  $\Gamma_r$ -events, giving correlations similar to those reported from JET [44].

### 6.4.3 Validity of the Expectation value

Ignoring for the moment the nature of the coupling between  $M_{||}$  and  $\Gamma_r$ , it is useful to discuss the possible *relevance* of the conditional statistic,  $E[M_{||}, \Gamma_r]$  in the region of the strongest correlation, which on TCV appears to be in the range  $0.7 < \rho < 1$ . In other words, in region of strongest apparent coupling we try to *quantify* to what extent the total flow,  $\langle M_{||} \rangle$  is influenced by this coupling with  $\Gamma_r$ . Note that the analysis technique presented previously in Fig. 6.11 (b,c) does *not* quantify how much rare events of large  $\Gamma_r$  influence the time-averaged flow value and therefore whether it then play a non-trivial role with regard to SOL flows. One way to do this is to observe how much the time-averaged  $\langle M_{||} \rangle$  changes by removing those  $M_{||}$  data points from the full time series which occur simultaneously with large  $\Gamma_r$  events, i.e. those time-instants which make  $E[M_{||}, \Gamma_r]$  dependent on  $\Gamma_r$ . Note that such an approach assumes nothing more than what the conditional statistic assumes already, namely no time delay between  $\Gamma_r$  and  $M_{||}$  bursts, but there is no need for linearity nor nonlinearity of the dynamics, discussed in [44].

The result of this exercise is shown in Fig. 6.12 . All values of  $M_{||}$  and  $\Gamma_r$  corresponding to bursts in  $\Gamma_r$  exceeding  $3\sigma_{\Gamma_r} \approx 1.2\langle \Gamma_r \rangle$  (chosen arbitrarily) have been removed, leaving the discontinuous time series (red thick line) in Fig. 6.12 (ab). This data-removal strongly affects  $E[M_{||}, \Gamma_r]$ , indeed the curve effectively *shrinks* into a small region near  $E[M_{||}|0]$ , as shown in Fig. 6.12 (c). In contrast, the PDF of  $M_{||}$  changes only slightly (Fig. 6.12 (d)). This is a consequence of the fact that the large  $\Gamma_r$  peaks are rare, a property which is not visible in the conditional statistic  $E[M_{||}, \Gamma_r]$ . As a result, the most crucial quantity, the time-averaged  $\langle M_{||} \rangle$ , changes for this particular example from -0.12 to -0.084 when the values of  $M_{||}$  corresponding to large bursts in  $\Gamma_r$  are removed from the time series. This analysis is extended in Fig. 6.13 for a wider TCV database, including various magnetic configurations (shown in Fig. 4.4 ) across the entire SOL. The essential conclusion does remain valid: quantified in the way proposed in this section, the effect of the coupling is small throughout most of the SOL. Near the wall, the mean value of  $M_{||}$  is influenced by  $\sim 0.06$  at most. In this region, the component identified in this way is comparable to  $\langle M_{||} \rangle$ .

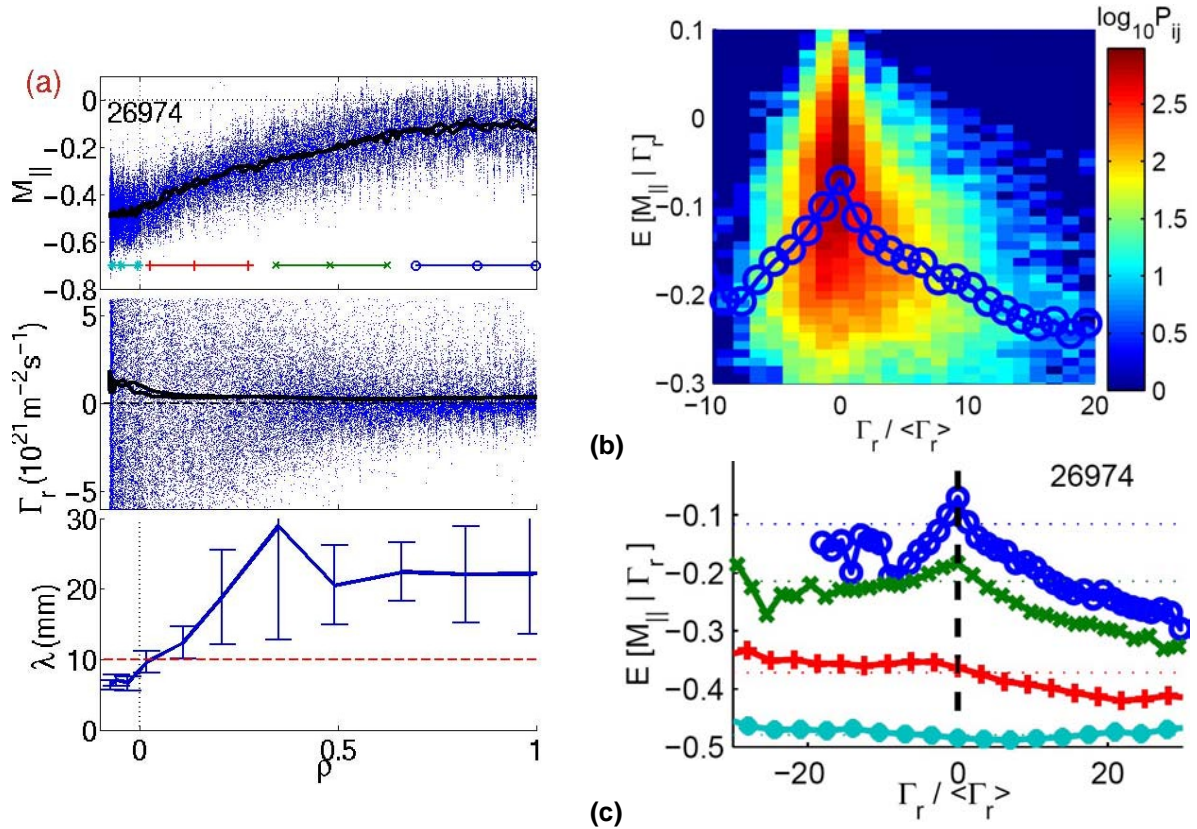


**Fig. 6.11 :** (a) SOL profiles of fluctuating  $M_{||}$  and  $\Gamma_r$  around their mean values (solid lines) and the estimated poloidal size of turbulent structures,  $\lambda$ . In (b) the colour (in  $\log_{10}$ -scale) corresponds to the conditional probability,  $P(M_{||}, \Gamma_r)$  of simultaneous appearance of a given  $M_{||}$  and  $\Gamma_r / \langle \Gamma_r \rangle$ . The expectation value,  $E[M_{||}, \Gamma_r]$ , corresponding to vertical average of  $P(M_{||}, \Gamma_r)$  according to Eq. (6.4) is overlaid. In (c),  $E[M_{||}, \Gamma_r]$  is plotted in the four radial regions marked in the  $M_{||}(\rho)$ -plot in (a).

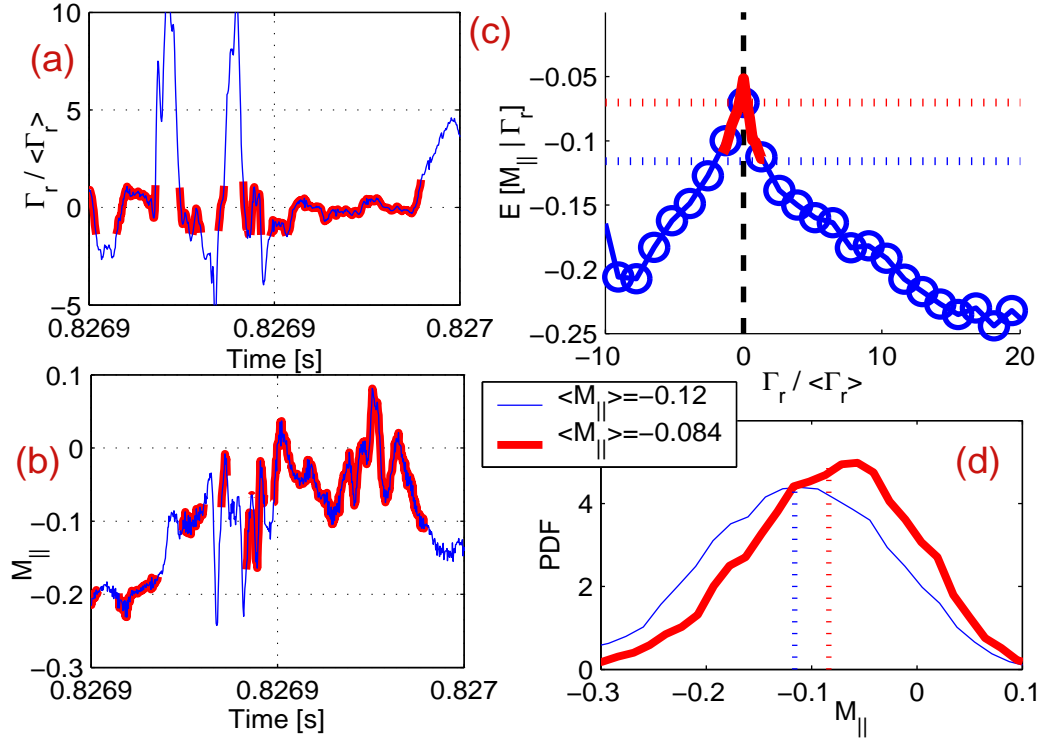


**Fig. 6.12** : Example (#26974) of time evolution of **(a)**  $\Gamma_r$  and **(b)**  $M_{||}$  in the region of strongest dynamical coupling (marked by blue circles in Fig. 6.11). Both signals are split into two data sets: the blue line corresponds to the full time series (of which only a short piece is shown), whilst the bold red regions delimit time-instants of small  $\Gamma_r$  bursts with  $|\Gamma_r| < \sigma_{\Gamma_r}/3$ , comprising  $\sim 65\%$  of the full time series. **(c)** the corresponding expectation value,  $E[M_{||}, \Gamma_r]$  for both sets of data: using the full time series (blue curve) and that with the bursts removed (red thick curve), corresponding to  $E[M_{||}, 0]$ . **(d)** the corresponding PDFs of  $M_{||}$  for these cases, with  $\langle M_{||} \rangle$  marked by the dotted lines.

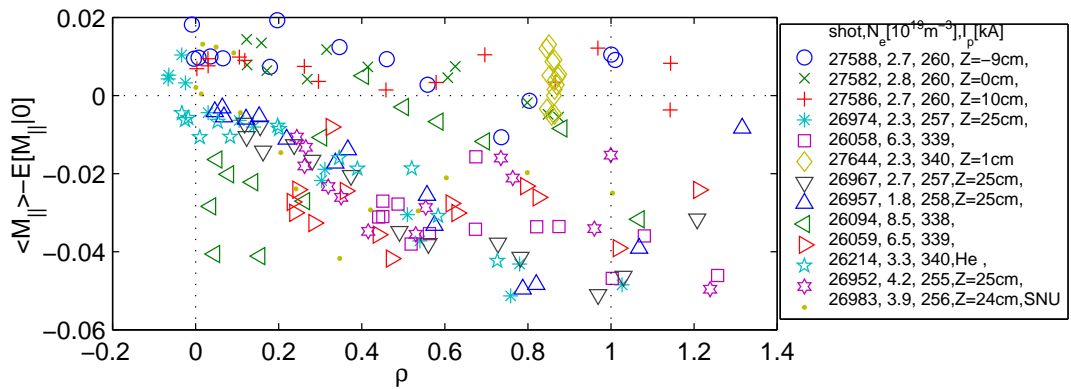


**Fig. 6.13** : The analysis, described in Fig. 6.12, extended to a larger database containing many discharges with varying  $\bar{n}_e$  and  $I_p$ , [D|He] fuel gas, plasma heights ( $z$ ) and [SNU|SNL] configurations (shown in Fig. 4.4). This is specified in the legend if different from the default configuration, [ $z = 23\text{cm}$ , SNL, D]. The impact of any "coupling" is expressed in terms of the difference between  $\langle M_{||} \rangle$  and the expectation value at  $\Gamma_r \approx 0$ .

#### 6.4.4 Alternative explanation due to probe location

With regard to the motivation in [44] for seeking a link between parallel flow and cross-field transport, the TCV case is less clear-cut. As shown in Fig. 6.10 and Fig. 6.9, the measured parallel flow does in fact appear to be reasonably well approximated by a Pfirsch-Schlüter return flow. It would not, therefore, appear necessary to invoke any additional mechanism to account for TCV flows measured in the outboard midplane vicinity and it is not surprising that no coupling is found. For the case of the JET measurements in [44], the Mach probe was located near the top of the poloidal cross-section, where  $\theta \approx 90^\circ$  in Eq. (6.2) with consequent negligible expected  $M_{\parallel}^{\text{PS}}$ . And yet, observed parallel flows are high on JET, rising from  $M_{\parallel} \approx 0.2$  at the separatrix to as much as  $M_{\parallel} \approx 0.5$  in the main SOL [150]. This was the primary motivation in [44] for seeking a turbulent mechanism for driving the flow. Since the level of  $M_{\parallel}$ - $\Gamma_r$  coupling reported in [44] is not linked quantitatively to a magnitude of flow-drive, it is difficult to judge to what extent the mechanism is valid.

Due to the known ballooning nature of radial SOL transport, a probe located above or below the outboard midplane will intercept the plasma filaments elongated in parallel direction which form due to parallel forces when the 2D blobs, shown in the ESEL simulation of Fig. 5.6, propagate radially. Thus, a Mach probe with sensors pointing towards and away from the location of filament formation will automatically register rapid increases in apparent Mach number as each filament arrives. This is exactly analogous to the mechanism proposed in [158] to explain the instantaneous increases in  $M_{\parallel}$  observed on the same JET probe during ELM events. Because the filament locally increases the density, these transient bursts in  $M_{\parallel}$  are also associated with an increase in  $\Gamma_r$ . Correlations might therefore be expected between  $M_{\parallel}$  and  $\Gamma_r$ . In Fig. 6.13 the observed coupling is weak across the entire database and is essentially absent for discharges in which the probe is located exactly at the plasma midplane (for example #27582 and #27644). At this point the measured Mach number would be less sensitive to the filaments since they are expected to form more readily at the outside midplane where ballooning is strongest. In this case, filament density increase is *symmetric* with respect to the up/downstream directions. In fact, the poloidal distribution of this excess radial transport may be quite extended, such that even the normal location of the TCV probe (under the midplane) might still be nominally in this "ballooning" region. The JET probe, however, is more likely to be well outside this region. In conclusion, some of the correlation (coupling) found between  $M_{\parallel}$  and  $\Gamma_r$  in Fig. 6.11 may be due to the arrival of filamentary structures at the probe, without the need for a Reynolds stress mechanism which has been proposed to explain this observed coupling. The results presented in this section have been published in [33].

Recently, this dynamical interplay has been observed also in a linear machine [159] with, as well as in TCV, negligible effect close to the velocity shear layer and some coupling of the order of  $M_{\parallel} \sim 0.02$  in the far SOL.

## 6.5 Dynamical interplay between density gradient and turbulent transport

Although Section 6.4 have not found a significant influence of  $\Gamma_r$  fluctuations on  $\langle M_{||} \rangle$ , similar analysis applied to alternative quantities may be more relevant. For example, the possibility of  $\Gamma_r$  being driven by dynamical coupling with fluctuations in the density gradient  $\nabla_r n_e$  has also been suggested in [10, 39]. To study this,  $\nabla_r n_e$  is estimated in the usual way using  $I_s$  from two radially separated pins, and normalized to its fluctuation level,  $\nabla_r I_s / \sigma_{\nabla_r I_s}$ . In analogy with Section 6.4, the variables are therefore simply replaced in the analysis of expectation values as

$$\frac{\Gamma_r}{\langle \Gamma_r \rangle} \rightarrow \frac{\nabla_r I_s}{\sigma_{\nabla_r I_s}} \approx \frac{\nabla_r n_e}{\sigma_{\nabla_r n_e}}, \quad M_{||} \rightarrow \frac{\Gamma_r}{\langle \Gamma_r \rangle}$$

and consequently, in analogy with Eq. (6.4)

$$E[\Gamma_r | \nabla_r I_s^{(i)}] = \frac{\sum_{\gamma} P(\gamma, i) \Gamma_r^{(\gamma)}}{\sum_{\gamma} P(\gamma, i)}. \quad (6.5)$$

Analogously with Fig. 6.12, this is shown in Fig. 6.14 : time series of  $\Gamma_r$  and  $M_{||}$  (only a short piece is shown in Fig. 6.14 (a,b)) are used to produce plot of  $E[\Gamma_r | \nabla_r I_s]$  in Fig. 6.14 (c) which shows that there does appear to be a statistical link between density gradient and cross-field turbulent flux. Large amplitude transport events  $\Gamma_r / \langle \Gamma_r \rangle > 1$  occur preferentially when the density gradient departs from its most probable value, either positive or negative.

Applying the same expectation value criterion to  $\Gamma_r$  and  $\nabla_r n_e$  as in Section 6.4.3, some influence is also found. In Fig. 6.14 (d) the PDF is only slightly modified when  $\Gamma_r$  events corresponding to large  $\nabla_r I_s$ -peaks are removed, but it is sufficient to affect significantly the average value of  $\Gamma_r$ , evaluated as the expectation value of  $\Gamma_r$  for small  $\nabla_r I_s \sim 0$ , i.e.  $E[\Gamma_r | 0] / \langle \Gamma_r \rangle = 0.6$ .

Using the same approach as in Fig. 6.13, the extension of this analysis to many discharges and radial positions is shown in Fig. 6.15. The strength of any modification to  $\langle \Gamma_r \rangle$  due to large peaks in  $\nabla_r n_e$  is expressed using the quantity  $E[\Gamma_r, 0] / \langle \Gamma_r \rangle$ . Unity corresponds to zero statistical coupling, which appears to be the case close to separatrix, whilst in the main SOL, as much as half of the total turbulent driven cross-field flux occurs during peaks in the density gradient. This observation suggest that the "dynamical coupling" identified in [10, 39], is also present in the TCV outboard main SOL and can modify the mean value of the radial particle flux,  $\langle \Gamma_r \rangle$ , by up to factor of 2. The reason why the dynamical coupling plays role for  $\Gamma_r$  driven by  $\nabla_r n_e$  is because  $\Gamma_r$  is strongly fluctuating quantity,  $\langle \Gamma_r \rangle / \sigma_{\Gamma_r} \ll 1$ , in contrary to  $M_{||}$  being driven by  $\Gamma_r$  where  $M_{||}$  does fluctuate significantly less,  $\langle M_{||} \rangle / \sigma_M \geq 1$ .

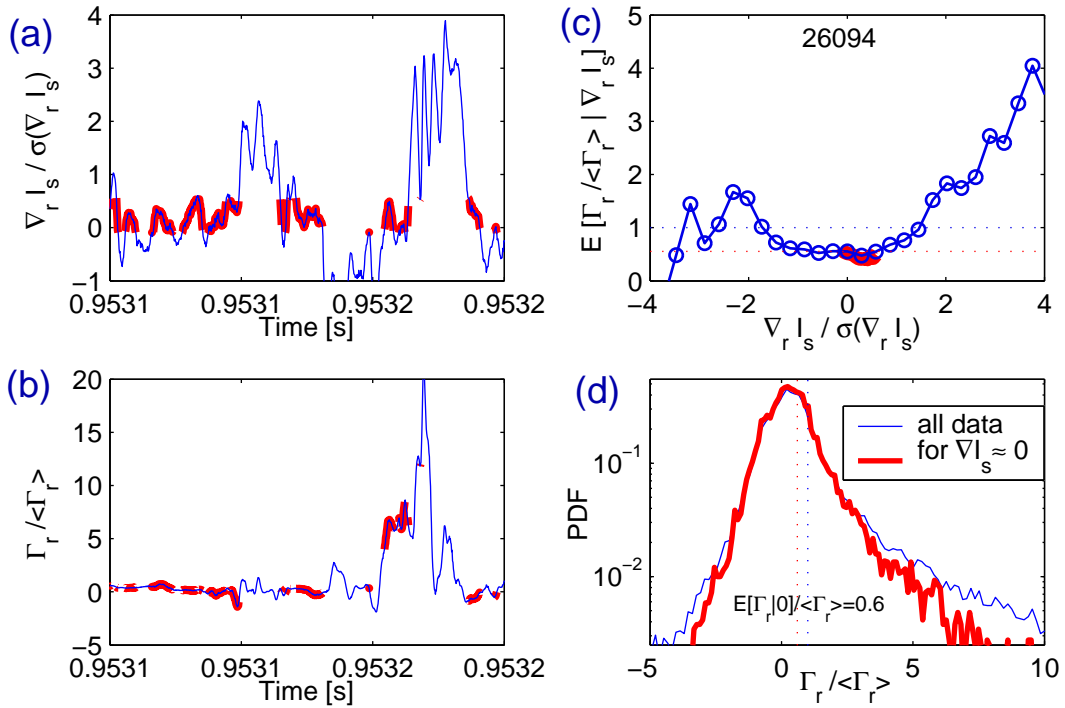


**Fig. 6.14 :** In analogy with Fig. 6.12, dynamical coupling is studied between density gradient,  $\nabla_r I_s$  and radial particle flux,  $\Gamma_r$ . In (a,b) a short part of the full time series (blue thin line) of  $\nabla_r I_s$  and  $\Gamma_r$  are split into discontinuities series (red thick) at instants of small  $\nabla_r I_s$ . The expected value is shown in (c). In (d) PDF the full  $\Gamma_r$  time series is similar to  $\text{PDF}(\Gamma_r)$  at instants of small  $\nabla_r I_s$  but because  $\langle \Gamma_r \rangle / \sigma_{\Gamma_r} \ll 1$ ,  $\langle \Gamma_r \rangle$  is strongly influenced.

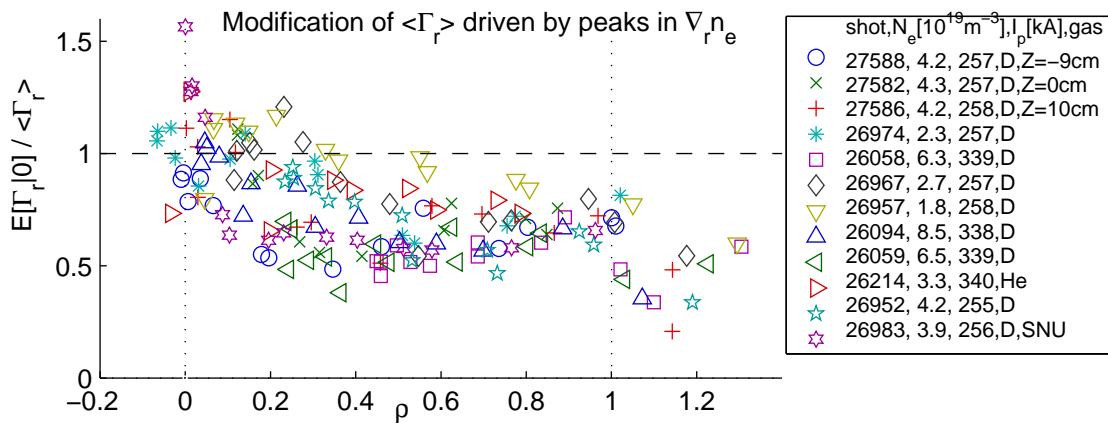


**Fig. 6.15 :** Dynamical coupling between density gradient  $\nabla_r I_s$  and radial particle flux  $\Gamma_r$ , extended over many discharges as in Fig. 6.13 and shown as a function of normalized radius.



# Chapter 7

## Summary and conclusions

It has long been recognized that the mechanism responsible for shaping the observed density profile and driving particle fluxes across the magnetic field in the tokamak SOL cannot be explained on the basis of classical (collisional) physics. Although in many cases where measurements have been made, exponential radial density profiles have been found (implying a "Fick's law" type diffusive ansatz), the associated particle diffusion coefficients are very much larger than expected on classical grounds. It has recently become increasingly evident, moreover, that at high density in many tokamaks, the edge density profile flattens, with long tails extending far out in the SOL (in fact contacting the main chamber walls) and associated with flat temperature profiles. Thus, the traditional picture (in a divertor tokamak) of particle exhaust in the edge being dominated by parallel conduction and convection (depending on the regime of operation) to the divertor targets and very little exhaust to the main chamber walls is not satisfied. The main chamber itself can be responsible for much of the particle recycling and, depending on the energy of particles arriving at those surfaces, could even become a region of energy deposition given that main chamber surface areas available for interaction are far greater than the narrow regions of deposition in the divertor. Whilst playing no role at all in current machines with regard to material migration, erosion or power loading (except possibly in the case of ELMs), this enhanced main chamber interaction is a potential threat to future power plants operating continuously. In today's smaller machines it can and does stimulate a shift to a "main chamber recycling" regime which has been shown to influence some aspects of tokamak operation (for example, divertor detachment or the density limit).

The question therefore is what is the transport mechanism controlling the cross-field fluxes? For years the cause has simply been attributed to "turbulence" and indeed Langmuir probe particle flux measurements in the SOL have always been found to exhibit high fluctuation levels and often skewed PDFs, pointing to an underlying turbulent mechanism.

This thesis provides the first ever convincing evidence that this anomalous transport can be understood in terms of a basic mechanism operating in many plasma and fluid systems - the interchange instability. It accomplishes this through the direct comparison, yielding quantitative agreement in many aspects, of high quality experimental measurements obtained on the Lausanne tokamak TCV with the results of two-dimensional fluid

turbulence code simulations adapted as closely as possible to the experimental conditions. Both code simulation and the (more extensive) experimental database provide compelling evidence for a "universal character" in terms of the statistical description of SOL density and particle turbulence. The clear identification on TCV of a strong candidate mechanism for the turbulent drive leads to the plausible extrapolation that a similar process operates in all tokamak SOLs, with the realistic hope that the holy grail of a first principles based prediction of cross-field transport rates is now within our grasp.

Using a fast reciprocating, multi-pin Langmuir probe diagnostic, radial and poloidal profiles of particle flux and electric potential at 6 MHz acquisition rates have been acquired in the low field side SOL of a wide range of ohmic TCV discharges, comprising variations in plasma shape and configuration (limiter and divertor), plasma current, confinement mode (L and H), plasma density, toroidal magnetic field direction and plasma fuel species (deuterium and helium). Analysis of the database in terms of density and ExB driven turbulent flux PDFs (and their moments) has demonstrated a remarkable degree of similarity in the statistics. The level of turbulence, quantified in terms of the fluctuation level,  $\sigma_n/n$  and  $\sigma_\Gamma/\Gamma_r$ , has been shown to in reasonable agreement, across the entire SOL width, with the well known Lognormal and Gamma analytic distributions, both of which can be characterized uniquely in terms these intermittency parameters. The key observation here is that because the level of observed fluctuation level increases steadily across the SOL, an analytic PDF (such as the extreme value Gumbel or BHP distributions which have been identified in the past as approximating measured SOL turbulence data) which does not vary in shape across the SOL cannot adequately describe the variation in the TCV data. Particularly in the vicinity of the SOL-main chamber interface, where particles interact with the walls, the density fluctuations exhibit clear evidence of self-similarity over two orders of magnitude in frequency and a PDF which is universal in shape with  $n/\sigma_n \sim 1.7$ . The observed constancy of the correlation between density and poloidal field fluctuations in turn implies a universal PDF for the radial particle flux which moreover scales almost linearly with the local mean density. The latter is further observed to scale with the square of the line averaged density over a wide range of density, providing a link between a main tokamak operating parameter and the wall flux. The observation on other tokamaks and by other means (not invoking turbulence measurements), of a total particle outflux also scaling with the square of line average density therefore suggests the cross-field turbulence drive to be the origin of the radial outflux.

Careful comparison of one particular case inside the experimental database with the results of a 2D fluid turbulence simulation of the TCV SOL using the Risø ESEL code has shown a remarkable level of agreement between theory and experiment when the simulation output time series is analyzed in exactly the same way as that applied to the tokamak data. Inevitably, the model contains a number of simplifying approximations which mean that the real physical situation in the SOL cannot be approached in practice. Nevertheless, appropriate choice of boundary conditions and the damping coefficients which represent parallel (along the field) dynamics has led to an extremely close match considering the simplifications. Indeed, the provision of such comprehensive experimental data and the code-experiment comparison has stimulated the development of a physics based

derivation of these damping coefficients which had previously been selected somewhat arbitrarily to provide the best match to experiment.

Quantitative agreement between model and experiment has been found for radial profiles of mean values, fluctuation levels, PDF shapes, timescales and power spectra of both density and turbulent driven flux throughout the main SOL and even partially inside the separatrix. Automatically, this level of agreement also implies that the code output conforms quite closely to the Gamma and Lognormal distributions. Indeed, deep in the wall shadow, where experimental data are unavailable due to the very low signal levels there, the code yields time series with PDFs which approximate the Gamma distribution extremely well. Thus far, a major area of disagreement has been found in the spatial sizes of the turbulence (potential structures), which are significantly larger in the simulations than implied by experiment. It is thought, however, that this is very likely due to the choice of too large a value of the collisional particle diffusion coefficient in the simulations. Decreasing the value to that suggested by the first principles argument is currently prevented in the code for reasons of the excessive computational time which would result. A further important conclusion of this work has been the demonstration that the experimentally derived magnitude of cross-field fluxes are perfectly consistent with the simulated values. The crucial inference here is that nominally perturbing solid probes can be used with impunity to estimate the turbulent driven flux.

Changes to the probe head geometry executed during this thesis research have allowed parallel SOL flow data to be gathered simultaneously with the turbulence measurements. An extensive database of radial Mach flow profiles has been assembled, most notably including a direct comparison of the density dependence of the flow dynamics in carefully matched discharges with forward and reversed toroidal field. These constitute the first measurements of their kind in TCV and provide a valuable contribution to the international SOL flow database which is currently receiving a great deal of attention in the context of the potential role of parallel flow in the large scale material migration which is now expected in future devices, such as ITER, with higher duty cycles than are presently achievable. The key issue here is the extent to which the measured flow can be explained on the basis of neoclassical "return parallel flows", compensating the poloidal flows driven by ExB and diamagnetic fluid drifts. These Pfirsch-Schlüter flow have been found on some machines to be an adequate description of the measured flow, on others to be insufficient by considerable margins. Reversing the toroidal field, reverses the direction of all classical poloidal drifts and hence normally of the return parallel flows.

Careful measurements on TCV in simple ohmic diverted plasmas have demonstrated that the flows are indeed well described by the Pfirsch-Schlüter picture with the exception of a slight offset, of order  $M \sim 0.05 - 0.1$ , revealed by computing the arithmetic mean of measurements at fixed density but opposite field directions. They have also been observed to behave with density as classically expected - decreasing substantially from values of  $M \sim 0.5$  at the lowest densities to flows approaching stagnation at high density. The high level of agreement with theory, despite the use of the simple large aspect ratio, cylindrical approximation applied to measurements in highly shaped and non-circular configurations is surprising. The flows are in the same direction as seen on other devices for given

direction of the ion  $\nabla B$ -drift.

The combination of parallel flow and turbulence measurements have also enabled a possible link between turbulence and flow generation first reported on JET to be tested at TCV. At JET, the high flows measured at the top, low field side of the poloidal cross-section cannot be explained neoclassically, leading to the suggestion that turbulence could be involved. On TCV, the correlations between parallel flow and cross-field turbulent fluxes found on JET are absent except in the very far SOL, where parallel flows are in any case small. Closer to the separatrix, where the natural flows are largest, no correlation is found. This is not perhaps surprising given that Pfirsch-Schlüter flows appear to be sufficient to account for most of the measured flow. Interestingly, however, the small parallel flow offset revealed by the field reversal experiment on TCV appears to be approximately consistent with the flow generation that would be expected from excess pressure, localized around the outboard midplane, released by the interchange motions found to be an excellent description of the TCV turbulence statistics. So indeed there is a connection between flow and cross-field turbulence, but not necessarily of the nature implied in the JET study.

Without doubt the single most important feature of the work described in this thesis has been the clear identification of fluid interchange motions, convecting plasma in complex vortex motions across the magnetic field, as the principle mechanism of anomalous particle transport in the tokamak SOL. As such it represents a major advance in our understanding of radial transport, opening the door towards a wider study of the phenomena, hopefully involving improvements to the physics description contained within the turbulence code and stimulating others to perform comparisons with equivalent data, treated in a similar fashion, from other tokamaks covering a wider range of parameters (such as field strength, curvature etc) than can be accessed on TCV. If similar levels of agreement can be demonstrated as has been found in TCV, confidence will grow that interchange turbulence does indeed govern radial SOL transport in a general sense. Should this prove to be the case, predictive simulations of the likely transport levels in future devices would be possible, as would the inclusion of a realistic model of particle and energy transport in the large edge fluid-Monte Carlo codes.

**Part III**  
**Appendices**



# Appendix A

## Vorticity link to potential

The link, expressed in Eq. (5.6), between vorticity and plasma potential is a non-trivial result. A derivation is provided here due to Odd Erik Garcia from the Risø National Laboratory, Denmark.

The electric drift for electrostatic perturbations is defined by

$$\mathbf{V}_E = \frac{1}{B} \mathbf{b} \times \nabla \phi, \quad (\text{A.1})$$

where  $B$  is the magnetic field strength and  $\mathbf{b}$  is the local unit vector along the magnetic field. The curl of this drift is then

$$\nabla \times \mathbf{V}_E = \nabla \left( \frac{1}{B} \right) \times (\mathbf{b} \times \nabla \phi) + \frac{1}{B} \nabla \times (\mathbf{b} \times \nabla \phi) \quad (\text{A.2a})$$

$$= -\frac{1}{B} \nabla \ln B \times (\mathbf{b} \times \nabla \phi) + \frac{1}{B} \nabla \times (\mathbf{b} \times \nabla \phi). \quad (\text{A.2b})$$

Using the formulae of standard vector calculus, the first term on the right hand side of the above equation can be written as

$$-\frac{1}{B} \nabla \ln B \times (\mathbf{b} \times \nabla \phi) = -\frac{1}{B} (\nabla \ln B \cdot \nabla_{\perp} \phi) \mathbf{b} + \frac{1}{B} (\mathbf{b} \cdot \nabla \ln B) \nabla_{\perp} \phi, \quad (\text{A.3})$$

while for the last term on the right hand side we have

$$\nabla \times (\mathbf{b} \times \nabla \phi) = (\nabla_{\perp}^2 \phi) \mathbf{b} - (\nabla \cdot \mathbf{b}) \nabla_{\perp} \phi + (\nabla_{\perp} \phi \cdot \nabla) \mathbf{b} - (\mathbf{b} \cdot \nabla) \nabla_{\perp} \phi. \quad (\text{A.4})$$

We further use the fact that the magnetic field is incompressible,  $\nabla \cdot \mathbf{B} = \nabla B \cdot \mathbf{b} + B \nabla \cdot \mathbf{b} = 0$ . It follows that  $\mathbf{b} \cdot \nabla \ln B = \nabla \cdot \mathbf{b}$ . Using this for the last term on the right hand side of equation (A.3) then yields

$$-\frac{1}{B} \nabla \ln B \times (\mathbf{b} \times \nabla \phi) = -\frac{1}{B} (\nabla \ln B \cdot \nabla_{\perp} \phi) \mathbf{b} + \frac{1}{B} (\nabla \cdot \mathbf{b}) \nabla_{\perp} \phi. \quad (\text{A.5})$$

It is readily seen that the last term in equation (A.5) cancels the second term on the right hand side of equation (A.4). Combining all terms, we find that the curl of the electric drift can be written as

$$B \nabla \times \mathbf{V}_E = (\nabla_{\perp}^2 \phi) \mathbf{b} + (\nabla_{\perp} \phi \cdot \nabla) \mathbf{b} - (\mathbf{b} \cdot \nabla) \nabla_{\perp} \phi - (\nabla \ln B \cdot \nabla_{\perp} \phi) \mathbf{b}. \quad (\text{A.6})$$

The third term on the right hand side is small since variations perpendicular to  $\mathbf{B}$  dominate those along the field. This is generally known as the *flute ordering*. This term exactly vanishes for flute perturbations which are symmetric along the field lines. Finally, the magnetic field variation is weak compared to that of the electrostatic potential. Indeed,  $k_{\perp}R \gg 1$ , where  $k_{\perp}$  and  $R$  is the perpendicular wave number and magnetic field radius of curvature. The curl of the electric drift can thus to lowest order be approximated by  $(\nabla_{\perp}^2 \phi) \mathbf{b}$ , ie.

$$\Omega = \nabla \times v_E = B^{-2} \nabla \times (\mathbf{B} \times \nabla \phi) = \nabla_{\perp}^2 \phi,$$

which is indeed Eq. (5.6).

# Appendix B

## Used Abbreviations and Symbols

$k_B$	Boltzmann constant: $k_B = 1.38 \times 10^{-23} \text{JK}^{-1}$
$e$	electron charge, $e = -1.6 \times 10^{-19} \text{C}$
$eV$	Electronvolt: energy, $1eV = 1.6 \times 10^{-19} \text{J}$
$L_c$	Connection Length, i.e. distance along magnetic field line with respect to a divertor target (where $L_c = 0$ )
$R, a$ $r = \perp, \parallel$	Major=875 mm, Minor=240 mm radius direction radial = cross-field, parallel to $\mathbf{B}$
HFS	high-field-side
LFS	low-field-side
LCFS	Last Closed (magnetic) Flux Surface, i.e. Separatrix, Fig. 3.1
PDF	Probability distribution function
SOL	Scrape-Off Layer, Fig. 3.1, layer with open field lines crossing limiter or divertor plate; SOL is radially outside separatrix
VSL	Velocity Shear Layer

Table B.1: Units, coordinates and abbreviations

$\tilde{n}$	fluctuation of $n$ ; $\tilde{n} \stackrel{\text{def}}{=} n - \langle n \rangle \Rightarrow \langle \tilde{n} \rangle \equiv 0$
$\propto$	proportionality; $n \propto p \Leftrightarrow n = k \cdot p$ , $k = \text{const}$
$\equiv$	equivalent (by definition)
$\stackrel{\text{def}}{=}$	defined
$\simeq$ or $\sim$	nearly equal
$\langle \dots \rangle$	in time mean value; $\langle n \rangle \stackrel{\text{def}}{=} \frac{1}{T} \int_a^{a+T} n(t) dt$
(...)	equation
[...]	bibliography citation, p. 157
$A$	inverse relative fluctuation level, $A \stackrel{\text{def}}{=} \mu/\sigma \equiv \langle n \rangle / \sqrt{\langle (n - \langle n \rangle)^2 \rangle}$
$\mathbf{B}, B_T, B_{\text{pol}}$	(Toroidal, Poloidal) magnetic field
$c_s = \sqrt{\frac{k_B(T_e + T_i)}{m_i}}$	ion sound speed, in SOL typically 40-80 km/s
$\lambda_D = \sqrt{\frac{\epsilon_0 k_B T_e}{n_e e^2}}$	Debye length, for $T_e = 20 \text{ eV}$ , $n_e = 10^{19} \text{ m}^{-3}$ in the SOL $\lambda_D = 10 \text{ } \mu\text{m}$
$\rho_L = c_s m / (eB)$	Larmor (or gyro) radius, in SOL $\approx 30 \text{ } \mu\text{m}$ for electrons and $\approx 0.7 \text{ mm}$ for ions
$\rho_s = \sqrt{\rho^*} = c_s / \omega_{\text{ci}}$	hybrid thermal Larmor radius, is identical to $\rho_{\text{Li}}$ for $T_i = T_e$
$\omega_c = eB/m$	Cyclotron frequency. In TCV edge for $\text{D}^+$ ions/electrons $\omega_{\text{ci}} = 60 \text{ MHz}$ , $\omega_{\text{ce}} = 220 \text{ GHz}$
D, T	deuterium ${}^2_1\text{H}$ , tritium ${}^3_1\text{H}$
$E_{\text{pol}}, E_r$	Poloidal, Radial electric field, $\mathbf{E} = -\nabla\phi$
$\phi$	plasma potential
$I_p$	Total Plasma Current
$I_s$	Ion Saturation Current, defined as $I_s \stackrel{\text{def}}{=} I(V \rightarrow -\infty)$
$V_{\text{fl}}$	Floating Potential defined as $I(V_{\text{fl}}) = 0$
$(m_e, m_i) m$	(Electron, Ion) Mass: $m_e = 9 \times 10^{-31} \text{ kg}$ , $\frac{m_i}{Z} = m_u = 1823 m_e$
$\epsilon_0$	dielectric constant $\epsilon_0 = 8.854 \times 10^{-12} \text{ Fm}^{-1}$
$n_e, n_i$	electron, ion plasma density
$q$	$q = \frac{r B_T}{R B_{\text{pol}}}$ the cylindrical Safety factor [2]
$(T_{e,i}) T$	(electron, ion) Temperature, always in units of [eV], i.e. [eT] = Joule
$M_{\parallel}$	parallel Mach number

Table B.2: Used symbols

# Appendix C

## Acknowledgments

Great thanks to all of you who helped me to write this thesis:

- thanks to my supervisor Richard A. Pitts for his magnificent leadership and advices in both professional and personal life, for so much of his always precious time dedicated to this thesis, especially for patience with correcting my dreadful English style - if you appreciate the way the thesis is written, the credit is purely to him :-)
- thanks to Jonathan P. Graves for his statistical knowledge and fruitful collaboration
- thanks to Marco Wischmeier and Stefan Müller for many fruitful discussions
- thanks to Peter C. Stangeby, O. V. Batishchev and A. Loarte for long-lasting and fruitful collaboration on numerical modelling [108]
- thanks the Risø "turbulent" group for collaboration: Anders H. Nielsen, Volker Naulin, Jens Juul Rasmussen and especially to Odd Erik Garcia for many useful discussions and lots of precise answers
- thanks to all other collaborators I had the pleasure to work with: Marco Wischmeier, Janos Marki, Wojtek Fundamenski, Barbora Gulejová, Jan Mlynář, Irina Condrea
- thanks the entire tokamak CASTOR group for the help with first steps on the way of science
- thanks to Roland Behn, Yanis Andrebe and Ge Zhuang for the edge Thomson scattering
- thanks for great technical help with computers to Xavier Llobet and Pierre Etienne
- thanks to the University of California at San Diego for having constructed and loaned the reciprocating probe to CRPP
- thanks to the CRPP mechanical workshop for the probe head modifications: Patrice Gorgerat, René Chavan, and especially Pascal Conti for his great mechanical abilities of rebuilding and preparing the probe again and again
- thanks to the electronic workshop for delivering the electronic hardware without which this thesis would not be possible, especially to Pierre Lavanchy and J.-C. de Giorgi for their willingness
- thanks to Jo Lister for offering a great job to my wife

- thanks to our perfect secretary, Edith Grüter, for that no administrative task has ever been a problem for me
- thanks to Prof. M. Quang Tran and Dr. Kurt Appert for having accepted me as PhD-student
- thanks to the entire CRPP group for running the TCV tokamak
- finally, I am thankful to Prof. H. Brune, Dr. R. A. Pitts, Dr. M. Endler, Dr. C. Hidalgo, Prof. A. Bay for accepting to be members of the thesis jury

Thanks a lot to all of my friends who helped me to stay human during this five-years research period, especially

- thanks to my beloved wife Šárka Horáčková ♡ for the everyday great private life and her patience and sacrifice due to living in a foreign country
- thanks to the CRPP friends who made my five years in Switzerland more friendly, especially to Richard, Jon, Maqbool, Yann, Stefan, Jan, Janos, Barbora, Costanza, Anja, Alessandro, Stefan, Daniel, Sudheer, ...
- thanks to our many Czech friends for their visits in Switzerland and thus healing our homesick
- díky tátovi, Irce a Šárce za jejich zájem o vědu

Thanks to Switzerland for financing this thesis through the Fonds National Suisse de la Recherche Scientifique.

Thanks  
Merci  
Děkuji

# Bibliography

- [1] G McCracken and P E Stott. *Fusion, the energy of the universe*. ISBN: 0-12-481851-X. Elsevier Academic press, 2005.
- [2] J.A. Wesson. *Tokamaks*. Clarendon Press, Oxford, 3rd edition, 2004.
- [3] Pitts R. A., Buttery R. J., and Pinches S. Fusion: the way ahead. *Physics World*, (50), 2006.
- [4] Lawson J D. Some criteria for a power producing thermonuclear reactor. *Proceedings of the physical society of London section B*, **70**(1):6–10, 1957.
- [5] the ITER Director. Summary of the ITER final design report. 2001. Available on [www.iter.org](http://www.iter.org).
- [6] F.F. Chen. *Introduction to Plasma Physics*. ISBN 0-471-55951-2. Plenum Press, New York, 1974.
- [7] P. C. Stangeby et al. A tutorial on some basic aspects of divertor physics. *Plasma Phys. Control. Fusion*, **42**:B271, 2000.
- [8] P. C. Stangeby. *The plasma boundary of magnetic fusion devices*. Institute of physics publishing, Bristol and Philadelphia, 2000.
- [9] ASDEX team. The H-mode of ASDEX. *Nucl. Fusion*, **29**(11):1959–2040, 1989.
- [10] B. Goncalves. *Statistical properties of turbulence: a new approach to characterize transport in fusion plasmas*. PhD thesis, Universidade Técnica de Lisboa, Spain, 2003.
- [11] R. J. Goldston and P. H. Rutherford. *Introduction to plasma physics*. Bristol: Institute of Physics Publishing, 1997.
- [12] G Y Antar, G Counsell, and Yang Yu *et al.* Universality of intermittent convective transport in the scrape-off layer of magnetically confined devices. *Phys. Plasmas*, **10**:419, 2003.

- [13] R.A. Pitts, W. Fundamenski, S.K. Erents, Y. Andrew, A. Loarte, C. Silva, and JET-EFDA contributors. Far SOL ELM ion energies in JET. *Nucl. Fusion*, **46**:82–98, 2006.
- [14] Marco Wischmeier. *Simulating divertor detachment in the TCV and JET tokamaks*. PhD thesis, École Polytechnique Fédérale de Lausanne, 2004. <http://library.epfl.ch/theses/>.
- [15] J.W. Connor, G.F. Counsell, and S.K. Erents *et al.* Comparison of theoretical models for scrape-off layer widths with data from COMPASS-D, JET and Alcator C-Mod. *Nucl. Fusion*, **39**(2):169–188, 1999.
- [16] A. Loarte. Comparison of B2-EIRENE calculations with multi-machine experimental measurements. *Journal of Nuclear Materials*, **266-269**:1123, 1999.
- [17] D. Bohm. In *The characteristics of electrical discharges in magnetic fields*.
- [18] B. LaBombard *et al.* Cross-field plasma transport and main-chamber recycling in diverted plasmas on Alcator C-Mod. *Nucl. Fusion*, **40**(12):2041, 2000.
- [19] B. LaBombard *et al.* Particle transport in the scrape-off layer and its relations to discharge density limit in Alcator C-Mod. *Phys. Plasmas*, **8**(5):2107, 2001.
- [20] R. Schneider, X. Bonnin, and K. Borrass *et al.* Plasma edge physics with B2-Eirene. *Contributions to Plasma Physics*, **46**(1-2):3–191, 2006.
- [21] D G Whyte, B L Lipschultz, and P C Stangeby *et al.* The magnitude of plasma flux to the main-wall in the DIII-D tokamak. *Plasma Phys. Control. Fusion*, **47**:1579–1607, 2005.
- [22] P.A. Davidson. *Turbulence (an introduction for scientists and engineers)*. ISBN 019852948. Oxford university press [www.oup.com](http://www.oup.com), 2004.
- [23] A. N. Kolmogorov. The local structure of turbulence in incompressible viscous fluid for very large Reynolds numbers. *Proc. R. Soc. Lond. A*, **434**:9–13, 1991. First published in Russian in Dokl. Akad. Nauk SSSR (1941) **30** 4.
- [24] Volker Naulin. Aspects of flow generation and saturation in drift-wave turbulence. *New Journal of Physics*, **4**:28.1–28.18, 2002.
- [25] M. Evans, N. Hastings, and B. Peacock. *Statistical distributions*. ISBN 0-471-55951-2. John Wiley & sons, Inc., 1993.
- [26] P. Bak, C. Tang, and K. Wiesenfeld. *Phys. Rev. Lett.*, **59**:381–384, 1987.
- [27] M. Boguna and A. Corral. Long-Tailed Trapping Times and Lévy Flights in a Self-Organized Critical Granular System. *Phys. Rev. Lett.*, **78**:4950, 1997.

- [28] L Garcia and B A Carreras. Avalanche properties in a transport model based on critical-gradient fluctuation dynamics. *Phys. Plasmas*, **12**:092305, 2005.
- [29] D.E. Newman, B.A. Carreras, P.H. Diamond, and T.S. Hahm. The dynamics of marginality and self-organized criticality as a paradigm for turbulent transport. *Phys. Plasmas*, **3**(5):1858, 1995.
- [30] J.P. Graves, R.O. Dendy, K.I. Hopcraft, and E. Jakeman. The role of clustering effects in interpreting nondiffusive transport measurements in tokamaks. *Phys. Plasmas*, **9**(5):1596, 2002.
- [31] B.D. Dudson, R.O. Dendy, A. Kirk, H. Meyer, and G.F. Counsell. Comparison of L- and H-mode plasma edge fluctuations in MAST. *Plasma Phys. Control. Fusion*, **47**:885–901, 2005.
- [32] J. Horacek, O.E. Garcia, and J.P. Graves *et al.* Plasma electrostatic turbulence in TCV tokamak edge: direct comparison of experiment with 2D simulation. 2005. Oral at the EPS conference, Tarragona, Spain, <http://eps2005.ciemat.es/>.
- [33] J. Horacek, R.A. Pitts, and J.P. Graves. Overview of edge electrostatic turbulence experiments on TCV. *Czechoslovak Journal of Physics*, **55**(3):271–283, 2005. Talk at the Workshop 'Electric Fields Structures and Relaxation in Edge Plasmas' in Nice, France (2004).
- [34] J.P. Graves, J. Horacek, R.A. Pitts, and K.I. Hopcraft. Self-similar density turbulence in the TCV tokamak scrape-off layer. *Plasma Phys. Control. Fusion*, **47**:L1–L9, 2005.
- [35] B. A. Carreras *et al.* Experimental evidence of long-range correlations and self-similarity in plasma fluctuations. *Phys. Plasmas*, **6**(5):1885, 1999.
- [36] P.S. Addison. *Fractals and chaos*. ISBN 0-7503-0399-9. Institute of Physics Publishing, Dirac House, Temple Back, Bristol, UK, 1997.
- [37] B. A. Carreras, B. van Milligen, M. A. Pedrosa, R. Balbin, and C. Hidalgo *et al.* Long-range time correlations in plasma edge turbulence. *Phys. Rev. Lett.*, **80**(20):4438, 1998.
- [38] B. A. Carreras, B. van Milligen, M. A. Pedrosa, R. Balbin, and C. Hidalgo *et al.* Self-similarity of the plasma edge fluctuations. *Phys. Plasmas*, **5**(10):3632, 1998.
- [39] C. Hidalgo, B. Goncalves, and M.A. Pedrosa *et al.* Experimental evidence of fluctuations and flows near marginal stability and dynamical interplay between gradients and transport in the JET plasma boundary region. *Journal of Nuclear Materials*, **313-316**:863–867, 2003.

- [40] G S Kirnev, V P Budaev, and S A Grashin *et al.* Intermittent transport in the plasma periphery of the T-10 tokamak. *Plasma Phys. Control. Fusion*, **46**:621, 2004.
- [41] T. S. Lee. *IEEE transactions on systems, man and cybernetics—part B: cybernetics*, **30**(4):549, 2000.
- [42] W M Manheimer. Marginal stability analysis - simpler approach to anomalous transport in plasmas. 1977. Bulletin of APS 22(4),609.
- [43] C. Hidalgo, M. A. Pedrosa, and C. Silva *et al.* Radial structure of reynolds stress in the plasma boundary of stellarator and tokamak plasmas. volume **22C**, page 2326. ICPP&EPS Conf. on Contr. Fusion and Plasma Physics, Prague, Czech republic, 1998.
- [44] C. Hidalgo, B. Goncalves, C. Silva, and *et al.* Experimental Investigation of Dynamical Coupling between Turbulent Transport and Parallel Flows in the JET Plasma-Boundary Region. *Phys. Rev. Lett.*, **91**:065001, 2003.
- [45] M Tendler. Different scenarios of transitions into improved confinement modes. *Plasma Phys. Control. Fusion*, **39**:B371–B382, 1997.
- [46] M Hron *et al* (incl. J Horacek). Edge turbulence at plasma polarisation on the CASTOR tokamak. *Czechoslovak Journal of Physics*, **49**:181, 1999.
- [47] J Bleuel, M Endler, and H Niedermeyer *et al.* The spatial structure of edge fluctuations in the Wendelstein 7-AS stellarator. *New Journal of Physics*, **4**:38, 2002.
- [48] R. A. Moyer, K. H. Burrell, and T. N. Carlstrom *et al.* Beyond paradigm: Turbulence, transport, and the origin of the radial electric field in low to high confinement mode transitions in the DIII-D tokamak. *Phys. Plasmas*, **2**(6):2397, 1995.
- [49] O E Garcia, V Naulin, A H Nielsen, and J Juul Rasmussen. Turbulence and intermittent transport at the boundary of magnetized plasmas. *Phys. Plasmas*, **12**:062309, 2005.
- [50] O E Garcia, N H Bian, and V Naulin *et al.* Two-dimensional convection and interchange motions in fluids and magnetized plasmas. *Phys. Scripta*, **T122**:104–124, 2006.
- [51] G R Tynan, C Holland, and J H Yu *et al.* Observation of turbulent-driven shear flow in a cylindrical laboratory plasma device. *Plasma Phys. Control. Fusion*, **48**:S51, 2006.
- [52] G. McKee *et al.* Observation and characterization of radially sheared zonal flows in DIII-D. *Plasma Phys. Control. Fusion*, **45**:A477–A485, 2003.

- [53] S. I. Krasheninnikov and A. I. Smolyakov. On neutral wind and blob motion in linear devices. *Phys. Plasmas*, **10**:3020, 2003.
- [54] O E Garcia. Collective motions in non-uniformly magnetized plasmas. *Euro. J. Phys.*, **24**:331–339, 2003.
- [55] H.M. Mott-Smith and I. Langmuir. The theory of collectors in gaseous discharges. *Physical Review*, **28**:727, 1926.
- [56] C. Hidalgo, R. Balbin, and M.A. Pedrosa *et al.* Experimental evidence of significant temperature fluctuations in the plasma edge region of the TJ-I tokamak. *Phys. Rev. Lett.*, **69**(8):1205, 1992.
- [57] D L Rudakov, J A Boedo, and R A Moyer *et al.* Fluctuation-driven transport in the DIII-D boundary. *Plasma Phys. Control. Fusion*, **44**(717), 2002.
- [58] M. Endler, H. Niedermeyer, and L. Giannone *et al.* Measurements and modelling of electrostatic fluctuations in the scrape-off layer of ASDEX. *Nucl. Fusion*, **35**:1307, 1995.
- [59] R Schrittwieser, J Adamek, and P Balan *et al.* Measurements with an emissive probe in the CASTOR tokamak. *Plasma Phys. Control. Fusion*, **44**:567–578, 2002.
- [60] J. Adamek, J. Stockel, and I. Duran *et al.* Comparative measurements of the plasma potential with the ball-pen and emissive probes on the CASTOR tokamak. *Czechoslovak Journal of Physics*, **55**(3):235, 2005.
- [61] J P Gunn, C Boucher, P Devynck, I Duran, K Dyabilin, J Horacek, M Hron, J Stockel, G Van Oost, H Van Goubergen, and F Zacek. Edge flow measurements with Gundestrup probes. *Phys. Plasmas*, **8**(5):1995–2001, 2001.
- [62] J P Gunn, R Panek, J Stockel, G Van Oost, and T Van Rompuy. Simultaneous measurements of fluctuations of ion current, electron temperature, and floating potential with a tunnel probe. *Czechoslovak Journal of Physics*, **55**(3):255, 2005.
- [63] G. F. Matthews. Tokamak plasma diagnostic by electrical probes. *Plasma Phys. Control. Fusion*, **36**:1595, 1994. Review article.
- [64] K. Rypdal V. I. Demidov, S. V. Ratynskaia. Electric probes for plasmas: The link between theory and instrument. *Review of Scientific Instruments*, **73**(10):3409–3439, 2002. Review article.
- [65] S H Mueller, A Fasoli, and B Labit *et al.* Basic turbulence studies on TORPEX and challenges in the theory-experiment comparison. *Phys. Plasmas*, **12**:090906, 2005.
- [66] E Martines, M Hron, and J Stockel. Coherent structures in the edge turbulence of the CASTOR tokamak. *Plasma Phys. Control. Fusion*, **44**:351–359, 2002.

- [67] P C Stangeby. *The interpretation of plasma probes for fusion experiments*. Plasma diagnostics, 1989.
- [68] J.A. Boedo *et al.* Intermittent convection in the boundary of DIII-D. *Journal of Nuclear Materials*, 313-316:813–819, 2003.
- [69] S.J. Zweben, R.J. Maqueda, and D.P. Stotler *et al.* High-speed imaging of edge turbulence in NSTX. *Nucl. Fusion*, **44**:134–153, 2004.
- [70] S. J. Zweben. Search for coherent structure within tokamak plasma turbulence. *Phys. Fluids*, **28**:974, 1985.
- [71] J. L. Terry, S. J. Zweben, O. Grulke, M J. Greenwald, and B. LaBombard. Velocity fields of edge/scrape-off-layer turbulence in Alcator C-Mod. *Journal of Nuclear Materials*, **337-339**:322–326, 2005.
- [72] G. R. McKee, R. Ashley, and R. Durst *et al.* The beam emission spectroscopy diagnostic on the DIII-D tokamak. *Review of Scientific Instruments*, **70**(1):913, 1999.
- [73] M. Endler. Turbulent SOL transport in stellarators and tokamaks. *Journal of Nuclear Materials*, **266-269**:84, 1999.
- [74] D.L. Rudakov, J.A. Boedo, R.A. Moyer, and P.C. Stangeby *et al.* Far SOL transport and main wall plasma interaction in DIII-D. *Nucl. Fusion*, **45**:1589–1599, 2005.
- [75] J. A. Boedo *et al.* Transport by intermittent convection in the boundary of the DIII-D tokamak. *Phys. Plasmas*, **8**:4826, 2001.
- [76] B. A. Carreras, V. E. Lynch, and B. LaBombard. Structure and properties of the electrostatic fluctuations in the far scrape-off layer region of Alcator C-Mod. *Phys. Plasmas*, **8**:3702, 2001.
- [77] P C Liewer. . *Nucl. Fusion*, **25**:543, 1985.
- [78] G. Vayakis. *Anomalous transport in the tokamak edge*. PhD thesis, University of Oxford, 1991.
- [79] G.A. Hallock, A.J. Wootton, and R.L. Hickok. Space-potential and density fluctuations in the ISX-B tokamak. *Phys. Rev. Lett.*, **59**(12):1301, 1987.
- [80] C. Hidalgo, B. Goncalves, M.A. Pedrosa, and *et al.* . *Plasma Phys. Control. Fusion*, **44**:1557, 2002.
- [81] B. A. Carreras, B. van Milligen, and C. Hidalgo *et al.* Self-similarity properties of the probability distribution function of turbulence-induced particle fluxes at the plasma edge. *Phys. Rev. Lett.*, **83**(18):3653, 1999.

- [82] S. I. Krasheninnikov *et al.* Modelling of fast transport in the SOL. 2002. 2nd ITPA SOL and divertor topical group meeting, CRPP Lausanne.
- [83] D.A. D'Ippolito, J.R. Myra, S.I. Krasheninnikov, G.Q. Yu, and A.Yu. Pigarov. Blob transport in the tokamak scrape-off-layer. *Contributions to Plasma Physics*, **44**(1-3):205–216, 2004.
- [84] N. Bian, S. Benkadda, J.-V. Paulsen, and O.E. Garcia. Blobs and front propagation in the scrape-off layer of magnetic confinement devices. *Phys. Plasmas*, **10**(3):671–676, 2003.
- [85] D. A. D'Ippolito *et al.* Cross-field blob transport in tokamak scrape-off-layer plasmas. *Phys. Plasmas*, **9**(1):222, 2002.
- [86] O E Garcia, N H Bian, V Naulin, A H Nielsen, and J Juul Rasmussen. Mechanism and scaling for convection of isolated structures in nonuniformly magnetized plasmas. *Phys. Plasmas*, **12**:090701, 2005.
- [87] S. I. Krasheninnikov. On scrape off layer plasma transport. *Physics Letters A*, **283**:368, 2001.
- [88] W. Fundamenski, O.E. Garcia, V. Naulin, R.A. Pitts, A.H. Nielsen, J J Rasmussen, J. Horacek, and J.P. Graves. Neoclassical dissipation and parallel losses in interchange driven scrape-off layer turbulence. *Nucl. Fusion*, 2006.
- [89] G. Q. Yu, S. I. Krasheninnikov, and P. N. Guzdar. Two-dimensional modelling of blob dynamics in tokamak edge plasmas. *Phys. Plasmas*, **13**:042508, 2006.
- [90] N. Bisai, A. Das, and S. Deshpande *et al.* Simulation of plasma transport by coherent structures in scrape-off-layer tokamak plasmas. *Phys. Plasmas*, **11**(8):4018, 2004. Importance of electron energy equation in 2D interchange simulations.
- [91] Y. Sarazin *et al.* Theoretical understanding of turbulent transport in the SOL. *Journal of Nuclear Materials*, **313-316**:796–803, 2003.
- [92] P. Ghendrih *et al.* Theoretical analysis of the influence of external biasing on long range turbulent transport in the scrape-off layer. *Nucl. Fusion*, **43**:1013–1022, 2003.
- [93] Y. Sarazin and Ph. Ghendrih. Intermittent particle transport in two-dimensional edge turbulence. *Phys. Plasmas*, **5**(12):4214, 1998.
- [94] K. Dyabilin, R. Klima, I. Duran, J. Horacek, M. Hron, P. Pavlo, J. Stockel, and F. Zacek. Modelling of effect of sheared poloidal flow on electrostatic turbulence on CASTOR tokamak. *Czechoslovak Journal of Physics*, **51**(10):1107, 2001.
- [95] B. Scott. Three-dimensional computation of collisional drift wave turbulence and transport in tokamak geometry. *Plasma Phys. Control. Fusion*, **39**:471–504, 1997.

- [96] T.D. Rognlien, M.V. Umansky, and X.Q. Xu *et al.* Simulation of plasma fluxes to material surfaces with self-consistent edge turbulence and transport for tokamaks. *Journal of Nuclear Materials*, **337-339**:327–331, 2005.
- [97] X.Q. Xu, R.H. Cohen, and G.D. Porter *et al.* Turbulence in boundary plasmas. *Journal of Nuclear Materials*, **266-269**:993–996, 1999.
- [98] D. A. Russell, D. A. D’Ippolito, and J. R. Myra *et al.* Blob dynamics in 3D BOUT simulations of tokamak edge turbulence. *Phys. Rev. Lett.*, **93**:265001.
- [99] X. Q. Xu, W. M. Nevins, and T. D. Rognlien *et al.* Transitions of turbulence in plasma density limits. *Phys. Plasmas*, **10**:1773, 2003.
- [100] M. Greenwald. *Nucl. Fusion*, **28**:2199, 1988.
- [101] J. A. Boedo *et al.* Fast scanning probe for tokamak plasmas. *Review of Scientific Instruments*, **69**(7):2663, 1998.
- [102] F. Hoffmann and G. Tonetti. Tokamak equilibrium reconstruction using Faraday rotation measurements. *Nucl. Fusion*, **39**(10):1871, 1988.
- [103] J-M. Moret. A software package to manipulate space dependencies and geometry in magnetic confinement fusion. *Review of Scientific Instruments*, **76**:073507, 2005.
- [104] R. A. Pitts, I. Duran, S. K. Erents, and J. Horacek *et al.* Retarding Field Analyser Measurements in the JET Plasma Boundary. volume **27A**, page P2.84. ECA, 2003. Poster at EPS conference, the corresponding paper at [http://epsppd.epfl.ch/StPetersburg/PDF/P2\\_084.PDF](http://epsppd.epfl.ch/StPetersburg/PDF/P2_084.PDF).
- [105] R.A. Pitts, J.P. Coad, and D.P. Coster *et al* (including J. Horacek). Material erosion and migration in tokamaks. *Plasma Phys. Control. Fusion*, **47**:B303–B322, 2005. Invited talk at EPS conference, Tarragona, Spain.
- [106] J.-M. Moret, F. Buhlmann, and D. Fasel *et al.* Magnetic measurements on the TCV Tokamak. *Review of Scientific Instruments*, **69**(6):2333, 1998.
- [107] I. H. Hutchinson. A fluid theory of ion collection by probes in strong magnetic fields with plasma flow. *Phys. Fluids*, **30**(12):3777, 1987.
- [108] J. Horacek, R.A. Pitts, P.C. Stangeby, O.V. Batishchev, and A. Loarte. Predicted effects of parallel temperature gradients on the overestimation of TCV divertor target Langmuir probe  $T_e$  measurements. *Journal of Nuclear Materials*, **313-316**:931, 2003. Poster at PSI-15 conference in Gifu, Japan 2002, and also published as LRP **734/02**.
- [109] J. Horacek. Turbulent structures in tokamak plasma, 2000. Master thesis, <http://go.to/horacek/thesis>.

- [110] J. A. Boedo *et al.* On the harmonic technique to measure electron temperature with high time resolution. *Review of Scientific Instruments*, **70**(7):2997–3006, 1999.
- [111] P.C. Stangeby, G.M. McCracken, S.K. Erents, and G. Matthews. DITE Langmuir probe results showing probe-size and limiter-shadow effects. *J. Vac. Sci. Technol. A*, **2**(2):702, 1984.
- [112] B. LaBombard. An interpretation of fluctuation induced transport derived from electrostatic probe measurements. *Phys. Plasmas*, **9**(4):1300–1311, 2002.
- [113] S. J. Zweben and R. W. Gould. *Nucl. Fusion*, **25**:171, 1985.
- [114] P. C. Stangeby. Measuring plasma drift velocities in tokamak edge plasmas using probes. *Phys. Fluids*, **27**(11):2699, 1984.
- [115] K-S. Chung and I.H. Hutchinson. Kinetic theory of ion collection by probing objects in flowing strongly magnetized plasmas. *Phys. Rev. A*, **38**(9):4721–4731, 1988.
- [116] I. H. Hutchinson. Ion collection by probes in strong magnetic fields with plasma flow. *Phys. Rev. A*, **37**(11):4358, 1988.
- [117] P J Harbour and G Proudfoot. Mach number deduced from probe measurements in the divertor and boundary layer of DITE. *Journal of Nuclear Materials*, **121**:222–228, 1984.
- [118] G Proudfoot, P J Harbour, J Allen, and A Lewis. Poloidal and radial variations in plasma transport in a limiter scrape-off layer in DITE. *Journal of Nuclear Materials*, **128&129**:180–185, 1984.
- [119] P R Tapster, A R Weeks, P N Pusey, and E Jakeman. Analysis of probability-density functions for laser scintillations in a turbulent atmosphere. *J. Opt. Soc. Am.*, **6**:782–785, 1989.
- [120] Bramwell S T, Holdsworth P C W, and Pinton J-F. *Nature*, **396**:552, 1998.
- [121] E. Jakeman. On the statistics of K-distributed noise. *J. Phys. A: Math. Gen.*, **13**:31–48, 1980.
- [122] S T Bramwell, T Fennell, P C W Holdsworth, and B Portelli. Universal fluctuations of the Danube water level: a link with turbulence, criticality and company growth. *Europhysics Letters*, **57**(3):310–314, 2002.
- [123] Pinton J-F, P C W Holdsworth, and R Labbe. *Physical Review E*, **60**:R2452, 1999.
- [124] van Milligen BP *et al.* Additional evidence for the universality of the probability distribution of turbulent fluctuations and fluxes in the scrape-off layer region of fusion plasmas. *Phys. Plasmas*, **12**(5):052507, 2005.

- [125] E. J. Gumbel. *Statistics of Extremes*. ISBN: 0486436047. Columbia University Press, New York, 1958.
- [126] S T Bramwell, J-Y Fortin, and P C W Holdsworth *et al.* *Physical Review E*, **63**:041106, 2001.
- [127] E Villermaux, P Marmottant, and J Duplat. *Phys. Rev. Lett.*, **92**:074501, 2004.
- [128] E. Jakeman and P N Pusey. Significance of K Distributions in Scattering Experiments. *Phys. Rev. Lett.*, **40**:546, 1978.
- [129] F. Sattin *et al.* *Phys. Plasmas*, **11**:5032, 2004.
- [130] B.P. Lathi. *Modern digital and analog communication systems*. ISBN 0-03-027933-X. The Dryden Press, USA, 1989.
- [131] M. Greenwald. Density limits in toroidal plasmas. *Plasma Phys. Control. Fusion*, **44**:R27, 2002.
- [132] Annual report, 2003. Published by CRPP EPFL Switzerland, <http://crppwww.epfl.ch>.
- [133] S. Franke. *Application of Thomson scattering at 1.06 $\mu$ s as a diagnostic for spatial profile measurements of electron temperature and density on the TCV tokamak*. PhD thesis, École Polytechnique Fédérale de Lausanne, 1997.
- [134] R Pasqualotto, P Nielsen, and L Guidicotti. The new RFX Thomson scattering system. *Review of Scientific Instruments*, **72**(1):1134, 2001.
- [135] B. LaBombard *et al.* Cross-Field Transport in the SOL: Its Relationship to Main Chamber and Divertor Neutral Control in Alcator C-Mod. 2000. IAEA Sorrento, Paper Ex5/6.
- [136] B Lipschultz, D Whyte, and B LaBombard. Comparison of particle transport in the scrape-off layer plasmas of Alcator C-Mod and DIII-D. *Plasma Phys. Control. Fusion*, **47**:1559–1578, 2005.
- [137] E. Sanchez, C. Hidalgo, and D. Lopez-Bruna *et al.* Statistical characterization of fluctuation waveforms in the boundary region of fusion and non-fusion plasmas. *Phys. Plasmas*, **7**(5):1408, 2000.
- [138] R Panek, L Krllin, and D Tskhakaya *et al.* Anomalous diffusion and radial electric field generation due to edge plasma turbulence. *Contributions to Plasma Physics*, **44**(1):203–204.
- [139] P. C. Stangeby. Modelling plasma contact with the main vessel walls of a divertor tokamak. *Phys. Plasmas*, **9**(8):3489, 2002.

- [140] G Y Antar. Universality of intermittent convective transport in the scrape-off layer of magnetically confined devices. *Contributions to Plasma Physics*, **44**:217–221, 2004.
- [141] O.E. Garcia, J. Horacek, R.A. Pitts, A.H. Nielsen, W. Fundamenski, J.P. Graves, V Naulin, and J. Juul Rasmussen. Evidence for interchange turbulence in the SOL of TCV. *Plasma Phys. Control. Fusion*, **48**(1), 2006.
- [142] O. E. Garcia, V. Naulin, A. H. Nielsen, and J. Juul Rasmussen. Computations of Intermittent Transport in Scrape-Off Layer Plasma. *Phys. Rev. Lett.*, **92**(165003), 2004.
- [143] O E Garcia. Two-field transport models for magnetized plasmas. *J. Plasma Physics*, **65**:81, 2001.
- [144] O.E. Garcia, R.A. Pitts, J. Horacek, A.H. Nielsen, W. Fundamenski, J.P. Graves, V Naulin, and J. Juul Rasmussen. Turbulence simulations of interchange motions and intermittent transport in TCV scrape-off layer plasmas. *Journal of Nuclear Materials*, 2007. Submitted to the PSI-17, Hefei Anhui, China, 22-26 May 2006.
- [145] O E Garcia. *Convective transport and sheared flows in fluids and magnetized plasmas*. PhD thesis, University of Tromsø, Norway, 2002.
- [146] G. Y. Antar, G. Counsell, and J.-W. Ahn. On the scaling of avaloids and turbulence with the average density approaching the density limit. *Phys. Plasmas*, **12**:082503, 2005.
- [147] R.A. Pitts, J. Horacek, and M. Wischmeier. *Journal of Nuclear Materials*, 2007. Submitted to the PSI-17 conference in Hefei Anhui, China, 2006.
- [148] R.A. Pitts and J. Horacek. Parallel SOL flows in TCV - first results. In *3rd SOL and Divertor ITPA meeting*, Lisbon, Portugal, 2004.
- [149] B. LaBombard et al. Transport-driven scrape-off-layer flows and the boundary conditions imposed at the magnetic separatrix in a tokamak plasma. *Nucl. Fusion*, **44**:1047, 2004.
- [150] S.K. Erents, R.A. Pitts, and W. Fundamenski *et al.* A comparison of experimental measurements and code results to determine flows in the JET SOL. *Plasma Phys. Control. Fusion*, **46**:1757, 2004.
- [151] N. Asakura *et al.* Plasma flow measurement in high- and low-field-side sol and influence on the divertor plasma in JT-60U. *Journal of Nuclear Materials*, **313-316**:820–827, 2003.
- [152] R. A. Pitts et al. Edge and divertor physics with reversed toroidal field in JET. *Journal of Nuclear Materials*, **337-339**:146–153, 2005. Presented at the PSI-16, Portland (ME), 2004.

- [153] G S Kirnev, G Corrigan, and D Coster *et al.* EDGE2D code simulations of SOL flows and in-out divertor asymmetries in JET. *Journal of Nuclear Materials*, **337-339**:271–275, 2005. Presented at PSI-16 Portland (ME), 2004.
- [154] A. V. Chankin. Classical drifts in the tokamak SOL and divertor: models and experiment. *Journal of Nuclear Materials*, **241-243**:199, 1997.
- [155] R. Schneider et al. B2-solps5.0: SOL transport code with drifts and currents. *Contributions to Plasma Physics*, **40**(3-4):328, 2000.
- [156] N. Asakura et al. Driving mechanism of sol plasma flow and effects on divertor performance in JT-60U. *Nucl. Fusion*, **44**:503, 2004.
- [157] N. Asakura, S. Sakurai, and M. Shimada *et al.* Measurement of Natural Plasma Flow along the Field Lines in the Scrape-Off Layer on the JT-60U Divertor Tokamak. *Phys. Rev. Lett.*, **84**(14):3093–3096, 2000.
- [158] R.A. Pitts, W Fundamenski, and S K Erents *et al.* Far SOL ELM ion energies in JET. *Nucl. Fusion*, **46**:82, 2006.
- [159] O F Castellanos, E Anabitarte, J M Senties, C. Hidalgo, and M A Pedrosa. Parallel flows and turbulence in a linear plasma machine. *Plasma Phys. Control. Fusion*, **47**:2067.

# Index

- ambipolar transport, 18
- anti-persistent, 32, 86
- arcing, 52, 61
- autocorrelation function, 78
- avalanche, 31, 45
  
- beam emission spectroscopy, 39
- blob formation, 122
- blobs, 42
- Bohm criterion, 18
- Bohm normalization, 99, 106
- Bohm scaling, 22, 120, 121
- boundary conditions, 102
- bursts, 38
  
- chaos, 27
- closure problem of turbulence, 34
- cluster parameter, 75
- collisionality, 101
- conditional averaging, 93
- correlation time, 78
- curvature operator, 99
  
- density limit, 46
- detachment, 17
- diamagnetic cancellation, 99
- diamagnetic drift, 99
- discharge groups, 125
- drift  $\nabla B \times \mathbf{B}$ , 16
- drift approximation, 98
- drift wave, 30, 44
  
- eddies, 27
- Electric field
  - radial,  $\mathbf{E}_r$ , 66
- energy cascade, 27, 86
- Engelhardt model, 93
  
- expectation value, 137
  
- forward field, 51
- fractals, 31
- Fusion, 13
  
- Gas puff imaging, 39
- Geodesic Acoustic Mode, 35
- Groups of shots, 126
  
- H-mode, 17
- Hurst exponent, 32, 78, 86
  
- interchange instability, 37, 44
- inverse energy cascade, 28, 81
  
- Kolmogorov 5/3 law, 28
  
- L-mode, 17
- Langmuir probe, 38, 61
- Larmor radius, 65
- last closed flux surface, 16
- Lawson criteria, 13
  
- main chamber recycling, 23, 93
- marginal stability, 33, 35
- microturbulence, 22
- multifractal behaviour, 32
  
- neoclassical transport, 22
- noise removal, 60
  
- persistent, 32, 86
- Pfirsch-Schlüter flow, 132
- plasma potential, 63
- plasma sheath, 62
- plasma wall interaction, 20
- polarization drift, 99
- power spectrum, 77

- probability distribution function, PDF, 73
- random walk, 32, 86
- reversed field, 51
- Reynolds number,  $Re$ , 27
- Reynolds stress, 33, 34, 137
  
- safety factor, 15
- sandpile, 28
- Scrape-Off Layer, 17
- self-organized criticality, 28, 109
- self-similar, 32
- separatrix, 17
- shear, 34, 86
- sheath, 18
- sound speed, 62
- statistical moments, 74
- streamers, 45
- structure function, 32, 78
  
- thin layer approximation, 44, 99
- tilting instability, 34, 105, 107
- Time
  - of energy confinement,  $\tau_e$ , 14
- Tokamak, 14, 16
- trailing wake, 122
- transport barriers, 34
- transport coefficients, 100
  
- vorticity, 99
  
- X-point, 17
  
- zonal flows, 34, 107

# Appendix D

## Curriculum Vitae

Name: Jan, Family name: Horáček

Date of birth: 24/10/1976

Place of birth: Valašské Meziříčí, Czech Republic

Nationality: Czech

### **Educational background:**

- Oct. 2000 - Jan. 2001 Doctoral study at the Department of Electronics and Vacuum Physics, Faculty of Mathematics and Physics, Charles University, Prague, Czech Republic, <http://www.mff.cuni.cz/>. Study cancelled because of movement to Switzerland.
- 1995 - 2000 Study of basic and later nuclear and particle physics at the Institute of Particle and Nuclear Physics of the Faculty of Mathematics and Physics, Charles University, Prague, Czech Republic. Study successfully finished with title Magister (Mgr.)
- 1990-1995 high school Gymnázium Fr. Palackého (<http://www.inext.cz/gfp/>) in Valašské Meziříčí, participation and some wins at the Czech physics olympiad
- 1984-1990 primary and secondary school in my native town Rožnov pod Radhoštěm ([www.roznov.cz](http://www.roznov.cz))

### **Employment and Experience**

- since May 2006: Institute of Plasma Physics, Czech Academy of Sciences, Prague, Czech Republic
- March 2001 - April 2006 assistant and PhD-student at TCV tokamak, CRPP EPFL, Lausanne, Switzerland, supervisor: Dr. R.A. Pitts
- Oct. 1996 - Jan. 2001 position at the CASTOR tokamak, Institute of Plasma Physics, Czech Academy of Sciences, Prague, Czech Republic, supervisor: RNDr. Jan Stöckel, CSc, [www.ipp.cas.cz](http://www.ipp.cas.cz)
- Aug. - Oct. 1999 summer student at the TCV tokamak, CRPP EPFL, Lausanne, Switzerland, supervisor: Dr. R.A. Pitts